Modeling and Numerical Simulation of Light Propagation through Biological Tissue with Implanted Structures

Chintha Chamalie Handapangoda
B.Sc.Eng.

Submitted in total fulfilment of the requirements of the degree of

Doctor of Philosophy

Department of Electrical and Computer Systems Engineering
MONASH UNIVERSITY
Clayton, Victoria, Australia.

November 2009

Copyright Notices

Notice 1

Notice 2

Contents

List of Figures

Summary

THIS dissertation proposes several numerical techniques for simulating laser pulse propagation through biological tissue with implants for sensing applications. The purpose of these implants is to enhance and condition the optical signals for better detection of the received signal. This work contributes to the development of methods for sensing and characterization of tissue properties and measuring concentrations of substances in blood or tissue fluid, thus making it possible to monitor these concentrations and detect anomalies.

The research was carried out in three major stages. In stage 1, a technique for simulating laser pulse propagation through tissue, which addresses some of the drawbacks of existing methods, was developed. The outcome of this stage was an efficient algorithm for solving the transient photon transport equation (PTE), which governs light propagation through tissue. The proposed algorithm was first implemented for the one-dimensional case and later extended for the two- and three-dimensional cases. This algorithm was also extended to inhomogeneous media.

The one-dimensional PTE is an integro-differential equation of four variables: distance, local zenith angle, local azimuthal angle and time. First, the original PTE was mapped to a moving reference frame co-moving with the incident pulse. This transformation eliminated the partial derivative term with respect to time in

the original equation. The dependence on the local azimuthal angle was then removed using the discrete ordinates method, which resulted in a set of coupled three-variable integro-differential equations. A Laguerre expansion was then used to represent the time dependency of this reduced PTE. With the Laguerre expansion, any arbitrary input pulse shape can be represented using a few polynomials, and also the causality is preserved. This step resulted in a two-variable integro-differential equation for each Laguerre coefficient. The dependence on the local zenith angle was removed by the use of the discrete ordinates method, thus resulting in a set of single-variable uncoupled differential equations. The Runge-Kutta-Fehlberg (RKF) method was then used to solve for the radiance.

In the proposed technique, all the sampling points in the time domain were obtained in a single execution of the algorithm, rather than having repeated executions for each time step as in time marching techniques used in most of the existing solution methods. This was made possible by expanding the time dependence using a Laguerre basis, thus making the proposed algorithm much faster when the intensity profile is required at a particular point or on a plane over a time interval. Also, since the RKF method was used to solve the final reduced equation, intensity profiles at several points and planes over the whole time spectrum were obtained in one execution of the algorithm. In addition, the causality of the system was implicitly imposed by the causal Laguerre polynomials. The use of the Runge-Kutta-Fehlberg method with respect to the spatial variable makes the extension to inhomogeneous media simple and straightforward. For the multi-dimensional cases, the Laguerre expansion was used to represent the time dependency as in the one-dimensional case. The discrete ordinates method was then used to solve for the radiance using a finite volume approach.

In stage 2, a technique for mapping the photon transport equation to Maxwell's

equations was developed. No work has been reported to date which addresses the problem of coupling the photon transport equation to Maxwell's equations. Since light propagation through tissue is modeled using the PTE and that through implants is modeled using Maxwell's equations, this mapping was required for simulating light propagation through tissue with implanted structures. The PTE solves for the radiance only. However, Maxwell's equations require electric and magnetic fields along with their phases. Therefore, the radiance profile obtained by solving the PTE had to be converted to an electromagnetic field, which involves constructing the phase from the radiance profile. For this purpose, the transport-of-intensity equation was solved using the full multigrid algorithm.

In the final stage, the numerical simulation of laser pulse propagation through biological tissue with implanted structures for sensing applications was carried out. Even though implanted structures within biological tissue have very useful and promising applications in the field of biomedical engineering, no work on the theoretical analysis and simulation of such compound structures has been reported in the research literature. In this dissertation, two examples, a metal screen with a slit implanted in tissue and a photonic crystal structure implanted in tissue, are considered. These simulations were carried out by integrating the work carried out in stages 1 and 2. The algorithm developed in stage 1 for solving the PTE was applied to simulate pulse propagation through the tissue layers. At the tissue-implant interface, the mapping of the PTE to Maxwell's equations, developed in stage 2, was applied. Electromagnetic propagation through the implanted structure was modeled using Maxwell's equations.

General Declaration

In accordance with Monash University Doctorate Regulation 17/ Doctor of Philosophy and Master of Philosophy (MPhil) regulations the following declarations are made:

I hereby declare that this thesis contains no material which has been accepted for the award of any other degree or diploma at any university or equivalent institution and that, to the best of my knowledge and belief, this thesis contains no material previously published or written by another person, except where due reference is made in the text of the thesis.

The core theme of the thesis is modeling and numerical simulation of light propagation through biological tissue with implanted structures. The ideas, development and writing up of all the work in the thesis were the principal responsibility of myself, the candidate, working within the Department of Electrical and Computer Systems Engineering under the supervision of Associate Professor Malin Premaratne.

Signed: Chintha C Handapangoda **Date** : November 2009

Education is that which remains when one has forgotten everything learned in school.

- Albert Einstein

Acknowledgements

I was very fortunate to have Assoc. Prof. Malin Premaratne as my main supervisor during my candidature as a PhD student. I believe, that with his advice and guidance I have been able to make a contribution to the field of biophotonics. His kind supervision is gratefully acknowledged. Also, many thanks are due to my associate supervisors, Assoc. Prof. James Friend and Dr. Leslie Yeo, for their support.

I extend my very special thanks to Assoc. Prof. David Paganin, for providing me with guidance and support during the second stage of the research, in formulating a mapping of the photon transport equation and Maxwell's equations. His kind advice is greatly appreciated.

I would also like to thank the administrative staff and the head of the Department of Electrical and Computer Systems Engineering for providing me with a very pleasant environment in which to study and work. Also, Ms Jane Moodie's assistance on reporting the research is gratefully acknowledged, and I wish to thank Dr. Alex McKnight for his proofreading. Special thanks are owed to the Monash Research Graduate School for providing me with a postgraduate scholarship, which enabled me to carry out a successful research program without having to worry about financial issues.

I sincerely thank my parents for their support throughout my life. Special thanks to my loving husband for his kind support, especially for taking care of our baby daughter Dinuri, which enabled me to spend more time on the research.

List of Publications

Journal Publications

1. Chintha C Handapangoda, Malin Premaratne, Leslie Yeo, James Friend, "Laguerre Runge–Kutta–Fehlberg Method for Simulating Laser Pulse Propagation in Biological Tissue," *IEEE Journal of Selected Topics in Quantum Electronics*, vol.14, no.1, pp.105–112, 2008.
2. Chintha C Handapangoda, Malin Premaratne, "An approximate numerical technique for characterizing optical pulse propagation in inhomogeneous biological tissue," *Journal of Biomedicine and Biotechnology*, vol.2008, pp.784354(5 pages), 2008.
3. Chintha C. Handapangoda, Malin Premaratne, David M. Paganin, Priyantha R. D. S. Hendahewa, "Technique for handling wave propagation specific effects in biological tissue: Mapping of the photon transport equation to Maxwell's equations," *Optics Express*, vol.16, no.22, pp.17792-17807, 2008.
4. Chintha C. Handapangoda, Malin Premaratne, "Implicitly causality enforced solution of multidimensional transient photon transport equation," *Optics Express*, vol.17, no.26, pp.23423-23442, 2009.

Conference Publications

1. Chintha C Handapangoda, Malin Premaratne, Leslie Yeo, James Friend, "Modeling of light propagation through biological tissues: a novel approach" in *Frontiers in the Convergence of Bioscience and Information Technologies (FBIT) 2007*, Jeju, Korea, October 2007.
2. Chintha C. Handapangoda, Malin Premaratne, David M. Paganin, "Simulation of a device concept for noninvasive sensing of blood glucose levels," in *Information and Automation for Sustainability, 2007. ICIAFS 2007. Third International Conference*, Melbourne, Australia, December 2007, pp. 3134.
3. Chintha C Handapangoda, Malin Premaratne, David M Paganin, "Simulation of embedded photonic crystal structures for blood glucose measurement using Raman spectroscopy" *2008 International Conference on Nanoscience and Nanotechnology*, Melbourne, Australia, February 2008.

CHAPTER 1

Introduction

This chapter presents a concise account of some of the available optical diagnostic techniques and introduces the research problem which has been investigated in this project and presented in this dissertation.

THE application of optical methods for biomedical applications and clinical therapeutics is emerging as a new technological paradigm [1]. Optical techniques for tissue diagnosis that are currently being developed offer significant advantages over standard biopsy and cytology techniques, in terms of both patient care and medical costs [2]. A good understanding of the relationship between the biochemical and morphological structure of cells and light scattering will assist the development of diagnostic applications [3]. Many light-based and spectroscopic techniques are already being practised in medical and other healthcare fields. Photodynamic therapy, the use of light to treat cancer, is one example [4].

There has been a rapid increase in the use of ultraviolet, visible and infrared radiation in both diagnostic and therapeutic medicine, and this has created a need to understand how this radiation propagates in tissue [5]. Such knowledge is

necessary for the optimum development of therapeutic techniques and for the quantitative analysis of diagnostic measurements [5]. For example, the local tissue temperature is of prime importance in laser surgery and depends, in turn, on the spatial distribution of the incident radiation. This variable is also of central importance in the photodynamic therapy of cancer where the local biological effect is directly related to the light fluence [5]. Diagnostic methods which use fluorescent, scattered or transmitted light to measure parameters such as drug concentration and blood oxygenation also require detailed information about the propagation of the excitation and observed light [5].

Biophotonics integrates four major technologies, namely, lasers, photonics, nanotechnology and biotechnology [4]. Light is an electromagnetic radiation consisting of oscillating electric and magnetic fields, and biological systems are molecular media [4]. Therefore, the interaction of biological media with light can be described by the electronic polarization of a molecule subjected to an electric field, which is called the electric dipole approximation [4]. The interaction of light with biological media is complex and involves a chain of events. These interactions can induce physical, thermal, mechanical and chemical effects from coupled events [4].

Most light-induced processes that are used in optical diagnostics and light-induced therapy are initiated by linear absorption of light. However, it is possible to induce nonlinear optical processes under an intense field using a short laser pulse [4]. In minimally invasive medicine such as optical biopsy, functional imaging and laser induced thermo-therapy, light in the range from 240 nm to 10,000 nm is used for diagnosis and therapy [6]. Lasers, which are the most commonly used light source for biophotonics, are devices that produce highly coherent, highly directional, monochromatic and intense beams of light [4]. The

usage of lasers can be categorized into two parts; the first category utilizes lasers as a highly concentrated source of photons and the second category utilizes the highly coherent nature of the light beam [4].

The main challenge in optical diagnosis is to understand the changes in the optical properties of tissues with abnormalities [6]. A change of physiological parameters will always change the amount and distribution of scattered light [6]. The potential of diagnostic optical imaging has generated considerable interest in the optical properties of tissues and cells at near infrared wavelengths where scattering is dominant over absorption [3].

The development of diagnostic techniques such as optical coherence tomography, confocal microscopy, light scattering spectroscopy and optical reflectance microscopy requires a fundamental understanding of how light scatters from normal and pathological structures within tissue [1]. These techniques are used for screening and diagnosis of epithelial precancerous tissues in various organs [1].

A concise account of some of the available optical diagnostic techniques is provided in the following section.

1.1 Optical diagnostic techniques

Optical diagnostic techniques include optical coherence tomography, confocal microscopy, light scattering spectroscopy, photodynamic therapy, laser-induced interstitial thermotherapy and optical biopsy. In addition to these, lasers are used in ophthalmology, gynaecology, urology and many other fields [3, 7–10]. Many clinical applications require the use of an endoscope, and therefore, many optical diagnostic methods employ fibre-optic probes. Hence, it is important to under-

stand the effects of various optical parameters on the collected signal in order to interpret these measurements appropriately [2].

Imaging techniques used for diagnostic purposes can be categorized as direct and indirect. Direct imaging techniques, such as confocal microscopy and optical coherence tomography (OCT), provide high resolution images of human tissue by constructing a three-dimensional backscattering map [3]. Indirect techniques such as near infrared spectroscopy relate changes in the amount of diffusely backscattered light to the optical properties of tissue [3]. The main problem with optical imaging of tissue is that the random scattering of light in tissue deteriorates the imaging resolution. Even early experiments had revealed that multiple scattering causes the images to appear extremely blurred [11]. There is a direct approach as well as an indirect approach to improve the performance of transillumination, thus enhancing imaging. The direct approach involves gating techniques which are used to isolate photons that are least scattered from the majority of multiply scattered photons. Some of these gating techniques rely on the fact that weakly scattered photons retain their initial coherence or polarization state. Others gate according to the lengths of the photon paths [11]. The indirect approach to imaging assumes that for a given set of measurements of transmitted light between two points there exists a unique three-dimensional distribution of internal scatterers and absorbers. In this approach, imaging is a task of solving an inverse problem using an appropriate model of photon transport [11].

Short light pulses can be used to enhance image resolution [12]. If a short light pulse is transmitted through biological tissue, the tissue properties can be extracted using various gating techniques such as time gating and polarization gating. These gating techniques are used to filter the weakly scattered photons from multiply scattered photons [12]. Time gating uses the fact that multiply

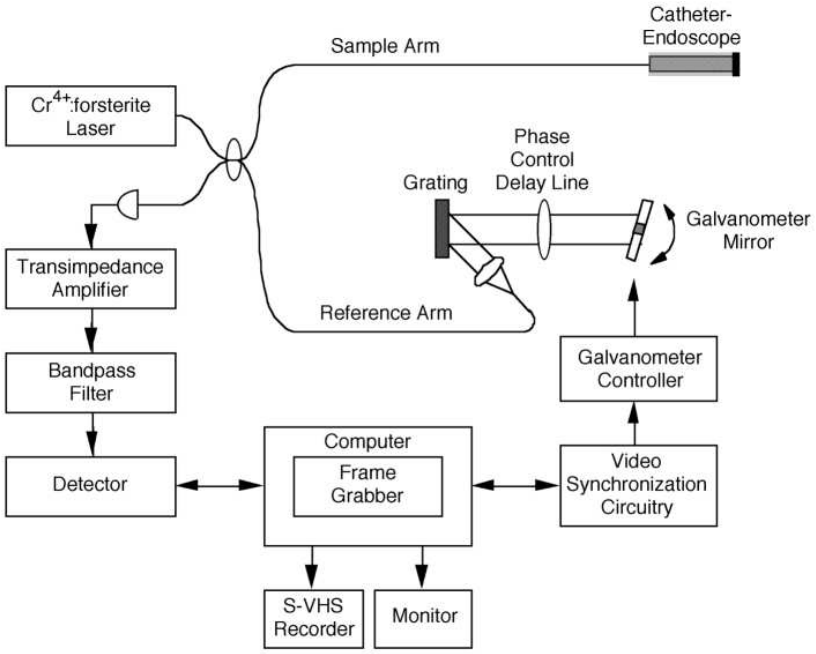

Figure 1.1: Schematic of the OCT system [19].

scattered photons have longer path lengths than weakly scattered photons [13, 14]. Polarization gating uses the fact that weakly scattered light preserves its original polarization better than multiply scattered light [15, 16]. Time-resolved spectroscopy is expected to be developed for optical imaging of biological tissues which strongly scatter and weakly absorb light [17]. This technique makes use of low-energy visible or near infrared light to probe highly scattering media to construct accurate qualitative or quantitative images of the optical properties of these media [18].

Among the optical diagnostic techniques, optical coherence tomography (OCT) is expected to be used in various fields such as medicine, physiology and biological physics. OCT is a technique that has been developed for non-invasive cross-sectional imaging of internal structures in biological tissues by measuring their optical reflections. The wide application of OCT is due to its potential for providing information on the oxygenation state of biological tissue by non-invasive

measurement [10, 17]. Figure 1.1 shows a schematic of the OCT system from reference [19]. The spectra of hemoglobin, myoglobin and some other chromophores and spectroscopic oxygen concentration indicators change with the change in the bonding state between the chromophores and oxygen. By using this change of spectra it is possible to measure the oxygen concentration in biological tissues non-invasively using spectroscopic methods [17]. OCT has great potential in diagnosis where conventional biopsy is either dangerous or ineffective [19]. Brezinski *et al.* [19] list three general clinical applications of OCT. The first application is in situations where conventional biopsy is difficult or impossible to perform, such as biopsies of the brain, coronary artery and cartilage surface of joints. The second application is in situations where biopsy is ineffective due to high "false negative" rates, such as early diagnosis of uterine and esophageal cancers. The third application is in guiding microsurgical procedures, such as the repair of peripheral nerves and blood vessels [19].

OCT uses low-coherence interferometry to produce a two-dimensional image of optical scattering from internal tissue microstructures in a way that is analogous to ultrasonic pulse-echo imaging [10]. Both low-coherence light and ultrashort laser pulses can be used to map internal structures of biological systems. An optical signal that is transmitted through or reflected from a biological tissue will contain time-of-flight information, which in turn yields spatial information about tissue microstructure [10]. Tomographic imaging has been demonstrated in vitro in the peripapillary area of the retina and in the coronary artery, two clinically relevant examples that are representative of transparent and turbid media, respectively [10].

Confocal optical microscopy is a technique for increasing the contrast of microscope images, particularly in thick specimens [8]. Figure 1.2 shows a schematic

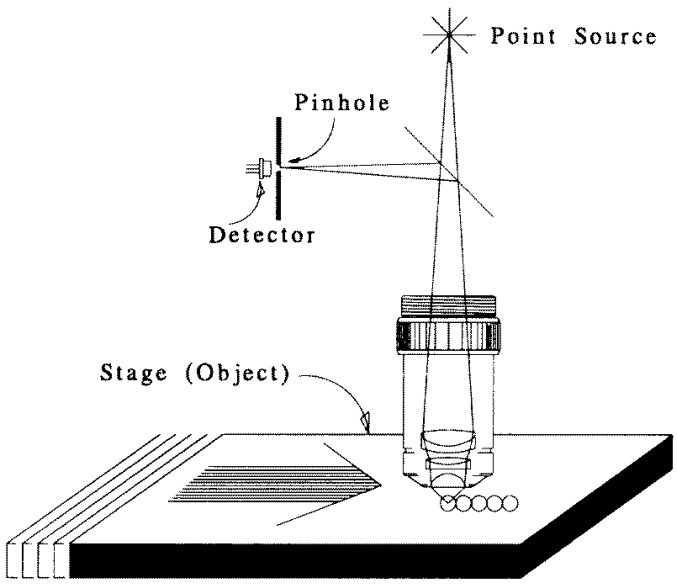

Figure 1.2: A stage scanning confocal microscope [8].

of a stage scanning confocal microscope from reference [8]. A confocal microscope is capable of imaging structures within thin optical sections beneath the surface of a sample which is its primary advantage in many applications [20]. By restricting the observed volume, confocal microscopy prevents overlying or nearby scatterers from contributing to the detected signal [8]. For the diagnosis of skin melanomas in vivo, a confocal microscope capable of viewing tissue microstructure to depths of 1 mm or more would be of clinical value [20].

Laser light scattering spectroscopy, which is a precise and simple technique, has emerged as a promising method for analysis of ciliary motion [9]. Figure 1.3 from reference [9] shows a set up for measuring ciliary activity by dynamic laser light scattering. This technique is based on the evaluation of the frequency shift of coherent light scattered by moving particles and uses the properties of monochromaticity, coherence and directionality of laser light [9]. Ciliary motion is measured as intensity fluctuations due to the interference of Doppler-shifted scattered light [9].

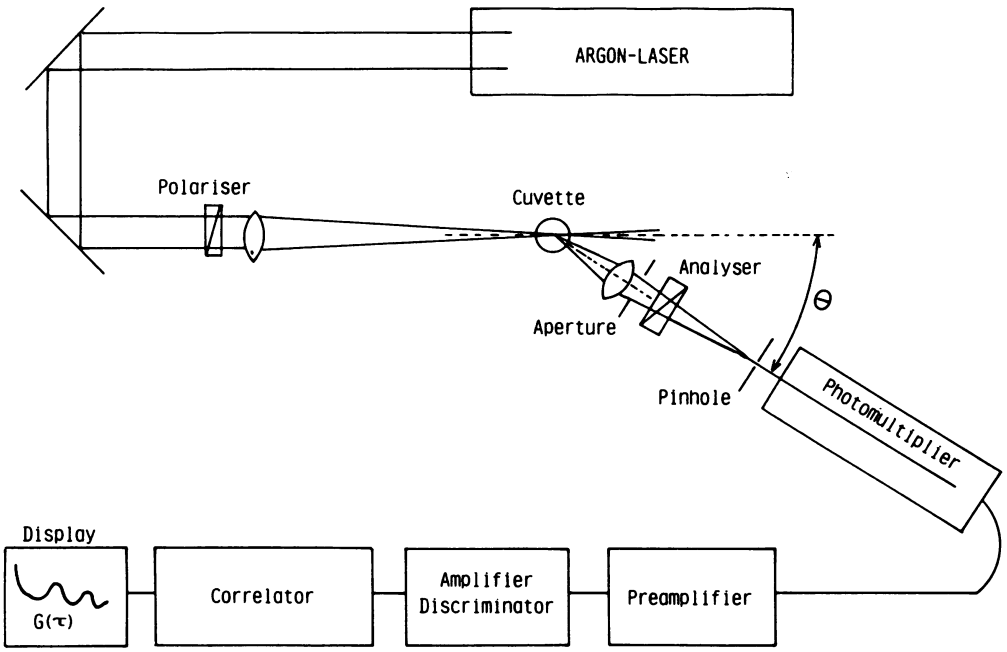

Figure 1.3: Set up for measuring ciliary activity by dynamic laser light scattering [9].

Photodynamic therapy is the use of drugs (photosensitizers) that are activated by visible or near infrared light to produce specific biological effects in cells or tissues that can be exploited to achieve a particular clinical endpoint [1]. In this technique, dyes are transferred to a toxic state by laser light and tumor cells can be treated [7]. Laser-Induced Interstitial Thermotherapy (LITT) is another technique used for tumor treatment, which makes use of the possibility of localized tissue coagulation [7]. LITT was recently introduced to treat tumors in the retina, brain, prostate, liver and uterus. This technique has already become a well established tool in minimally invasive surgery [7]. With optical biopsy it is possible to detect cancerous tissues using optical methods [1]. The basic principle used here is that the emission and scattering of light are strongly influenced by the composition and the cellular structure of tissues [1]. Thus it is possible to detect a cancerous tissue by non-invasive or minimally invasive *in vivo* methods [1].

Lasers are also being used for diagnostic and therapeutic purposes in ophthalmology, where the conventional incoherent light sources fail [7]. Retinal glaucoma and retinal detachment can be treated by using confocal laser microscopy [7]. Another application of an optical diagnostic technique using lasers is to treat cervical intraepithelial neoplasia (CIN), which might lead to cervical cancer if untreated [7].

A significant percentage of the population is diabetic and millions of diabetics around the world are required to monitor their blood glucose level by measuring the concentration several times a day [21, 22]. Research has shown that frequent control of blood glucose in insulin-dependent diabetics reduces the severity of long-term complications such as retinopathy and nephropathy [23]. All the monitoring methods currently available for patients require blood samples obtained by pricking a finger, and a drop of blood is placed on a test strip that undergoes a colour change due to an enzymatic chemical reaction [21, 24]. This invasive procedure is inconvenient and unpleasant for the patient and often leads to poor compliance and inadequate blood glucose monitoring and control [23]. Small children are especially reluctant to undergo constant finger pricks. The development of non-invasive methods for monitoring blood glucose levels has been under investigation for several years, and these proposed techniques to date include implants based on electrochemical sensors and non-invasive optical methods. These methods are based on photoacoustic, absorbance or Fourier transform spectroscopy in the infrared region [22, 24]. A recently proposed method for this purpose is based on the changes of the refractive index resulting from the dissolved glucose concentration [24].

The next section introduces the research problem investigated.

1.2 Research problem

In many research studies of biomedical and photonic micro-structures and nano-structures, optical software simulation and modeling tools are the only means to obtain a deeper understanding of the underlying scientific issues [1]. Thus, a good simulation model for laser pulse propagation in tissue is required to assist further development of the treatment procedures outlined in Section 1.1.

A number of researchers have been working on modeling light propagation through biological tissue, as well as through tissue with inhomogeneities. Of the existing modeling techniques for optical diagnostic applications, many approximate the actual Gaussian pulse by a perfect square pulse. In addition, the extension of existing techniques to multiple layers increases the computational complexity quite considerably. Extension of these methods to multi-dimensions is not easy and involves approximations to the governing equation. Thus, a better numerical technique, which addresses these drawbacks of the existing methods, is required for efficiently simulating light propagation through biological tissue.

The intensity of incident light used for optical diagnostic techniques is very low because using a high intensity damages tissue. With this low incident intensity, the detection techniques become inefficient. For example, spectroscopic methods such as Raman spectroscopy are very inefficient when used with an incident pulse of low intensity. However, an implant such as a photonic crystal structure can be used inside the tissue layers in order to increase the efficiency of these diagnostic techniques by producing enhanced optical signals for detection. To the best of the author's knowledge, a numerical technique for modeling tissue with implanted structures has not been reported in the research literature. This dissertation provides a comprehensive treatment of the numerical modeling of light propagation through tissue with implanted structures.

1.3 Research aims

This research has two main aims. The first is to develop a better method for simulating laser pulse propagation through tissue. The second is to develop a technique for numerically simulating laser pulse propagation through tissue with implants, which has very promising applications in the field of biomedical engineering.

The research conducted to achieve these aims was broken down into three major stages. In stage 1, a technique for simulating laser pulse propagation through tissue was developed. This involved first developing and implementing a numerical technique for solving the one-dimensional transient photon transport equation. Extensions of this technique to be used in inhomogeneous tissue media and in multi-dimensional geometries were then carried out. In stage 2, a technique for mapping the photon transport equation to Maxwell's equations was developed. In the final stage, numerical simulation of laser pulse propagation through biological tissue with implanted foreign structures was carried out by combining the techniques developed in stages 1 and 2. The main application of the research presented in this dissertation is non-invasive or minimally invasive sensing of the constituents of tissue fluid or blood, such as the glucose concentration in diabetics.

1.4 Structure of the dissertation

This dissertation consists of nine chapters and three appendices. Chapter 2 provides a general literature review related to the research problem together with some background information required in later chapters. Chapter 3 provides a more detailed review of numerical simulation of light propagation through bio-

logical tissue. It also contains detailed technical descriptions of several widely-used models for this purpose. Chapters 4, 5 and 6 present the work carried out in stage 1. Chapter 4 proposes an efficient algorithm for solving the one-dimensional transient photon transport equation, and contains some results of a numerical simulation of pulse propagation through a layer of tissue that were obtained using this proposed algorithm. Chapter 5 shows how this technique can be extended for use in inhomogeneous media. Chapter 6 presents a technique for solving the three-dimensional transient photon transport equation. Chapter 7 presents the work carried out in stage 2. It proposes a technique for mapping the photon transport equation to Maxwell's equations. Chapter 8 and Appendix C present the work carried out in the final stage. They contain detailed analyses of simulating pulse propagation through tissue with implants. Chapter 8 provides a numerical method to simulate light propagation through a slit in a metal screen implanted in tissue. Chapter 9 concludes the research presented in this dissertation, highlighting the key contributions it makes to the biophotonics field. It also contains some recommendations for further research which may be carried out by extending the work presented in this dissertation. Appendix A provides a discussion of the relationship between the electromagnetic theory and the photon transport theory. Appendix B provides an introduction to photonic crystals. Appendix C proposes a numerical method to simulate light propagation through tissue with an implanted photonic crystal structure.

References

[1] B. C. Wilson, V. V. Tuchin, and S. Tanev, *Advances in Biophotonics*. Netherlands: IOS Press, 2005.

[2] J. R. Mourant, J. P. Freyer, A. H. Hielscher, A. A. Eick, D. Shen, and T. M. Johnson, "Mechanisms of light scattering from biological cells relevant to noninvasive optical-tissue diagnostics," *Applied Optics*, vol. 37, no. 16, pp. 3586–3593, 1998.

[3] A. Dunn and R. R. Kortum, "Three-dimensional computation of light scattering from cells," *IEEE Journal of Selected Topics in Quantum Electronics*, vol. 2, no. 4, pp. 898–905, 1996.

[4] P. N. Prasad, *Introduction to Biophotonics*. New Jersey: John Wiley and Sons Inc., 2003.

[5] M. S. Patterson, B. C. Wilson, and D. R. Wyman, "The propagation of optical radiation in tissue 1. Models of radiation transport and their application," *Lasers in Medical Science*, vol. 6, pp. 155–168, 1991.

[6] J. Beuthan, O. Minet, J. Helfmann, M. Herrig, and G. Muller, "The spatial variation of the refractive index in biological cells," *Physics in Medicine & Biology*, vol. 41, pp. 369–382, 1996.

[7] M. H. Niemz, *Laser-Tissue Interactions: Fundamentals and Applications*, 3rd ed. Germany: Springer, 2004.

[8] R. H. Webb, "Confocal optical microscopy," *Reports on Progress in Physics*, vol. 59, pp. 427–471, 1996.

[9] K. Svartengren, L.-G. Wiman, P. Thyberg, and R. Rigler, "Laser light scattering spectroscopy: a new method to measure tracheobronchial mucociliary activity," *Thorax*, vol. 44, pp. 539–547, 1989.

[10] Huang, David, E. A. Swanson, C. P. Lin, J. S. Schuman, W. G. Stinson, W. Chang, M. R. Hee, T. Flotte, K. Gregory, C. A. Puliafito, and J. G. Fujimoto, "Optical coherence tomography," *Science*, vol. 254, no. 5035, pp. 1178–1181, 1991.

[11] J. C. Hebden, S. R. Arridge, and D. T. Delpy, "Optical imaging in medicine: I. Experimental techniques," *Physics in Medicine & Biology*, vol. 42, pp. 825–840, 1997.

[12] X. Wang, L. V. Wang, C. W. Sun, and C. C. Yang, "Polarized light propagation thorugh scattering media: time-resolved Monte Carlo simulations and experiments," *Journal of Biomedical Optics*, vol. 8, no. 4, pp. 608–617, 2003.

[13] L. Wang, P. P. Ho, C. Liu, G. Zhang, and R. R. Alfano, "Ballistic 2-D imaging through scattering walls using an ultrafast optical Kerr gate," *Science*, vol. 253, pp. 769–771, 1991.

[14] M. D. Duncan, R. Mahon, L. L. Tankersley, and J. Reintjes, "Time-gated imaging through scattering media using stimulated Raman amplification," *Optics Letters*, vol. 16, pp. 1868–1870, 1991.

[15] J. M. Schmitt, A. H. Gandjbakhche, and R. F. Bonner, "Use of polarized light to discriminate short-path photons in a multiply scattering medium," *Applied Optics*, vol. 31, pp. 6535–6546, 1992.

[16] H. Horinaka, K. Hashimoto, K. Wada, Y. Cho, and M. Osawa, "Extraction of quasi-straightforward-propagating photons from diffused light transmitting through a scattering medium by polarization modulation," *Optics Letters*, vol. 20, pp. 1501–1503, 1995.

[17] Y. Yamada and Y. Hasegawa, "Time-dependent FEM analysis of photon migration in biological tissues," *JSME International Journal Series B*, vol. 39, no. 4, pp. 754–761, 1996.

[18] S. R. Arridge, "Optical tomography in medical imaging," *Inverse Problems*, vol. 15, pp. R41–R93, 1999.

[19] M. E. Brezinski and J. G. Fujimoto, "Optical coherence tomography: high-resolution imaging in nontransparent tissue," *IEEE Journal of Selected Topics in Quantum Electronics*, vol. 5, no. 4, pp. 1185–1192, 1999.

[20] J. M. Schmitt, A. Knuttel, and M. Yadlowsky, "Confocal microscopy in turbid media," *Journal of Optical Society of America A*, vol. 11, no. 8, pp. 2226–2235, 1994.

[21] J. S. Maier, S. A. Walker, S. Fantini, M. A. Franceschini, and E. Gratton, "Possible correlation between blood glucose concentration and the reduced scattering coefficient of tissues in the near infrared," *Optics Letters*, vol. 19, no. 24, pp. 2062–2064, 1994.

[22] M. Kohl, M. Cope, M. Essenpreis, and D. Bocker, "Influence of glucose concentration on light scattering in tissue-simulating phantoms," *Optics Letters*, vol. 19, no. 24, pp. 2170–2172, 1994.

[23] J. T. Bruulsema, J. E. Hayward, T. J. Farrell, M. S. Patterson, L. Heinemann, M. Berger, T. Koschinsky, J. S. Christiansen, H. Orskov, M. Essenpreis, G. S. Redeker, and D. Bocker, "Correlation between blood glucose concentration in diabetics and noninvasively measured tissue optical scattering coefficient," *Optics Letters*, vol. 22, no. 3, pp. 190–192, 1997.

[24] M. Kohl, M. Essenpreis, and M. Cope, "The influence of glucose concentration upon the transport of light in tissue-simulating phantoms," *Physics in Medicine & Biology*, vol. 40, pp. 1267–1287, 1995.

CHAPTER 2

Literature Review

This chapter presents a general literature review related to the research problem with some background information required to discuss the research reported in this dissertation.

2.1 Introduction

IN order to discuss numerical modeling of light propagation through tissue and tissue with implanted structures, it is necessary to have some background knowledge of a number of basic topics such as optical properties of tissue, and the theory and characterization of light propagation in tissue including the governing equations. This chapter provides a literature review for this purpose.

The literature review is presented in seven major sections. Section 2.2 discusses the optical properties of tissue and introduces the problem of modeling tissue. Section 2.3 gives a brief overview of propagation of light in tissue. In this section, the definitions of the scattering coefficient, absorption coefficient, the albedo and the optical thickness are introduced, followed by a concise discussion of light absorption and scattering in tissue. A brief account of the applicability of the photon transport theory for modeling light propagation in tissue is also

provided, as opposed to using Maxwell's equations. In addition, a more detailed discussion of the photon transport theory as applied to tissue optics is provided in this section. The governing equation for modeling light propagation in tissue, the photon transport equation (PTE), is also introduced in this section. A brief account of statistical and deterministic methods for analyzing light propagation through turbid media is presented along with a comparison of different existing models used for this purpose. Detailed mathematical descriptions of the most widely used models are provided in the next chapter.

Section 2.4 provides a very brief description of Maxwell's equations, which govern the modeling of light propagation through implanted structures. Section 2.5 reviews phase retrieval techniques, which are necessary for mapping the photon transport equation to Maxwell's equations in modeling light propagation through tissue with implanted structures. Section 2.6 concludes the chapter summarizing the key information outlined in this chapter.

2.2 Optical properties of tissue

Tissue is a complicated medium, which is treated as an absorbing and scattering medium, and many of the optical-thermal events produced by laser radiation are interdependent [1]. However, methods have been proposed for calculating and measuring light propagation in tissue [1]. Both scattering and absorption provide important information about the physiological condition of tissue [2]. Figure 2.1 shows a cross-section of a skin specimen of a human shoulder. This figure shows several constituents of the skin. The epidermis of the skin absorbs and propagates light. The absorption property is mostly due to the natural pigment melanin [3]. When a biological cell is illuminated with laser light, the light is scattered in all directions to form a light-scattering pattern, which is dependent on the size and

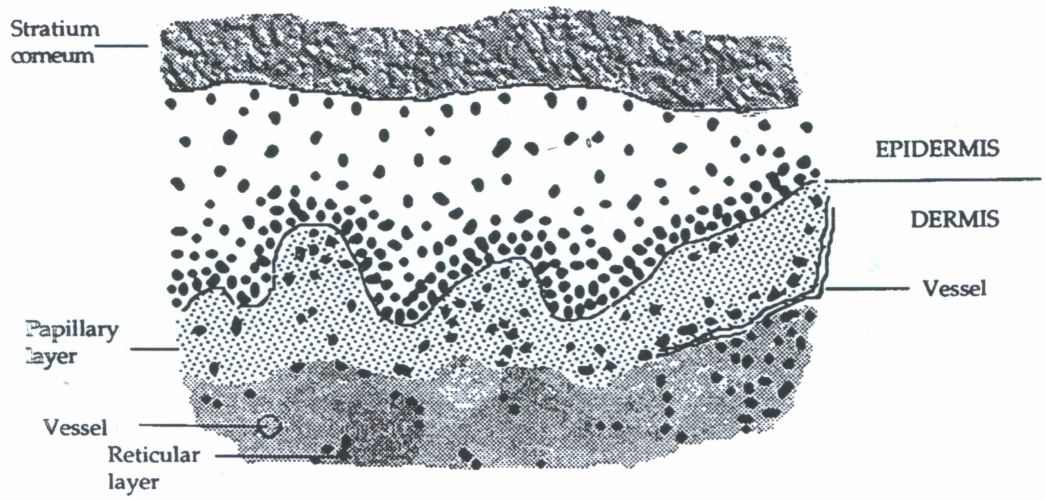

Figure 2.1: A section through skin of human shoulder [1].

internal structure of the cell [4]. Therefore, appropriate measurements of this light-scattering pattern can provide morphological information about the cell [4].

Light propagation in tissue depends on scattering and absorption properties of its components such as cells, cell organelles and various fibre structures. The size, shape, density and relative refractive index of these structures affects the propagation of light [5]. Figure 2.2 from reference [5] shows major organelles and inclusions of the cell. This figure depicts the wide variety of structures within a cell that determine scattering of light in tissue.

Scattering of light in tissue is due to scattering centres such as cells, nuclei, other organelles and structures within organelles [2]. Multiple scattering and absorption in tissue result in laser beam broadening and decay as it travels through tissue [5]. Cells and tissue structure elements can be as small as a few tenths of nanometers or as large as hundreds of micrometers [5].

Mammalian cells are typically in the order of 10 to 30 μm in diameter and the

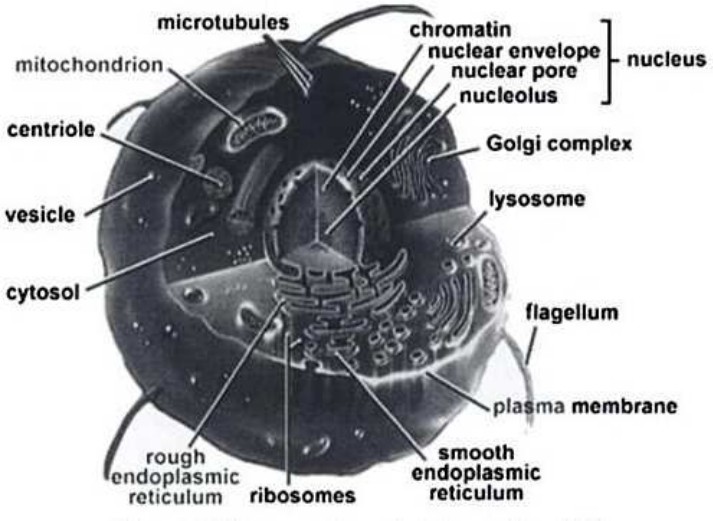

Figure 2.2: Major organelles and inclusions of the cell [5].

nuclei are in the order of 3 to 10 μm in diameter [2]. Mitochondria are 0.3 to 0.7 μm in diameter and lysosomes and peroxisomes are 0.2 to 0.5 μm in diameter. These structures are roughly spherical in shape, but other organelles such as Golgi apparatus and endoplasmic reticulum, from which light scatter, have complicated shapes [2]. A normal erythrocyte in plasma has the shape of a concave-concave disk with a diameter varying from 7.1 to 9.2 μm, a thickness of 0.9 to 1.2 μm in the centre and 1.7 to 2.4 μm on the periphery, and a volume of 90 μm^3. Leukocytes are spheres with a diameter of 8 to 22 μm. Platelets are biconvex disklike particles with a diameter of 2 to 4 μm. Erythrocytes in blood are as many as 10 times the number of platelets and about 300 times the number of leukocytes [5].

An exact assessment of light propagation in tissue would require a model that characterizes the spatial and size distribution of tissue structures, their absorbing properties and their refractive indices [1]. However, for real tissues, such as the skin, the task of creating a precise representation, either as a tissue phantom or as a computer simulation, is formidable if not totally impossible. Therefore, tissue is represented as an absorbing bulk material with scatterers randomly distributed

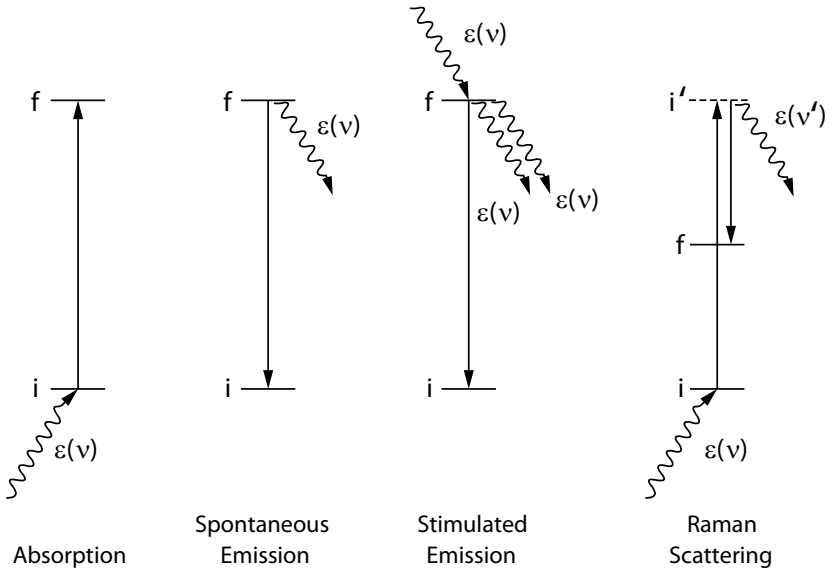

Figure 2.3: The four basic light-molecule interaction processes [6].

over the volume [1].

Even though this approximation does not provide any information about the microscopic structure of tissue, it has provided accurate agreement with experimental measurements [7, 8]. Two approaches are currently used for modeling tissues [5]. The first approach is to model tissue as a medium with a continuous random spatial distribution of optical parameters; and the second approach is to consider tissue as a discrete ensemble of scatterers [5]. The choice of the appropriate model of these two depends on the structure of the tissue under study and the kind of light scattering characteristics that are to be obtained.

At a microscopic level, the tissue can be described as a medium with a spatially dependent refractive index. At this level, light interaction with tissue results in reflection, refraction, absorption and diffraction processes [9]. On a macroscopic scale these processes are summarized as scattering [9]. On the macroscopic level, mean optical values can be used instead of spatially dependent parameters

to model light interaction with tissue. These mean values are the scattering coefficient, absorption coefficient and the phase function [9].

The four basic light-molecule interaction processes are, absorption, spontaneous emission, stimulated emission and Raman scattering. The schematic diagram shown in Fig. 2.3, which is adopted from [6], shows these four interaction processes. The absorption process describes the transition from a quantized lower energy initial level to a higher energy level, with the energy gap between them matching the photon energy [6]. The spontaneous emission process describes the return of the molecule from the excited state to its lower energy state by emission of a photon of energy corresponding to the energy gap between the two levels [6]. The stimulated emission is a process of emission triggered by an incident photon of an energy corresponding to the energy gap between the lower and higher energy levels [6]. Raman scattering describes a process that is a single-step scattering of a photon of energy being scattered into another photon of energy, the difference corresponding to the energy gap. The interaction of light with tissue, which is a bulk matter, involves reflection, refraction and scattering in addition to absorption [6].

Both cw and pulse lasers are available in the UV, visible, and IR ranges. Since the absorption and scattering of any tissue varies with wavelength, there are dramatic differences in the penetration depth of the radiation from the various lasers [1]. For example, light at either 193 nm or 2.96 μm is totally absorbed in the first μm of tissue owing to amino acid absorption in the UV band and water absorption in the IR band. In contrast, light from 600 nm to 1.1 μm can penetrate several millimeters in tissue. This is owing to the fact that within this red and near-IR wavelength window there is a lack of strongly absorbing tissue chromophores [1]. In general, in the UV and IR spectral regions light does not penetrate deep

into tissue because of high absorption and low scattering. Short-wave visible light penetrates as deep as 0.5 to 2.5 mm and light in wavelength range 600-1500 nm penetrates to a depth of 8 to 10 mm because scattering prevails over absorption [10].

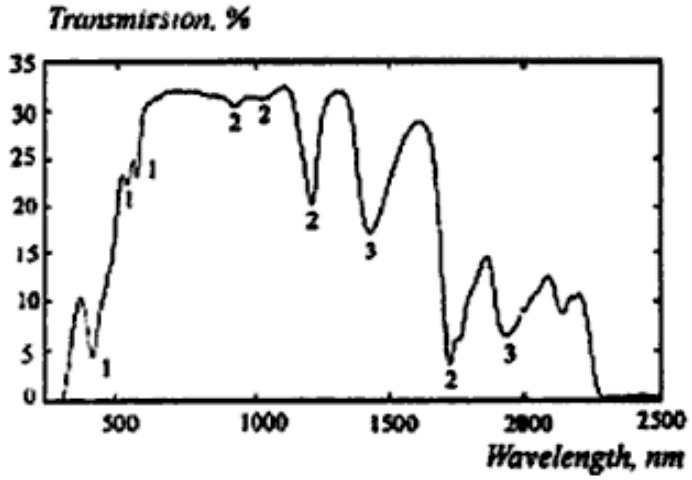

Figure 2.4: The transmission spectrum of a 3 mm thick slab of female breast tissue. A spectrometer with an integrating sphere was used. The contributions of absorption bands of the tissue components are marked: 1-hemoglobin; 2-fat; 3-water [5].

Figure 2.4 from reference [5] shows the transmission spectrum of a 3 mm thick slab of female breast tissue. Figure 2.5 from reference [10] shows attenuation spectra for several human skin pigments. These figures show that the absorption spectrum depends on the type of ***predominant*** absorption centres and water content of tissue. Absolute values of absorption coefficients for typical tissues range from 10^{-2} cm^{-1} to 10^{4} cm^{-1} [10].

Propagation of the scattered light is described by the photon transport equation which examines the change in radiance with distance in a particular direction $\mathbf{\Omega}$, at position $\mathbf{r} = (x, y, z)$ [1]. The characteristics of photon propagation,

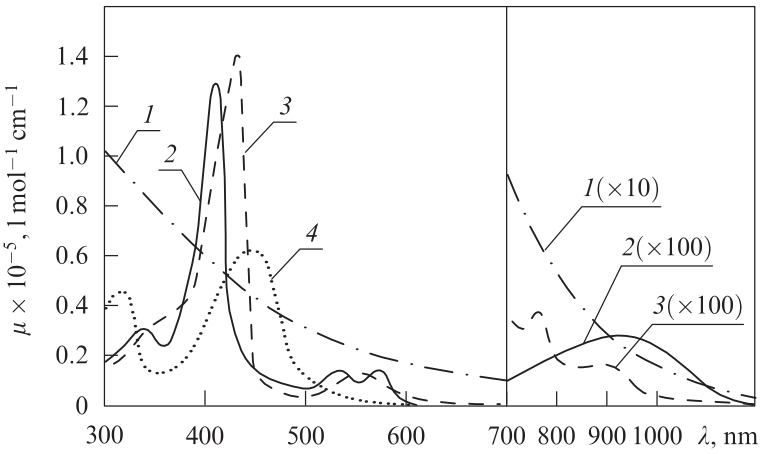

Figure 2.5: Molar attenuation spectra for solutions of main human skin pigments: 1- DOPA-melanin (H_2O); 2 - oxyhemoglobin (H_2O), 3 - hemoglobin (H_2O); 4 - bilirubin ($CHCl_3$) [10].

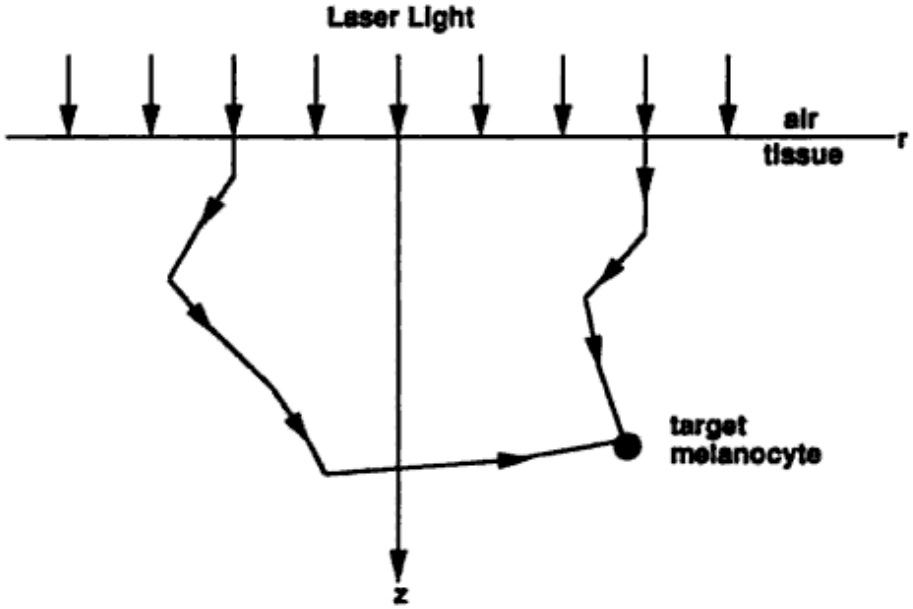

Figure 2.6: Random paths of two photons from a laser beam that are absorbed by a target melanocyte at **r** [1].

which include scattering and absorption events within tissue, and reflection and transmission at boundaries, govern the number of photons that will reach the melanocyte at coordinate **r** [1]. Figure 2.6 shows random paths of two photons from a laser beam that are absorbed by a target melanocyte positioned at

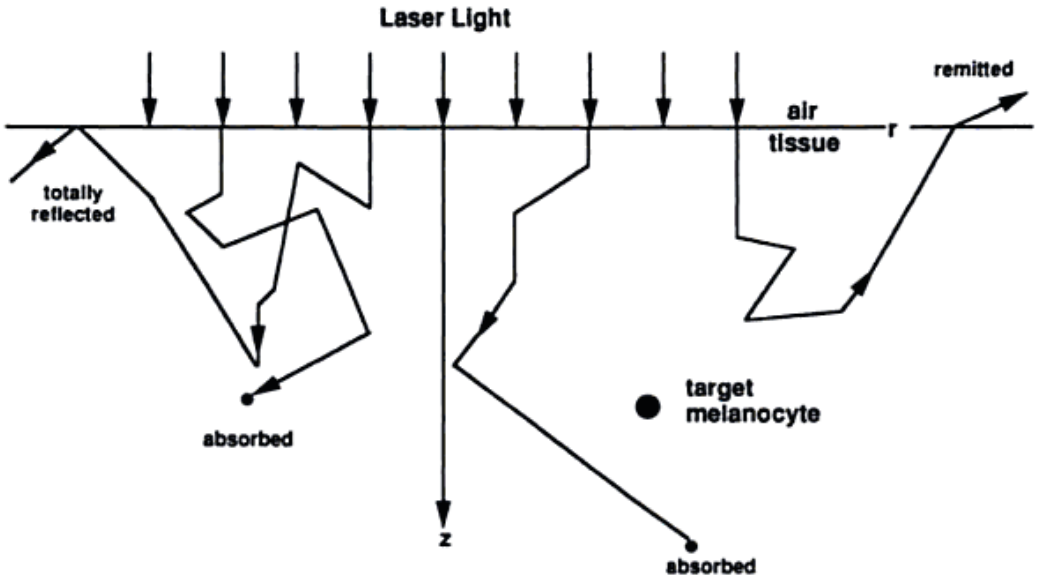

Figure 2.7: Random paths of most photons missing a target melanocyte at **r** [1].

r, whereas Fig. 2.7 shows random paths of most of the photons missing a target melanocyte.

According to Ashley *et al.* [1], tissue optics involves two major tasks. The first task is finding the light energy per unit area per unit time that reaches a target chromophore at some position **r** [1]. The second task, which has so far been the most difficult one, is developing methods by which the absorbing and scattering properties of tissue can be measured. Such properties are called the optical properties of tissue and they are, (i) the absorption coefficient, (ii) the scattering coefficient, (iii) the probability density function that scattering occurs from a certain direction (with unit vector $\mathbf{\Omega}'$) into another direction (with unit vector $\mathbf{\Omega}$, as shown in Fig. 2.8), sometimes also called the phase function of single particle scattering, and (iv) the index of refraction of the tissue [1]. The ultimate goal of the second task of tissue optics is to have methods available that can assess all optical properties non-invasively in living tissues [1].

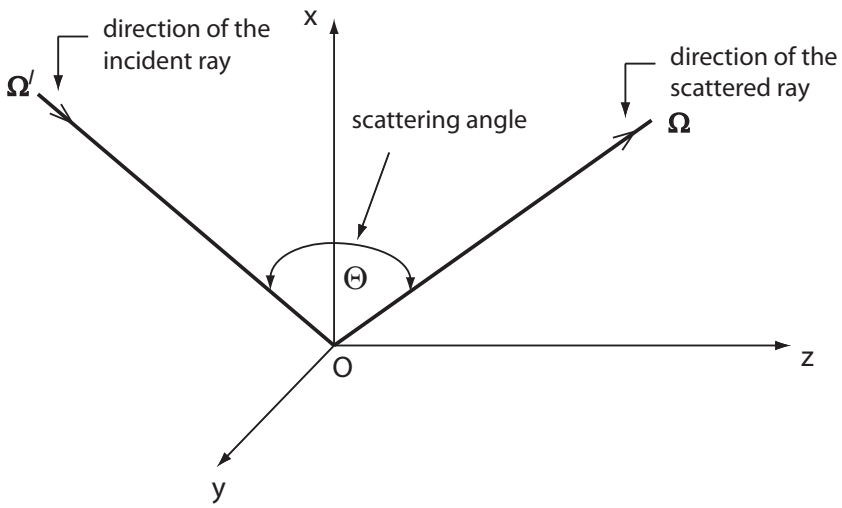

Figure 2.8: Incident and scattered directions.

2.3 Propagation of light in tissue

In order to assist the development of optical treatment procedures in medical fields such as optical tomography, it is necessary to understand the transmission behavior of light impulses incident on tissue, which is a scattering and absorbing media [11]. A medium in which both absorption and scattering occur simultaneously, such as biological tissue, is called a turbid medium [12]. Optical properties of a turbid medium are characterized by the absorption coefficient, the scattering coefficient and the single-scattering phase function [13]. The reciprocal of the absorption coefficient is defined as the average distance a photon travels before being absorbed by the medium [13]. Similarly, the reciprocal of the scattering coefficient is defined as the average distance a photon travels before being scattered by the medium [13]. Ashley *et al.* [1] have defined the absorption (σ_a) and the scattering (σ_s) coefficients such that the probability of absorption in infinitesimal distance ds is $\sigma_a ds$ and the probability of scattering in infinitesimal distance ds is $\sigma_s ds$, respectively.

A collimated beam incident on a tissue specimen attenuates exponentially

with tissue depth and the light scattered from the collimated beam becomes the source for the resulting diffuse or scattered light in the tissue [1]. The scattering coefficient and the absorption coefficient are wavelength dependent [1]; and the absorption of light by blood is highly dependent upon wavelength and oxygenation [1].

Two dimensionless quantities can be used to characterize light propagation in a turbid medium. They are the albedo, α, and the optical thickness, τ, that are defined as [13]:

$$\alpha = \frac{\sigma_s}{\sigma_s + \sigma_a}, \tag{2.1}$$

$$\tau = (\sigma_s + \sigma_a)d, \tag{2.2}$$

where d is the physical thickness of the slab [13].

Biological tissues are relatively transparent to light in the near infrared wavelength range from 700 nm to 1 μm, and it is easier to detect the transmitted light in this wavelength range than in other wavelengths [11]. Tissue components that absorb light are called chromophores. Some of the most important chromophores for visible wavelengths are blood and melanin; the latter are small (around 1 μm in dimension) pigment granules in the skin and the eye [1].

Scattering is usually caused by spatial variations in tissue density, refractive index and dielectric constant [1]. The larger the difference in the index of refraction between a cell component and its surrounding, the greater the scattering [14]. For isotropic scattering, absorption and scattering coefficients can be determined by measuring diffuse reflection and diffuse transmission for a thin sample of tissue [15]. However, biological tissue exhibits strong forward-peaked scattering,

and the scattering albedo is usually higher than 0.9 [1, 11].

Scattering can cause the light intensity (irradiance) just below the surface of the tissue to be greater than the incident irradiance. At wavelengths where tissue absorption is low (600 nm - 1300 nm) and boundary conditions are matched, the increase in irradiance may be a factor of two to three, with a maximum of 5 [1]. The degree of scattering depends upon the wavelength of the laser beam and the optical properties of the tissue [15].

For wavelengths that are much longer than cell diameters (frequencies lower than 300 GHz), where there is little scattering from the cellular structures, the reflection, absorption and transmission are described best using electromagnetic theory [15]. However, the electromagnetic spectrum of lasers lies in the infrared to ultraviolet wavelength band; substantial multiple scattering in tissue occurs in this band due to the comparable size of cells with respect to the irradiation wavelength. For laser wavelengths, the photon transport theory provides a practical description for the optical propagation of light in tissue [15].

Since the light scattered from a collimated beam undergoes multiple scattering events as it propagates through tissue, a rigorous description of this propagation in terms of Maxwell's equations is not possible due to computational reasons. An approach that has proven effective is the photon transport equation that describes the transfer of energy through a turbid medium [16]. The theory is heuristic and is based on a statistical approximation of photon particle transport in the multiple scattering medium. Ishimaru [16] points out that "although the transport theory was developed on the addition of powers, it contains information about the correlation of the fields" . Although polarization can be included in transport theory, polarization of laser sources is neglected in most of the reported analyses

[1]. The polarization of incident light is usually lost in highly scattering media within a few millimeters from the surface [1].

When an ultrashort laser pulse hits a thin plane-parallel layer of a scattering medium such as tissue, the transmitted pulse consists of a ballistic (coherent) component, a group of photons having zigzag trajectories, and a highly intensive diffuse component [10]. The ballistic component is resulted from both unscattered photons and photons undergoing forward-directed scattering, and is subject to exponential attenuation with increasing sample thickness. The group of photons with zigzag trajectories experiences only a few collisions and slightly deviates from the direction of the incident beam. These form the first-arriving part of the diffuse component. The diffuse component is broad and contains photons that experience many scattering events [10].

For a laser beam incident normally on an interface, the total reflectance is primarily due to backscattering, except when the absorption is much larger than scattering. In the latter case, mainly Fresnel reflection occurs. In Fresnel reflection, usually about 5 percent of a normally incident laser beam is reflected from the surface due to the mismatch in the refractive indices [15]. The remaining light, which is transmitted at the interface, is attenuated in the tissue by absorption and scattering according to Beer's law [1, 17]:

$$I(z) = I_0(1 - r_{sc})e^{-(\sigma_a+\sigma_s)z}, \tag{2.3}$$

where $I(z)$ [W/m^2] is the intensity (irradiance) of collimated light at position z in the tissue.

However, if scattering is substantial, the distribution of the laser light in tissue cannot be predicted by Beer's law and neither absorption nor scattering can be

individually estimated from attenuation measurements of the laser beam [13, 15]. Since scattering is usually caused by random spatial variations in tissue density, refractive index and dielectric constant, actual light distributions can be substantially different from distributions estimated by Beer's law [1].

2.3.1 The electromagnetic theory and the photon transport theory

The electromagnetic theory provides exact expressions for the absorption and scattering parameters of a uniform, non-scattering medium with ensembles of random scatterers. These scatterers consist of discrete scattering and absorbing "particles", possibly of different sizes, that are distributed randomly [1]. However, because of the inhomogeneity of biological tissue, analytic approaches using Maxwell's equations do not lead to solvable equations for any case of practical interest in tissue [17]. Also, there has been little progress in developing even approximate solutions which are applicable to optical propagation in biological media [1]. While the description of light propagation in tissue in terms of electromagnetic fields is intractable, the application of photon transport (radiative transfer) theory has proven to be a considerable success [1]; and most recent advances in describing the transfer of laser energy in tissue are based upon transport theory [17].

Fante [18] studied the relationship between Maxwell's equations and the photon transport theory for isotropic, nondispersive media that have arbitrary permittivity variations. A brief outline of how the electromagnetic theory compares with the postulates of the photon transport theory is provided in this section, based on Fante's [18] work.

Using the electromagnetic theory it can be shown that for an isotropic, non-

dispersive medium the ensemble-averaged electromagnetic energy density can be written as [18]

$$\langle U(\mathbf{r})\rangle = \int Q(\mathbf{r},\mathbf{s})d\Omega, \tag{2.4}$$

where Q is the angular component of the average energy density in the direction $\mathbf{s}$ (see Appendix A for the derivation). The energy dW which is transported across a surface element dA onto the solid angle $d\Omega$ centered about $\mathbf{s}$ in a time interval dt is given by [18]

$$dW = (\mathbf{R}\cdot\mathbf{n})dAd\Omega dt, \tag{2.5}$$

where $\mathbf{R}$ is the angular component in the direction of $\mathbf{s}$ of the Poynting vector and $\mathbf{n}$ is the unit normal to the element dA. The derivation of Eq. (2.5) is presented in Appendix A. In the photon transport theory it is postulated that the energy dW which is transported across a surface element dA onto the solid angle $d\Omega$ centered about $\mathbf{s}$ in a time interval dt is given by

$$dW = I(\mathbf{r},\mathbf{s})(\mathbf{s}\cdot\mathbf{n})dAd\Omega dt, \tag{2.6}$$

where $\mathbf{n}$ is the unit normal to dA and I is the radiance. The radiance, I, is postulated to be related to the average energy density through [18]

$$\langle U(\mathbf{r})\rangle = \frac{1}{v}\int I(\mathbf{r},\mathbf{s})d\Omega, \tag{2.7}$$

where v is the propagation speed in the medium. By comparing Eq. (2.7) and Eq. (2.4) it can be seen that these two expressions are consistent when

$$I(\mathbf{r},\mathbf{s}) = vQ(\mathbf{r},\mathbf{s}). \tag{2.8}$$

A more detailed analysis of the relationship between the photon transport theory and Maxwell's equations can be found in reference [18].

2.3.2 The photon transport theory

In the photon transport (PT) formalism, light propagation is considered equivalent to the flow of discrete photons which may be locally absorbed or scattered by the medium. The scattering is usually energy conserving (although effects such as fluorecence or Raman scattering which involves wavelength and hence energy shift can be incorporated). The photon-tissue interactions are described in terms of absorption and (elastic) scattering cross-sections (or equivalent linear interaction coefficients) and the scattering angular distribution by phase functions [1].

The PT theory is a heuristic model which lacks the physical rigor of multiple scattering electromagnetic theory. For example, it does not in itself include effects such as diffraction or interference, even though the absorption and scattering properties of the individual constituent particles may do so. It is fundamental to PT theory that there should be no correlation between the radiation fields. Only quantities such as power or intensity are considered, and the method ignores the behavior of the component wave amplitudes and phases [1]. However, PT has provided a self-consistent framework for studies of light propagation in tissues [1].

If the absorption and scattering properties of tissue are determined according to the conditions of the PT theory (i.e., only radiometric quantities, not wave amplitudes and phases are measured) and, subsequently, these data are used as inputs to a PT model to calculate the spatial distribution of irradiance within a tissue volume for given incident irradiation and boundary conditions, then it is found in general that such distributions agree with experimental values (again measured ignoring light wave properties), although this has never been demonstrated rigorously [1].

In past years, a number of investigators have reported values for the total attenuation coefficient, the effective attenuation coefficient, the effective penetration depth, the absorption and scattering coefficients, and the scattering anisotropy factor for a variety of tissues at a variety of light wavelengths. The majority of these results are based upon approximations to the photon transport theory [17]. However, there are some indications that the PT theory may break down in the case of highly structured tissues such as muscle, where the alignment of fibres may cause measurable wave interference effects and the scattering cannot be considered random [1].

The propagation of visible or IR photons in a turbid medium, without change in energy (i.e. neglecting Raman scattering and fluorescence), is described by the photon transport equation, Eq.(2.9) [19].

The transport equation relates the gradient of radiance, I, at position $\mathbf{r}$ in the direction $\mathbf{\Omega}$ to losses owing to absorption and scattering and to a gain owing to light scattered from all other directions $\mathbf{\Omega}'$ into the direction $\mathbf{\Omega}$ [1, 17, 20, 21]. The equation has the form

$$\frac{1}{v}\frac{\partial}{\partial t}I(\mathbf{r},\mathbf{\Omega},t) + \mathbf{\Omega}\cdot\nabla_{\mathbf{r}}I(\mathbf{r},\mathbf{\Omega},t) - \sigma_s\int_{4\pi} P(\mathbf{\Omega}',\mathbf{\Omega})I(\mathbf{r},\mathbf{\Omega}',t)\,d\mathbf{\Omega}' + \sigma_t I(\mathbf{r},\mathbf{\Omega},t) = F(\mathbf{r},\mathbf{\Omega},t), \tag{2.9}$$

where I [W/m^2.sr] is the radiance, σ_t [1/m] is the extinction coefficient, σ_s [1/m] is the scattering coefficient, P [1/sr] is the phase (scattering) function, and F [W/m^3.sr] is the source of power generated at $\mathbf{r}$ in direction $\mathbf{\Omega}$. The speed of light in the medium is v.

2.3.3 Research on light propagation in turbid media

The ratio of scattering to absorption in tissue varies from nearly zero in both the UV (due to protein absorption) and mid-infrared (due to water absorption) ranges to large values in the therapeutic window in the red and near-infrared ranges. Tissue scattering tends to be strongly forward-peaked with an anisotropy factor in the range 0.7–0.99 [1]. Thus, an accurate model for simulating light propagation in tissue should not have restrictions on the ratio of scattering to absorption and on the scattering anisotropy [1]. When any wave phenomenon associated with light, such as diffraction and interference, is neglected, the modeling of light propagation in tissue is essentially equivalent to solving the full time-dependent photon transport equation [1].

Methods used to analyze the propagation of light in strongly scattering media are divided into two main types; statistical and deterministic [11]. Monte Carlo and random walk are examples of statistical methods. Deterministic methods are based on the photon transport equation. Statistical methods require very long computation times in order to obtain statistically meaningful results. These methods are carried out by tracing the paths of photon bundles with simulation of the scattering and absorbing pattern of light. Therefore, it is almost impossible to obtain solutions within practical limits of computation time when the media are large in size and complex in configuration [11]. On the other hand, deterministic methods are based on the photon transport equation, which is in the form of an integro-differential equation and is difficult to solve [11].

The Monte Carlo method is a stochastic (or statistical) method. It is sufficiently flexible to handle complex geometrical shapes, anisotropic scattering and nonhomogeneous properties, but the results obtained by this method always have unavoidable random errors due to practical finite sampling. In contrast, determinis-

tic methods do not suffer from this defect [22]. Among the popular deterministic methods, the adding-doubling method has been proposed to solve the transient response of a medium with a unit-step external source [22].

Most previous studies of photon transport through scattering-absorbing media assume the photon transport to be steady state (i.e. independent of time) [23]. With the advent of short pulse lasers and their rapid deployment in a variety of engineering applications such as ocean and atmosphere remote sensing, optical tomography, laser surgery, combustion product characterization and combustion diagnostics, the traditional steady-state photon transport formulations cannot be used to analyze their interaction with participating media [23].

The transient solution for photon transport in one-dimensional geometry for the case of laser incidence on a surface and propagating at speed v inside a scattering-absorbing medium has been developed and reported [23]. Yamada and Hasegawa [11] employed the finite element method (FEM) to solve the parabolic diffuse approximation equation to analyze the transient photon transport in two- and three-dimensional cylindrical media with light impulses [22]. They used a commercially available FEM software package that was developed for solving the heat conduction problem [11]. Even though the finite element method (FEM) can be used to solve any diffusion equation such as that for heat, mass and photons, this method does not necessarily produce correct solutions if the sizes of the elements are not appropriate and if the time steps are too large in a time-dependent calculation [11]. In particular, a very sharp gradient of the fluence rate may produce unreasonable temporal and spatial fluctuations [11].

Mitra *et al.* [22] applied the hyperbolic P_1 approximation to the transient photon transport within a two-dimensional rectangular medium. Wu [24] developed

an integral equation of transient photon transport in an isotropically scattering planar medium, and it was shown that the integral equation can be solved accurately by a quadrature method [22].

Many models have been developed to solve the one-dimensional PTE, which assumes horizontally-uniform plane-parallel media. However, in order to model three-dimensional inhomogeneous media, the three-dimensional PTE should be used [25]. Many diverse methods for solving the multi-dimensional steady state photon transport problem for atmospheric sciences have been reported [25, 26]. However, most of the work related to this problem has generally focused on the problem of the transfer of non-uniform sources of radiation through a spatially uniform media [26]. The most common type of model used to study three-dimensional cloud effects has been the Monte Carlo method; but this method is rather slow for results with good accuracy [25].

Among the methods proposed for solving the three-dimensional steady state PTE are the Monte Carlo simulations [12], the interaction principle [26], the Fourier-Riccati method [27], the spherical harmonics discrete ordinate method [25] and the diffusive approximation [28]. Stephens [26] used a general transform method to model media with vertically and horizontally varying optical properties.

For applications in which ultrashort pulses are used as the incident source, the medium can be treated as cold because the emission from the medium is negligible [29]. This is because the small amount of energy deposited per pulse is not sufficient to raise the temperature significantly, and hence any emission can be neglected when compared to the intensity of the scattered incident pulse [29]. In addition, any emission from the medium will be at higher wavelengths due to the low temperature in the medium and therefore need not be included in the

monochromatic analysis which is conducted at the wavelength of the laser [29]. When the radiation propagates at the speed of light, the time is in the order of 1 ns or less. With such a time scale, the medium can be generally treated as cold because the heat-diffusion and heat-capacity effects are negligible [30].

Common approximations to light propagation in tissue-like media, such as the diffusion equation, random walk models, the Kubelka-Munk method, the seven-flux model and Chandrasekhar's X and Y functions place restrictions on one or more of the basic tissue properties [1]. In the X and Y functions technique, the radiance at the entrance and exit surfaces of a slab is expressed in terms of X and Y functions [31]. These X and Y functions are solutions of nonlinear integral equations [31]. The two methods, the discrete ordinates and the adding-doubling, allow accurate solution of the PTE for anisotropic scattering and mismatched boundaries [1]. The adding-doubling method works naturally with layered media and yields reflection and transmission readily, while the discrete ordinates method generates internal fluences easily [1].

Methods based on the diffusion approximation or a similar approximation (e.g., uniform radiances over the forward and backward hemispheres) tend to be more accurate than the Kubelka-Munk method [13]. However, the diffusion approximation assumes that the internal radiance is nearly isotropic and consequently, it is inaccurate when scattering is comparable with absorption [13, 32].

Concise mathematical descriptions of some of the very commonly used models are presented in Chapter 3.

2.4 Maxwell's equations

An electromagnetic field, which is represented by two vectors, the electric vector ($\mathbf{E}$) and magnetic induction ($\mathbf{B}$), is created by the state of excitation which is established in space by the presence of electric charges [33]. The three vectors, the electric current density ($\mathbf{J}$), the electric displacement ($\mathbf{D}$) and the magnetic vector ($\mathbf{H}$), are necessary in order to describe the effect of the electromagnetic field on material objects [33]. The following Maxwell's equations relate the space and time derivatives of these five vectors, that hold at every point in a continuous medium [33].

$$\nabla \times \mathbf{H} - \frac{\partial \mathbf{D}}{\partial t} = \mathbf{J}, \tag{2.10}$$

$$\nabla \times \mathbf{E} + \frac{\partial \mathbf{B}}{\partial t} = \mathbf{0}, \tag{2.11}$$

$$\nabla \cdot \mathbf{D} = \rho, \tag{2.12}$$

$$\nabla \cdot \mathbf{B} = 0, \tag{2.13}$$

where ρ is the electric charge density. Equation (2.10) is the Ampère's circuit law with Maxwell's correction. Equation (2.11) is the Maxwell-Faraday equation. Equations (2.12) and (2.13) are Gauss' law and Gauss' law for magnetism, respectively. For dielectric media without free charges or currents, $\mathbf{J} = \mathbf{0}$ and $\rho = 0$ in the above set of equations [34].

In order to uniquely determine the field vectors from a given distribution of currents and charges, the four Maxwell's equations should be supplemented by relations which describe the behaviour of substances under the influence of the field. These relations, that are known as constitution relations, are complicated in general. However, if the field is time-harmonic, and if the bodies are at rest, or very slowly moving relative to each other, and if the material is isotropic, these

material equations take the relatively simple form [33]

$$\mathbf{J} = \sigma\mathbf{E}, \tag{2.14}$$

$$\mathbf{D} = \varepsilon\mathbf{E}, \tag{2.15}$$

$$\mathbf{B} = \mu\mathbf{H}, \tag{2.16}$$

where σ is the specific conductivity, ε is the dielectric constant, which is also known as the permittivity, and μ is the magnetic permeability.

2.5 Phase retrieval techniques

The visualization of the information imprinted by a weakly absorbing object into the phase of a transmitted electromagnetic wave, which is called phase imaging, has been studied in optics [35]. However, more recently, various techniques have been developed for retrieving the phase by numerical processing of data obtained by non-interferometric measurements of optical intensity, rather than visualizing the phase directly [35]. The optical phase-retrieval problem, which is to deduce optical phase from minimal irradiance measurements by using non-interferometric techniques, has been studied extensively in recent years [36]. Optical phase retrieval from intensity measurements has been an important issue in many fields including optics, electron and x-ray microscopy, crystallography and diffraction tomography [37]. Phase recovery is used in these disciplines as an essential component of the imaging technique, which enables the acquisition of important additional information about a sample [37]. Further, phase retrieval has been used in adaptive optical systems being developed in disciplines such as astronomy, synchrotron x-ray optics and ophthalmology. The recovered aberrations of the wave front are compensated with the help of a flexible mirror, which results in a significant improvement in the imaging quality of the optical system

[37]. Phase retrieval offers the advantage of recovering the phase in digital form, thus making it useful in quantitative analysis of samples [35].

Non-interferometric methods of phase retrieval, which attempt to recover the phase of an electromagnetic wave on the basis of direct measurements of its intensity, can be divided into two categories depending on the conditions of the intensity measurements [37]. In one category, the intensity of the wave field is measured in the far zone, and therefore, the complex amplitude of the scalar wave can be considered as a Fourier transform of the amplitude distribution in the object plane. When this amplitude distribution in the object plane is bounded by a finite aperture, its Fourier transform will be an analytic function whose phase and intensity depend on each other [37, 38]. Thus, the phase can be recovered in this case if the intensity data are known. In the other category, which was originally proposed by Teague [36, 39] and later developed by Roddier [40, 41], the intensity is measured in the Fresnel zone at two adjacent planes orthogonal to the optical axis and then the phase on the first plane is recovered by use of the information about the evolution of the intensity distribution [37].

Starting from the Schrödinger equation, an equation for the phase can be obtained, which expresses conservation of flux in a paraxial approximation [42]. This equation is referred to as the transport of intensity equation (TIE):

$$\nabla_{xy} \cdot \left[I\left(\mathbf{r}_{\perp}, z\right) \nabla_{xy} \phi\left(\mathbf{r}_{\perp}, z\right) \right] = -k \partial_z I\left(\mathbf{r}_{\perp}, z\right), \tag{2.17}$$

where ∇_{xy} is the gradient operator in the x-y plane, I is the irradiance, ϕ is the phase, k is the wave number and $\partial_z I\left(\mathbf{r}_{\perp}, z\right)$ is the intensity derivative along the direction of propagation at an image plane [42].

Teague [36] derived equations for the propagation of phase and irradiance,

and a Green's function solution for the phase in terms of irradiance and perimeter phase values has been presented. In this method the phase is given directly in terms of the measured irradiance data and hence it is a deterministic phase-retrieval scheme. However, the phase uniqueness question does not arise here as it does in methods based on iterative algorithms [36].

Gurevey *et al.* [37] proposed a method for phase recovery in the case of non-uniform illumination, which is based on the orthogonal series expansion. They claim that this method does not require any separate boundary conditions and that it can be more easily adjusted for apertures of various shapes. Gureyev *et al.* [35] proposed another method for digital phase imaging which requires the measurement of intensity in two adjacent planes orthogonal to the optical axis. The phase was proposed to be recovered by a Fast Fourier Transform of the TIE, and the phase was reconstructed as a sum of its Fourier components [35]. Their method assumed the Fresnel approximation. They claimed that their method was non-iterative and could cope with non-uniform intensity distributions in the plane in which the phase was reconstructed. Further, they stated that their method did not require separate boundary conditions for phase recovery [35].

Paganin *et al.* [43] proposed an algorithm that started from Teague's approximation which required the use of the calculus of pseudo-differential operators [42]. Allen *et al.* [42] developed and compared three different methods of phase retrieval from series of image measurements obtained at different defocus values. The first method was an approximate solution to the transport of intensity equation (TIE) based on Fourier transforms, the second method was an exact solution of the TIE based on multigrid methods and the third method was an iterative approach, that used the free space propagator between image planes [42]. In their first method, Allen *et al.* [42] presented an approximate solution to the TIE, start-

ing out by making an approximation to obtain an equation of the Poisson type for an auxiliary function. They showed that by differentiation, a second Poisson equation can be obtained for the phase itself [42] as opposed to Teague's approach based on Green functions [36]. They claimed that all the steps in their approach could be cast in terms of Fourier transforms [42].

2.6 Conclusions

This chapter has provided brief discussions of some of the basic topics which are required to understand the content of this dissertation. The way researchers model tissue was discussed very briefly, stating the assumptions they made. The propagation of light in tissue was discussed, along with the introduction of the definitions of absorption and scattering coefficients, albedo and optical thickness. A brief account of the applicability of the photon transport theory was provided as opposed to using Maxwell's equations for modeling light propagation in tissue, along with the introduction of the photon transport equation. The photon transport equation is used to model light propagation through biological tissue. A concise comparison of existing models for light propagation in turbid media was also presented.Maxwell's equations were introduced, followed by a discussion of phase retrieval techniques using intensity profiles.

2.7 References

[1] A. J. Welch and M. J. V. Gemert, *Optical-Thermal Response of Laser-Irradiated Tissue*. New York: Plenum Press, 1995.

[2] J. R. Mourant, J. P. Freyer, A. H. Hielscher, A. A. Eick, D. Shen, and T. M. Johnson, "Mechanisms of light scattering from biological cells relevant to noninvasive optical-tissue diagnostics," *Applied Optics*, vol. 37, no. 16, pp. 3586–3593, 1998.

[3] G. V. G. Baranoski and A. Krishnaswamy, "An introduction to light interaction with human skin," *RITA*, vol. XI, no. 1, pp. 33–62, 2004.

[4] R. A. Meyer, "Light scattering from biological cells: dependence of backscatter radiation on membrane thickness and refractive index," *Applied Optics*, vol. 18, no. 5, pp. 585–588, 1979.

[5] V. Tuchin, *Tissue Optics: Light Scattering Methods and Instruments for Medical Diagnosis*, 2nd ed. Washington, USA: SPIE Press, 2007.

[6] P. N. Prasad, *Introduction to Biophotonics*. New Jersey: John Wiley and Sons Inc., 2003.

[7] A. Dunn, *Light Scattering Properties of Cells*. Austin, USA: The University of Texas, 1998.

[8] D. A. Boas, M. A. O'Leary, B. Chance, and A. G. Yodh, "Scattering of diffuse photon density waves by spherical inhomogeneities within turbid media: Analytic solution and applications," *Proceedings of the National Academy of Sciences, USA*, vol. 91, pp. 4887–4891, 1994.

[9] J. Beuthan, O. Minet, J. Helfmann, M. Herrig, and G. Muller, "The spatial variation of the refractive index in biological cells," *Physics in Medicine & Biology*, vol. 41, pp. 369–382, 1996.

[10] V. V. Tuchin, "Light scattering study of tissues," *Physics-Uspekhi*, vol. 40, no. 5, pp. 495–515, 1997.

[11] Y. Yamada and Y. Hasegawa, "Time-dependent FEM analysis of photon migration in biological tissues," *JSME International Journal Series B*, vol. 39, no. 4, pp. 754–761, 1996.

[12] M. H. Niemz, *Laser Tissue Interactions: Fundamentals and Applications*. Germany: Springer, 2004.

[13] S. A. Prahl, J. C. van Gemert, and A. J. Welch, "Determining the optical properties of turbid media by using the adding-doubling method," *Applied Optics*, vol. 32, no. 4, pp. 559–568, 1993.

[14] A. Dunn and R. R. Kortum, "Three-dimensional computation of light scattering from cells," *IEEE Journal of Selected Topics in Quantum Electronics*, vol. 2, no. 4, pp. 898–905, 1996.

[15] G. Yoon, A. J. Welch, M. Motamedi, and M. C. J. van Germert, "Development and application of three-dimensional light distribution model for laser irradiated tissue," *IEEE Journal of Quantum Electronics*, vol. 23, no. 10, pp. 1721–1733, 1987.

[16] A. Ishimaru, *Wave Propagation and Scattering in Random Media, Vol. 1: Single Scattering and Transport Theory*. New York: Academic Press, 1978.

[17] W. Cheong, S. A. Prahl, and A. J. Welch, "A review of the optical properties of biological tissues," *IEEE Journal of Quantum Electronics*, vol. 26, no. 12, pp. 2166–2185, 1990.

[18] R. L. Fante, "Relationship between radiative-transport theory and Maxwell's equations in dielectric media," *Journal of the Optical Society of America*, vol. 71, no. 4, pp. 460–468, 1981.

[19] A. E. Profio, "Light transport in tissue," *Applied Optics*, vol. 28, no. 12, pp. 2216–2222, 1989.

[20] P. Edstrom, "A fast and stable solution method for the radiative transfer problem," *SIAM Review*, vol. 47, no. 3, pp. 447–468, 2005.

[21] M. Sakami, K. Mitra, and P. F. Hsu, "Analysis of light pulse transport through two-dimensional scattering and absorbing media," *Journal of Quantitative Spectroscopy & Radiative Transfer*, vol. 73, pp. 169–179, 2002.

[22] C. Y. Wu and S. H. Wu, "Integral equation formulation for transient radiative transfer in an anisotropically scattering medium," *International Journal of Heat and Mass Transfer*, vol. 43, pp. 2009–2020, 2000.

[23] K. Mitra, M. S. Lai, and S. Kumar, "Transient radiation transport in participating media within a rectangular enclosure," *Journal of Thermophysics and Heat Transfer*, vol. 11, no. 3, pp. 409–414, 1997.

[24] C. Y. Wu, "Propagation of scattered radiation in a participating planar medium with pulse irradiation," *Journal of Quantitative Spectroscopy & Radiative Transfer*, vol. 64, pp. 537–548, 2000.

[25] K. F. Evans, "The spherical harmonics discrete ordinate method for three-dimensional atmospheric radiative transfer," *Journal of the Atmospheric Sciences*, vol. 55, pp. 429–446, 1998.

[26] G. L. Stephens, "Radiative transfer through arbitrarily shaped optical media. Part I: A general method of solution," *Journal of the Atmospheric Sciences*, vol. 45, no. 12, pp. 1818–1836, 1988.

[27] P. M. Gabriel, S. C. Tsay, and G. L. Stephens, "A Fourier-Riccati approach to radiative transfer. Part I: Foundations," *Journal of the Atmospheric Sciences*, vol. 50, no. 18, pp. 3125–3147, 1993.

[28] V. L. Galinsky and V. Ramanathan, "3D radiative transfer in weakly inhomogeneous medium. Part I: Diffusive approximation," *Journal of the Atmospheric Sciences*, vol. 55, pp. 2946–2959, 1998.

[29] Z. Guo and S. Kumar, "Three-dimensional discrete ordinates method in transient radiative transfer," *Journal of Thermophysics and Heat Transfer*, vol. 16, no. 3, pp. 289–296, 2002.

[30] Z. Guo and K. Kim, "Ultrafast-laser-radiation transfer in heterogeneous tissues with the discrete-ordinates method," *Applied Optics*, vol. 42, no. 16, pp. 2897–2905, 2003.

[31] M. S. Patterson, B. C. Wilson, and D. R. Wyman, "The propagation of optical radiation in tissue I. Models of radiation transport and their application," *Lasers in Medical Science*, vol. 6, pp. 155–168, 1991.

[32] G. Yoon, S. A. Prahl, and A. J. Welch, "Accuracies of the diffusion approximation and its similarity relations for laser irradiated biological media," *Applied Optics*, vol. 28, pp. 2250–2255, 1989.

[33] M. Born and E. Wolf, *Principles of Optics*, 7th ed. Cambridge: Cambridge University Press, 1999.

[34] J. D. Joannopoulos, R. D. Meade, and J. N. Winn, *Photonic Crystals: Molding the Flow of Light*. Princeton University Press, 1995.

[35] T. E. Gureyev and K. Nugent, "Phase retrieval with the transport-of-intensity equation. II. Orthogonal series solution for non-uniform illumination," *Journal of Optical Society of America A*, vol. 13, pp. 1670–1682, 1996.

[36] M. R. Teague, "Deterministic phase retrieval: a Green's function solution," *Journal of Optical Society of America*, vol. 73, no. 11, pp. 1434–1441, 1983.

[37] T. E. Gureyev and K. A. Nugent, "Phase retrieval with the transport-of-intensity equation II. Orthogonal series solution for nonuniform illumination," *Journal of Optical Society of America A*, vol. 13, no. 8, pp. 1670–1682, 1996.

[38] M. V. Klibanov, P. E. Sacks, and A. V. Tikhonravov, "The phase retrieval problem," *Inverse Problems*, vol. 11, pp. 1–28, 1995.

[39] M. R. Teague, "Irradiance moments: their propagation and use for unique retrieval of phase," *Journal of Optical Society of America*, vol. 72, pp. 1199–1209, 1982.

[40] F. Roddier, "Curvature sensing and compensation: a new concept in adaptive optics," *Applied Optics*, vol. 27, no. 7, pp. 1223–1225, 1988.

[41] ——, "Wavefront sensing and the irradiance transport equation," *Applied Optics*, vol. 29, no. 10, pp. 1402–1403, 1990.

[42] L. J. Allen and M. P. Oxley, "Phase retrieval from series of images obtained by defocus variation," *Optics Communications*, vol. 199, pp. 65–75, 2001.

[43] D. Paganin and K. A. Nugent, "Non-interferometric phase imaging with partially coherent light," *Physical Review Letters*, vol. 80, pp. 2586–2589, 1998.

CHAPTER 3

Modeling Light Propagation in Tissue

This chapter presents the problem of numerical modeling of light propagation through tissue with detailed mathematical descriptions.

3.1 Introduction

NUMERICAL modeling of light propagation through tissue involves numerically solving the governing photon transport equation. As outlined in the previous chapter, many numerical techniques have been introduced by researchers in the field over the past decades. Most of these techniques developed in the last few decades have concentrated on solving the steady-state (i.e. time-independent) PTE, mainly focusing in the fields of astrophysical and atmospheric sciences. Only recently have researchers started developing models for the time-dependent PTE to be used in tissue optics. However, each of these techniques has relative advantages and disadvantages.

This chapter provides the basic mathematical descriptions required to discuss the techniques proposed in this dissertation in later chapters, and is divided into eight major sections. Section 3.2 provides some basic radiometric definitions of

radiance, irradiance and net flux vector. Section 3.3 provides a detailed mathematical description of the photon transport equation along with a description of the phase function of scattering. This section includes a discussion of how the complicated angular dependence of the phase function is simplified in most of the existing techniques that are used to analyze the PTE. Section 3.4 provides detailed descriptions of some of the widely-used existing models for simulating light propagation in turbid media. Section 3.5 provides a review of research on modeling light propagation through tissue with inhomogeneities to identify anomalies in tissue. Section 3.6 presents a brief account of the use of modeling light propagation through tissue with implanted structures for optical sensing of substances in blood or tissue fluid. This problem has not been discussed in the literature and a novel technique for this purpose is proposed in this dissertation. Section 3.7 concludes the chapter by summarizing the main points discussed in this chapter.

3.2 Radiometric definitions

Figure 3.1 shows the flow of radiative energy carried by a beam in the direction $\mathbf{\Omega}$ through a transparent surface element dA. $\mathbf{n}$ is the surface normal such that $\cos\theta = \mathbf{n} \cdot \mathbf{\Omega}$ [1].

RADIANCE (I)

Radiance is defined as the "radiant power per unit of solid angle about unit vector $\mathbf{\Omega}$ and per unit area perpendicular to $\mathbf{\Omega}$" [2]. That is, at a point on a surface and in a given direction, the radiant intensity of an element on the surface, divided by the area of the orthogonal projection of this element on a plane perpendicular to the given direction is defined as the radiance. Thus, the radiance,

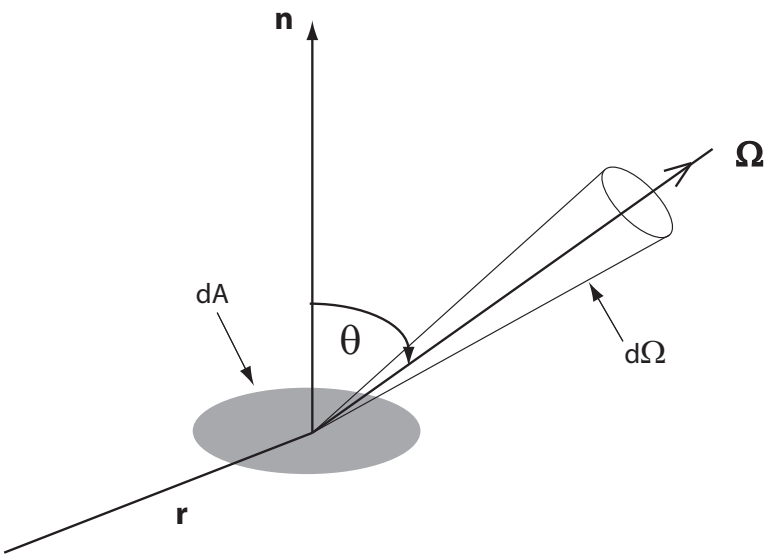

Figure 3.1: The flow of radiative energy carried by a beam in the direction $\mathbf{\Omega}$ through surface element dA [1].

I, can be expressed as

$$I(\mathbf{r}, \mathbf{\Omega}) = \frac{dP(\mathbf{r}, \mathbf{\Omega})}{dA cos\theta d\Omega} \quad \left[\text{W.m}^{-2}\text{.sr}^{-1}\right], \tag{3.1}$$

where $dP(\mathbf{r}, \mathbf{\Omega})$ [W] is the power flowing through an infinitesimal area dA, located at $\mathbf{r}$, in the direction of the unit vector $\mathbf{\Omega}$ (perpendicular to dA), within the infinitesimal solid angle $d\Omega$ [2].

Net Flux Vector

Flux is a description of photon energy transfer per unit area. The net flux vector, $\mathbf{F}(\mathbf{r})$, is the vector sum of elemental flux vectors $I(\mathbf{r}, \mathbf{\Omega})\mathbf{\Omega} d\Omega$ [2]. That is,

$$\mathbf{F}(\mathbf{r}) = \int_{4\pi} I(\mathbf{r}, \mathbf{\Omega})\mathbf{\Omega}\, d\Omega. \tag{3.2}$$

Hemispherical fluxes are defined as the energy flux through dA in either the forward direction $\mathbf{n}$, or the backward direction $-\mathbf{n}$. The hemispherical flux $\mathbf{F}_{n^+}(\mathbf{r})$ is an integral over the solid angle of 2π $(0 < \theta \leq \pi/2)$ and $\mathbf{F}_{n^-}(\mathbf{r})$ is an integral over the solid angle of 2π $(-\pi/2 < \theta \leq 0)$ [2]. Thus,

$$\mathbf{F}_{n^+}(\mathbf{r}) = \int_{2\pi} I(\mathbf{r}, \mathbf{\Omega})(\mathbf{\Omega} \cdot \mathbf{n})\, d\Omega \tag{3.3}$$

and

$$\begin{aligned} \mathbf{F}_{n^-}(\mathbf{r}) &= \int_{2\pi} I(\mathbf{r}, \mathbf{\Omega})(\mathbf{\Omega} \cdot -\mathbf{n})\, d\Omega, \\ &= -\int_{2\pi} I(\mathbf{r}, \mathbf{\Omega})(\mathbf{\Omega} \cdot \mathbf{n})\, d\Omega. \end{aligned} \tag{3.4}$$

From these forward and backward hemispherical fluxes, Eq. (3.3) and Eq. (3.4), and the basic definition of the net flux vector, Eq. (3.2), the net flux vector is related to the hemispherical fluxes as [2]

$$\mathbf{F}(\mathbf{r}) \cdot \mathbf{n} = \mathbf{F}_{n^+}(\mathbf{r}) - \mathbf{F}_{n^-}(\mathbf{r}). \tag{3.5}$$

IRRADIANCE ($\tilde{I}$)

Consider the flow of radiative energy across a surface element dA, located at a specific position, and having a unit normal $\mathbf{n}$ (as shown in Fig. 3.1). The net rate of radiative energy flow, or power per unit area within a small spectral range, is called the spectral net flux or irradiance [1] and can be expressed as

$$\tilde{I} = \frac{d^3E}{dAdtdv} \quad [\mathrm{W.m^{-2}.Hz^{-1}}]. \tag{3.6}$$

The irradiance (net flux) through a surface element dA depends upon the cumulative effect of all the angular beams crossing it in different directions. This quantity conveys little information about the directional dependence of the en-

ergy flow [1]. However, an absorbing chromophore at location **r** inside the tissue can absorb photons irrespective of their direction of propagation, and therefore, the integral of the radiance over all directions, (i.e. the irradiance), has more practical significance than the radiance itself [2].

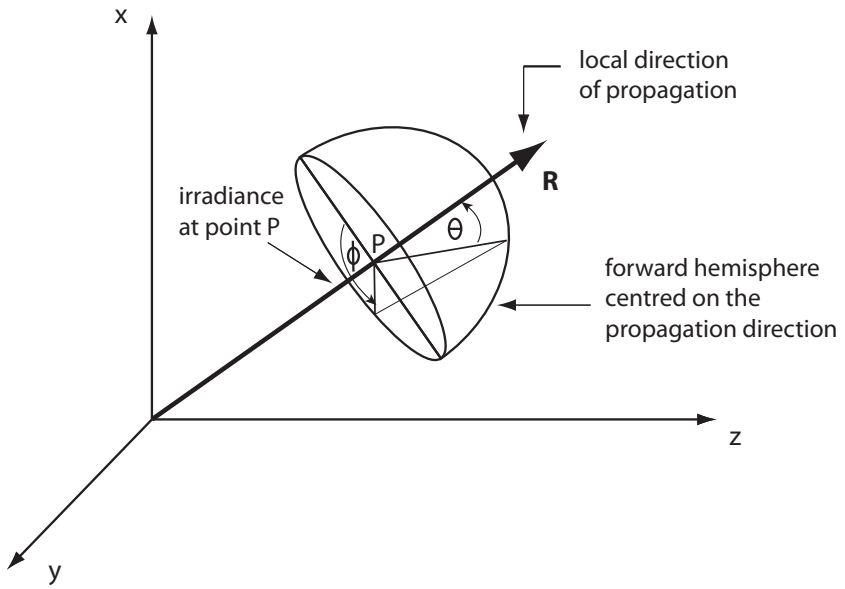

Figure 3.2: An illustration of the strategy used for mapping radiance to irradiance.

The radiance and irradiance can be related by [1]

$$\tilde{I} = \int_{4\pi} I \cos\theta \, d\Omega, \tag{3.7}$$

and this idea is graphically illustrated in Fig. 3.2.

3.3 The Photon Transport Equation

As mentioned in the previous chapter, the modeling of light propagation in tissue is governed by the photon transport equation, Eq. (2.9). Until recently, most tissue

optics studies considered only the steady-state (time-independent) transport of light [3]. The radiance in the transient PTE is dependent on the position, local solid angle as well as on time. The solid angle $\mathbf{\Omega}$ can be written in terms of the azimuthal angle, ϕ, and the zenith angle, θ, as

$$d\mathbf{\Omega} = \sin\theta \, d\theta \, d\phi. \tag{3.8}$$

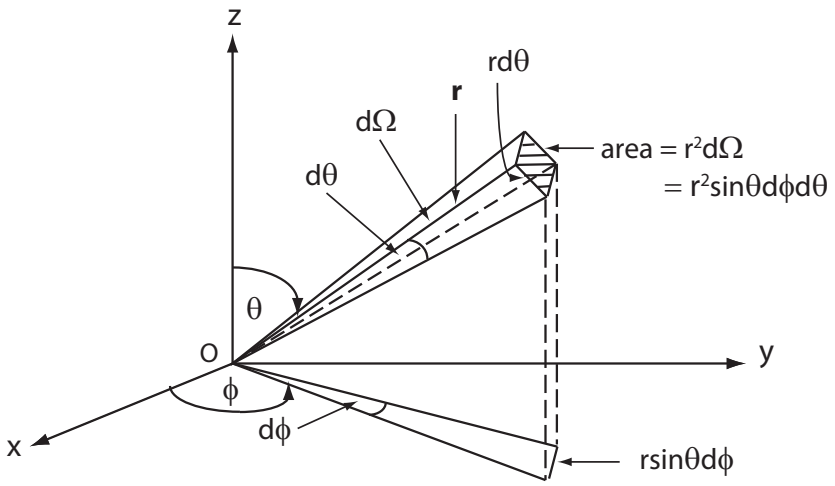

Figure 3.3: The relationship of the solid angle with the zenith and azimuthal angles.

The relationship given by Eq. (3.8) is graphically illustrated in Fig. 3.3. Thus, Eq. (2.9) can be written in terms of θ and ϕ [4]:

$$\begin{aligned}
&\frac{1}{v}\frac{\partial}{\partial t}I(x,y,z,u,\phi,t) + \xi\frac{\partial}{\partial x}I(x,y,z,u,\phi,t) + \eta\frac{\partial}{\partial y}I(x,y,z,u,\phi,t) \\
&+ u\frac{\partial}{\partial z}I(x,y,z,u,\phi,t) - \frac{\sigma_s}{4\pi}\int_0^{2\pi}\int_{-1}^{1} P(u',\phi';u,\phi)I(x,y,z,u',\phi',t)\,du'\,d\phi' \\
&+ \sigma_t I(x,y,z,u,\phi,t) = F(x,y,z,u,\phi,t),
\end{aligned} \tag{3.9}$$

where (x,y,z,θ,ϕ) are the standard coordinates, u, ξ and η are direction cosines such that $u = \cos\theta$, $\xi = \sin\theta\cos\phi$, $\eta = \sin\theta\sin\phi$ and t is time.

Equation (3.9) can be reduced to the two-dimensional transient PTE, where the radiance is considered to be a function of (y, z, u, ϕ, t):

$$\frac{1}{v}\frac{\partial}{\partial t}I(y,z,u,\phi,t) + \eta\frac{\partial}{\partial y}I(y,z,u,\phi,t) + u\frac{\partial}{\partial z}I(y,z,u,\phi,t) + \sigma_t I(y,z,u,\phi,t) - \frac{\sigma_s}{4\pi}\int_0^{2\pi}\int_{-1}^{1} P(u',\phi';u,\phi)I(y,z,u',\phi',t)\,du'\,d\phi' = F(y,z,u,\phi,t). \tag{3.10}$$

This can be reduced to the one-dimensional transient PTE, where the radiance is considered to be a function of only (z, u, ϕ, t):

$$\frac{1}{v}\frac{\partial}{\partial t}I(z,u,\phi,t) + u\frac{\partial}{\partial z}I(z,u,\phi,t) + \sigma_t I(z,u,\phi,t) - \frac{\sigma_s}{4\pi}\int_0^{2\pi}\int_{-1}^{1} P(u',\phi';u,\phi)I(z,u',\phi',t)\,du'\,d\phi' = F(z,u,\phi,t). \tag{3.11}$$

The source term, $F(\mathbf{r}, \mathbf{\Omega}, t)$, can incorporate the irradiance, but can also be used to represent fluorescence light generated within tissue or the internal light source during interstitial laser therapy [2].

Calculations of light distribution based on the photon transport equation require knowledge of the absorption and scattering coefficients and the phase function. Yet to arrive at these parameters, one must first have a solution of the photon transport equation [3]. Typical optical properties are obtained by using solutions of the PTE that express the optical properties in terms of readily measurable quantities [5].

In most existing methods for solving the PTE, first the phase function is expanded using Legendre polynomials [6]. With this expansion, the phase function is expressed as [6]

$$P\left(u',\phi';u,\phi\right) = \sum_{m=0}^{2N-1}\left(2-\delta_{0m}\right)p^m\left(u',u\right)\cos\left(m(\phi'-\phi)\right), \tag{3.12}$$

where δ_{0m} is Kronecker's delta defined as

$$\delta_{0m} = \begin{cases} 1, & \text{for } m = 0 \quad (3.13a) \\ 0, & \text{for } m \neq 0. \quad (3.13b) \end{cases}$$

The radiance is then expanded in Fourier cosine series:

$$I(x, y, z, u, \phi, t) = \sum_{m=0}^{2N-1} I^m(x, y, z, u, t) \cos(m(\phi - \phi_0)). \quad (3.14)$$

Use of Eq. (3.12) and Eq. (3.14) in the one-dimensional PTE removes the azimuthal dependence resulting in a set of $2N$ equations, one for each Fourier component. Thus, for the one-dimensional case, the PTE reduces to [7]

$$\frac{1}{v}\frac{\partial}{\partial t} I(z, u, t) + u\frac{\partial}{\partial z} I(z, u, t) + \sigma_t I(z, u, t) - \frac{\sigma_s}{2}\int_{-1}^{1} P(u'; u) I(z, u', t)\, du' = F(z, u, t). \quad (3.15)$$

However, this approach cannot be used to remove the azimuthal dependence in two-dimensional and three-dimensional PTE, because the direction cosines ξ and η in these cases are functions of the azimuthal angle, ϕ.

3.3.1 Phase function of scattering

The single-scattering phase function describes the amount of light scattered at an angle Θ from the incoming direction [5]. We assume that the scattering depends only on the angle Θ between unit vector directions $\mathbf{\Omega}$ and $\mathbf{\Omega}'$. Therefore, we assume that tissue is isotropic in terms of physical properties (such as refractive index and density) [2]. The phase function is normalized such that its integral over all directions is unity [5]. Figure 3.4 shows the incident and scattered directions and the scattering angle.

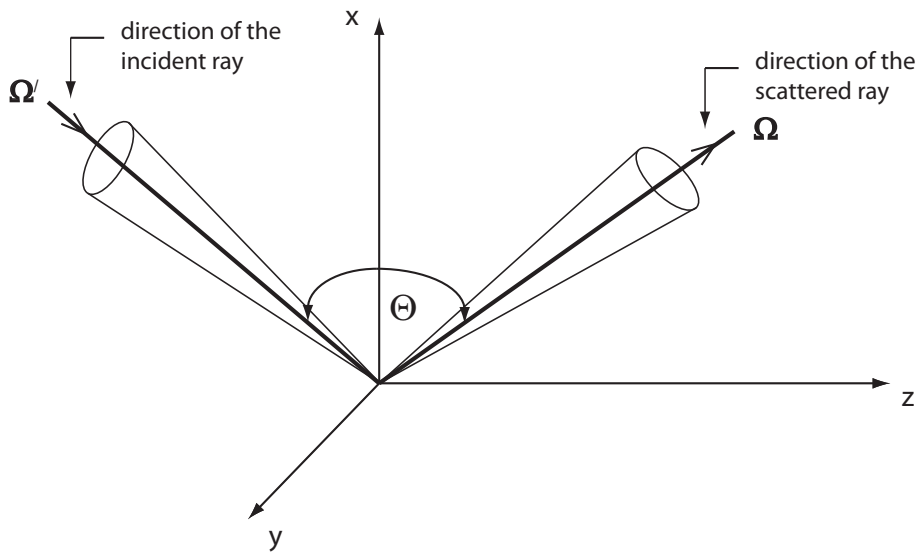

Figure 3.4: Illustration of the incident direction, scattered direction and the scattering angle.

Several phase functions, such as the Henyey-Greenstein, the modified Henyey-Greenstein, the Eddington, the delta-Eddington, the isotropic, the delta-isotropic and a combination of the Rayleigh phase function and the Henyey-Greenstein phase function [8] have been postulated to represent single scattering phase functions for tissue [2, 3]. Among these, the Henyey-Greenstein phase function can be used to model dermal and aortic tissues [3] and this phase function has been used widely in modeling light propagation in tissue.

Isotropic scattering implies that the phase function is unity [1]; i.e. $P(\mathbf{\Omega}', \mathbf{\Omega}) = 1$. Light scattering in tissue is not isotropic but strongly forward-directed [2]. A measure of the degree of anisotropy in scattering is the anisotropy factor g. Total forward scattering means $g = 1$ and isotropic scattering means $g = 0$; but for *in vitro* tissues at the visible and near-infrared wavelengths, g is found to be between about 0.7 and 0.99 [2].

Mathematically, g is defined as the expectation value of the cosine of the scat-

tering angle Θ [2]. That is

$$g = \frac{\int_{4\pi} P(\mathbf{\Omega}', \mathbf{\Omega})(\mathbf{\Omega}' \cdot \mathbf{\Omega})\, d\mathbf{\Omega}'}{\int_{4\pi} P(\mathbf{\Omega}', \mathbf{\Omega})\, d\mathbf{\Omega}'}. \tag{3.16}$$

The phase function is normalized such that [2]

$$\int_{4\pi} P(\mathbf{\Omega}', \mathbf{\Omega})\, d\mathbf{\Omega}' = 1. \tag{3.17}$$

Therefore, Eq. (3.16) reduces to

$$g = \int_{4\pi} P(\mathbf{\Omega}', \mathbf{\Omega})(\mathbf{\Omega}' \cdot \mathbf{\Omega})\, d\mathbf{\Omega}'. \tag{3.18}$$

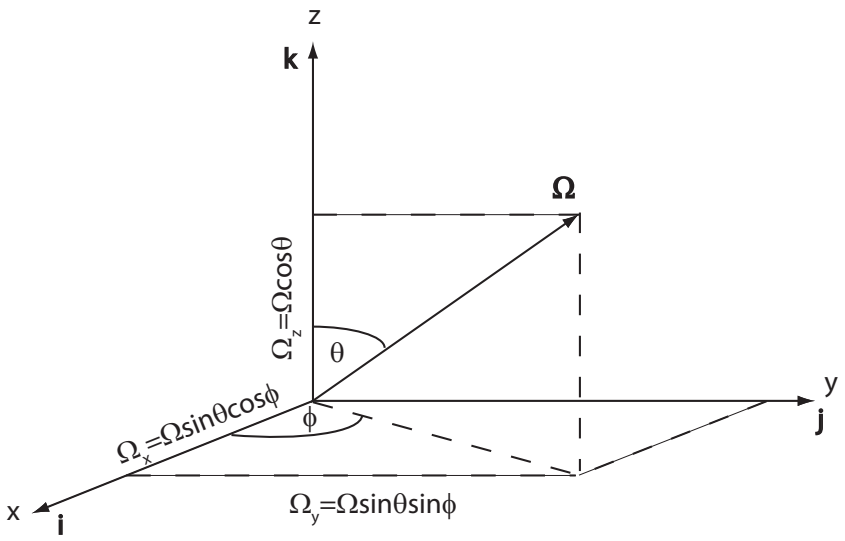

Figure 3.5: Relationship between the Cartesian and spherical coordinates.

In most of the models that have been proposed to solve the photon transport equation, the phase function is not used as it is, but rather as its expansion in Legendre polynomials [1]. The direction of the incident ray, $\mathbf{\Omega}$, and the direction of the scattered ray, $\mathbf{\Omega}'$, can be expressed in terms of unit vectors $\mathbf{i}, \mathbf{j}, \mathbf{k}$ along the

axes x, y, z, respectively. As shown in Fig. 3.5,

$$\mathbf{\Omega} = \Omega_x \mathbf{i} + \Omega_y \mathbf{j} + \Omega_z \mathbf{k}, \tag{3.19}$$

$$\mathbf{\Omega}' = \Omega'_x \mathbf{i} + \Omega'_y \mathbf{j} + \Omega'_z \mathbf{k}. \tag{3.20}$$

The dot product of $\mathbf{\Omega}$ and $\mathbf{\Omega}'$ results in,

$$\mathbf{\Omega} \cdot \mathbf{\Omega}' = \Omega\Omega' \cos\Theta = \Omega_x\Omega'_x + \Omega_y\Omega'_y + \Omega_z\Omega'_z. \tag{3.21}$$

Thus, Eq. (3.21) can be expressed in spherical coordinates as

$$\Omega\Omega' \cos\Theta = \Omega\Omega' \sin\theta \cos\phi \sin\theta' \cos\phi' + \Omega\Omega' \sin\theta \sin\phi \sin\theta' \sin\phi' + \Omega\Omega' \cos\theta \cos\theta', \tag{3.22}$$

where θ is the zenith angle and ϕ is the azimuthal angle. Equation 3.22 reduces to,

$$\cos\Theta = \cos\theta \cos\theta' + \sin\theta \sin\theta' \cos(\phi' - \phi). \tag{3.23}$$

The phase function can be expanded using Legendre polynomials of degree l, given by $\tilde{P}_l(\cos\Theta)$, as

$$P(\cos\Theta) \approx \sum_{l=0}^{2N-1} (2l+1)\chi_l \tilde{P}_l(\cos\Theta), \tag{3.24}$$

where

$$\chi_l = \frac{1}{2} \int_{-1}^{1} \tilde{P}_l(\cos\Theta) P(\cos\Theta)\, d(\cos\Theta). \tag{3.25}$$

Using the spherical harmonic addition theorem, the phase function can be written in terms of the azimuthal and zenith angles as [6]

$$P\left(u', \phi'; u, \phi\right) = \sum_{m=0}^{2N-1} (2 - \delta_{0m}) p^m\left(u', u\right) \cos(m(\phi' - \phi)), \tag{3.26}$$

where

$$p^m(u', u) = \sum_{l=m}^{2N-1} (2l+1)\chi_l \Lambda_l^m(u')\Lambda_l^m(u), \tag{3.27}$$

$$\Lambda_l^m(u) = \sqrt{\frac{(l-m)!}{(l+m)!}} \tilde{P}_l^m(u), \tag{3.28}$$

$\Lambda_l^m(u)$ are the normalized associate Legendre functions and $\tilde{P}_l^m(u)$ are the associate Legendre functions [6].

3.4 Existing models for simulating light propagation in turbid media

In this section, some of the widely used models for light propagation in turbid media are described in detail with an evaluation of the relative advantages and disadvantages of each method.

The Monte Carlo Method

Monte Carlo simulations of photon propagation offer a flexible but rigorous approach to photon transport in tissues [2]. The principal idea of Monte Carlo simulations applied to absorption and scattering phenomena is to follow the optical path of a photon through the turbid medium. In this method, the rules of photon propagation are expressed as probability distributions for the incremental steps of photon movement between sites of photon-tissue interaction, for the angles of deflection in a photon's trajectory when a scattering event occurs, and for the probability of transmittance or reflectance at boundaries [2].

This method simulates the "random walk" of photons in a medium that contains absorption and scattering. It is based on a set of rules that govern the movement of a photon in tissue. The two key decisions are the mean free path for a

scattering or absorption event and the scattering angle [2].

The five principal steps of Monte Carlo simulations of absorption and scattering as described in [9] are given below.

1. **Source photon generation**: Photons are generated at a surface of the considered medium. Their spatial and angular distributions can be fitted to a given light source (e.g. a Gaussian beam).
2. **Pathway generation**: After generating a photon, the distance to the first collision is determined. Absorbing and scattering particles in the turbid medium are assumed to be randomly distributed. Thus, the mean free path is $1/\varrho\sigma_s$, where ϱ is the density of particles and σ_s is their scattering cross-section. A random number ξ_1, such that $0 < \xi_1 < 1$, is generated by the computer, and the distance $L(\xi_1)$ to the next collision is calculated from
$$L(\xi_1) = -\frac{\ln(\xi_1)}{\varrho\sigma_s}. \tag{3.29}$$
Since
$$\int_0^1 \ln(\xi_1)\, d\xi_1 = -1 \tag{3.30}$$
the average value of $L(\xi_1)$ is indeed $1/\varrho\sigma_s$. Hence, a scattering point has been obtained. The scattering angle is determined by a second random number, ξ_2, in accordance with a certain phase function. The corresponding azimuth angle ϕ is chosen as $\phi = 2\pi\xi_3$ where ξ_3 is a third random number between 0 and 1.
3. **Absorption**: To account for absorption, a weight is attributed to each photon. When entering a turbid medium, the weight of the photon is unity. Due to absorption (in a more accurate program also due to reflection), the weight is reduced by $exp(-\alpha L(\xi_1))$, where α is the absorption coefficient. As an alternative to implementing a weight, a fourth random number ξ_4

between 0 and 1 can be drawn. Instead of assuming only scattering events in step 2, scattering takes place if $\xi_4 < a$, where a is the albedo. For $\xi_4 > a$, on the other hand, the photon is absorbed, which then is equivalent to step 4.

4. **Elimination**: This step only applies if a weight has been attributed to each photon. When this weight reaches a certain cutoff value, the photon is eliminated. A new photon is then launched, and the program proceeds with step 1.
5. **Detection**: After having repeated steps 1-4 for a sufficient number of photons, a map of pathways is calculated and stored in the computer. Thus, statistical statements can be made about the fraction of incident photons being absorbed by the medium as well as the spatial and angular distributions of photons having escaped from it.

In summary, the distance between two collisions is selected from a logarithmic distribution, using a random number generated by a computer. The absorption is accounted for by implementing a weight to each photon and permanently reducing this weight during propagation. If scattering is to occur, a new direction of propagation is chosen according to a given phase function and another random number is generated [9]. The whole procedure continues until the photon escapes from the considered volume or its weight reaches a given cutoff value [9].

Even though the Monte Carlo method is rigorous, it is computationally intense. This method is basically statistical in nature and requires a computer to calculate the propagation of a large number of photons [2]. This is because the error bound of the Monte Carlo method is inversely proportional to the square root of the number of statistical samplings and hence it requires a large number of samples to reach the satisfactory accuracy [10].

Various variance reduction techniques are used to increase the efficiency of Monte Carlo simulations [11]. The most fundamental of these is a technique in which absorption is modeled by reducing photon weights rather than by photon termination [11]. Other techniques include photon splitting, electron history repetition, Russian roulette and the use of quasi-random numbers [12]. Variance reduction techniques are used to decrease the statistical fluctuations of Monte Carlo calculations without increasing the number of particle histories [12].

Sawetprawichkul *et al.* [10] implemented a three-dimensional transient radiative transport model using Monte Carlo method on a parallel computer system. Their coding was based on a single program multiple data model and a message passing interface was used to achieve parallelization. A single program multiple data model uses the same program in all nodes, but these nodes may produce different data depending on the given input [10]. Sawetprawichkul *et al.* [10] showed that the Monte Carlo method is very adaptable to parallel computing, despite being computationally intensive.

Graphics processing units (GPUs) can be used to dramatically increase the speed of Monte Carlo simulations of photon transport applications [11]. Alerstam *et al.* [11] showed that a simulation of a standard time-resolved photon migration problem in a semi-infinite geometry on a low-cost GPU was 1000 times faster than on a single standard processor. On a GPU, a single program multiple data model works by launching thousands of threads running the same program, which is called the kernel, working on different data [11]. Alerstam *et al.* [11] compared central processing unit (CPU) and GPU speeds by executing the same Monte Carlo code of photon migration. They showed that the GPU implementation was about 1080 times faster than the conventional CPU implementation.

Even though the use of GPUs for Monte Carlo simulations of photon migration has been suggested in literature, they have never been used for this purpose [11]. However, GPUs have been used for Monte Carlo simulations in other fields [11]. The choice of the method of random number generation is a very important aspect of executing Monte Carlo simulations in parallel. This is due to the fact that the same random number generator with the same seed (e.g. when a timestamp is used as the seed) would most likely result in many threads performing exactly the same computations [11]. Therefore, when Monte Carlo codes are executed in parallel different threads should be properly and differently seeded [11].

THE ADDING-DOUBLING METHOD

The adding-doubling method is a general numerical solution of the photon transport equation [5, 13]. This method works naturally with layered media and yields reflection and transmission information readily. Reflectance is important for diagnostic applications using light. For measuring the optical properties of a sample, the only values needed are the total reflection and transmission of the sample [2]. The doubling method was introduced by Van de Hulst to solve the photon transport equation in a slab geometry [2].

The adding-doubling method involves obtaining the reflection and the transmission matrices. Here, doubling refers to how one finds the reflection and transmission matrices of two layers with identical optical properties from those of the individual layers [1]. Thus, the doubling method assumes knowledge of the reflection and transmission properties of a single thin homogeneous layer. The reflection and transmission of a slab twice as thick is found by juxtaposing two identical slabs, and summing the contributions from each slab [2, 5]. To start the

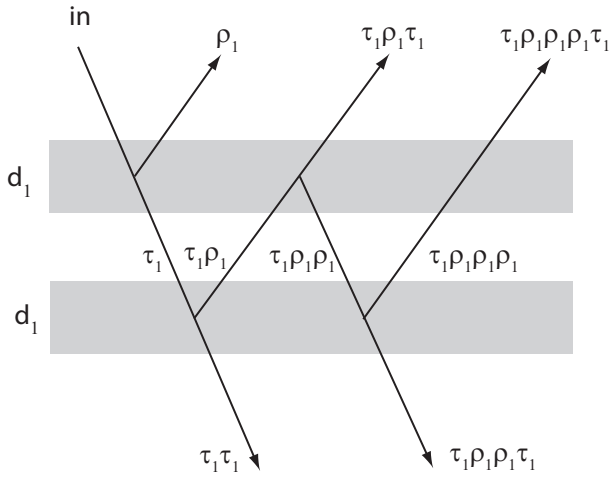

Figure 3.6: Illustration of the doubling concept [1].

doubling procedure the initial layer is frequently taken to be thin enough that its reflection and transmission properties can be computed from single scattering [1]. The reflection and transmission from an arbitrarily thick slab are obtained by repeatedly doubling until the desired thickness is reached [1, 2].

The adding method refers to the combination of two or more layers with different optical properties [1]. That is, the adding method extends the doubling method to dissimilar slabs, thus making it possible to simulate media with different layers and/or internal reflection at boundaries [2].

The solution technique for the adding-doubling method proceeds by first applying doubling to find the reflection and transmission matrices for each of the homogeneous layers, whereupon adding is subsequently used to find the solution for all the different layers combined [1].

Figure 3.6 shows an illustration of the doubling concept. Basically, the doubling concept starts with the notion that the emergent intensities $\mathbf{I}^+(0)$ (the backscattered intensity at $z = 0$) and $\mathbf{I}^-(d)$ (the forward intensity at $z = d$) are determined

by a reflection matrix, $\boldsymbol{\rho}$, and a transmission matrix, $\boldsymbol{\tau}$, through the relations [1]

$$\mathbf{I}^{-}(d) = \boldsymbol{\tau}\mathbf{I}^{-}(0) + \boldsymbol{\rho}\mathbf{I}^{+}(d), \tag{3.31}$$

$$\mathbf{I}^{+}(0) = \boldsymbol{\rho}\mathbf{I}^{-}(0) + \boldsymbol{\tau}\mathbf{I}^{+}(d), \tag{3.32}$$

for a homogeneous slab of thickness d.

Equation (3.31) and Eq. (3.32) can be written in matrix form as

$$\begin{pmatrix} \mathbf{I}^{-}(d) \\ \mathbf{I}^{+}(d) \end{pmatrix} = \begin{pmatrix} \boldsymbol{\tau} - \boldsymbol{\rho}\boldsymbol{\tau}^{-1}\boldsymbol{\rho} & \boldsymbol{\rho}\boldsymbol{\tau}^{-1} \\ -\boldsymbol{\tau}^{-1}\boldsymbol{\rho} & \boldsymbol{\tau}^{-1} \end{pmatrix} \begin{pmatrix} \mathbf{I}^{-}(0) \\ \mathbf{I}^{+}(0) \end{pmatrix}. \tag{3.33}$$

If $\boldsymbol{\tau}_1 = \boldsymbol{\tau}(d)$, $\boldsymbol{\rho}_1 = \boldsymbol{\rho}(d)$, $\boldsymbol{\tau}_2 = \boldsymbol{\tau}(2d)$ and $\boldsymbol{\rho}_2 = \boldsymbol{\rho}(2d)$, then comparing Eq. (3.33) with the re-arranged steady-state PTE in matrix form, it can be shown that [1]

$$\begin{pmatrix} \boldsymbol{\tau}_2 - \boldsymbol{\rho}_2\boldsymbol{\tau}_2^{-1}\boldsymbol{\rho}_2 & \boldsymbol{\rho}_2\boldsymbol{\tau}_2^{-1} \\ -\boldsymbol{\tau}_2^{-1}\boldsymbol{\rho}_2 & \boldsymbol{\tau}_2^{-1} \end{pmatrix} = \begin{pmatrix} \boldsymbol{\tau}_1 - \boldsymbol{\rho}_1\boldsymbol{\tau}_1^{-1}\boldsymbol{\rho}_1 & \boldsymbol{\rho}_1\boldsymbol{\tau}_1^{-1} \\ -\boldsymbol{\tau}_1^{-1}\boldsymbol{\rho}_1 & \boldsymbol{\tau}_1^{-1} \end{pmatrix}^{2}. \tag{3.34}$$

Solutions for $\boldsymbol{\tau}_2$ and $\boldsymbol{\rho}_2$ are obtained by,

$$\boldsymbol{\tau}_2 = \boldsymbol{\tau}_1(\mathbf{I} - \boldsymbol{\rho}_1^2)^{-1}\boldsymbol{\tau}_1, \tag{3.35}$$

$$\boldsymbol{\rho}_2 = \boldsymbol{\rho}_1 + \boldsymbol{\tau}_1\boldsymbol{\rho}_1(\mathbf{I} - \boldsymbol{\rho}_1^2)^{-1}\boldsymbol{\tau}_1, \tag{3.36}$$

where $\mathbf{I}$ is the identity matrix [1]. Equation (3.35) and Eq. (3.36) constitute the basic doubling rules from which the reflection and transmission matrices for a layer of thickness $2d$ are obtained from those of half the thickness, d [1].

The adding-doubling method is based on the numerical integration of func-

tions with quadrature [5]:

$$\int_0^1 f(v, v')\, dv' = \sum_{k=1}^{N} H_k f(x_k). \tag{3.37}$$

The quadrature points, x_k, and weights, H_k, are chosen so that the integral is approximated exactly for a polynomial of order $2N - 1$ [5]. Use of N quadrature points (Gaussian quadrature) is equivalent to the spherical harmonic method of order P_{N-1} [5].

The adding-doubling method is sufficiently fast that iterated solutions are possible on microcomputers [5]. This method is also sufficiently flexible that anisotropic scattering and internal reflection at the boundaries may be included [5]. Internal reflection at the boundaries (caused by mismatched indices of refraction) can be included in the calculation by adding an additional layer for each mismatched boundary. The reflection and transmission of this layer is equal to the Fresnel reflection and transmission for unpolarized light incident on a plane boundary between two transparent media with the same indices of refraction [5].

For a medium characterized by any phase function adding-doubling method can be used for any tissue optical thickness [2]. This method is accurate for any ratio of scattering to absorption and the adding method can be used to obtain the reflection and transmission of inhomogeneous layered media with different optical properties [2]. The adding method is a powerful technique for computing the radiance at the entrance and exit surfaces of a slab [14].

The adding-doubling method assumes that the distribution of light is independent of time, samples have homogeneous optical properties, the sample geometry is an infinite plane-parallel slab of finite thickness, the tissue has a uni-

form index of refraction, internal reflection at boundaries is governed by Fresnel's law, the light is unpolarized and the slab has no internal sources [2, 5]. The adding-doubling method has several advantages over most other techniques, because it permits asymmetric scattering, arbitrarily thick samples, Fresnel boundary conditions and relatively fast computations [15]. In addition, in this method only integrations over angle are required and physical interpretation of results can be made at each step. This method is equivalent for isotropic and anisotropic scattering and the results are obtained for all angles of incidence used in the integration [2, 5]. Two disadvantages of the adding-doubling method are that it is restricted to layered geometries with uniform irradiation and it is necessary that each layer has homogeneous optical properties [2, 5].

When a one-dimensional geometry is a reasonable representation, then the adding-doubling method provides an accurate solution of the photon transport equation for any phase function [3]. However, since it is incapable of providing the radiance at arbitrary positions within the slab, its application to tissue optics is limited [14].

THE DIFFUSION APPROXIMATION

The diffusion equation is derived as an approximate solution of the photon transport equation [2]. It combines the scattering and the phase function in one parameter, called the reduced scattering coefficient [15]. The photon diffusion approximation is often employed to simplify the photon transport equation into a partial differential equation with respect to space and time. However, the photon diffusion equation involves some errors due to the approximation used in its derivation [16].

In this theory, light is principally described by particles with energy $h\nu$ and velocity c [2]. These particles are scattered or absorbed by structures in turbid media, and reflected at boundaries. These reflections can be determined by equations of Fresnel reflection [2].

In diffusion theory, the radiance in the steady-state PTE is separated into unscattered, $I_c(\mathbf{r}, \mathbf{\Omega})$, and scattered, $I_d(\mathbf{r}, \mathbf{\Omega})$, components [3];

$$I(\mathbf{r}, \mathbf{\Omega}) = I_c(\mathbf{r}, \mathbf{\Omega}) + I_d(\mathbf{r}, \mathbf{\Omega}). \tag{3.38}$$

The unscattered portion contains all the light that has not interacted with tissue and it satisfies Beer's law [3]. The scattered portion contains all the light that has been scattered at least once and can be expressed exactly with an infinite sum of Legendre polynomials. However, the diffusion approximation truncates this sum to the first two terms (an isotropic and a slightly forward- directed term) [3]. This approximation simplifies the photon transport equation to the diffusion equation given by

$$\left(\nabla^2 - \kappa^2\right) \Phi(\mathbf{r}) = -Q_0(\mathbf{r}), \tag{3.39}$$

where the constant κ is an approximation of the actual measured effective attenuation coefficient when absorption is dominated by scattering, the source term $Q_0(\mathbf{r})$ is generated by scattering of collimated normal irradiation and the total scattered fluence rate $\Phi(\mathbf{r})$ is given by [3]

$$\Phi(\mathbf{r}) = \int_{4\pi} I_d(\mathbf{r}, \mathbf{\Omega})\, d\mathbf{\Omega}. \tag{3.40}$$

The diffusion model is approximately valid if the optical mean free path $(1/\sigma_t)$ is much smaller than the typical dimensions of the problem considered and if a photon is scattered many times before it is absorbed or leaves a medium [2]. Un-

der these conditions, the density of photons at a given position is nearly uniform in all directions [2]. The accuracy of the diffusion equation is affected by the ratio of scattering and absorption, the scattering anisotropy, and the distance from light sources and boundaries [3]. When absorption is small compared to scattering, scattering is not very anisotropic and the irradiance is not needed close to the source or a strong absorber or boundary, then diffusion theory may be used [17]. Despite these assumptions, the fact that a three-dimensional problem can be solved at all is a clear advantage of the diffusion theory [2].

When the absorption coefficient is not significantly smaller than the scattering coefficient, the diffusion approximation provides a poor approximation of the photon transport equation. It is worth noting that the human skin is characterized by the presence of pigments, such as melanin particles, which have a significant absorption cross-section [15]. In addition, the diffusion approximation is not applicable when scattering is mostly forward-peaked, which is the usual case in tissue [15]. Diffusion theory can be derived from general principles using only macroscopic tissue properties and is therefore expected to hold with the restrictions involved in the approximation [2]. The time-dependent photon diffusion equation is believed to give inaccurate solutions at early times and in the vicinity of boundaries. In addition, there is controversy about how the diffusion coefficient should be specified [16].

THE KUBELKA-MUNK THEORY

The Kubelka-Munk (K-M) theory describes the propagation of a uniform, diffuse irradiance through a one-dimensional isotropic slab with no reflection at the boundaries [3, 18, 19]. This theory is a special case of the so-called many flux theory, where the PTE is converted into a matrix differential equation by considering

the radiance at many discrete angles [9]. The original K-M theory is considered to be a two-flux theory, which involves only two types of diffuse irradiance, forward irradiance and backward irradiance [15]. However, this theory has been recently extended to the many flux theory, hence improving its applicability to tissue optics [15].

The Kubelka-Munk expressions for reflection (R) and transmission (T) of diffuse irradiance on a slab of thickness t are [3];

$$R = \frac{\sinh(S_{KM}yt)}{x\cosh(S_{KM}yt) + y\sinh(S_{KM}yt)}, \tag{3.41}$$

$$T = \frac{y}{x\cosh(S_{KM}yt) + y\sinh(S_{KM}yt)}, \tag{3.42}$$

where A_{KM} and S_{KM} are the Kubelka-Munk absorption and scattering coefficients, respectively, and have units of inverse length (m^{-1}). The parameters x and y are found using the equations given below [3].

$$A_{KM} = (x-1)S_{KM}, \tag{3.43}$$

$$S_{KM} = \frac{1}{yt} ln\left[\frac{1-R(x-y)}{T}\right], \tag{3.44}$$

$$x = \frac{1+R^2-T^2}{2R}, \tag{3.45}$$

$$y = +\sqrt{x^2-1}. \tag{3.46}$$

With these parameters two differential equations can be formed [9]:

$$\frac{dJ_1}{dz} = -S_{KM}J_1 - A_{KM}J_1 + S_{KM}J_2, \tag{3.47}$$

$$\frac{dJ_2}{dz} = -S_{KM}J_2 - A_{KM}J_2 + S_{KM}J_1, \tag{3.48}$$

where J_1 is the flux in the direction of the incident radiation, J_2 is the backscattered flux in the opposite direction and z denotes the mean direction of incident

radiation. The general solutions to Eq. (3.47) and Eq. (3.48) can be expressed by [9]:

$$J_1(z) = c_{11}e^{-\gamma z} + c_{12}e^{+\gamma z}, \tag{3.49}$$

$$J_2(z) = c_{21}e^{-\gamma z} + c_{22}e^{+\gamma z}, \tag{3.50}$$

where $\gamma = \sqrt{A_{KM}^2 + 2A_{KM}S_{KM}}$.

One advantage of the Kubelka-Munk model is that the scattering and absorption coefficients may be directly expressed in terms of the measured reflection and transmission [3]. The simplicity of the Kubelka-Munk model has made it a popular method for measuring the optical properties of tissue. Unfortunately, the assumptions of isotropic scattering, matched boundaries and diffuse irradiance are atypical of the interaction of laser light with tissue [3].

K-M model is not a thorough model of photon transport [15]. Even though this model allows rapid determination of the optical parameters of tissue, its relative simplicity and the speed are achieved at the expense of the accuracy [15]. Despite attempts to extend the Kubelka-Munk model to collimated irradiance and anisotropic scattering, this method remains a poor approximation for laser light propagation in tissue [3].

The Discrete Ordinates Method

The discrete ordinates method (DOM) is a numerical technique in which the angular distribution as well as the spatial distribution are defined by a finite number of coordinates (cosines of the angle or dimensions of volume cells) rather than continuously [17]. The essence of this technique is the conversion of the photon transport equation to a system of linear algebraic equations suitable for numerical

solution. The DOM can be carried out to any arbitrary order and accuracy [20]. To do this, the radiance is represented only by its value at discrete values of the independent variables. A solution of the transport problem is found by solving the PTE for a set of discrete directions spanning the total solid angle range of 4π [20]. In addition, the operations of differentiation and integration are replaced by their discrete counterparts, finite differences and summation (or quadrature) [14]. The idea of discretizing the radiance was first proposed by Schuster [21] who considered only the forward and backward fluxes. Chandrasekhar later generalized this scheme by using the Gaussian quadrature technique [22].

The discrete ordinate approximation to the photon transport equation is obtained by replacing the integrals by quadrature sums and thus transforming the integro-differential equation into a system of coupled differential equations [1] given by

$$\frac{1}{v}\frac{\partial}{\partial t}I(\mathbf{r},\mathbf{\Omega}_i,t)+\mathbf{\Omega}_i\cdot\nabla_{\mathbf{r}}I(\mathbf{r},\mathbf{\Omega}_i,t)+\sigma_t I(\mathbf{r},\mathbf{\Omega}_i,t)-\sigma_s\sum_{j=1}^{N}P(\mathbf{\Omega}_j,\mathbf{\Omega}_i)I(\mathbf{r},\mathbf{\Omega}_j,t)$$
$$=F(\mathbf{r},\mathbf{\Omega}_i,t). \tag{3.51}$$

For the discrete ordinate approximation many quadrature rules, such as Gaussian, Lobatto, Chebyshev or Fiveland [7] can be used. However, the use of the Gaussian quadrature is preferred because it ensures the correct normalization of the phase function, implying that the energy is conserved in the computation [1]. The main advantage of the discrete ordinates model over stochastic approaches using Monte Carlo methods is the speed, which is sustained using precomputation and compressing schemes [15].

The two main drawbacks of the discrete ordinates method are false scattering and the ray effect [20, 23]. False scattering is due to spatial discretization errors.

When a single collimated beam is traced through an enclosure by the discrete ordinates method, the beam will gradually widen as it moves farther away from its point of origin; this unphysical effect, even in the absence of real scattering, is called false scattering [20]. False scattering can be reduced by using finer meshes [20]. The ray effect is due to the errors in angular discretization and can be reduced by increasing the sizes of the meshes [20]. Therefore, if a finer spatial mesh is used to reduce the false scattering, a finer angular quadrature scheme should be used to reduce the ray effect [20].

FUNCTIONAL EXPANSION METHODS

As in the discrete ordinates method, the goal of this technique is to reduce the integro-differential equation of photon transport to a set of coupled differential equations which can be solved by standard techniques [14]. As opposed to the discrete ordinates method, where a number of discrete directions of the radiance are considered, the angular, spatial or temporal dependence of the radiance is here approximated by a finite series expansion of orthogonal functions [14].

For example, Kim *et al.* [24] expanded the spatial dependence using Chebyshev polynomials. In their work, after representing the azimuthal dependence of the radiance in Fourier series, the spatial dependence is approximated by the Chebyshev spectral expansion as

$$I_n(z,u,t) \cong \sum_{k=0}^{N} a_k(u,t) T_k(z), \tag{3.52}$$

where $I_n(z,u,t)$ is the n^{th} Fourier coefficient of the radiance and $T_k(z)$ are the orthogonal Chebyshev polynomials [24].

In the novel technique for solving the transient PTE proposed in the next chapter, the temporal dependence is approximated by Laguerre polynomials as

$$I\left(z,u,t\right)=\sum_{k=0}^{N}B_{k}\left(z,u\right)L_{k}\left(t\right), \tag{3.53}$$

where $I\left(z,u,t\right)$ is the radiance and $L_{k}\left(t\right)$ are the orthogonal Laguerre polynomials.

THE TWO-FLUX MODEL

In the two-flux method the scattered intensity is considered to be constant over the forward- and backward-facing hemispheres [7]:

$$I(z,u,t)=\begin{cases} I^{+}(z,t), & \text{for } u>0 \quad (3.54a)\\ I^{-}(z,t), & \text{for } u<0. \quad (3.54b)\end{cases}$$

and thus the dependence on u is removed.

This model is used to simplify the integral in the PTE, which is then integrated separately over the backward- and forward-facing hemispheres [7]. If the one-dimensional PTE is considered, the resultant equations are:

$$\frac{1}{v}\frac{\partial}{\partial t}I^{+}+\frac{1}{2}\frac{\partial}{\partial z}I^{+}+(\sigma_{t}+\sigma_{s}B)I^{+}-\sigma_{s}BI^{-}=\int_{0}^{1}F\,du, \tag{3.55}$$

and

$$\frac{1}{v}\frac{\partial}{\partial t}I^{-}-\frac{1}{2}\frac{\partial}{\partial z}I^{-}+(\sigma_{t}+\sigma_{s}B)I^{-}-\sigma_{s}BI^{+}=\int_{-1}^{0}F\,du, \tag{3.56}$$

where

$$B = \frac{1}{2}\int_0^1 \int_{-1}^0 P(u';u)\,du'\,du.$$

THE P_1 MODEL

The P_1 model can be used when the scattered intensity is a linear function of u [7]. In this model

$$I(z,u,t) = u(z,t) + \frac{3}{4\pi}q(z,t)u, \tag{3.57}$$

$$u(z,t) = \frac{1}{4\pi}\int_{4\pi} I(z,u,t)\,d\Omega = \frac{1}{2}\int_{-1}^1 I(z,u,t)\,du, \tag{3.58}$$

$$q(z,t) = \int_{4\pi} I(z,u,t)u\,d\Omega = 2\pi\int_{-1}^1 I(z,u,t)u\,du, \tag{3.59}$$

where $u(z,t)$ is the average intensity over all angles, $q(z,t)$ is the heat flux and Ω is the solid angle.

Equation (3.57) is then substituted in the transient photon transport equation and two equations are obtained; the first by integrating the resulting equation with respect to Ω and the second by multiplying the resulting equation by u and then integrating with respect to Ω [7]. Those two equations are then combined, which yields a hyperbolic equation which indicates that the propagation speed of u along the z direction is $v/\sqrt{3}$ [7].

Mitra *et al.* [25] used the P_1 approximation to analyze the two-dimensional effects in a scattering-absorbing medium having a rectangular geometry. Steady-state studies have shown that the P_1 approximation for the intensity distribution is not as accurate as more sophisticated approximations and that the P_1 approximation fails to match the correct propagation speed [25].

THE P_N MODEL

The general P_N method models the intensity by expanding it as a series of Legendre polynomials of u [26]:

$$I(z,u,t) = \sum_{m=0}^{N} I_m(z,t)p_m(u), \tag{3.60}$$

which is then substituted into the photon transport equation. The PTE is subsequently multiplied by a Legendre polynomial P_k of order k less than or equal to N and integrated with respect to u [7]. Use of the orthogonality property of the Legendre polynomials results in [7]:

$$\frac{1}{v}\frac{\partial I_k}{\partial t} + \frac{k+1}{2k+3}\frac{\partial I_{k+1}}{\partial z} + \frac{k}{2k-1}\frac{\partial I_{k-1}}{\partial z} + \left(\sigma_t - \sigma_s \frac{a_k}{2k+1}\right) I_k = \frac{2k+1}{2}\int_{-1}^{1} SP_k\, du, \tag{3.61}$$

for intensity coefficient I_k where $0 \leq k \leq N$. In Eq. (3.61), a_k are the Legendre coefficients of the phase function. Thus, $N+1$ coupled hyperbolic equations are obtained, one for each k [7].

THE DISCRETE DIPOLE APPROXIMATION

The discrete dipole approximation (DDA) is a flexible and powerful technique used to model scattering and absorption of electromagnetic waves by particles having arbitrary geometry and composition [27, 28]. DDA was initially proposed by Purcell and Pennypacker [27, 28]. The DDA is an approximate method used to solve Maxwell's equations for which exact solutions are known only for special geometries [28]. In DDA, the scatterer is replaced by a finite array of point dipoles (or polarizable points) [27, 28]. They interact with the incident field as

well as each other. These interactions can be represented by a system of linear equations which can be solved to obtain dipole polarizations [27]. The scattering quantities such as the extinction, scattering and absorption coefficients, can be obtained from these dipole polarizations [27].

The geometry of the DDA array has a minimum length scale that is equal to the interdipole spacing. Therefore, the principal limitation of the DDA involves handling target boundaries [28]. When the refractive index of the target is large, the accuracy of the DDA is less [28]. In order to increase the accuracy the number of dipoles should be increased, but as this number increases the computational efficiency decreases [28]. In DDA, the continuum target is replaced by an array of N-point dipoles for which the location, $\mathbf{r}_j$ $(j = 1, \ldots, N)$ and the dipole polarizabilities, α_j are defined [28].

The Clausius-Mossotti polarizabilities given below can be used in DDA [28].

$$\alpha_j = \frac{3d^3}{4\pi}\frac{\epsilon_j - 1}{\epsilon_j + 2}, \tag{3.62}$$

where ϵ_j is the dielectric function of the target material at location $\mathbf{r}_j$ and d is the interdipole spacing. Each dipole has a polarization given by

$$\mathbf{P}_j = \alpha_j \mathbf{E}_j, \tag{3.63}$$

where $\mathbf{E}_j$ is the electric field at $\mathbf{r}_j$ due to the incident wave and the contribution of other $N - 1$ dipoles. The incident wave is expressed as [28]

$$\mathbf{E}_{inc,j} = \mathbf{E}_0 e^{j\mathbf{k}\cdot\mathbf{r}_j - j\omega t}. \tag{3.64}$$

The electric field $\mathbf{E}_j$ can be expressed as [28]

$$\mathbf{E}_j = \mathbf{E}_{inc,j} - \sum_{k \neq j} \mathbf{A}_{jk}\mathbf{P}_k, \tag{3.65}$$

where $\mathbf{A}_{jk}\mathbf{P}_k$ is the electric field at $\mathbf{r}_j$ that is due to dipole $\mathbf{P}_k$ located at $\mathbf{r}_k$. $\mathbf{A}_{jk}$ is given by

$$\mathbf{A}_{jk} = \frac{e^{jkr_{jk}}}{r_{jk}} \times \left[k^2(\mathbf{r}_{jk}\mathbf{r}_{jk} - \mathbf{I}) + \frac{jkr_{jk} - 1}{r_{jk}^2}(3\mathbf{r}_{jk}\mathbf{r}_{jk} - \mathbf{I}) \right], j \neq k, \tag{3.66}$$

where $r_{jk} \equiv |\mathbf{r}_j - \mathbf{r}_k|$, $\mathbf{r}_{jk} \equiv (\mathbf{r}_j - \mathbf{r}_k)/r_{jk}$, $\mathbf{I}$ is the 3×3 identity matrix and k is the wave number. $\mathbf{A}_{jj}$ is defined to be α_j^{-1}. Thus, the scattering problem reduces to finding $\mathbf{P}_j$ that satisfies the set of equations

$$\sum_{k=1}^{N} \mathbf{A}_{jk}\mathbf{P}_k = \mathbf{E}_{inc,j}. \tag{3.67}$$

The attenuation (extinction) cross section, C_t, and the absorption cross section, C_a, can be obtained using [28]

$$C_t = \frac{4\pi k}{|\mathbf{E}_0|^2} \sum_{j=1}^{N} \mathrm{Im}(\mathbf{E}_{inc,j}^* \cdot \mathbf{P}_j) \tag{3.68}$$

$$C_a = \frac{4\pi k}{|\mathbf{E}_0|^2} \sum_{j=1}^{N} \left[\mathrm{Im}\left[\mathbf{P}_j \cdot (\alpha_j^{-1})^* \mathbf{P}_j^* \right] - \frac{2}{3}k^3 |\mathbf{P}_j|^2 \right]. \tag{3.69}$$

In the above expressions, the attenuation cross section is computed from the forward-scattering amplitude and the absorption cross section is obtained by summing over the rate of energy dissipation by each of the dipoles [29]. The scattering cross section is given by $C_s = C_t - C_a$.

Of the existing techniques for solving the PTE, the Monte Carlo method is

time consuming, requires high computer memory and its results are subject to statistical errors [23, 30]. The diffusion theory presumes that the scattering predominates and that the medium is optically diffuse so that the angle-dependent radiant intensity can be replaced by an angle-independent photon flux and the photon transport equation is approximated by the diffusion equation [30]. In addition, the diffusion approximation cannot be applied to heterogeneous media with non-scattering or low-scattering regions, and it has been shown that it fails to match experimental data when the medium is not optically diffuse [30]. However, the discrete ordinates method (DOM) can be accomplished to high-order accuracy. Also, the derivation of DOM schemes is relatively simple and the DOM is compatible with the finite-difference or finite-element schemes for specular or diffuse phenomena [30]. Drawbacks of the discrete ordinates method include the ray effect, false scattering and the large memory requirement [23].

In general, the incident laser beam has a Gaussian profile in both time and spatial domains [7, 30]. However, most existing models for pulse propagation use square pulses as an approximation to the real Gaussian pulse [7], which is not very accurate. Another problem with the existing models is that extending the single layer model to multiple layers increases the complexity (sizes of the matrices etc.) quite considerably. Also, extension of these methods to multi-dimensional cases is not easy and requires approximations to the PTE. Thus, there is a need for the development of a better model which overcomes these problems.

3.5 Models for light propagation through tissue with inhomogeneities

An understanding of the properties of light scattering caused by an anomaly in tissue is essential to develop methods to locate and identify anomalies such as

tumors. Therefore, light propagation in tissue with obstacle scattering is an important problem for analysis [31]. The direct imaging of an object placed in a highly scattering medium is not possible [32]. In order to overcome this problem, the multiple scattering contribution to the image should be reduced, either by making the media absorb or by filtering out the lowest order of scattering with the help of femtosecond light pulses and ultrafast detection methods [32].

A large number of researchers are working on developing non-invasive optical methods for imaging breast lesions using time and frequency-domain techniques [33]. Manoharan *et al.* [33] developed optical methods based on near infrared Raman spectroscopy and fluorescence photon migration for diagnosis and localization of breast cancer. They showed that photon migration imaging can be used to accurately localize small fluorescent objects embedded in a thick turbid medium [33]. Scientists have carried out experiments on using microwaves for breast cancer detection. A breast tumor exhibits electrical properties that are significantly different from those of healthy breast tissues when exposed to microwaves [34]. Microwave breast imaging is preferred to X-ray imaging, because both ionizing radiation and breast compressions are avoided [35]. Also, microwave breast tumor detection has the potential to detect small tumors and is less expensive than other methods such as magnetic resonance imaging (MRI) and nuclear medicine [35]. Plewes *et al.* [36] proposed a quasistatic magnetic resonance elastography (MRE) method for the evaluation of breast cancer.

Most solutions to the problem of modeling light propagation through tissue with an embedded obstacle have used the diffusion approximation to the photon transport equation [31]. The accuracy of the techniques based on diffusion approximation is valid only for optically thick media with weak absorption [31].

Pulsed, continuous-wave and amplitude-modulated sources of near-infrared light are used to detect tumors and hematomas in tissue [37]. An intensity-modulated source of light produces a wave of light energy density, which is called a diffuse photon density wave, and this intensity wave can be used to detect optical inhomogeneities [37]. Diffuse photon flux at a tissue surface can be used to obtain information about the location and size of foreign objects and growths in human tissue [38].

Theoretical results for obstacle scattering in biological tissues are limited [31]. Kim [31] studied light propagation in tissue containing an absorbing plate. He considered a perfectly absorbing plate of vanishing thickness placed inside a tissue specimen [31]. Since biological tissues scatter light with a sharp forward peak, Kim used the Fokker-Plank equation instead of the photon transport equation as the former is easier to solve than the latter [31]. Although a validation of results from the Fokker-Plank equation with experimental data for biological tissues has not been carried out, Kim used this approach as it does not limit the analysis to weak absorption and optically thick media. Another reason for his using this approach is that it does not assume that the radiance is independent of the direction [31]. In his analysis Kim assumed a sharply forward-peaked phase function with $\mathbf{\Omega} \cdot \mathbf{\Omega}' \approx 1$ [31].

Feng *et al.* [39] presented an analytical perturbation analysis for studying the sensitivity of diffusive photon flux to the addition of a small spherical defect object in multiple-scattering media such as human tissues. They based their perturbation analysis on the diffusion theory for photon migration in tissue [39]. In their study they first analytically derived the photon migration path distributions and the shapes of the regions in which the photon migration paths are concentrated (the so-called banana regions). The sensitivity of detected photon flux densities

to the inclusion of small spherical defects was then analyzed [39].

Zhu *et al.* [38] analyzed the sensitivity of a diffuse photon density wave in a homogeneous multiple-scattering medium to the presence of a small spherical object. Outer *et al.* [32] used the stationary diffusion equation to derive the disturbance in the transmitted and backscattered light intensity when a small object is placed in a multiple-scattering medium. They showed that with the use of continuous light sources, it may be possible to recover the location of objects accurately inside a diffusive scattering medium [32]. Furutsu [37] established a basic theory for the detection of a fixed scatterer embedded in a turbid medium by obtaining several diffuse expressions for a scattered wave both reflected and transmitted through a turbid layer, and also within the layer [37].

All of these analyses are based on an approximation to the photon transport equation, such as the diffusion approximation or the Fokker-Plank approximation. These analyses aim to detect and locate anomalies in biological tissue. However, the next section focuses on light propagation through tissue with implanted structures for optical sensing of substances in blood or tissue fluid.

3.6 Models for light propagation through tissue with implanted structures

Optical techniques such as near-infrared spectroscopy and mid-infrared spectroscopy (which use absorption of light to determine the concentration of substances), Raman spectroscopy (which uses Raman scattering of laser light by target molecules) and photoacoustic spectroscopy (which uses laser excitation of fluids to generate an acoustic response and a spectrum as the laser is tuned) are preferable to invasive techniques, such as the fingerstick test, for detecting and

determining the concentration of substances in blood [40].

A glucose sensor which can be implanted in tissue has been recognized as a critical component for the optimal control of blood glucose concentrations in diabetics [41]. Most such glucose sensors currently being developed, which are intended for *in vivo* implantation, are electroenzymatic [41]. Johnson *et al.* [41] carried out a study to assess the feasibility of safely and accurately monitoring blood glucose levels continuously for 72 hours via a glucose sensor implanted in the subcutaneous tissue of the abdomen of humans. Moatti-Sirat *et al.* [42] evaluated a miniaturized amperometric, enzymatic glucose sensor implanted in the subcutaneous tissue of normal rats.

For safety reasons, the incident intensity used in these optical detection techniques should not be more than 0.1 J/cm^2 per laser light pulse and if continuous exposure is used, it should be less than 1 W/cm^2 [43]. With this limitation it is difficult to obtain a detectable signal or spectrum of the concentration of blood. However, structures such as photonic crystals, can be implanted within tissue, by which the scattered signal can be enhanced, thus providing a detectable spectrum [44, 45]. The probability of spontaneous photon scattering for a given frequency is directly proportional to the photon density of states (i.e. the density of electromagnetic modes) [45]. Hence an enhancement of the spontaneous photon scattering can be achieved by engineering the photon density of states of the photonic crystal. Thus, if, for example, the detection technique being used is Raman spectroscopy, further enhancement of the Raman scattered signal can be achieved by having gold or silver clusters within the implanted photonic crystal structure. Having such metallic clusters results in an enhancement of up to 10^6 times due to surface-enhanced Raman scattering (SERS) [46, 47].

Despite these very useful and promising applications of implanted structures within biological tissue, to the author's best knowledge no work on the theoretical analysis and simulation of such compound structures has been reported. This dissertation proposes a numerical technique for this purpose by mapping the photon transport equation to Maxwell's equations. The photon transport equation models light propagation using only the magnitude of the intensity (radiance), whereas Maxwell's equations require both the magnitude and the phase of the electric and magnetic fields. Thus, for the mapping of these two sets of equations, a phase retrieval technique should be used in order to retrieve the phase information from the intensity profile.

Beuthan *et al.* [48] used computer aided phase microscope to study the variation of refraction of living cells due to strong alterations of surrounding parameters. They showed that the phase shift, $\Delta\phi$, of a wave with wavelength λ after passing through a sample with diameter d is given by

$$\Delta\phi = 2\pi d\Delta n/\lambda, \tag{3.70}$$

where Δn is the difference of the refractive index of the sample and the surrounding [48]. Eq.(3.70) may be used to determine the phase shift of a pulse propagating through a thin tissue sample when the refractive index difference are taken into account. However, the work presented in this dissertation uses a different phase retrieval approach. This approach solves the transport of intensity equation [49] to retrieve the phase profile using two intensity profiles.

3.7 Conclusions

This chapter has discussed in detail the problem of numerical modeling of light propagation through tissue. There are a number of widely used numerical methods for solving the time-independent photon transport equation. However, the number of existing methods for solving the transient PTE, which is used for biomedical simulations, is limited. These existing methods each have relative advantages and disadvantages. Most existing methods for modeling transient photon transport approximate the actual Gaussian input pulse by a square pulse. Another problem with many of the existing methods is the difficulty of extending them to multi-dimensional photon transport and to inhomogeneous media. Thus, there is a need for a better numerical technique which can overcome these problems.

Modeling of light propagation through tissue with inhomogeneities can be found in the research literature. However, the problem of numerically simulating light propagation through tissue with implanted structures has not been addressed to date. This idea of having implanted structures in tissue has very promising biomedical applications. Thus, a good numerical technique for simulating light propagation through tissue with implants is needed for the development of relevant optical diagnostic procedures. Development of such a technique is the main aim of this research. The other aim is to develop a better model for simulating laser pulse propagation through tissue.

3.8 References

[1] G. E. Thomas and K. Stamnes, *Radiative Transfer in the Atmosphere and Ocean*. Cambridge: Cambridge University Press, 1999.

[2] A. J. Welch and M. J. V. Gemert, *Optical-Thermal Response of Laser-Irradiated Tissue*. New York: Plenum Press, 1995.

[3] W. Cheong, S. A. Prahl, and A. J. Welch, "A review of the optical properties of biological tissues," *IEEE Journal of Quantum Electronics*, vol. 26, no. 12, pp. 2166–2185, 1990.

[4] M. P. Menguc and R. Viskanta, "Radiative transfer in three-dimensional rectangular enclosures containing inhomogeneous, anisotropically scattering media," *Journal of Quantitative Spectroscopy & Radiative Transfer*, vol. 33, pp. 533–549, 1985.

[5] S. A. Prahl, J. C. van Gemert, and A. J. Welch, "Determining the optical properties of turbid media by using the adding-doubling method," *Applied Optics*, vol. 32, no. 4, pp. 559–568, 1993.

[6] P. Edstrom, "A fast and stable solution method for the radiative transfer problem," *SIAM Review*, vol. 47, no. 3, pp. 447–468, 2005.

[7] K. Mitra and S. Kumar, "Development and comparison of models for light-pulse transport through scattering-absorbing media," *Applied Optics*, vol. 38, no. 1, pp. 188–196, 1999.

[8] F. Bevilacqua, D. Piguet, P. Marquet, J. D. Gross, B. J. Tromberg, and C. Depeursinge, "In vivo local determination of tissue optical properties: applications to human brain," *Applied Optics*, vol. 38, pp. 4939–4950, 1999.

[9] M. H. Niemz, *Laser Tissue Interactions: Fundamentals and Applications*. Germany: Springer, 2004.

[10] A. Sawetprawichkul, P. F. Hsu, and K. Mitra, "Parallel computing of three-dimensional Monte Carlo simulation of transient radiative transfer in participating

media," 8th AIAA/ASME Joint Thermophysics and Heat Transfer Conference. St. Louis, Missouri: American Institute of Aeronautics and Astronautics, June 2002, pp. 1–10.

[11] E. Alerstam, T. Svensson, and S. A. Engels, "Parallel computing with graphics processing units for high-speed Monte Carlo simulation of photon migration," *Journal of Biomedical Optics*, vol. 13, no. 6, p. 060504, 2008.

[12] I. Kawrakow and M. Fippel, "Investigation of variance reduction techniques for Monte Carlo photon dose calculation using XVMC," *Physics in Medicine & Biology*, vol. 45, pp. 2163–2183, 2000.

[13] H. C. van de Hulst, *Multiple Light Scattering, Vol.1*. New York: Academic, 1980.

[14] M. S. Patterson, B. C. Wilson, and D. R. Wyman, "The propagation of optical radiation in tissue 1. Models of radiation transport and their application," *Lasers in Medical Science*, vol. 6, pp. 155–168, 1991.

[15] G. V. G. Baranoski and A. Krishnaswamy, "An introduction to light interaction with human skin," *RITA*, vol. XI, no. 1, pp. 33–62, 2004.

[16] Y. Yamada and Y. Hasegawa, "Time-dependent FEM analysis of photon migration in biological tissues," *JSME International Journal Series B*, vol. 39, no. 4, pp. 754–761, 1996.

[17] A. E. Profio, "Light transport in tissue," *Applied Optics*, vol. 28, no. 12, pp. 2216–2222, 1989.

[18] P. Kubelka, "New contributions to the optics of intensely light-scattering materials. Part I," *Journal of Optical Society of America*, vol. 38, pp. 448–457, 1948.

[19] ——, "New contributions to the optics of intensely light-scattering materials. Part II: Nonhomogeneous layers," *Journal of Optical Society of America*, vol. 44, pp. 330–335, 1954.

[20] M. F. Modest, *Radiative Heat Transfer*, 2nd ed. California: Academic Press, 2003.

[21] A. Schuster, "Radiation through a foggy atmosphere," *Astrophysical Journal*, vol. 21, pp. 1–22, 1905.

[22] M. S. Patterson, B. C. Wilson, and D. R. Wyman, "The propagation of optical radiation in tissue I. Models of radiation transport and their application," *Lasers in Medical Science*, vol. 6, pp. 155–168, 1991.

[23] Z. M. Tan and P. F. Hsu, "Transient radiative transfer in three-dimensional homogeneous and non-homogeneous participating media," *Journal of Quantitative Spectroscopy & Radiative Transfer*, vol. 73, pp. 181–194, 2002.

[24] A. D. Kim and M. Moscoso, "Chebyshev spectral methods for radiative transfer," *SIAM Journal on Scientific Computing*, vol. 23, no. 6, pp. 2074–2094, 2002.

[25] K. Mitra, M. S. Lai, and S. Kumar, "Transient radiation transport in participating media within a rectangular enclosure," *Journal of Thermophysics and Heat Transfer*, vol. 11, no. 3, pp. 409–414, 1997.

[26] Y. Bayazitoglu and J. Higenyi, "The higher order differential equations of radiative transfer: P3 approximation," *AIAA Journal*, vol. 17, pp. 424–431, 1979.

[27] M. A. Yurkin and A. G. Hoekstra, "The discrete dipole approximation: An overview and recent developments," *Journal of Quantitative Spectroscopy & Radiative Transfer*, vol. 106, pp. 558–589, 2007.

[28] B. T. Draine and P. J. Flatau, "Discrete-dipole approximation for scattering calculations," *Journal of the Optical Society of America A*, vol. 11, no. 4, pp. 1491–1499, 1994.

[29] B. T. Draine, "The discrete-dipole approxiamtion and its application to interstellar graphite grains," *The Astrophysical Journal*, vol. 333, pp. 848–872, 1988.

[30] Z. Guo and K. Kim, "Ultrafast-laser-radiation transfer in heterogeneous tissues with the discrete-ordinates method," *Applied Optics*, vol. 42, no. 16, pp. 2897–2905, 2003.

[31] A. D. Kim, "Light propagation in biological tissues containing an absorbing plate," *Applied Optics*, vol. 43, no. 3, pp. 555–563, 2004.

[32] P. N. D. Outer, T. M. Nieuwenhuizen, and A. Lagendijk, "Location of objects in multiple-scattering media," *Journal of Optical Society of America A*, vol. 10, no. 6, pp. 1209–1218, 1993.

[33] R. Manoharan, K. Shafer, L. Perelman, J. Wu, K. Chen, G. Deinum, M. Fitzmaurice, J. Myles, J. Crowe, R. R. Dasari, and M. S. Feld, "Raman spectroscopy and fluorescence photon migration for breast cancer diagnosis and imaging," *Photochemistry and Photobiology*, vol. 67, no. 1, pp. 15–22, 1998.

[34] G. Bindu, A. Lonappan, V. Thomas, C. K. Aanandan, and K. T. Mathew, "Active microwave imaging for breast cancer detection," *Progress in Electromagnetic Research*, vol. 58, pp. 149–169, 2006.

[35] E. C. Fear, P. M. Meaney, and M. A. Stuchly, "Microwaves for breast cancer detection?" *IEEE Potentials*, vol. 22, no. 1, pp. 12–18, 2003.

[36] D. B. Plewes, J. Bishop, A. Samani, and J. Sciarretta, "Visualization and quantification of breast cancer biomechanical properties with magnetic resonance elastography," *Physics in Medicine & Biology*, vol. 45, pp. 1591–1610, 2000.

[37] K. Furutsu, "Theory of a fixed scatterer embedded in a turbid medium," *Journal of Optical Society of America A*, vol. 15, no. 5, pp. 1371–1382, 1998.

[38] X. D. Zhu, S. P. Wei, S. C. Feng, and B. Chance, "Analysis of a diffuse-photon-density wave in multiple-scattering media in the presence of a small spherical object," *Journal of Optical Society of America A*, vol. 13, no. 3, pp. 494–499, 1996.

[39] S. Feng, F. Zeng, and B. Chance, "Photon migration in the presence of a single defect: a perturbation analysis," *Applied Optics*, vol. 34, no. 19, pp. 3826–3837, 1995.

[40] R. W. Waynant and V. M. Chenault, "Overview of non-invasive fluid glucose measurement using optical techniques to maintain glucose control in diabetes mellitus," *LEOS Newsletter*, pp. 3–38, 1998.

[41] K. W. Johnson, J. J. Mastrototaro, D. c. Howey, R. L. Brunelle, P. L. Burden-Brady, N. A. Bryan, C. C. Andrew, H. M. Rowe, D. J. Allen, B. W. Noffke, W. C. McMahan,

R. J. Morff, D. Lipson, and R. S. Nevin, "In vivo evaluation of an electroenzymatic glucose sensor implanted in subcutaneous tissue," *Biosensors & Bioelectronics*, vol. 7, pp. 709–714, 1992.

[42] D. Miatti-Sirat, F. Capron, V. Poitout, G. Reach, D. S. Bindra, Y. Zhang, G. S. Wilson, and D. R. Thévenot, "Towards continuous glucose monitoring: in vivo evaluation of a miniaturized glucose sensor implanted for several days in rat subcutaneous tissue," *Diabetologia*, vol. 35, pp. 224–230, 1992.

[43] W. D. Burnett, "Evaluation of laser hazards to the eye and the skin," *American Industrial Hygiene Association Journal*, vol. 30, no. 6, pp. 582–587, 1969.

[44] L. Florescu and X. Zhang, "Semiclassical model of stimulated Raman scattering in photonic crystals," *Physical Review E*, vol. 72, p. 016611, 2005.

[45] S. V. Gaponenko, "Effects of photon density of states on Raman scattering in mesoscopic structures," *Physical Review B*, vol. 65, p. 140303(R), 2002.

[46] F. J. G. Vidal and J. B. Pendry, "Collective theory for surface enhanced Raman scattering," *Physical Review Letters*, vol. 77, no. 6, pp. 1163–1166, 1996.

[47] M. Moskovits, "Surface-enhanced spectroscopy," *Reviews of Modern Physics*, vol. 57, no. 3, pp. 783–826, 1985.

[48] J. Beuthan, O. Minet, J. Helfmann, M. Herrig, and G. Muller, "The spatial variation of the refractive index in biological cells," *Physics in Medicine & Biology*, vol. 41, pp. 369–382, 1996.

[49] L. J. Allen and M. P. Oxley, "Phase retrieval from series of images obtained by defocus variation," *Optics Communications*, vol. 199, pp. 65–75, 2001.

CHAPTER 4

A Numerical Technique for Simulating One-dimensional Transient Photon Transport in Biological Tissue

---

This chapter presents an efficient algorithm for solving the transient photon transport equation for laser pulse propagation in biological tissue. The original one-dimensional PTE is mapped to a moving reference frame with the incident pulse. This transformation eliminates the partial derivative term with respect to time in the original equation. The dependence on the local azimuthal angle is then removed using the discrete ordinates method. A Laguerre expansion is used to represent the time dependency of this reduced PTE. This step results in a two-variable integro-differential equation for each Laguerre coefficient. The dependence on the local zenith angle is removed by using the discrete ordinates method, thus resulting in a set of single-variable uncoupled differential equations. The Runge-Kutta-Fehlberg (RKF) method is then used to solve for the radiance.

4.1 Introduction

INVESTIGATIONS of short laser pulse propagation in biological media have attracted the attention of researchers over the last two decades [1], in particular, for light-based diagnostic and imaging purposes [1] such as optical tomography for cancer detection [2] and non-invasive detection of diabetes mellitus [3]. There has been growing interest in these optical techniques of late due to the fact that they are non-invasive and non-ionizing [4].

Photon transport through scattering and absorbing media, such as biological tissue, can be described by the photon transport equation (PTE) [5–7]. Biological tissue is a highly forward-scattering medium with moderate amounts of photon attenuation. In soft tissue, scattering is much greater than absorption [8]. The scattering and absorption coefficients are wavelength-dependent. Troy *et al.* [9] provide measured values for the absorption coefficient and the isotropic scattering coefficient for 22 human skin samples, in the near infrared wavelength range of 1000 nm to 2200 nm. The average value of the absorption coefficient for human skin at 1600 nm is around 5.5 cm^{-1} [9]. The average value of the isotropic scattering coefficient for human skin at the same wavelength is around 8.0 cm^{-1} according to these data [9].

For the application of pulsed light interaction with biological tissue, the time-dependent PTE can be used. A number of models for solving the steady state PTE has been developed over the past four decades [10–16], ignoring the time dependency of the intensity profile. Some of these models include the discrete ordinates method [10], integral transformation techniques and the F_N method [13]. Siewert [14] and Larsen *et al.* [16] worked on the inverse-source problem where the source term is determined from the known angular distribution of radiation that exits the surface. Pomraning *et al.* [15] coupled the diffusion approximation and

photon transport equation for boundary treatment for the steady state case.

The work reported in this chapter deals with short pulse propagation in a tissue medium and hence the focus is on developing efficient and accurate techniques for time integration of the PTE. In the past, Dorn [17] used the inverse problem of the time-dependent transport equation for modeling optical tomography; Larsen *et al.* [18] carried out asymptotic analysis of photon transport problems and Tarvainen *et al.* [19] worked on finite element modeling of the coupled photon transport equation and diffusion approximation considering the time dependency.

However, only recently have researchers started developing models for pulse propagation in biological tissue [20]. Existing methods for modeling short pulse propagation through tissue include numerical methods [21–23] and semi-analytical methods [24, 25]. Mitra and Kumar [6] compared several models for solving the transient PTE. Also, Tan and Hsu [20] developed an integral equation formulation to treat the general transient PTE and Fleck used the Monte Carlo simulations [26]. Even though the Monte Carlo method is a flexible technique, due to its statistical nature, it requires tracing a large number of photon paths to obtain accurate and statistically confident results [21].

Kim, Ishimaru and Moscoso applied Chebyshev collocation techniques to solve the PTE [22, 23]. Kim [23] used the Chebyshev expansion for the spatial discretization and the Crank-Nicholson method for time marching. In many of the existing techniques, the short pulse is approximated by a square pulse [6, 21], which is not very accurate.

The work reported in this chapter addresses some of the deficiencies in ex-

isting methods and a better algorithm for solving the one-dimensional transient photon transport equation is developed. This work is not limited to a particular pulse shape (e.g. square). The fact that any pulse shape can be represented as a superposition of Laguerre orthogonal polynomials is used. The main advantage of the proposed algorithm is that an arbitrary pulse shape can be represented using only a few Laguerre polynomials, considerably reducing the subsequent computational overhead. The resulting equations are then solved using the Runge-Kutta-Fehlberg method. Extension of the model to inhomogeneous media can be carried out without considerable increase in computational power. The work presented in this chapter has been published in the IEEE Journal of Selected Topics in Quantum Electronics [27].

This chapter is divided into five sections. Section 4.2 introduces the formulation of the proposed method. It provides an overview of the technique and contains three subsections with a detailed description and derivation of each step. Section 4.3 provides a discussion with some numerical results obtained using this algorithm. This section is further divided into six sections. Separate sections on the normalization of the units, computational complexity and validation of the method are provided. Discussions of extending the proposed technique to more complex systems are also provided in this section. Section 4.4 concludes the chapter highlighting key features and relative advantages of the proposed method over existing methods.

4.2 Formulation

Light propagation through biological tissue can be modeled by the photon transport equation given below [23]:

$$\frac{1}{v}\frac{\partial}{\partial t}I\left(z,u,\phi,t\right)+u\frac{\partial}{\partial z}I\left(z,u,\phi,t\right)+\sigma_t I\left(z,u,\phi,t\right)$$
$$-\frac{\sigma_s}{4\pi}\int_0^{2\pi}\int_{-1}^{1}P\left(u',\phi';u,\phi\right)I\left(z,u',\phi',t\right)\,du'\,d\phi'=F\left(z,u,\phi,t\right), \tag{4.1}$$

where $I\left(z,u,\phi,t\right)$ is the light intensity (radiance), (z,θ,ϕ) are the standard spherical coordinates as shown in Fig. 4.1 below, $u=\cos\theta$, t represents time, σ_t and σ_s are attenuation and scattering coefficients, respectively, and $\sigma_t=\sigma_s+\sigma_a$ where σ_a is the absorption coefficient. The speed of light in the medium is denoted by v, $P\left(u',\phi';u,\phi\right)$ is the phase function and $F\left(z,u,\phi,t\right)$ refers to the source term. For applications where there is no source present inside the medium, $F\left(z,u,\phi,t\right)=0$. Without loss of generality, this source free condition is considered in the current work to highlight important aspects of the algorithm.

Figure 4.1 shows a short pulse incident on a tissue specimen from the left. In general, due to the index mismatch at the interface, radiation is reflected. Even though the method proposed in this chapter can handle such reflections at interfaces, due to the increased mathematical complexity in formulation which masks the main points of the proposed algorithm, this analysis is limited to an index-matched surrounding. This is because the focus of this work is on presenting the main aspects of the proposed numerical solution technique. However, a short discussion of index-mismatched cases is provided in Section 4.3.6.

The incident pulse is taken to be a source incident at $z=0$, $u=u_0$ and $\phi=\phi_0$.

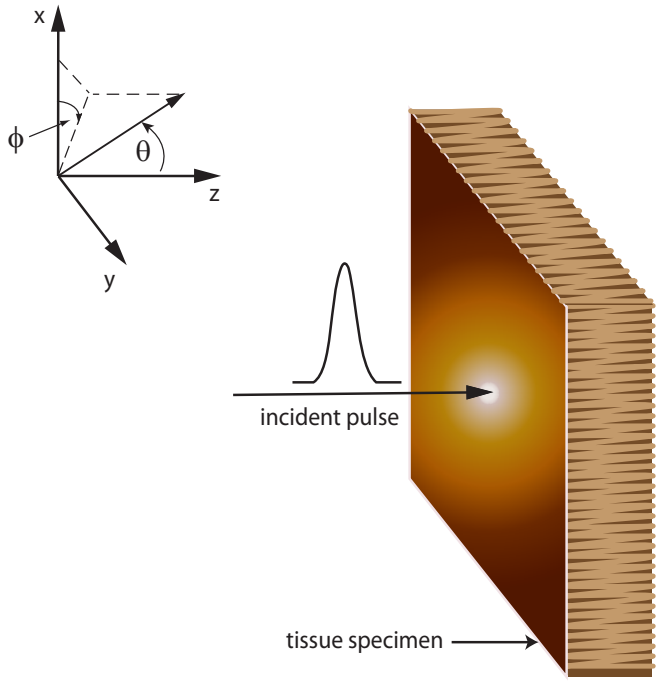

Figure 4.1: Short light pulse incident on the biological tissue.

Thus, the boundary condition can be written as

$$I\left(z=0,u,\phi,t\right) = f\left(t\right)\delta\left(u-u_0\right)\delta\left(\phi-\phi_0\right), \tag{4.2}$$

where $\delta(x)$ is the Dirac's delta function [28] and $f\left(t\right)$ is the temporal profile of the pulse. Before proceeding to solve the PTE, the following substitution is used to map Eq. (4.1) to a moving reference frame with the pulse:

$$\tau = t-\frac{z}{vu}, \tag{4.3}$$

$$\xi = z. \tag{4.4}$$

It is interesting to note that by using the transformation given by Eq. (4.3) the delay in the pulse in a particular u direction is calculated by using its projection in the z direction (i.e. z/u gives the actual propagation distance along the u di-

rection). Use of the chain rule on Eq. (4.3) and Eq. (4.4) results in,

$$\begin{aligned}\frac{\partial}{\partial t} &= \frac{\partial}{\partial \tau}\frac{\partial \tau}{\partial t} + \frac{\partial}{\partial \xi}\frac{\partial \xi}{\partial t} \\ &= \frac{\partial}{\partial \tau}(1) + \frac{\partial}{\partial \xi}(0) \\ &= \frac{\partial}{\partial \tau}\end{aligned} \tag{4.5}$$

$$\begin{aligned}\frac{\partial}{\partial z} &= \frac{\partial}{\partial \tau}\frac{\partial \tau}{\partial z} + \frac{\partial}{\partial \xi}\frac{\partial \xi}{\partial z} \\ &= \frac{\partial}{\partial \tau}(-\frac{1}{vu}) + \frac{\partial}{\partial \xi}(1) \\ &= (-\frac{1}{vu})\frac{\partial}{\partial \tau} + \frac{\partial}{\partial \xi}\end{aligned} \tag{4.6}$$

Use of Eq. (4.5) and Eq. (4.6) in Eq. (4.1) results in,

$$\begin{aligned}&u\frac{\partial}{\partial \xi}I\left(\xi, u, \phi, \tau\right) + \sigma_t I\left(\xi, u, \phi, \tau\right) - \frac{\sigma_s}{4\pi}\int_0^{2\pi}\int_{-1}^{1} P\left(u', \phi'; u, \phi\right) I\left(\xi, u', \phi' 0, \tau\right)\, du'\, d\phi' \\ &= 0.\end{aligned} \tag{4.7}$$

This transformed PTE is then solved numerically.

Figure 4.2 below shows a flow chart of the proposed method and Fig. 4.3 below shows the zenith and azimuthal angles graphically. In the proposed algorithm, first, the azimuthal angle is discretized using the discrete ordinates method [10, 29, 30]. This results in a set of uncoupled three-variable integro-differential equations, one for each quadrature point, ϕ_r. A Laguerre expansion [31] is then used to remove the time dependence in the main integro-differential equation. This results in a two-variable integro-differential equation for each Laguerre coefficient at each ϕ_r. Discretization of the zenith angle, θ, is then performed using

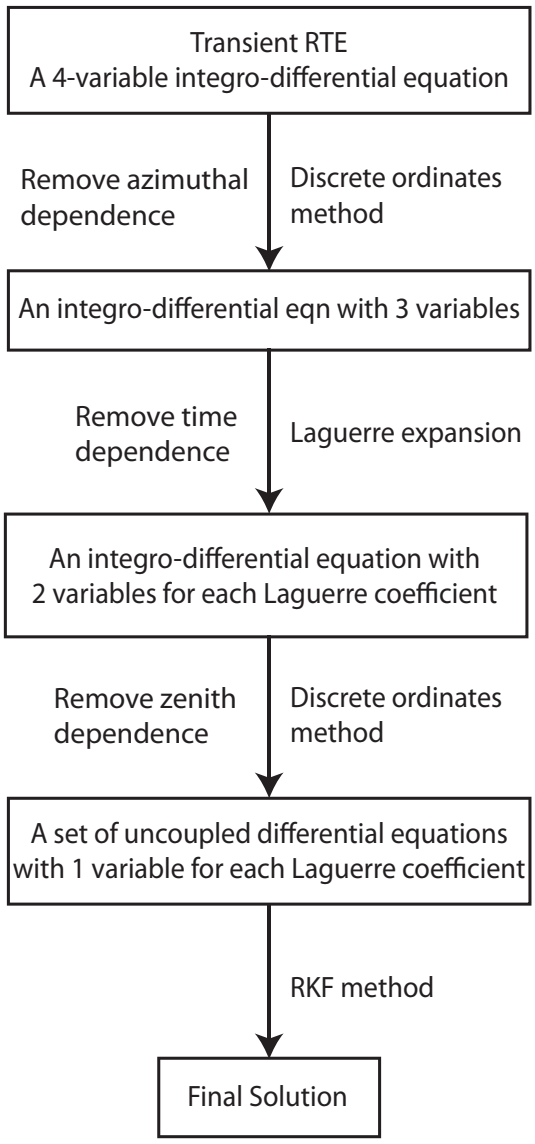

Figure 4.2: A flow chart of the proposed method.

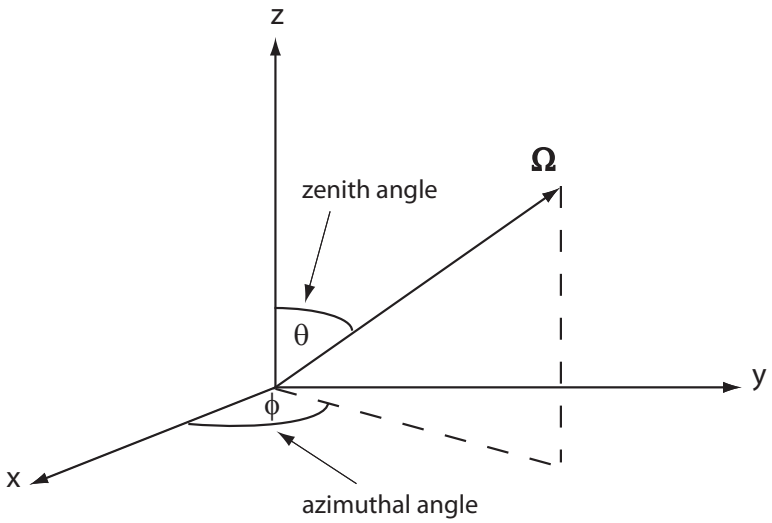

Figure 4.3: The zenith and azimuthal angles.

the discrete ordinates method [10, 29, 30]. This action results in a set of uncoupled single variable differential equations for each Laguerre coefficient. The reduced form of the PTE, subject to the boundary conditions given by Eq. (4.2) can thus be solved using the Runge-Kutta-Fehlberg method [32]. A detailed description of each stage is given below.

4.2.1 Discretization of the azimuthal dependence

First, the azimuthal angle, ϕ, is discretized using the discrete ordinates method [10, 29, 30] by applying the Gaussian quadrature rule [33] for the integral that corresponds to ϕ.

Gaussian quadrature is used to approximate an integral of the form $\int_a^b W(x) f(x)\, dx$ by a summation [33] as shown below.

$$\int_a^b W(x) f(x)\, dx \approx \sum_{j=0}^{N-1} w_j f(x_j), \tag{4.8}$$

where $W(x)$ is the weight function and $f(x)$ is any arbitrary function. Weighting coefficients, w_j, and abscissas, x_j, can be chosen so that the approximation in Eq. (4.8) is exact when $f(x)$ is a polynomial [33]. Even though one can generate his/her own abscissas and weights for a given integral [33], it is often convenient to use the well-known orthogonal polynomials [34], such as the Legendre, Chebyshev or Laguerre [33]. In the present work, the Gauss-Legendre quadrature [10] formula is used. In the Gaussian quadrature technique the weight function, $W(x)$, is 1 and the domain of the independent variable, x, is $(-1, 1)$. The following mapping is used to set the domain of θ and ϕ to $(-1, 1)$. Consider the general integral

$$\int_0^1 f(\mu)\, d\mu. \tag{4.9}$$

This integral can be mapped to the interval $[-1, 1]$ by using the transformation

$$\mu = \frac{u+1}{2}. \tag{4.10}$$

Use of Eq. (4.10) in Eq. (4.9) results in

$$\int_0^1 f(\mu)\, d\mu = \frac{1}{2}\int_{-1}^1 f\left(\frac{u+1}{2}\right)\, du. \tag{4.11}$$

Then, Gaussian quadrature can be applied for N points to obtain

$$\int_0^1 f(\mu)\, d\mu = \frac{1}{2}\sum_{j=1}^{N} \widetilde{w}_j f\left(\frac{u_j+1}{2}\right), \tag{4.12}$$

where u_j are the discrete ordinates and $\widetilde{w}_j$ are the corresponding weights. Defining

$$w_j = \frac{1}{2}\widetilde{w}_j, \tag{4.13}$$

and

$$\mu_j = \frac{u_j+1}{2}, \tag{4.14}$$

Eq. (4.12) can be written as

$$\int_0^1 f(\mu)\, d\mu = \sum_{j=1}^{N} w_j f(\mu_j). \tag{4.15}$$

The discrete ordinates method is a technique used to replace an integro-differential equation by a system of ordinary differential equations [30]. Once the integral is approximated by Gaussian quadrature, the integro-differential equation may be written as a set of uncoupled ordinary differential equations, where each equation corresponds to each abscissa [10, 29, 30].

Application of the discrete ordinates method to Eq. (4.7) results in a set of uncoupled equations, one for each quadrature point. That is,

$$u\frac{\partial}{\partial\xi} I\left(\xi, u, \phi_r, \tau\right) + \sigma_t I\left(\xi, u, \phi_r, \tau\right) - \frac{\sigma_s}{4\pi}\sum_{j=1}^{L} w_j^{\phi} \int_{-1}^{1} P\left(u', \phi_j; u, \phi_r\right) I\left(\xi, u', \phi_j, \tau\right)\, du'$$

$$= 0, \tag{4.16}$$

where $r = 1, \ldots, L$. The integral with respect to ϕ in Eq. (4.7) has been replaced by a summation in Eq. (4.16). The original four variable PTE has therefore been reduced to a three-variable integro-differential equation, but with only a simple integral instead of the double integral in the original equation. In Eq. (4.16), ϕ_r is the r^{th} quadrature point and w_j^{ϕ} is the corresponding Gaussian weight.

The removal of the time dependence is then performed using a Laguerre expansion.

4.2.2 Removal of the time dependence

The time dependence is represented using a Laguerre expansion. Laguerre polynomials are the canonical solutions of the differential equation

$$xy'' + (1-x)y' + ny = 0, \tag{4.17}$$

which is also known as Laguerre's equation [31]. These solutions are a sequence of orthogonal polynomials which can be generated by Rodrigues' formula [31]

$$L_n(x) = \frac{e^x}{n!}\frac{d^n}{dx^n}\left(e^{-x}x^n\right). \tag{4.18}$$

These polynomials satisfy the orthogonality property

$$\int_0^\infty L_n(x)L_m(x)e^{-x}\,dx = \delta_{nm}, \tag{4.19}$$

where δ_{nm} is Kronecker's delta [35]. Laguerre polynomials are causal [36] (i.e. they are defined in the domain $(0,\infty)$). The time is also defined in the same domain. Therefore, the use of Laguerre polynomials to represent the time dependency implicitly imposes the causality constraint of the system. Any causal compact continuous function can be expanded using a Laguerre basis because it forms a complete orthogonal basis in real space [34]. Since such expansions are a linear superposition of causal Laguerre polynomials, the causality property of the original system is implicitly retained.

Using relatively a few number of Laguerre polynomials it is possible to accurately represent the actual Gaussian time profile of the incident pulse. Chapter 6 presents a more detailed discussion of how a Laguerre expansion can be used to represent broad as well as very narrow Gaussian pulses. Due to these advantages a Laguerre expansion is used to represent the time dependence in

the proposed algorithm. In addition, the use of Laguerre expansion avoids time marching techniques. Therefore, this analytical approach of representing time eliminates numerical artefacts which would be introduced if time marching was used instead.

A Laguerre expansion will be accurate only if the function is continuous and compact. Hence, it is not possible to represent an impulse or a square pulse shaped input using a Laguerre expansion. However, the Gaussian shaped pulse, which can be represented accurately using a Laguerre basis, is the most commonly used input in practice.

In this proposed algorithm, the radiance is expanded as a summation of N Laguerre polynomials;

$$I(\xi, u, \tau) = \sum_{k=0}^{N} B_k(\xi, u) L_k(\tau), \tag{4.20}$$

where

$$\int_0^\infty L_n(\tau) L_m(\tau) e^{-\tau} d\tau = \delta_{mn}. \tag{4.21}$$

By using Eq. (4.20) in Eq. (4.16) and taking moments (i.e. multiplying by $L_n(\tau) e^{-\tau}$ and integrating over $[0, \infty)$), Eq. (4.22) is obtained.

$$\begin{aligned}
&\int_0^\infty u \frac{\partial}{\partial \xi} \sum_{k=0}^{N} B_k(\xi, u, \phi_r) L_k(\tau) L_n(\tau) e^{-\tau} d\tau + \int_0^\infty \sigma_t \sum_{k=0}^{N} B_k(\xi, u, \phi_r) L_k(\tau) L_n(\tau) e^{-\tau} d\tau \\
&- \int_0^\infty \frac{\sigma_s}{4\pi} \sum_{j=1}^{L} w_j^\phi \int_{-1}^{1} P(u', \phi_j; u, \phi_r) \sum_{k=0}^{N} B_k(\xi, u', \phi_r) L_k(\tau) L_n(\tau) e^{-\tau} d\tau du' = 0,
\end{aligned} \tag{4.22}$$

Re-arranging, Eq. (4.22) can be written as

$$u\frac{\partial}{\partial\xi}\sum_{k=0}^{N}B_k\left(\xi,u,\phi_r\right)\int_0^{\infty}L_k\left(\tau\right)L_n\left(\tau\right)e^{-\tau}\,d\tau+\sigma_t\sum_{k=0}^{N}B_k\left(\xi,u,\phi_r\right)\int_0^{\infty}L_k\left(\tau\right)L_n\left(\tau\right)e^{-\tau}\,d\tau$$
$$-\frac{\sigma_s}{4\pi}\sum_{j=1}^{L}w_j^{\phi}\int_{-1}^{1}P\left(u',\phi_j;u,\phi_r\right)\sum_{k=0}^{N}B_k\left(\xi,u',\phi_r\right)\int_0^{\infty}L_k\left(\tau\right)L_n\left(\tau\right)e^{-\tau}\,d\tau\,du'=0. \tag{4.23}$$

Using the property given in Eq. (4.21), Eq. (4.23) can be written as,

$$u\frac{\partial}{\partial\xi}\sum_{k=0}^{N}B_k\left(\xi,u,\phi_r\right)\delta_{kn}+\sigma_t\sum_{k=0}^{N}B_k\left(\xi,u,\phi_r\right)\delta_{kn}$$
$$-\frac{\sigma_s}{4\pi}\sum_{j=1}^{L}w_j^{\phi}\int_{-1}^{1}P\left(u',\phi_j;u,\phi_r\right)\sum_{k=0}^{N}B_k\left(\xi,u',\phi_r\right)\delta_{kn}\,du'=0. \tag{4.24}$$

Therefore, the time dependence of Eq. (4.16) can be removed as shown below:

$$u\frac{\partial}{\partial\xi}B_n\left(\xi,u,\phi_r\right)+\sigma_tB_n\left(\xi,u,\phi_r\right)-\frac{\sigma_s}{4\pi}\sum_{j=1}^{L}w_j^{\phi}\int_{-1}^{1}P\left(u',\phi_j;u,\phi_r\right)B_n\left(\xi,u',\phi_r\right)\,du'=0. \tag{4.25}$$

Similar operations should be carried out on the boundary condition. The boundary condition given by Eq. (4.2) can be written using the new variables as,

$$I\left(\xi=0,u,\phi,\tau\right)=f\left(\tau+\frac{\xi}{uv}\right)\delta\left(u-u_0\right)\delta\left(\phi-\phi_0\right). \tag{4.26}$$

Since $\xi=0$ at the boundary

$$I\left(\xi=0,u,\phi,\tau\right)=f\left(\tau\right)\delta\left(u-u_0\right)\delta\left(\phi-\phi_0\right). \tag{4.27}$$

Expanding $f\left(\tau\right)$ using Laguerre polynomials and using Eq. (4.20) in Eq. (4.27)

and taking moments results in

$$\int_0^\infty \sum_{k=0}^{N} B_k(\xi = 0, u, \phi) L_k(\tau) L_n(\tau) e^{-\tau}\, d\tau = \int_0^\infty \sum_{k=0}^{N} C_k \delta(u - u_0)\delta(\phi - \phi_0) L_k(\tau) L_n(\tau) e^{-\tau}\, d\tau. \tag{4.28}$$

Re-arranging, Eq. (4.28) can be written as

$$\sum_{k=0}^{N} B_k(\xi = 0, u, \phi) \int_0^\infty L_k(\tau) L_n(\tau) e^{-\tau}\, d\tau = \sum_{k=0}^{N} C_k \delta(u - u_0)\delta(\phi - \phi_0) \int_0^\infty L_k(\tau) L_n(\tau) e^{-\tau}\, d\tau. \tag{4.29}$$

Using the property given in Eq. (4.21) in Eq. (4.29) results in

$$\sum_{k=0}^{N} B_k(\xi = 0, u, \phi)\delta_{kn} = \sum_{k=0}^{N} C_k \delta(u - u_0)\delta(\phi - \phi_0)\delta_{kn}. \tag{4.30}$$

Thus for each ϕ_r the boundary condition becomes

$$B_n\left(\xi = 0, u, \phi_r\right) = C_n \delta\left(u - u_0\right) \delta\left(\phi_r - \phi_0\right), \tag{4.31}$$

where,

$$C_n \approx \sum_{j=1}^{q} w_j f\left(\tau_j\right) L_n\left(\tau_j\right). \tag{4.32}$$

The reduced PTE, Eq. (4.25), remains an integro-differential equation, but with only two independent variables, ξ and u. The next step is to replace the integral term by a summation using the discrete ordinates method for u.

4.2.3 Discretization of the zenith angle

The discrete ordinates method [10, 29, 30] is used for this purpose as for the azimuthal discretization. Thus, the integral term in Eq. (4.25) is approximated by a summation using the Gaussian quadrature [10, 33]. It is then followed by replac-

ing Eq. (4.25) by the set of equations

$$u_i \frac{\partial}{\partial \xi} B_n\left(\xi, u_i, \phi_r\right) + \sigma_t B_n\left(\xi, u_i, \phi_r\right) - \frac{\sigma_s}{4\pi} \sum_{j=1}^{L} w_j^{\phi} \sum_{k=1}^{K} w_k^u P\left(u_k, \phi_j; u_i \phi_r\right) B_n\left(\xi, u_k, \phi_r\right) = 0, \tag{4.33}$$

where $i = 0, \ldots, K$, $r = 0, \ldots, L$ and $n = 0, \ldots, N$.

In Eq. (4.33), u_i is the i^{th} quadrature point and w_i^u is the corresponding Gaussian weight. There are K number of uncoupled equations corresponding to each quadrature point of the azimuthal angle, ϕ_r. Considering all the quadrature points for the azimuthal angle, there is a set of L equations similar to Eq. (4.33), which represents the r^{th} equation of this set. Therefore, it is possible to combine this set and write it in the matrix format as shown below:

$$\frac{\partial}{\partial \xi} \mathbf{\Lambda} \mathbf{B}_n + \sigma_t \mathbf{B}_n - \frac{\sigma_s}{4\pi} \mathbf{P} \mathbf{W} \mathbf{B}_n = \mathbf{0}, \tag{4.34}$$

where $n = 0, \ldots, N$, $\mathbf{B}_n = \left[B_n\left(\xi, u_i, \phi_r\right)\right]_{(K \times L),1}$, $\mathbf{P} = \left[P\left(u_k, \phi_j; u_i, \phi_r\right)\right]_{(K \times L),1}$ and $\mathbf{\Lambda}$ is a $(K \times L)$ by $(K \times L)$ diagonal matrix with diagonal elements u_1 to u_K repeating L times. The matrix $\mathbf{W}$ is also a $(K \times L)$ by $(K \times L)$ diagonal matrix with diagonal elements $w_r^{\phi} \times w_k^u$ with the pattern $w_1^{\phi} \times w_1^u, w_1^{\phi} \times w_2^u, \ldots, w_1^{\phi} \times w_K^u, w_2^{\phi} \times w_1^u, \ldots, w_L^{\phi} \times w_K^u$.

Rearranging, Eq. (4.34) can be written as

$$\frac{\partial}{\partial \xi} \mathbf{B}_n = \mathbf{\Gamma} \mathbf{B}_n, \tag{4.35}$$

where

$$\mathbf{\Gamma} = \mathbf{\Lambda}^{-1} \left[\frac{\sigma_s}{4\pi} \mathbf{P} \mathbf{W} - \sigma_t \mathbf{I}\right]. \tag{4.36}$$

Hence, the original PTE is reduced to a one-variable ordinary differential equation. The boundary condition given by Eq. (4.31) is simplified in a similar fashion, which results in

$$\mathbf{B}_n\left(\xi = 0\right) = \begin{cases} C_n, & \text{for } u = u_0 \text{ and } \phi = \phi_0{}' \quad (4.37a) \\ 0, & \text{for } u \neq u_0 \text{ or } \phi \neq \phi_0. \quad (4.37b) \end{cases}$$

Thus, Eq. (4.35), subject to the above boundary condition, can be solved using the 4^{th} order Runge-Kutta-Fehlberg(RKF) method [32]. The 4^{th} order RKF method is chosen for the simulations because a compromise should be made between the accuracy and the execution time of the algorithm. However, for applications where very high precision is essential, a higher-order RKF method may be used. The RKF method can be used to find the solution to an ordinary differential equation numerically, at a given value of the independent variable, provided that the initial condition is given. This method uses adaptive step sizes and the error at each step is estimated as the difference between the fifth and fourth order estimates [32].

The next section presents some results obtained using this algorithm and a discussion of relative advantages of the proposed algorithm.

4.3 Numerical results and discussion

Matlab™ was used to implement the proposed solution strategy for the PTE. It is interesting to make the following note about the phase function used in the numerical simulations. Even though the proposed algorithm does not depend on the specific nature of the phase function, it has significant influence on the interpretation of results. The most suitable phase function for biological tissue is still a research issue [37]. In the past, the Henyey-Greenstein phase function was widely

used for modeling photon transport in many applications [37, 38]. However, due to some discrepancies, recently, researchers have combined a highly anisotropic phase function (eg. the Henyey-Greenstein phase function (HGPF)), and a low anisotropic phase function (eg. the Rayleigh phase function (RLPF)) [39] to approximate the phase function in biological tissue [39]. The HGPF represents large particles and the RLPF represents small particles compared to the wavelength of the incident light [39]. Bevilacqua *et al.* [39] used the following phase function to model biological tissue:

$$P_{tissue}\left(\cos\Theta\right) = \left(1-\alpha\right) P_{HG}\left(\cos\Theta\right) + \alpha P_{RL}\left(\cos\Theta\right), \tag{4.38}$$

where

$$P_{HG}\left(\cos\Theta\right) = \frac{1-g^2}{2\left(1+g^2-2g\cos\Theta\right)^{3/2}}, \tag{4.39}$$

is the Henyey-Greenstein phase function where g is the asymmetry factor and

$$P_{RL}\left(\cos\Theta\right) = \frac{3}{8}\left(1+\cos^2\Theta\right), \tag{4.40}$$

is the Rayleigh phase function [38, 39]. In Eq. (4.38) the value of α depends on the properties of the tissue specimen [39]. Figure 4.4 is a plot of Henyey-Greenstein phase function versus scattering angle for different values of the asymmetry factor (g). Figure 4.5 is a plot of Rayleigh phase function versus scattering angle and Fig. 4.6 shows the phase function used by Bevilacqua *et al.* [39] to model biological tissue. In this figure $\alpha = 0.2$ and $g = 0.9$. The solution technique proposed in the present work is independent of the selection of the phase function. To illustrate this independence, simulation results for all of the above three phase functions are presented in this section.

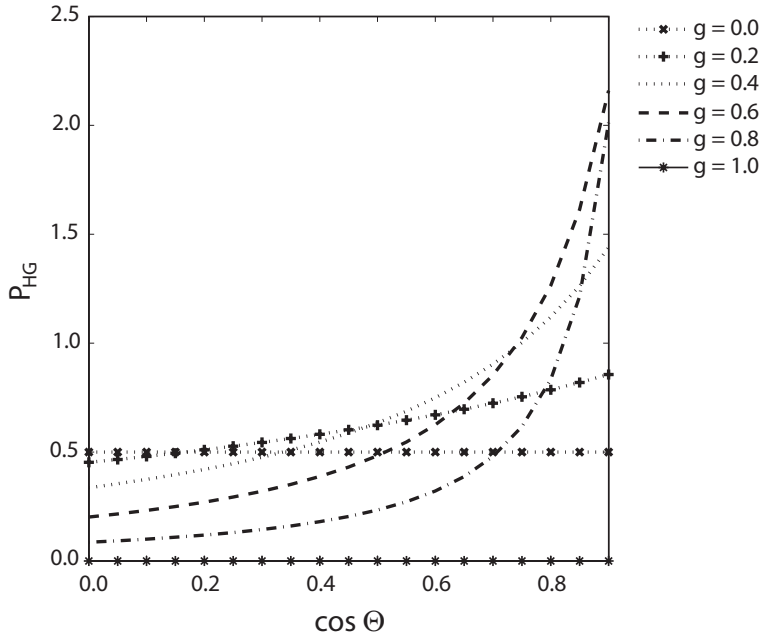

Figure 4.4: Henyey-Greenstein phase function versus scattering angle for different g values.

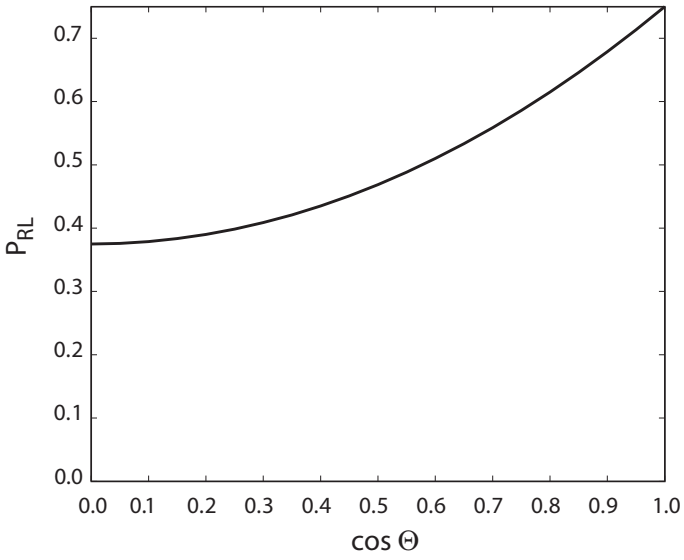

Figure 4.5: Rayleigh phase function versus scattering angle.

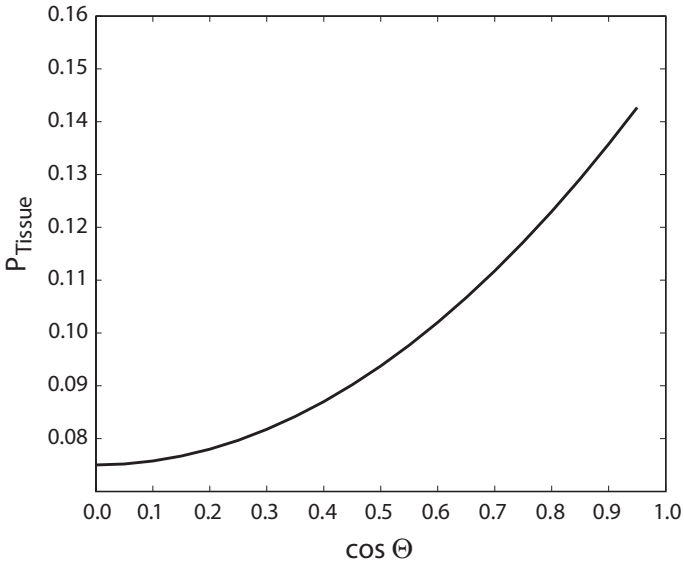

Figure 4.6: Phase function used to model tissue.

In the simulations, the input pulse was taken to be a Gaussian pulse given by

$$f(t) = I_0 e^{-\left(\frac{(t-t_0)}{T}\right)^2}, \tag{4.41}$$

where I_0 is the magnitude of the input radiance, t_0 is the initial time shift of the Gaussian pulse (which determines the time at which pulse attains its peak value), T is the factor determining the width of the pulse and t is time.

4.3.1 Normalization of the units

The PTE, Eq. (4.1), is linear in intensity, I, and thus representing I as I/I_0 does not change the equation. Therefore, the scale I/I_0 was used for the radiance throughout the present work. The time units were normalized by T_s, spatial units by Z_s and scattering and absorption coefficients by $1/Z_s$, unless specified otherwise. With this normalization Eq. (4.1) can be written as

$$\begin{aligned}&\frac{\partial}{\partial \widetilde{t}}\widetilde{I}\left(\widetilde{z},u,\phi,\widetilde{t}\right)+u\frac{\partial}{\partial \widetilde{z}}\widetilde{I}\left(\widetilde{z},u,\phi,\widetilde{t}\right)+\widetilde{\sigma}_t\widetilde{I}\left(\widetilde{z},u,\phi,\widetilde{t}\right)\\&-\frac{\widetilde{\sigma}_s}{4\pi}\int_0^{2\pi}\int_{-1}^{1}P\left(u',\phi';u,\phi\right)\widetilde{I}\left(\widetilde{z},u',\phi',\widetilde{t}\right)\,du'\,d\phi'=0,\end{aligned}\tag{4.42}$$

In the present study, $T_s = T/T_{nf}$, where T is the factor determining the width of the input pulse and T_{nf} is a factor that was chosen to obtain a good Laguerre fit. T_{nf} is recommended to be 1 or 1.5. For the simulations presented in this chapter T_{nf} was taken to be 1. This normalization factor was chosen due to the fact that the Laguerre approximation of the Gaussian pulse is very accurate for pulses with $T = 1$ or greater. Therefore, with this scaling it was possible to obtain very accurate results even for very narrow pulses, which are used in many biomedical applications. (A more detailed discussion of Laguerre fitting and choosing a scaling factor can be found in Section 6.3 of Chapter 6). For pulses with other shapes, it is recommended that a least square error fit is used to obtain a Gaussian approximation and then T_s is set to be the width of that Gaussian pulse divided by T_{nf}.

In addition, Z_s was set to $Z_s = v \times \overline{T}$. Here, $\overline{T}$ can be chosen to suit the particular application. However, these scaling factors should be chosen carefully so that the matrices remain well-conditioned. For the simulations presented in the present work, without loss of generality, the normalization was set such that $T/\overline{T} = 1$ and $Z_s = v \times T$.

The classical Laguerre polynomials given in Eq. (4.18) tend to infinity at a very high rate for $x > 10$. Thus, the approximation of a pulse at $\widetilde{z} = 0$ will be accurate only in the domain $[0, 10]$. However, since in the proposed algorithm the Laguerre polynomials are propagated with the pulse, the approximation is always accurate in the domain $[0, a]$ where $a = 10 + \widetilde{z}/(vu)$ (i.e. the domain in which the Laguerre fit is accurate extends by up to 10 time units beyond the required observation point).

4.3.2 Computational complexity

The proposed algorithm involves only one matrix inversion, which is a diagonal matrix. The sizes of this matrix and other matrices depend on the product of the number of quadrature points for ϕ and u. These numbers should be chosen according to the required resolution of the application. One matrix multiplication and one matrix addition are involved in the present algorithm. The RKF method involves only six function evaluations in each step. If $\mathbf{\Gamma}$ in Eq. (4.35) is made a scalar (i.e. if the number of quadrature points for ϕ and u is set to 1), the RKF routine takes around 100 steps to solve for a unit distance along the z axis (i.e. for $\widetilde{z} = 1$). Doubling the distance requires only 20 additional steps. If $\mathbf{\Gamma}$ in Eq. (4.35) is set to a 16×16 matrix (by taking 4 quadrature points for each angle), the number of steps required would be around 200. Doubling the distance in this case requires only 60 additional steps.

The simulation results presented in this chapter were obtained using 63 Laguerre modes, 15 quadrature points for the zenith angle, θ, and 20 quadrature points for the azimuthal angle, ϕ.

4.3.3 Validation of the proposed method

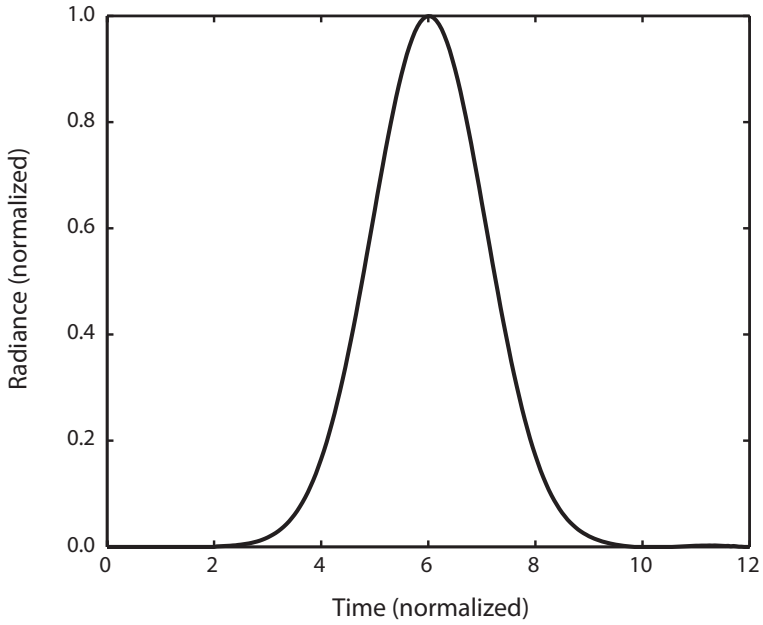

Figure 4.7: Variation of radiance with time, along the incident angle, at $\widetilde{z} = 2$ with no scattering or absorption.

For the simulations presented in this section, an input Gaussian pulse with $T = 1.5$ and $t_0 = 4$ was used. The results of the simulations presented in Figures 4.7, 4.8 and 4.9 were used for validation of the proposed technique. These figures were obtained for special cases for which the results are intuitive. For Fig. 4.7, the tissue medium was assumed to be lossless, without any scattering or absorption. That is, σ_s and σ_t in the PTE were set to zero. With this setup, there should be neither a decay in the intensity, nor scattering to other directions. Figure 4.7 shows the variation of radiance with time, along the direction of incidence (ie. $u = 1$), at $\widetilde{z} = 2$. As expected, at $\widetilde{z} = 2$, the same Gaussian pulse was obtained, without any loss, but with the corresponding time delay.

For the simulation shown in Fig. 4.8, the medium was assumed to have a normalized absorption coefficient, $\widetilde{\sigma_a}$, of 0.2 but without any scattering (hence, the

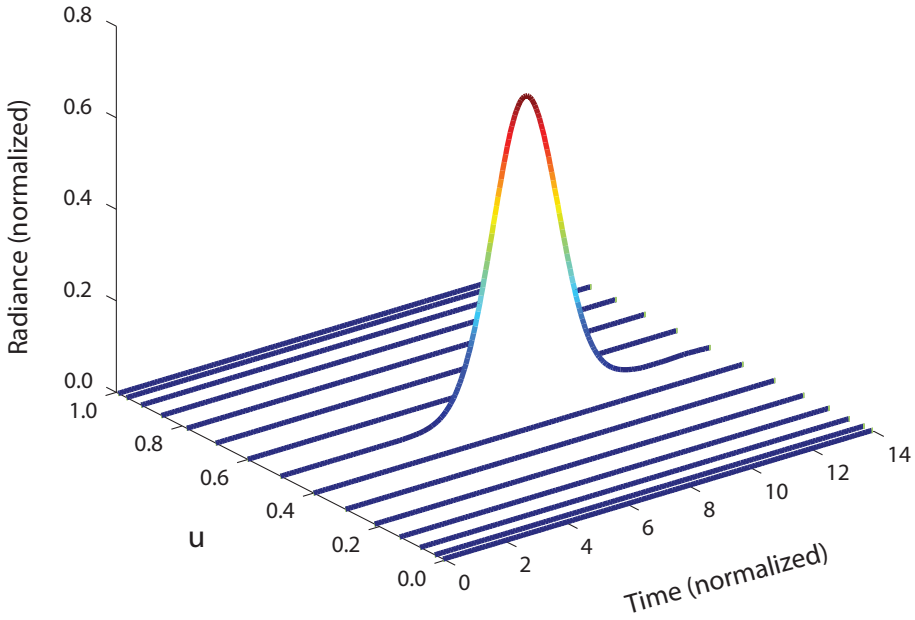

Figure 4.8: Variation of radiance with time and u, at $\widetilde{z} = 2$ with absorption but no scattering.

normalized attenuation coefficient, $\widetilde{\sigma_t} = 0.2$ as well). The direction of incidence for this simulation was taken to be at $u = 0.5$. Figure 4.8 shows the variation of radiance with time and the cosine of the zenith angle, u, at $\widetilde{z} = 2$. As expected, a decayed radiance profile existed along the incident direction, $u = 0.5$, but since there was no scattering, no radiance values were seen along other directions.

For Fig. 4.9, the medium was assumed to have a normalized absorption coefficient, $\widetilde{\sigma_a}$, of 0.02 and a normalized scattering coefficient, $\widetilde{\sigma_s}$, of 0.98 (hence, $\widetilde{\sigma_t} = 1$). The direction of incidence for this simulation was taken to be at $u = 0.17$. Figure 4.9 shows the variation of radiance with time and u. In this figure, the scattering to other directions is exhibited clearly. Thus, the simulation results presented in Figures 4.7 to 4.9 validate the proposed algorithm by producing the expected (or intuitive) results for the three special cases considered.

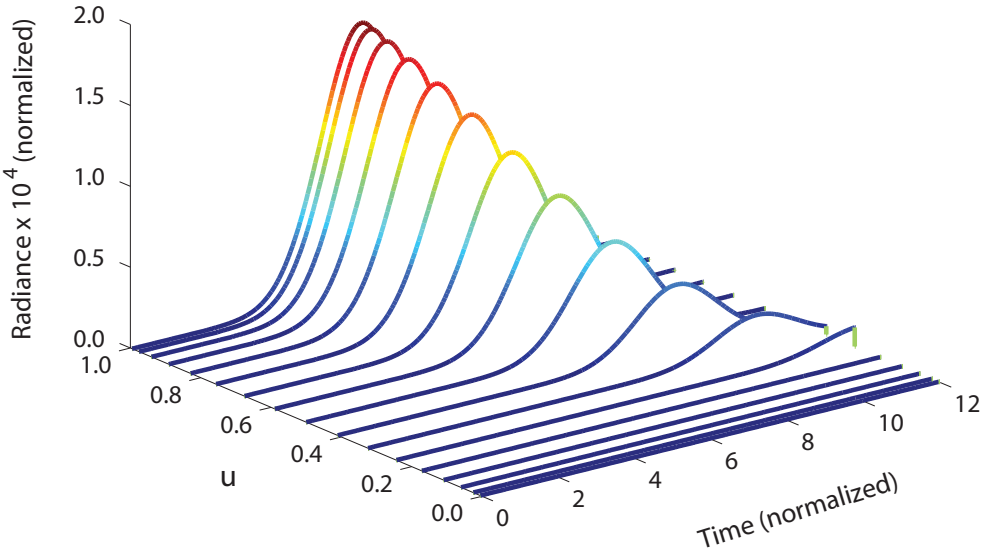

Figure 4.9: Variation of radiance with time and u, at $\widetilde{z} = 2$ with scattering and absorption.

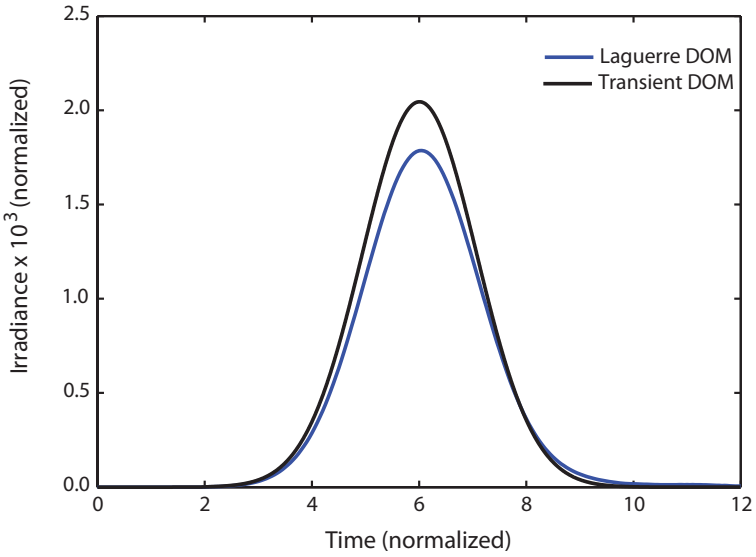

Figure 4.10: Comparison: Variation of irradiance with time for 1D PTE.

In Figures 4.7 to 4.9, the radiance profile was shown so that it was possible to explain the known results when there was no attenuation, when only absorption was present, and when both absorption and scattering were present. However,

an irradiance profile has more practical meaning than a radiance profile, as mentioned in Chapter 3. Therefore, in all the other figures presented in this section irradiance profiles are presented.

Figure 4.10 shows a comparison of the proposed method (LRKF) with the method proposed in reference [40] (Transient DOM), adopted for the one-dimensional case. In [40], the transient discrete ordinate method was introduced for the three-dimensional case. For the comparison shown in Fig. 4.10 Guo and Kumar's method was adopted for the one-dimensional case. It can be seen from Fig. 4.10 that the irradiance profile obtained using the method proposed in this chapter very closely agrees with that obtained using the Transient DOM.

4.3.4 Other simulation results

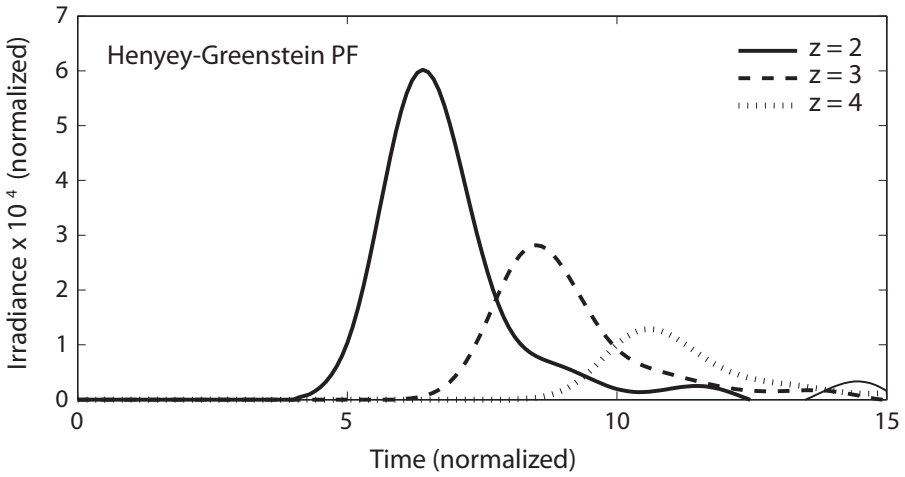

Figure 4.11: Variation of the irradiance with time at different locations along the z-axis.

For the simulations presented in this section, an input Gaussian pulse with $T = 1$ and $t_0 = 3$ was used. Figure 4.11 shows the variation of the irradiance with time taken at different locations along the z-axis. For this simulation the ab-

sorption coefficient, $\widetilde{\sigma_a}$, was taken to be 0.002 and the scattering coefficient, $\widetilde{\sigma_s}$, was kept at 0.988. As $\widetilde{z}$ increased, the peak value of the irradiance dropped and the pulse was shifted in time by the amount $\left(t - t_0 - \frac{z}{vu}\right)$. The Henyey-Greenstein phase function with $g = 0.7$ was used for this simulation.

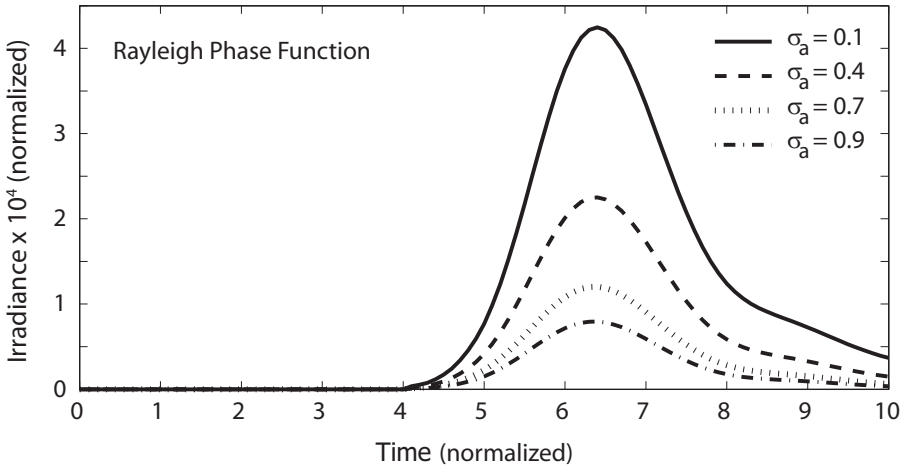

Figure 4.12: Variation of the irradiance with time at $\widetilde{z} = 2$ with different values of the absorption coefficient.

Figure 4.12 shows the variation of the irradiance with time at $\widetilde{z} = 2$ for different values of $\widetilde{\sigma_a}$. It can be seen that, as $\widetilde{\sigma_a}$ increases, the peak value of the irradiance drops. For this set of plots, $\widetilde{\sigma_s}$ was kept constant at 0.9 and the Rayleigh phase function was used. Figure 4.13 shows the variation of the irradiance with time at $\widetilde{z} = 2$ for different values of $\widetilde{\sigma_s}$. It is evident that as $\widetilde{\sigma_s}$ increases, the peak value of the irradiance drops. For this case, $\widetilde{\sigma_a}$ was kept constant at 0.02 and again the Henyey-Greenstein phase function was used with $g = 0.7$. Figure 4.14 shows the variation of the irradiance at different $\widetilde{z}$ values for an arbitrary-shaped pulse with the same phase function. This figure shows that the proposed algorithm is capable of handling arbitrary-shaped input pulses.

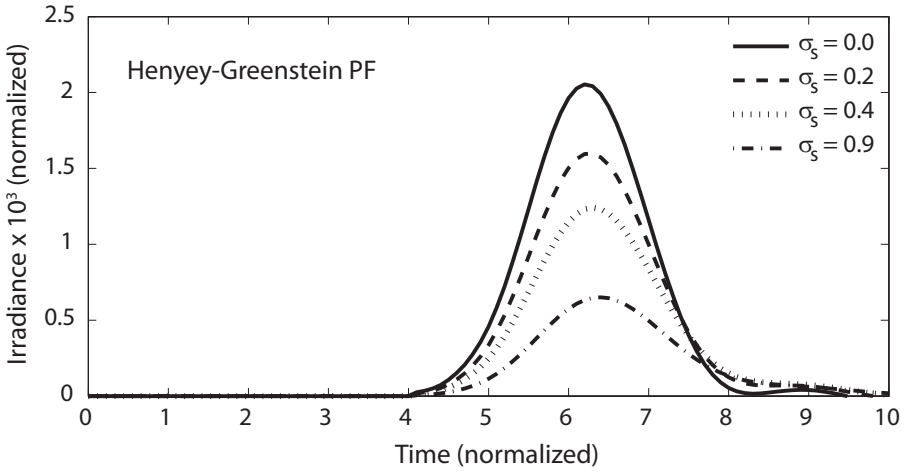

Figure 4.13: Variation of the irradiance with time at $\widetilde{z} = 2$ with different values of the scattering coefficient.

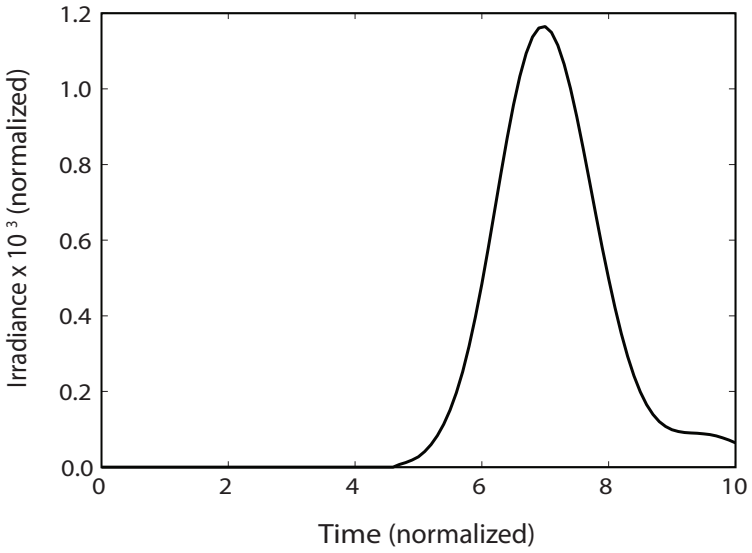

Figure 4.15: Variation of the irradiance with time for a human skin specimen.

In the above figures the values for scattering and absorption coefficients were arbitrarily selected in order to demonstrate different aspects of the proposed algorithm. Figure 4.15 shows the variation of irradiance for a human skin specimen with an incident pulse of the form given in Eq. (4.41) with $T = 1$ ps, with $\sigma_a = 0.5$

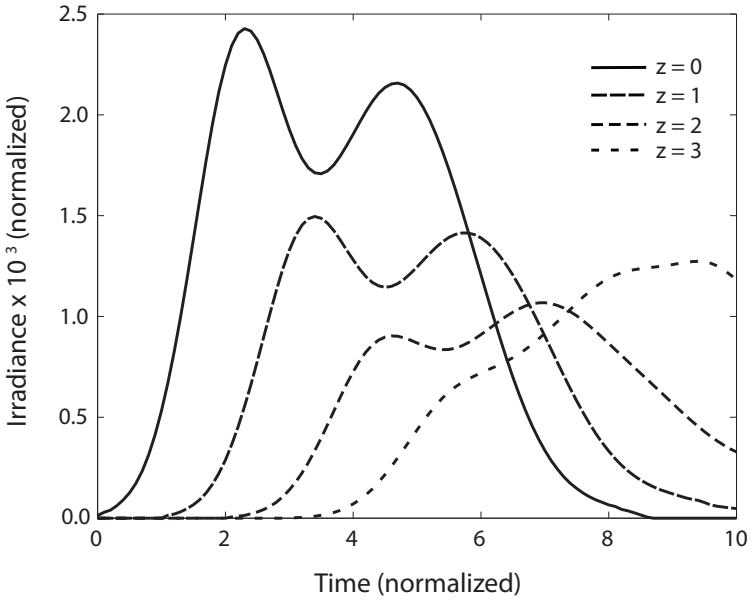

Figure 4.14: Variation of the irradiance with z for an arbitrary input.

mm^{-1} and $\sigma_s = 0.8\ mm^{-1}$ [41]. For this simulation $v = 0.215$ mm/ps and the plot was obtained at $z = 1$ mm. Time and spatial units or scattering and absorption coefficients were not normalized in this simulation and data for a human skin specimen were used. However, the irradiance has the same unit as that of the input pulse, I_0. For this simulation the combined phase function, $P_{tissue}(\cos\Theta)$, [39] was used.

The extension of the proposed technique for inhomogeneous media is straightforward as detailed in the next section. This method can also be used to solve the two-dimensional and three-dimensional PTE with only slight modifications to the formulation. Extension to multi-dimensions was carried out and is reported in detail in Chapter 6.

4.3.5 Extension to inhomogeneous media

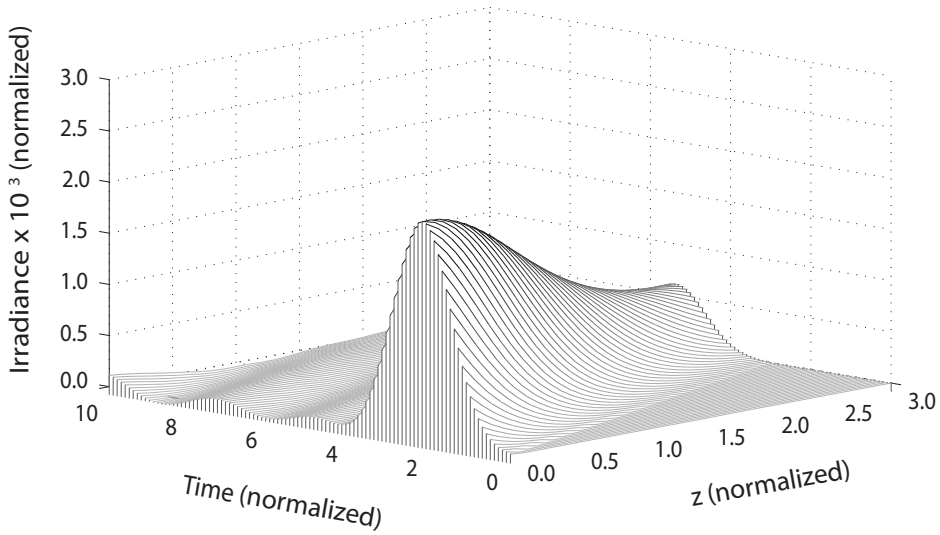

Figure 4.16: Variation of the irradiance with time and distance in an inhomogeneous medium.

The proposed formulation can be easily extended for inhomogeneous media. In an inhomogeneous medium, the scattering and absorption coefficients are a function of z. The PTE for this case is

$$\frac{1}{v}\frac{\partial}{\partial t}I\left(z,u,\phi,t\right)+u\frac{\partial}{\partial z}I\left(z,u,\phi,t\right)+\sigma_t(z)I\left(z,u,\phi,t\right)$$
$$-\frac{\sigma_s(z)}{4\pi}\int_0^{2\pi}\int_{-1}^{1}P\left(u',\phi';u,\phi\right)I\left(z,u',\phi',t\right)\,du'\,d\phi'=F\left(z,u,\phi,t\right). \tag{4.43}$$

When all the steps in the proposed algorithm are followed, Eq. (4.43) reduces to

$$\frac{\partial}{\partial\xi}\mathbf{B}_n\left(\xi\right)=\mathbf{\Gamma}\left(\xi\right)\mathbf{B}_n\left(\xi\right), \tag{4.44}$$

where

$$\mathbf{\Gamma}=\mathbf{\Lambda}^{-1}\left[\frac{\sigma_s(\xi)}{4\pi}\mathbf{PW}-\sigma_t(\xi)\mathbf{I}\right]. \tag{4.45}$$

Thus, Eq. (4.44), subject to the boundary conditions, can be solved using the RKF method as described previously.

A simulation was carried out for the inhomogeneous case by solving Eq.(4.44) and the result is presented in Fig. 4.16. Figure 4.16 shows the irradiance variation with time and distance in an inhomogeneous medium with $\widetilde{\sigma_a} = 0.05$, $\widetilde{\sigma_s} = \sin(z) \times e^{-z/5}$ and Rayleigh scattering. As explained above, an extension to inhomogeneous media is straightforward.

4.3.6 Refractive index-mismatched interfaces

If the refractive index-mismatch between the tissue and air interface is considered, the specular and diffuse reflectivities of the interface should be incorporated into the boundary conditions of the photon transport equation. The specular reflectivity at the interface can be calculated from Fresnel's equations and the diffuse reflectivity may assumed to be uniform [42]. The proposed method can incorporate such changes in boundary conditions easily. This is due to the fact that the numerical integration strategy is independent of the format of the boundary conditions because the zenith and azimuthal angle dependencies are removed by the discrete ordinate method and a Laguerre series is used to represent the time evolution.

4.4 Conclusions

This chapter has introduced a novel and efficient approach to solve the one-dimensional transient photon transport equation. The proposed method uses a Laguerre approximation to represent the time dependence and the discrete ordinates method to discretize the azimuthal and zenith angles. This reduces the orig-

inal integro-differential equation to a single-variable ordinary differential equation, which is then solved using the 4^{th} order Runge-Kutta-Fehlberg method.

There are a number of advantages of this technique over most other existing methods. Since the time dependence is expanded using a Laguerre basis, all the sampling points in the time domain are obtained in a single execution, as opposed to the time marching techniques used in existing solution methods. This makes the proposed algorithm much faster when the intensity profile is required at a particular point or on a plane over a time interval. The incident pulse can be approximated using a relatively small number of Laguerre polynomials. The causality of the system is implicitly imposed by the causal Laguerre polynomials. Any causal function can be expanded using Laguerre polynomials because it forms a complete orthogonal basis in real space. Since such expansions are a linear superposition of causal Laguerre polynomials, the causality property of the original system is implicitly retained. The use of the Runge-Kutta-Fehlberg method for the spatial variable z makes the extension to inhomogeneous media simple and straightforward.

4.5 References

[1] F. Liu, K. M. Yoo, and R. R. Alfano, "Ultrafast laser-pulse transmission and imaging through biological tissues," *Applied Optics*, vol. 32, pp. 554–558, 1993.

[2] S. B. Colak, M. B. van der Mark, G. W. 't Hooft, J. H. Hoogenraad, E. S. van der Linden, and F. A. Kuijpers, "Clinical optical tomography and NIR spectroscopy for breast cancer detection," *IEEE Journal of Selected Topics in Quantum Electronics*, vol. 5, pp. 1143–1158, 1999.

[3] B. D. Cameron, H. W. Gorde, B. Satheesan, and G. L. Cote, "The use of polarized laser light through the eye for non-invasive glucose monitoring," *Diabetes Technology and Therapeutics*, vol. 1, pp. 135–143, 1999.

[4] G. Yao and L. V. Wang, "Theoretical and experimental studies of ultrasound-modulated optical tomography in biological tissue," *Applied Optics*, vol. 39, no. 4, pp. 659–664, 2000.

[5] A. D. Klose, U. Netz, J. Beuthan, and A. H. Hielscher, "Optical tomography using the time-independent equation of radiative transfer Part 1: Forward model," *Journal of Quantitative Spectroscopy & Radiative Transfer*, vol. 72, pp. 691–713, 2002.

[6] K. Mitra and S. Kumar, "Development and comparison of models for light-pulse transport through scattering-absorbing media," *Applied Optics*, vol. 38, pp. 188–196, 1999.

[7] M. Premaratne, E. Premaratne, and A. J. Lowery, "The photon transport equation for turbid biological media with spatially varying isotropic refractive index," *Optics Express*, vol. 13, pp. 389–399, 2005.

[8] S. P. Treweek and J. C. Barbenel, "Direct measurement of the optical properties of human breast skin," *Medical & Biological Engineering & Computing*, vol. 34, pp. 285–289, 1996.

[9] T. L. Troy and S. N. Thennadil, "Optical properties of human skin in the near infrared wavelength range of 1000 to 2200 nm," *Journal of Biomedical Optics*, vol. 6, no. 2, pp. 167–176, 2001.

[10] K. Stamnes, S. C. Tsay, W. Wiscombe, and K. Jayaweera, "Numerically stable algorithm for discrete-ordinate-method radiative transfer in multiple scattering and emitting layered media," *Applied Optics*, vol. 27, pp. 2502–2509, 1988.

[11] J. L. Deuz, M. Herman, and R. Santer, "Fourier series expansion of the transfer equation in the atmosphere-ocean system," *Journal of Quantitative Spectroscopy & Radiative Transfer*, vol. 41, pp. 483–494, 1989.

[12] Z. Jin and K. Stamnes, "Radiative transfer in nonuniformly refracting layered media: Atmosphere-ocean system," *Applied Optics*, vol. 33, pp. 431–442, 1994.

[13] C. E. Siewert and J. R. Thomas, "Radiative transfer calculations in spheres and cylinders," *Journal of Quantitative Spectroscopy & Radiative Transfer*, vol. 34, pp. 59–64, 1985.

[14] C. E. Siewert, "A radiative-transfer inverse-source problem for a sphere," *Journal of Quantitative Spectroscopy & Radiative Transfer*, vol. 52, pp. 157–160, 1994.

[15] G. C. Pomraning and G. M. Foglesong, "Transport-diffusion interfaces in radiative transfer," *Journal of Computational Physics*, vol. 32, pp. 420–436, 1979.

[16] E. W. Larsen, "The inverse source problem in radiative transfer," *Journal of Quantitative Spectroscopy & Radiative Transfer*, vol. 15, pp. 1–5, 1975.

[17] O. Dorn, "A transport-backtransport method for optical tomography," *Inverse Problems*, vol. 14, pp. 1107–1130, 1998.

[18] E. W. Larsen, G. C. Pomraning, and V. C. Badham, "Asymptotic analysis of radiative transfer problems," *Journal of Quantitative Spectroscopy & Radiative Transfer*, vol. 29, pp. 285–310, 1983.

[19] T. Tarvainen, M. Vauhkonen, V. Kolehmainen, and J. P. Kaipio, "Finite element model for the coupled radiative transfer equation and diffusion approximation," *International Journal for Numerical Methods in Engineering*, vol. 65, pp. 383–405, 2006.

[20] Z. M. Tan and P. F. Hsu, "An integral formulation of transient radiative transfer," *Journal of Heat Transfer*, vol. 123, pp. 466–475, 2001.

[21] M. Sakami, K. Mitra, and P. Hsu, "Analysis of light pulse transport through two-dimensional scattering and absorbing media," *Journal of Quantitative Spectroscopy & Radiative Transfer*, vol. 73, pp. 169–179, 2002.

[22] A. D. Kim and A. Ishimaru, "A Chebyshev spectral method for radiative transfer equations applied to electromagnetic wave propagation and scattering in discrete random media," *Journal of Computational Physics*, vol. 152, pp. 264–280, 1999.

[23] A. D. Kim and M. Moscoso, "Chebyshev spectral methods for radiative transfer," *SIAM Journal on Scientific Computing*, vol. 23, pp. 2074–2094, 2002.

[24] J. V. P. de Oliveira, A. V. Cardona, and M. T. M. B. de Vilhena, "Solution of the one-dimensional time-dependent discrete ordinates problem in a slab by the spectral and LTSN methods," *Annals of Nuclear Energy*, vol. 29, pp. 13–20, 2002.

[25] J. V. P. de Oliveira, A. V. Cardona, M. T. Vilhena, and R. C. Barros, "A semi-analytical numerical method for time-dependent radiative transfer problems in slab geometry with coherent isotropic scattering," *Journal of Quantitative Spectroscopy & Radiative Transfer*, vol. 73, pp. 55–62, 2002.

[26] J. Fleck, *Methods in Computational Physics*. New York: Academic Press, 1963.

[27] C. C. Handapangoda, M. Premaratne, L. Yeo, and J. Friend, "Laguerre Runge–Kutta–Fehlberg method for simulating laser pulse propagation in biological tissue," *IEEE Journal of Selected Topics in Quantum Electronics*, vol. 14, no. 1, pp. 105–112, 2008.

[28] A. B. Carlson, *Communication Systems: An Introduction to Signals and Noise in Electrical Communication*. Singapore: McGraw-Hill, 1986.

[29] S. Chandrasekhar, *Radiative Transfer*. New York: Dover Publications, 1960.

[30] K. Stamnes and R. A. Swanson, "A new look at the discrete ordinate method for radiative transfer calculations in anisotropically scattering atmospheres," *Journal of the Atmospheric Sciences*, vol. 38, pp. 387–399, 1981.

[31] M. Abramomitz and I. A. Stegun, *Handbook of Mathematical Functions with Formulas, Graphs and Mathematical Tables*. New York: Dover Publications, 1965.

[32] S. C. Chapra and R. P. Canale, *Numerical Methods for Engineers*, 4th ed. New York: McGraw-Hill, 2002.

[33] W. H. Press, S. A. Teukolsk, W. T. Vetterling, and B. P. Flannery, *Numerical Recipes in C++*, 2nd ed. New York: Cambridge University Press, 2003.

[34] G. A. Korn and T. M. Korn, *Mathematical Handbook for Scientists and Engineers: Definitions, Theorems and Formulas for Reference and Review*, 2nd ed. New York: Dover, 2000.

[35] ——, *Mathematical Handbook for Scientists and Engineers: Definitions, Theorems and Formulas for Reference and Review*, 2nd ed. New York: Dover, 2000.

[36] S. B. C. J. Rivero-Moreno, "Video spatio-temporal signatures using polynomial transforms," *Lecture Notes in Computer Science*, vol. 3736, pp. 50–59, 2005.

[37] S. K. Sharma and S. Banerjee, "Role of approximate phase functions in Monte Carlo simulation of light propagation in tissues," *Journal of Optics A: Pure and Applied Optics*, vol. 5, pp. 294–302, 2003.

[38] G. E. Thomas and K. Stamnes, *Radiative Transfer in the Atmosphere and Ocean*. Cambridge University Press, 1999.

[39] F. Bevilacqua, D. Piguet, P. Marquet, J. D. Gross, B. J. Tromberg, and C. Depeursinge, "In vivo local determination of tissue optical properties: Applications to human brain," *Applied Optics*, vol. 38, pp. 4939–4950, 1999.

[40] Z. Guo and S. Kumar, "Three-dimensional discrete ordinates method in transient radiative transfer," *Journal of Thermophysics and Heat Transfer*, vol. 16, no. 3, pp. 289–296, 2002.

[41] T. L. Troy and S. N. Thennadil, "Optical properties of human skin in the near infrared wavelength range of 1000 to 2200 nm," *Journal of Biomedical Optics*, vol. 6, pp. 167–176, 2001.

[42] A. R. Degheidy and M. S. A. Krim, "Effects of Fresnel and diffused reflectivities on light transport in a half-space medium," *Journal of Quantitative Spectroscopy & Radiative Transfer*, vol. 61, pp. 751–757, 1999.

CHAPTER 5

A Numerical Technique for Characterizing Light Propagation through Inhomogeneous Biological Tissue

An approximate numerical technique for modeling light propagation through weakly scattering biological tissue is developed by solving the photon transport equation in biological tissue that includes a varying refractive index and varying scattering/absorption coefficients. The proposed technique involves first tracing the ray paths defined by the refractive index profile of the medium by solving the Eikonal equation using a Runge-Kutta integration algorithm. The photon transport equation is solved only along these ray paths, minimizing the overall computational burden of the resulting algorithm. The main advantage of the current algorithm is that it enables discretization of the pulse propagation space adaptively by taking the optical depth into account. Therefore, computational efficiency can be increased without compromising the accuracy of the algorithm.

5.1 Introduction

RESEARCHERS have been working on modeling biological tissue over the last two decades [1, 2] and several numerical models have been developed to solve the PTE over recent years [3–6]. These models include techniques for solving the steady state PTE [3], as well as the transient PTE for short pulse propagation [4–6].

Several different variations of PTE for inhomogeneous media have been proposed in the research literature [7–12]. However, most of these variations are not a result of fundamental errors or differences but due to different assumptions about the medium or wave field properties. For example, references [7], [8] and [10] look at spatially slowly varying isotropic refractive index profiles in their work. Interestingly, the approach given in [12] is formulated to accommodate geometric optics approximations but ignores the wavefront curvature in the derivation. Wavefront curvature in the context of slowly varying refractive index approximation is considered in [7]. Numerical considerations necessary to account for such slowly varying spatial refractive profiles are considered in [9] and [11].

This chapter proposes a numerical technique for characterizing light propagation through inhomogeneous tissue. In an inhomogeneous weakly scattering medium the ray paths can be approximated by the Eikonal equation [13]. A set of ray paths can be calculated depending on the refractive index profile of the medium. There are several existing methods to do this [13–15]. The work reported in this chapter adopts the ray tracing technique proposed by Sharma *et al.* [13]. The next step is to solve the PTE written in terms of the path length [7] on each of these paths. The Laguerre Runge-Kutta-Fehlberg method, proposed in the previous chapter, can be used for this purpose. The work presented in this

chapter has been published in the Journal of Biomedicine and Biotechnology [16].

This chapter is divided into five sections. Section 5.2 introduces the formulation. It carries a detailed mathematical description of the proposed method. Section 5.3 provides some simulation results with a discussion. Section 5.4 concludes the chapter by summarizing key features of the method and includes a discussion of its relative advantages.

5.2 Formulation

The photon transport equation for a medium with a spatially varying isotropic refractive index in standard spherical coordinates is [7]

$$\frac{n(\mathbf{r})}{c}\frac{\partial}{\partial t}I\left(\mathbf{r},\mathbf{\Omega},t\right)+\left(\frac{1}{R_1(s)}+\frac{1}{R_2(s)}\right)I\left(\mathbf{r},\mathbf{\Omega},t\right)+n^2(\mathbf{r})\frac{\partial}{\partial s}\left(\frac{I\left(\mathbf{r},\mathbf{\Omega},t\right)}{n^2(\mathbf{r})}\right)$$
$$+\sigma_t(\mathbf{r})I\left(\mathbf{r},\mathbf{\Omega},t\right)=\sigma_s(\mathbf{r})\int_{4\pi}P\left(\mathbf{\Omega}',\mathbf{\Omega}\right)I\left(\mathbf{r},\mathbf{\Omega}',t\right)\,d\mathbf{\Omega}'+F\left(\mathbf{r},\mathbf{\Omega},t\right), \tag{5.1}$$

where $\mathbf{r}$ is the position vector of a point on a path of a ray, s is the arc length along a ray, $\mathbf{\Omega}=\frac{d\mathbf{r}}{ds}$, t is time, $I\left(\mathbf{r},\mathbf{\Omega},t\right)$ is the radiance, $n(\mathbf{r})$ is the refractive index profile, c is the speed of light in vacuum, $R_1(s)$ and $R_2(s)$ are the principal radii of curvatures of the geometrical wave-fronts, σ_t is the attenuation coefficient with $\sigma_t=\sigma_a+\sigma_s$, σ_a is the absorption coefficient and σ_s is the scattering coefficient, $P\left(\mathbf{\Omega}',\mathbf{\Omega}\right)$ is the phase function and $F\left(\mathbf{r},\mathbf{\Omega},t\right)$ represents sources inside the medium.

The path of rays in a medium with a spatially varying refractive index is given

by the Eikonal equation [13–15]

$$\frac{d}{ds}\left(n(\mathbf{r})\frac{d\mathbf{r}}{ds}\right) = \nabla n(\mathbf{r}), \tag{5.2}$$

where $\mathbf{r} = x\mathbf{i} + y\mathbf{j} + z\mathbf{k}$, $\mathbf{i}$, $\mathbf{j}$ and $\mathbf{k}$ are unit vectors along x, y and z axes, respectively, and $\nabla = \left(\frac{\partial}{\partial x}\mathbf{i} + \frac{\partial}{\partial y}\mathbf{j} + \frac{\partial}{\partial z}\mathbf{k}\right)$. Ray tracing is a valid and practically used method for analyzing light propagation through biological tissue [17]. Ray picture of light derives from geometrical optics approximation [18]. The Eikonal equation is the basic equation of geometrical optics (i.e. ray optics) [19]. This is analogous to the wave equation for wave optics. The Eikonal equation is an approximation to the wave equation, which is very accurate when the wavelength is small compared with the propagation distance [19]. Thus, this approximation will be valid for modeling light propagation through inhomogeneous biological tissue in which the properties vary very slowly compared to the wavelength of the incident light. In addition, the geometrical optic techniques assume that the field behaves locally as a plane wave and that the intensity does not change rapidly [19].

The technique proposed is to first solve Eq. (5.2) to obtain a set of possible ray paths and then solve the PTE, Eq. (5.1), for each of these paths. The main advantage of the current algorithm is that it enables adaptive discretization of the pulse propagation space by taking the optical depth into account. Therefore, computational efficiency can be increased without compromising the accuracy of the algorithm [20].

Several techniques have been introduced for solving the Eikonal equation by various research groups [13–15]. The technique proposed by Sharma *et al.* [13] is adopted for this study because it uses Runge-Kutta integration, which will be used again later to solve the photon transport equation in the discrete ordinate method setting. In this method, a new variable q is introduced such that $dq = \frac{ds}{n}$.

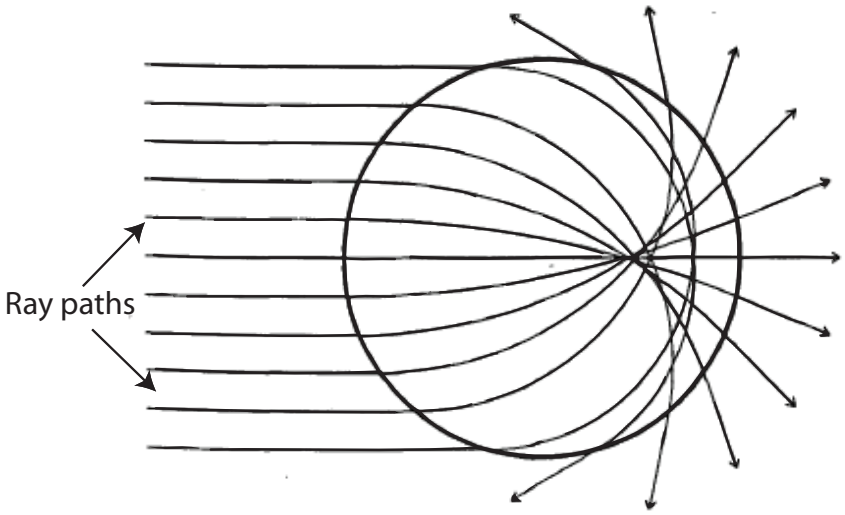

Figure 5.1: A set of possible ray paths in a Maxwell's fish-eye

Then, Eq. (5.2) can be written as

$$\frac{d^2\mathbf{r}}{dq^2} = n(\mathbf{r})\nabla n(\mathbf{r}). \tag{5.3}$$

The optical ray vector is defined as

$$\begin{aligned} \mathbf{Q} &= \frac{d\mathbf{r}}{dq} \\ &= n\xi\mathbf{i} + n\eta\mathbf{j} + nu\mathbf{k}, \end{aligned} \tag{5.4}$$

where $\xi = \sin\theta\cos\phi$, $\eta = \sin\theta\sin\phi$ and $u = \cos\theta$. Equation (5.3) can be written in matrix format as

$$\frac{d^2R}{dq^2} = D(R), \tag{5.5}$$

where $R = \begin{pmatrix} x \\ y \\ z \end{pmatrix}$, $Q = \begin{pmatrix} n\xi \\ n\eta \\ nu \end{pmatrix}$ and $D = n \begin{pmatrix} \frac{\partial n}{\partial x} \\ \frac{\partial n}{\partial y} \\ \frac{\partial n}{\partial z} \end{pmatrix}$. Thus, Eq. (5.5) can be solved using the Runge-Kutta algorithm starting from a known point (R_0, Q_0). That is, Eq. (5.5), with the initial condition (R_0, Q_0) successively generates points (R_1, Q_1), (R_2, Q_2), ..., (R_n, Q_n) along the path [13]. Therefore, if a set of starting points and initial directions, Q_0, is selected, a set of ray paths is obtained by numerically integrating Eq. (5.5). For example, such ray tracing for Maxwell's fish-eye gives the paths as shown in Fig. 5.1 [21]. The Maxwell's fish-eye is a non-homogeneous lens invented by James Clerk Maxwell in 1860. This lens has a refractive index given by [22]

$$n(r) = \frac{2}{1 + (r/R)^2} \,, \tag{5.6}$$

where R is the radius of the sphere and r is the radial distance from the centre of the sphere. This lens will focus the rays coming from a point source located at the rim of the sphere to another point on the rim at the opposite side [22].

The next step is to solve the PTE, Eq. (5.1), for a weakly scattering medium on each of the above set of paths by numerically integrating Eq. (5.5). While tracing the ray paths from the above algorithm, the PTE can be solved to find the intensity at each point on the path.

First, the following transformation is used which maps the PTE to a moving coordinate system on ray paths:

$$\tau \quad = \quad t - \frac{s}{v} \,, \tag{5.7}$$

where v is the speed of light inside the medium along the ray path. Using Eq. (5.7) in Eq. (5.1) results in

$$n^2(\mathbf{r})\frac{\partial}{\partial s}\left(\frac{I(\mathbf{r},\mathbf{\Omega},\tau)}{n^2(\mathbf{r})}\right)+\left(\frac{1}{R_1(s)}+\frac{1}{R_2(s)}\right)I(\mathbf{r},\mathbf{\Omega},\tau)+\sigma_t(\mathbf{r})I(\mathbf{r},\mathbf{\Omega},\tau)$$
$$=\sigma_s(\mathbf{r})\int_{4\pi}P(\mathbf{\Omega}',\mathbf{\Omega})\,I(\mathbf{r},\mathbf{\Omega}',\tau)\,d\mathbf{\Omega}'+F(\mathbf{r},\mathbf{\Omega},\tau), \tag{5.8}$$

In the present work, plane waves are considered so that the second term on the left hand side of Eq. (5.8) vanishes. That is,

$$n^2(\mathbf{r})\frac{\partial}{\partial s}\left(\frac{I(\mathbf{r},\mathbf{\Omega},\tau)}{n^2(\mathbf{r})}\right)+\sigma_t(\mathbf{r})I(\mathbf{r},\mathbf{\Omega},\tau)$$
$$=\sigma_s(\mathbf{r})\int_{4\pi}P(\mathbf{\Omega}',\mathbf{\Omega})\,I(\mathbf{r},\mathbf{\Omega}',\tau)\,d\mathbf{\Omega}'+F(\mathbf{r},\mathbf{\Omega},\tau). \tag{5.9}$$

The Laguerre Runge-Kutta-Fehlberg (LRKF) method, proposed in Chapter 4, can be used to solve Eq. (5.9) for radiance at selected points on each ray path. The LRKF method is briefly described here. Since Eq. (5.9) is solved on a known ray path at a known point, $n(\mathbf{r})$, $\sigma_t(\mathbf{r})$ and $\sigma_s(\mathbf{r})$ are constants at that point. First, Gaussian quadrature [23] is used to approximate the integral which results in

$$n^2(\mathbf{r})\frac{\partial}{\partial s}\left(\frac{I(\mathbf{r},\mathbf{\Omega},\tau)}{n^2(\mathbf{r})}\right)+\sigma_t(\mathbf{r})I(\mathbf{r},\mathbf{\Omega},\tau)=\sigma_s(\mathbf{r})\sum_{j=1}^{q}w_jP(\mathbf{\Omega}_j,\mathbf{\Omega})\,I(\mathbf{r},\mathbf{\Omega}_j,\tau)+F(\mathbf{r},\mathbf{\Omega},\tau), \tag{5.10}$$

where $\mathbf{\Omega}_j$ is the j^{th} quadrature point and w_j is the corresponding Gaussian weight [23]. Then, time dependence is represented using a Laguerre expansion [24]

$$I(\mathbf{r},\mathbf{\Omega},\tau)=\sum_{k=0}^{N}B_k(\mathbf{r},\mathbf{\Omega})\,L_k(\tau), \tag{5.11}$$

$$F(\mathbf{r},\mathbf{\Omega},\tau)=\sum_{k=0}^{N}F_k(\mathbf{r},\mathbf{\Omega})\,L_k(\tau), \tag{5.12}$$

where $F_n(\mathbf{r},\mathbf{\Omega})$ is the Laguerre coefficient of the source term, $F(\mathbf{r},\mathbf{\Omega},\tau)$. Using Eq. (5.11) and Eq. (5.12) in Eq. (5.10) and taking moments results in

$$\int_0^\infty n^2(\mathbf{r})\frac{\partial}{\partial s}\left(\frac{\sum_{k=0}^N B_k(\mathbf{r},\mathbf{\Omega})\,L_k(\tau)}{n^2(\mathbf{r})}\right)L_n(\tau)e^{-\tau}\,d\tau+\int_0^\infty \sigma_t(\mathbf{r})\sum_{k=0}^N B_k(\mathbf{r},\mathbf{\Omega})\,L_k(\tau)L_n(\tau)e^{-\tau}\,d\tau$$
$$=\int_0^\infty \sigma_s(\mathbf{r})\sum_{j=1}^q w_j P(\mathbf{\Omega}_j,\mathbf{\Omega})\sum_{k=0}^N B_k(\mathbf{r},\mathbf{\Omega}_j)\,L_k(\tau)L_n(\tau)e^{-\tau}\,d\tau$$
$$+\int_0^\infty \sum_{k=0}^N F_k(\mathbf{r},\mathbf{\Omega})\,L_k(\tau)L_n(\tau)e^{-\tau}\,d\tau. \tag{5.13}$$

Re-arranging, Eq. (5.13) can be written as

$$n^2(\mathbf{r})\frac{\partial}{\partial s}\left(\frac{\sum_{k=0}^N B_k(\mathbf{r},\mathbf{\Omega})\int_0^\infty L_k(\tau)L_n(\tau)e^{-\tau}\,d\tau}{n^2(\mathbf{r})}\right)+\sigma_t(\mathbf{r})\sum_{k=0}^N B_k(\mathbf{r},\mathbf{\Omega})\int_0^\infty L_k(\tau)L_n(\tau)e^{-\tau}\,d\tau$$
$$=\sigma_s(\mathbf{r})\sum_{j=1}^q w_j P(\mathbf{\Omega}_j,\mathbf{\Omega})\sum_{k=0}^N B_k(\mathbf{r},\mathbf{\Omega}_j)\int_0^\infty L_k(\tau)L_n(\tau)e^{-\tau}\,d\tau$$
$$+\sum_{k=0}^N F_k(\mathbf{r},\mathbf{\Omega})\int_0^\infty L_k(\tau)L_n(\tau)e^{-\tau}\,d\tau. \tag{5.14}$$

Use of the property given in Eq. (4.21) in Eq. (5.14) results in

$$n^2(\mathbf{r})\frac{\partial}{\partial s}\left(\frac{\sum_{k=0}^N B_k(\mathbf{r},\mathbf{\Omega})\,\delta_{kn}}{n^2(\mathbf{r})}\right)+\sigma_t(\mathbf{r})\sum_{k=0}^N B_k(\mathbf{r},\mathbf{\Omega})\,\delta_{kn}$$
$$=\sigma_s(\mathbf{r})\sum_{j=1}^q w_j P(\mathbf{\Omega}_j,\mathbf{\Omega})\sum_{k=0}^N B_k(\mathbf{r},\mathbf{\Omega}_j)\,\delta_{kn}+\sum_{k=0}^N F_k(\mathbf{r},\mathbf{\Omega})\,\delta_{kn}. \tag{5.15}$$

Thus, the time dependence of Eq. (5.10) is removed, which results in

$$n^2(\mathbf{r})\frac{\partial}{\partial s}\left(\frac{B_n(\mathbf{r},\mathbf{\Omega})}{n^2(\mathbf{r})}\right)+\sigma_t(\mathbf{r})B_n(\mathbf{r},\mathbf{\Omega})=\sigma_s(\mathbf{r})\sum_{j=1}^q w_j P(\mathbf{\Omega}_j,\mathbf{\Omega})\,B_n(\mathbf{r},\mathbf{\Omega}_j)+F_n(\mathbf{r},\mathbf{\Omega}). \tag{5.16}$$

Since the ray paths have been previously traced, a set of $\mathbf{r}$ and $\mathbf{\Omega}$ values is known.

Thus, Eq. (5.16) can be solved using the Runge-Kutta-Fehlberg algorithm [25].

The next section presents some results obtained using this algorithm and a discussion of relative advantages of the proposed algorithm.

5.3 Results and discussion

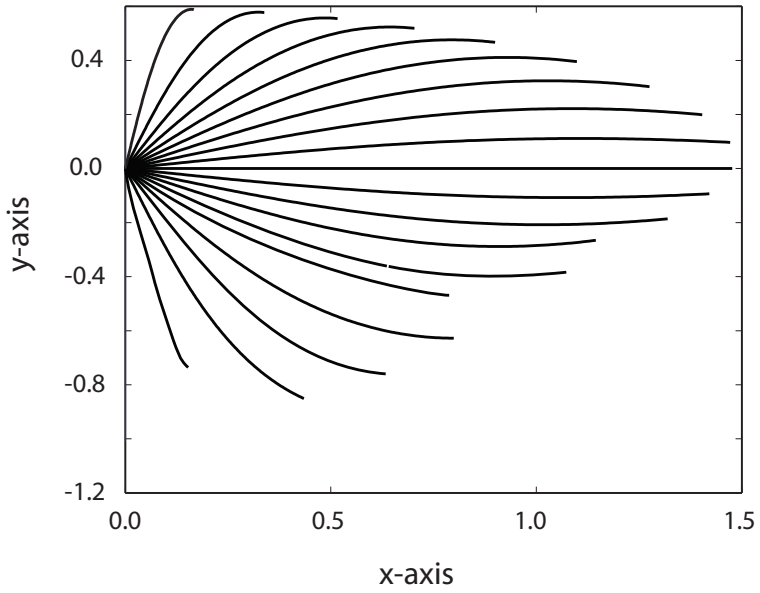

Figure 5.2: Some ray paths for a medium with a refractive index profile given by Eq. (5.17)

Figure 5.2 shows some ray paths for a medium with a refractive index profile given by

$$n(x) \quad = \quad n_0\, e^{-x^2} \tag{5.17}$$

where $n_0 = 2$. Figures 5.3 and 5.4 were obtained from the above algorithm. These results were obtained for a pulse propagating through a single ray path. The Henyey-Greenstein phase function [26] was used for the simulation where g is

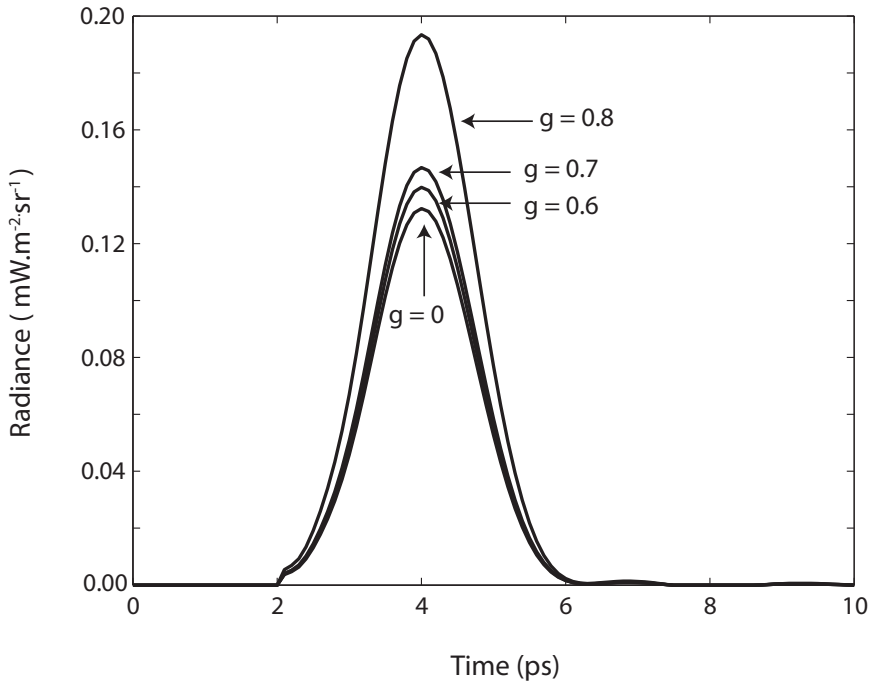

Figure 5.3: Variation of radiance with time at z = 1 mm for different asymmetry factor (g) values

the asymmetry factor.

Figure 5.3 shows the variation of radiance with time at $z = 1$ mm with varying g. The graphs corresponds to $g = 0.8$, $g = 0.7$, $g = 0.6$ and $g = 0$. Other parameters such as the scattering coefficient and the absorption coefficient were kept constant for all four graphs. The condition $g = 0$ corresponds to the isotropic scattering case while $g = 0.8$ represents forward scattering. This is illustrated by the above four graphs.

Figure 5.4 shows the variation of the forward radiance at different locations, that is, corresponding to different z values (in mm), with a constant asymmetry factor, $g = 0$. It can be clearly seen from this figure that the intensity reduces with increasing distance due to scattering and absorption. The pulse is also shifted in time as shown.

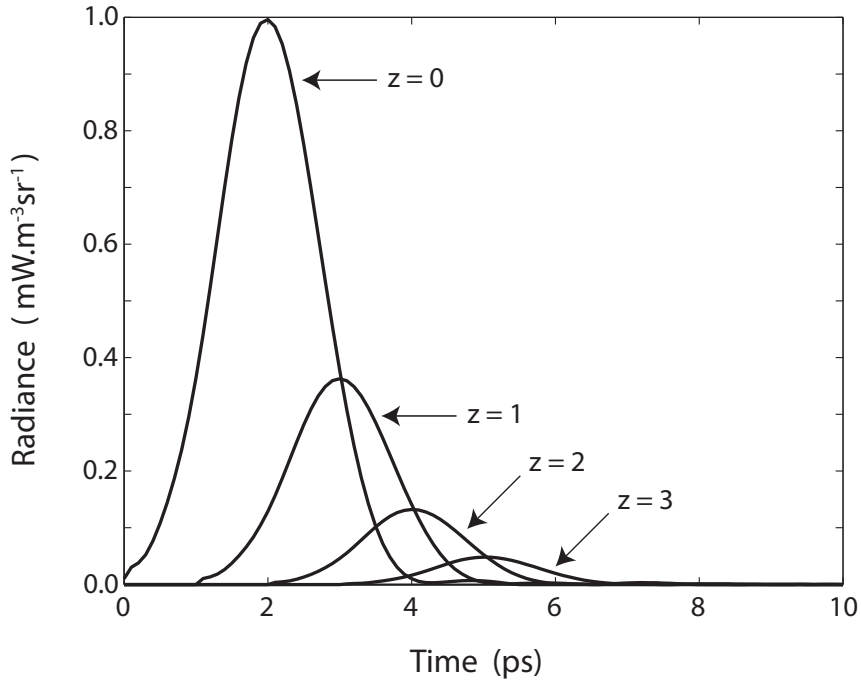

Figure 5.4: Forward radiance at different locations for isotropic (g = 0) scattering

5.4 Conclusions

This chapter has introduced a novel approximate numerical model to solve the photon transport equation with inhomogeneous refractive index and inhomogeneous scattering and absorption cross-sections for weakly scattering biological tissue. The proposed technique consists of two steps: first, the Eikonal equation describing the geometric-optic ray paths is solved using an efficient Runge-Kutta routine to construct a set of possible photon migration paths through the inhomogeneous tissue sample. Thereafter, the transient photon transport equation, written in terms of the arc length, is solved along each ray path to construct the optical intensity variation as time progresses. The main advantage of the current algorithm is that it enables adaptive discretization of the pulse propagation space by taking the optical depth into account. Therefore, computational efficiency can be increased without compromising the accuracy of the algorithm. Computational

efficiency becomes a bottle-neck when large, realistic simulations of optical pulse propagation in tissue are required. Therefore, the current proposed method is very suitable for extensive computation work in time-resolved photon-diffusion tomography.

5.5 References

[1] F. Liu, K. M. Yoo, and R. R. Alfano, "Ultrafast laser-pulse transmission and imaging through biological tissues," *Applied Optics*, vol. 32, no. 4, pp. 554–558, 1993.

[2] G. Yao and L. V. Wang, "Theoretical and experimental studies of ultrasound-modulated optical tomography in biological tissue," *Applied Optics*, vol. 39, no. 4, pp. 659–664, 2000.

[3] K. Stamnes, S. C. Tsay, W. Wiscombe, and K. Jayaweera, "Numerically stable algorithm for discrete-ordinate-method radiative transfer in multiple scattering and emitting layered media," *Applied Optics*, vol. 27, pp. 2502–2509, 1988.

[4] A. D. Kim and M. Moscoso, "Chebyshev spectral methods for radiative transfer," *SIAM Journal on Scientific Computing*, vol. 23, pp. 2074–2094, 2002.

[5] J. V. P. de Oliveira, A. V. Cardona, and M. T. M. B. de Vilhena, "Solution of the one-dimensional time-dependent discrete ordinates problem in a slab by the spectral and LTSN methods," *Annals of Nuclear Energy*, vol. 29, pp. 13–20, 2002.

[6] M. Sakami, K. Mitra, and P. Hsu, "Analysis of light pulse transport through two-dimensional scattering and absorbing media," *Journal of Quantitative Spectroscopy & Radiative Transfer*, vol. 73, pp. 169–179, 2002.

[7] M. Premaratne, E. Premaratne, and A. J. Lowery, "The photon transport equation for turbid biological media with spatially varying isotropic refractive index," *Optics Express*, vol. 13, pp. 389–399, 2005.

[8] T. Khan and H. Jiang, "A new diffusion approximation to the radiative transfer equation for scattering media with spatially varying refractive indices," *Journal of Optics A: Pure and Applied Optics*, vol. 5, pp. 137–141, 2003.

[9] H. Dehghani, B. Brooksby, K. Vishwanath, B. W. Pogue, and K. D. Paulsen, "The effects of internal refractive index variation in near-infrared optical tomography: A finite element modeling approach," *Physics in Medicine and Biology*, vol. 48, pp. 2713–2727, 2003.

[10] G. Bal, "Radiative transfer equations with varying refractive index: A mathematical perspective," *Journal of the Optical Society of America A*, vol. 23, pp. 1639–1644, 2006.

[11] M. L. Shendeleva and J. A. Molly, "Scaling property of the diffusion equation for light in a turbid medium with varying refractive index," *Journal of the Optical Society of America A*, vol. 24, pp. 2902–2910, 2007.

[12] L. Martí-López, J. Bouza-Domínguez, R. A. Martínez-Celorio, and J. C. Hebden, "An investigation of the ability of modified radiative transfer equations to accommodate laws of geometrical optics," *Optics Communications*, vol. 266, pp. 44–49, 2006.

[13] A. Sharma, D. V. Kumar, and A. K. Ghatak, "Tracing rays through graded-index media: A new method," *Applied Optics*, vol. 21, no. 6, pp. 984–987, 1982.

[14] B. Richerzhagen, "Finite element ray tracing: A new method for ray tracing in gradient-index media," *Applied Optics*, vol. 35, no. 31, pp. 6186–6189, 1996.

[15] H. A. Ferwerda, "The radiative transfer equation for scattering media with a spatially varying refractive index," *Journal of Optics A: Pure and Applied Optics*, vol. 1, pp. L1–L2, 1999.

[16] C. C. Handapangoda and M. Premaratne, "An approximate numerical technique for characterizing optical pulse propagation in inhomogeneous biological tissue," *Journal of Biomedicine and Biotechnology*, vol. 2008, p. 784354, 2008.

[17] B. Michel and T. Beck, "Ray tracing in medical applications," *Lasers & Photonics*, vol. 5, pp. 38–41, 2005.

[18] M. Campos-Garcia and R. Diaz-Urib, "Irradiance transport equation from geometrical optics considerations," *Revista Mexicana De Fisica*, vol. 52, no. 6, pp. 546–549, 2006.

[19] M. Born and E. Wolf, *Principles of Optics*, 7th ed. Cambridge: Cambridge University Press, 1999.

[20] M. Premaratne, "Numerical simulation of nonuniformly time sampled pulse propagation in nonlinear fiber," *IEEE Journal of Lightwave Technology*, vol. 23, no. 8, pp. 2434–2442, 2005.

[21] A. D. Greenwood and J. M. Jin, "A field picture of wave propagation in inhomogeneous dielectric lenses," *IEEE Antennas and Propagation Magazine*, vol. 41, no. 5, pp. 9–18, 1999.

[22] C. T. Tai, "Maxwell fish-eye treated by Maxwell equations," *Nature*, vol. 182, pp. 1600–1601, 1958.

[23] W. H. Press, S. A. Teukolsk, W. T. Vetterling, and B. P. Flannery, *Numerical Recipes in C++*, 2nd ed. New York: Cambridge University Press, 2003.

[24] M. Abramomitz and I. A. Stegun, *Handbook of Mathematical Functions with Formulas, Graphs and Mathematical Tables*. New York: Dover Publications, 1965.

[25] S. C. Chapra and R. P. Canale, *Numerical Methods for Engineers*, 4th ed. New York: McGraw-Hill, 2002.

[26] G. E. Thomas and K. Stamnes, *Radiative Transfer in the Atmosphere and Ocean*. Cambridge University Press, 1999.

CHAPTER 6

A Numerical Technique for Simulating Multi-dimensional Transient Photon Transport in Biological Tissue

A novel method for solving the multi-dimensional transient photon transport equation for laser pulse propagation in biological tissue is presented. A Laguerre expansion is used to represent the time dependence of the incident short pulse. Owing to the intrinsic causal nature of Laguerre functions, this technique automatically always preserves the causality constraints of the transient signal. This expansion of the radiance using a Laguerre basis transforms the transient photon transport equation to the steady state version. The resulting equations are solved using the discrete ordinates method, using a finite volume approach. Therefore, this method enables the handling of general anisotropic, inhomogeneous media using a single formulation but with an added degree of flexibility owing to the ability to invoke higher-order approximations of discrete ordinate quadrature sets. Therefore, compared with existing strategies, this method offers the advantage of representing the intensity with high accuracy thus minimizing numerical dispersion and false propagation errors.

6.1 Introduction

MANY models have been developed to solve the one-dimensional photon transport equation (PTE), which assumes horizontally uniform plane-parallel media. However, in order to model three-dimensional inhomogeneous media, the three-dimensional PTE should be used [1]. The modeling of the three-dimensional photon transport is usually considered difficult, even for the steady state case, because it involves solving integro-differential equations of four or five variables [2]. However, many diverse methods for solving the multi-dimensional steady state photon transport problem can be found in the research literature [1, 3], which discard the time-dependence complications of the transient problem considered here.

The use of short pulse lasers in engineering and biomedical applications, such as optical tomography and laser ablation has motivated research in transient photon transport through biological media [2]. Transient signals have the possibility to probe specific resonances in biological media, which far exceed the capabilities rendered by steady state methods. Most existing transient models have been developed for the one-dimensional PTE, but some have been developed for the two-dimensional PTE [4]. Only recently have researchers started to work on models for three-dimensional transient photon transport in scattering media such as biological tissue. There has been renewed interest in having sensors implanted in tissue for monitoring and characterization [5–10].

Many three-dimensional photon transport problems have been modeled by reducing the three-dimensional propagation to equivalent one-dimensional models. However, such mapping inevitably discards the inhomogeneities and anisotropic characteristics of such media. For example, realistic analysis of light propagation in biological tissue must be carried out in a framework which accounts for

both weak anisotropy and inhomogeneity. Moreover, if sensors are implanted in such scattering media, one-dimensional models in general have difficulty accounting for both scattering and diffraction effects. Also, specific surface features of a model problem may be more accurately incorporated into three-dimensional photon transport. For these reasons, three-dimensional models can provide quantitatively superior realistic results compared with their one- or two-dimensional counterparts.

Most recent developments on solving the three-dimensional transient PTE rely on approximate methods such as diffusion approximation and spherical harmonics approximation, which are used to simplify the PTE [4]. These approximate methods fail to predict the correct propagation speed within the medium and the solution accuracy is not satisfactory except for specific cases that consider optically thick media at asymptotically longer time scales [4]. Tan *et al.* [4] proposed an integral equation technique to model the transient radiative transfer in three-dimensional homogeneous as well as non-homogeneous participating media. Guo *et al.* [2] formulated a complete transient three-dimensional discrete ordinates method to solve the transient PTE in a nonhomogeneous turbid medium with a rectangular enclosure. Guo *et al.* [11] modeled heterogeneous biological tissues using the discrete ordinates method, incorporating the Fresnel specularly reflecting boundary condition. They treated the laser intensity as having a diffuse part and a specular part. The reflectivity at the tissue-air interface was calculated using Snell's law and the Fresnel equations [11]. Chai *et al.* [12] proposed a finite-volume method to calculate transient radiative transfer in a three-dimensional enclosure, while Sawetprawichkul *et al.* [13] implemented the Monte Carlo method for modeling three-dimensional transient photon transport in a parallel computer system.

Oliveira *et al.* [14] proposed a semi-analytical numerical method for solving the one-dimensional transient PTE in slab geometry. They represented the time dependence of the radiance and its time derivative using a truncated series of Laguerre polynomials. This resulted in a set of time-independent equations which were then solved recursively using a Laplace transform method in the space variable with analytical inversion.

This chapter proposes a novel method to solve the three-dimensional transient PTE, which can also be easily adopted for solving one- and two-dimensional cases. The current work uses a transformation which eliminates the partial derivative term with respect to time. The radiance is then expanded using a Laguerre basis which transforms the transient PTE to the steady state version, which is then solved using a finite volume approach with the discrete ordinates method (DOM) [15]. With the use of a Laguerre basis, any arbitrary pulse shape can be represented using only a few Laguerre polynomials, considerably reducing subsequent computational overhead. The causality of the system is implicitly imposed by the Laguerre expansion. The use of the discrete ordinates method has several advantages. It requires only a single formulation to invoke higher-order approximations of discrete ordinate quadrature sets; also, the DOM is applicable to the complete anisotropic scattering phase function and inhomogeneous media [2]. The work presented in this chapter has been published in Optics Express [16].

This chapter is divided into five sections. Section 6.2 provides a detailed mathematical description of the proposed model. This section is further broken down into three subsections. The first subsection carries a step-by-step derivation of the proposed algorithm for the more general three-dimensional case. In the second and third subsections, descriptions of how the model reduces to the two- and the one-dimensional geometries are provided. Section 6.3 presents results

obtained by numerically implementing the proposed algorithm. A comparison of the results obtained using the proposed method is provided against the results obtained using the algorithm proposed by Guo *et al.* in reference [2]. Section 6.4 concludes the chapter by highlighting the relative advantages of the proposed technique.

6.2 Formulation

This section presents a Laguerre method developed to solve the multi-dimensional PTE. In the first sub-section, a detailed mathematical description of the method as applied for the three-dimensional PTE is presented. In the second sub-section, a description of how this method can be adopted to solve the two-dimensional PTE is provided. In the last sub-section, a description of how to adopt the proposed method for the one-dimensional case is presented.

6.2.1 For the three-dimensional PTE

The three-dimensional transient photon transport equation (PTE) is given by [2]

$$\frac{1}{v}\frac{\partial}{\partial t}I(x,y,z,\mathbf{\Omega},t)+\xi\frac{\partial}{\partial x}I(x,y,z,\mathbf{\Omega},t)+\eta\frac{\partial}{\partial y}I(x,y,z,\mathbf{\Omega},t)+u\frac{\partial}{\partial z}I(x,y,z,\mathbf{\Omega},t)$$
$$-\frac{\sigma_s(x,y,z)}{4\pi}\int_{4\pi}P(\mathbf{\Omega}';\mathbf{\Omega})I(x,y,z,\mathbf{\Omega}',t)d\mathbf{\Omega}'+\sigma_t(x,y,z)I(x,y,z,\mathbf{\Omega},t)=F(x,y,z,\mathbf{\Omega},t), \tag{6.1}$$

where $I(x,y,z,\mathbf{\Omega},t)$ is the light intensity (radiance), (x,y,z) are the Cartesian co-ordinates, $\mathbf{\Omega}$ is the local solid angle, u, ξ and η are the direction cosines such that $u=\cos\theta$, $\xi=\sin\theta\cos\phi$, $\eta=\sin\theta\sin\phi$ and t is time. $\sigma_t(x,y,z)$ and $\sigma_s(x,y,z)$ represent the position dependent attenuation and scattering coefficients, respectively. The speed of light in the medium is v, $P(\mathbf{\Omega}';\mathbf{\Omega})$ is the phase function and

$F(x, y, z, \mathbf{\Omega}, t)$ is the source term. Since a constant refractive index is considered, the speed of light in the medium is a constant. This formulation assumes that there are no internal sources inside the medium and hence $F = 0$.

Before proceeding to solve the PTE, the following substitution is used to map Eq. (6.1) to a moving reference frame with the pulse:

$$\tau = t - \frac{x}{3v\xi} - \frac{y}{3v\eta} - \frac{z}{3vu}. \tag{6.2}$$

Use of Eq. (6.2) in Eq. (6.1) eliminates the partial derivative term with respect to time in the original PTE, as shown below.

$$\begin{aligned}
&\frac{1}{v}\frac{\partial}{\partial\tau}I(x,y,z,\mathbf{\Omega},\tau) - \frac{\xi}{3v\xi}\frac{\partial}{\partial\tau}I(x,y,z,\mathbf{\Omega},\tau) + \xi\frac{\partial}{\partial x}I(x,y,z,\mathbf{\Omega},\tau) - \frac{\eta}{3v\eta}\frac{\partial}{\partial\tau}I(x,y,z,\mathbf{\Omega},\tau)\\
&+ \eta\frac{\partial}{\partial y}I(x,y,z,\mathbf{\Omega},\tau) - \frac{u}{3vu}\frac{\partial}{\partial\tau}I(x,y,z,\mathbf{\Omega},\tau) + u\frac{\partial}{\partial z}I(x,y,z,\mathbf{\Omega},\tau)\\
&- \frac{\sigma_s(x,y,z)}{4\pi}\int_{4\pi}P(\mathbf{\Omega}';\mathbf{\Omega})I(x,y,z,\mathbf{\Omega}',t)d\mathbf{\Omega}' + \sigma_t(x,y,z)I(x,y,z,\mathbf{\Omega},\tau) = 0,
\end{aligned} \tag{6.3}$$

which can be simplified to obtain,

$$\begin{aligned}
&\xi\frac{\partial}{\partial x}I(x,y,z,\mathbf{\Omega},\tau) + \eta\frac{\partial}{\partial y}I(x,y,z,\mathbf{\Omega},\tau) + u\frac{\partial}{\partial z}I(x,y,z,\mathbf{\Omega},\tau)\\
&- \frac{\sigma_s(x,y,z)}{4\pi}\int_{4\pi}P(\mathbf{\Omega}';\mathbf{\Omega})I(x,y,z,\mathbf{\Omega}',\tau)d\mathbf{\Omega}' + \sigma_t(x,y,z)I(x,y,z,\mathbf{\Omega},\tau) = 0.
\end{aligned} \tag{6.4}$$

Time dependence is then represented using Laguerre polynomials. Laguerre functions are used to expand $I(x, y, z, \mathbf{\Omega}, \tau)$ in the summation

$$I\left(x,y,z,\mathbf{\Omega},\tau\right) = \sum_{k=0}^{N} B_k\left(x,y,z,\mathbf{\Omega}\right) L_k\left(\tau\right), \tag{6.5}$$

where

$$\int_0^\infty L_n\left(\tau\right) L_m\left(\tau\right) e^{-\tau} d\tau = \delta_{mn}. \tag{6.6}$$

Using Eq. (6.5) in Eq. (6.4) and taking moments (i.e. multiplying by $L_n(\tau)\, e^{-\tau}$ and integrating over $[0,\infty)$), the time dependence can be removed, resulting in N uncoupled equations, one for each Laguerre coefficient, B_n.

$$\xi\frac{\partial}{\partial x}B_n(x,y,z,\mathbf{\Omega}) + \eta\frac{\partial}{\partial y}B_n(x,y,z,\mathbf{\Omega}) + u\frac{\partial}{\partial z}B_n(x,y,z,\mathbf{\Omega}) \\ -\frac{\sigma_s(x,y,z)}{4\pi}\int_{4\pi} P(\mathbf{\Omega}';\mathbf{\Omega})B_n(x,y,z,\mathbf{\Omega}')d\mathbf{\Omega}' + \sigma_t(x,y,z)B_n(x,y,z,\mathbf{\Omega}) = 0, \qquad (6.7)$$

where $n = 1,\ldots,N$. Thus, the transient photon transport equation has been reduced to a set of uncoupled steady state photon transport equations. Equation (6.7) can be solved using the discrete ordinates method as detailed in reference [15], which is outlined below.

The solid angle dependence of Eq. (6.7) can be discretized using the discrete ordinates method [17], resulting in L coupled equations for each Laguerre coefficient:

$$\xi^i\frac{\partial}{\partial x}B_n(x,y,z,\mathbf{\Omega}^i) + \eta^i\frac{\partial}{\partial y}B_n(x,y,z,\mathbf{\Omega}^i) + u^i\frac{\partial}{\partial z}B_n(x,y,z,\mathbf{\Omega}^i) \\ -\frac{\sigma_s(x,y,z)}{4\pi}\sum_{j=1}^{L} w_j P(\mathbf{\Omega}^j;\mathbf{\Omega}^i)B_n(x,y,z,\mathbf{\Omega}^j) + \sigma_t(x,y,z)B_n(x,y,z,\mathbf{\Omega}^i) = 0, \qquad (6.8)$$

where w_j are quadrature weights, $i = 1,\ldots,L$ and $n = 1,\ldots,N$. The tissue specimen is divided into infinitesimally small control volumes and the discrete ordinates method is applied. Integrating Eq. (6.8) over a control volume results in:

$$\int_V \frac{\partial B_n^i}{\partial x}dV = (B_n^i)_{xu}A_{xu} - (B_n^i)_{xd}A_{xd}, \qquad (6.9)$$

where $V = \Delta x\Delta y\Delta z$ is the volume of the control volume, $(B_n)_{xu}$ and $(B_n)_{xd}$ are average values of B_n over the faces A_{xu} and A_{xd} of the control volume, respec-

tively. Similarly,

$$\int_V \frac{\partial B_n^i}{\partial y} dV = (B_n^i)_{yu} A_{yu} - (B_n^i)_{yd} A_{yd}, \tag{6.10}$$

and

$$\int_V \frac{\partial B_n^i}{\partial z} dV = (B_n^i)_{zu} A_{zu} - (B_n^i)_{zd} A_{zd}. \tag{6.11}$$

Here, $B_n^i = B_n(x, y, z, \mathbf{\Omega}^i)$. Use of Eq. (6.9) to Eq. (6.11) in Eq. (6.8) results in

$$\begin{aligned}
&\xi^i \left((B_n^i)_{xu} A_{xu} - (B_n^i)_{xd} A_{xd} \right) + \eta^i \left((B_n^i)_{yu} A_{yu} - (B_n^i)_{yd} A_{yd} \right) \\
&+ u^i \left((B_n^i)_{zu} A_{zu} - (B_n^i)_{zd} A_{zd} \right) + \sigma_t(x, y, z) V (B_n^i)_p \\
&- \frac{\sigma_s(x, y, z)}{4\pi} V \sum_{j=1}^{L} w_j P(\mathbf{\Omega}^j; \mathbf{\Omega}^i) (B_n^j)_p = 0,
\end{aligned} \tag{6.12}$$

where $(B_n^i)_p$ is the Laguerre coefficient of the radiance at the centre of the control volume. The average values of B_n on the faces of the control volume and that at the centre are related by [15]:

$$(B_n^i)_p = (\gamma^i)_x (B_n^i)_{xd} + \left(1 - (\gamma^i)_x\right) (B_n^i)_{xu}, \tag{6.13}$$

$$= (\gamma^i)_y (B_n^i)_{yd} + \left(1 - (\gamma^i)_y\right) (B_n^i)_{yu}, \tag{6.14}$$

$$= (\gamma^i)_z (B_n^i)_{zd} + \left(1 - (\gamma^i)_z\right) (B_n^i)_{zu}. \tag{6.15}$$

The weights γ_x, γ_y and γ_z can be determined using the scheme proposed by Lathrop [2, 18]:

$$(\gamma^i)_x = \max\left(0.5, 1 - \frac{|\xi^i|/\Delta x}{2\left(|\eta^i|/\Delta y + |u^i|/\Delta z\right) + \sigma_t}\right), \tag{6.16}$$

$$(\gamma^i)_y = \max\left(0.5, 1 - \frac{|\eta^i|/\Delta y}{2\left(|\xi^i|/\Delta x + |u^i|/\Delta z\right) + \sigma_t}\right), \tag{6.17}$$

$$(\gamma^i)_z = \max\left(0.5, 1 - \frac{|u^i|/\Delta z}{2\left(|\xi^i|/\Delta x + |\eta^i|/\Delta y\right) + \sigma_t}\right). \tag{6.18}$$

Using Eq. (6.13) to Eq. (6.15) in Eq. (6.12) and eliminating $(B_n^i)_{xd}$, $(B_n^i)_{yd}$ and $(B_n^i)_{zd}$ results in

$$(B_n^i)_p = \frac{V(S^i)_p + \frac{|\xi^i|A_{xu}}{(\gamma^i)_x}(B_n^i)_{xu} + \frac{|\eta^i|A_{yu}}{(\gamma^i)_y}(B_n^i)_{yu} + \frac{|u^i|A_{zu}}{(\gamma^i)_z}(B_n^i)_{zu}}{\sigma_t V + |\xi^i|A_{xu}/(\gamma^i)_x + |\eta^i|A_{yu}/(\gamma^i)_y + |u^i|A_{zu}/(\gamma^i)_z}, \tag{6.19}$$

where

$$(S^i)_p = \frac{\sigma_s(x,y,z)}{4\pi}\sum_{j=1}^{L} w_j P(\mathbf{\Omega}^j;\mathbf{\Omega}^i)(B_n^j)_p. \tag{6.20}$$

Dividing the numerator and the denominator of the right hand side of Eq. (6.19) by V, results in

$$(B_n^i)_p = \frac{(S^i)_p + \left(\frac{|\xi^i|}{((\gamma^i)_x\Delta_x)}\right)(B_n^i)_{xu} + \left(\frac{|\eta^i|}{((\gamma^i)_y\Delta_y)}\right)(B_n^i)_{yu} + \left(\frac{|u^i|}{((\gamma^i)_z\Delta_z)}\right)(B_n^i)_{zu}}{\sigma_t + |\xi^i|/\left((\gamma^i)_x\Delta_x\right) + |\eta^i|/\left((\gamma^i)_y\Delta_y\right) + |u^i|/\left((\gamma^i)_z\Delta_z\right)}. \tag{6.21}$$

In the present work, the spatial differencing scheme suggested by Fiveland [19] is used to determine the step sizes Δx, Δy and Δz. According to this scheme

$$\Delta x < \frac{|\xi^i|_{\min}}{\sigma_t\left(1-(\gamma^i)_x\right)}, \tag{6.22}$$

$$\Delta y < \frac{|\eta^i|_{\min}}{\sigma_t\left(1-(\gamma^i)_y\right)}, \tag{6.23}$$

$$\Delta z < \frac{|u^i|_{\min}}{\sigma_t\left(1-(\gamma^i)_z\right)}. \tag{6.24}$$

The algorithm of discrete ordinates for solving the PTE, which is reduced to the steady state version given by Eq. (6.8), starts at corner control volumes. The $(B_n^i)_{xu}$, $(B_n^i)_{yu}$ and $(B_n^i)_{zu}$ values for each corner control volume are given by the Laguerre coefficients of the boundary condition. Hence, the centre values,

$(B_n^i)_p$, are determined from Eq. (6.21). Once $(B_n^i)_p$ is calculated $(B_n^i)_{xd}$, $(B_n^i)_{yd}$ and $(B_n^i)_{zd}$ are determined using Eq. (6.13) to Eq. (6.15). $(S^i)_p$, which is initially assumed to be equal to zero, is then updated using the calculated $(B_n^i)_p$ value from Eq. (6.20). $(B_n^i)_{xd}$, $(B_n^i)_{yd}$ and $(B_n^i)_{zd}$ of the current control volume are equal to $(B_n^i)_{xu}$, $(B_n^i)_{yu}$ and $(B_n^i)_{zu}$ of the adjacent control volumes, respectively. A more detailed description of this method can be found in reference [15].

The overall algorithm proposed is summarized in ALGORITHM 1 below.

ALGORITHM 1

1. Use the transformation given by Eq. (6.2) in the transient PTE, Eq. (6.1).
2. Expand the radiance, $I(x, y, z, \mathbf{\Omega}, t)$, using a Laguerre basis.
3. Expand the time-dependent boundary condition using a Laguerre basis.
4. Divide the specimen geometry into infinitesimally small control volumes (finite volume approach).
5. Apply the discrete ordinates method to Eq. (6.7) in order to solve for each Laguerre coefficient of the radiance iteratively until convergence is achieved.
6. Combine the Laguerre coefficients using Eq. (6.5) to obtain the radiance values.

The main steps of the discrete ordinates method using the finite volume approach are listed in ALGORITHM 2 below.

ALGORITHM 2

1. Start at a corner control volume. $(B_n^i)_{xu}$, $(B_n^i)_{yu}$ and $(B_n^i)_{zu}$ for this control volume are known from the boundary condition.
2. $(S^i)_p$ is assumed to be zero initially for all control volumes.
3. Calculate $(B_n^i)_p$ of the current control volume from Eq. (6.21).

4. Determine $(B_n^i)_{xd}$, $(B_n^i)_{yd}$ and $(B_n^i)_{zd}$ using Eq. (6.13) to Eq. (6.15).
5. The quantities calculated in step 4 become $(B_n^i)_{xu}$, $(B_n^i)_{yu}$ and $(B_n^i)_{zu}$ for adjacent control volumes.
6. Repeat steps 3 to 5 until all control volumes are traversed.
7. Move to the next discrete ordinate (of the solid angle, $\mathbf{\Omega}$) in the currently considered quadrant.
8. Repeat steps 2 to 7 until all discrete ordinates corresponding to the current quadrant are covered.
9. Move to the next corner control volume.
10. Repeat steps 1 to 9 until all the corners are considered.
11. Update $(S^i)_p$ for all discrete ordinates using Eq. (6.20).
12. Repeat steps 1 to 11 until $(S^i)_p$ is converged.
13. Repeat steps 1 to 12 for all Laguerre coefficients of I.

6.2.2 For the two-dimensional PTE

The two-dimensional transient photon transport equation (PTE), for a medium without any internal sources, is given by

$$\frac{1}{v}\frac{\partial}{\partial t}I(x,z,\mathbf{\Omega},t)+\xi\frac{\partial}{\partial x}I(x,z,\mathbf{\Omega},t)+u\frac{\partial}{\partial z}I(x,z,\mathbf{\Omega},t)$$
$$-\frac{\sigma_s(x,z)}{4\pi}\int_{4\pi}P(\mathbf{\Omega}';\mathbf{\Omega})I(x,z,\mathbf{\Omega}',t)d\mathbf{\Omega}'+\sigma_t(x,z)I(x,z,\mathbf{\Omega},t)=0. \tag{6.25}$$

Instead of the transformation given by Eq. (6.2), the transformation

$$\tau=t-\frac{x}{2v\xi}-\frac{z}{2vu}, \tag{6.26}$$

must be used in order to make the partial derivative term with respect to time of Eq. (6.25) vanish. After using Eq.(6.26) in Eq.(6.25) to eliminate the time derivative term, the radiance, I, is then expanded using a Laguerre basis using Eq. (6.5)

and taking moments as for the three-dimensional case. This results in the two-dimensional steady state PTE:

$$\xi\frac{\partial}{\partial x}B_n(x,z,\mathbf{\Omega})+u\frac{\partial}{\partial z}B_n(x,z,\mathbf{\Omega})+\sigma_t(x,z)B_n(x,z,\mathbf{\Omega}) \\ -\frac{\sigma_s(x,z)}{4\pi}\int_{4\pi}P(\mathbf{\Omega}';\mathbf{\Omega})B_n(x,z,\mathbf{\Omega}')d\mathbf{\Omega}'=0. \tag{6.27}$$

ALGORITHM 2 can then be used to solve Eq.(6.27)for B_n and using Eq. (6.5) the radiance, I, can be determined. However, when applying ALGORITHM 2, in the equations used for the three-dimensional case, terms corresponding to the variable y vanish.

6.2.3 For the one-dimensional PTE

The one-dimensional transient photon transport equation (PTE), for a medium without any internal sources, is given by

$$\frac{1}{v}\frac{\partial}{\partial t}I(z,\mathbf{\Omega},t)+u\frac{\partial}{\partial z}I(z,\mathbf{\Omega},t)-\frac{\sigma_s(z)}{4\pi}\int_{4\pi}P(\mathbf{\Omega}';\mathbf{\Omega})I(z,\mathbf{\Omega}',t)d\mathbf{\Omega}'+\sigma_t(z)I(z,\mathbf{\Omega},t)=0. \tag{6.28}$$

For this case, instead of the transformation given by Eq. (6.2), the following transformation is used.

$$\tau=t-\frac{z}{vu}. \tag{6.29}$$

Use of Eq.(6.29) in Eq.(6.28) eliminates the time derivative term in Eq.(6.28). Then, expanding the transformed one-dimensional PTE using a Laguerre basis and taking moments results in,

$$u\frac{\partial}{\partial z}B_n(z,\mathbf{\Omega})-\frac{\sigma_s(z)}{4\pi}\int_{4\pi}P(\mathbf{\Omega}';\mathbf{\Omega})B_n(z,\mathbf{\Omega}')d\mathbf{\Omega}'+\sigma_t(z)B_n(z,\mathbf{\Omega})=0, \tag{6.30}$$

where $n = 1, \ldots, N$. Then the solid angle, $\mathbf{\Omega}$, of Eq. (6.30) is discretized using the discrete ordinates method, which results in

$$u^i \frac{\partial}{\partial z} B_n(z, \mathbf{\Omega}^i) - \frac{\sigma_s(z)}{4\pi} \sum_{j=1}^{L} w_j P(\mathbf{\Omega}^j; \mathbf{\Omega}^i) B_n(z, \mathbf{\Omega}^j) + \sigma_t(z) B_n(z, \mathbf{\Omega}^i) = 0, \qquad (6.31)$$

where $i = 1, \ldots, L$ and $n = 1, \ldots, N$. Thus, there are L coupled equations for each Laguerre coefficient, B_n. They can be written in matrix form as:

$$\frac{\partial}{\partial z} \mathbf{A}\mathbf{B}_n + \sigma_t \mathbf{B}_n - \frac{\sigma_s}{4\pi} \mathbf{P}\mathbf{W}\mathbf{B}_n = \mathbf{0}, \qquad (6.32)$$

where $\mathbf{B}_n = \left[B_n\left(z, \mathbf{\Omega}^i\right)\right]_{L,1}$, $\mathbf{P} = \left[P\left(\mathbf{\Omega}^j; \mathbf{\Omega}^i\right)\right]_{L,L}$ and $\mathbf{A}$ is a L by L diagonal matrix with diagonal elements u^i. The matrix $\mathbf{W}$ is also a L by L diagonal matrix with diagonal elements w_j.

Rearranging, Eq. (6.32) can be written as

$$\frac{\partial}{\partial z} \mathbf{B}_n = \mathbf{Y}\mathbf{B}_n, \qquad (6.33)$$

where

$$\mathbf{Y} = \mathbf{A}^{-1} \left[\frac{\sigma_s}{4\pi} \mathbf{P}\mathbf{W} - \sigma_t \mathbf{I}\right]. \qquad (6.34)$$

Hence, the original transient PTE is reduced to a one-variable ordinary differential equation. The boundary condition should also be expanded using a Laguerre basis as described for the three-dimensional case. Thus, Eq. (6.33), subject to the given boundary condition, can be solved using the 4^{th} order Runge-Kutta-Fehlberg(RKF) method [20]. The technique is essentially the same as that described for the one-dimensional PTE in Chapter 4, the only difference being the matrix sizes. This difference is due to the fact that in Chapter 4 the radiance was considered as a function of the zenith angle and the azimuthal angle, but in this

chapter it is taken to be a function of the solid angle.

The next section presents some results obtained using this algorithm and a discussion of relative advantages of the proposed algorithm.

6.3 Numerical results and discussion

Simulations of the proposed technique were carried out using Matlab^{TM}. A comparison for the two- and three-dimensional problems are provided, with results obtained from the technique proposed by Guo *et al.* [2]. In reference [2] these researchers provided a complete transient three-dimensional discrete ordinates method to solve the three-dimensional PTE in a rectangular enclosure. In that paper, they extended the discrete ordinates algorithm described above in ALGORITHM 2, to include the transient term. For the simulations presented in this section, their method has been adopted for the two-dimensional case as well for the purpose of comparison. In the figures, the label "Laguerre DOM" is assigned for the method proposed in this chapter and the label "Transient DOM" is assigned for the method proposed in reference [2].

6.3.1 Normalization of units

The PTE is linear in intensity, I, and thus arbitrary units for intensity can be used. It is a first order, linear differential equation in time and thus time units can also be selected to enhance the numerical accuracy. It is very clear that the input pulse parameters influence the numerical accuracy and efficiency of the algorithm. The input pulse was taken to be a Gaussian pulse described mathematically by

$$f(t) = I_0 e^{-\left(\frac{(t-t_0)}{T}\right)^2}, \tag{6.35}$$

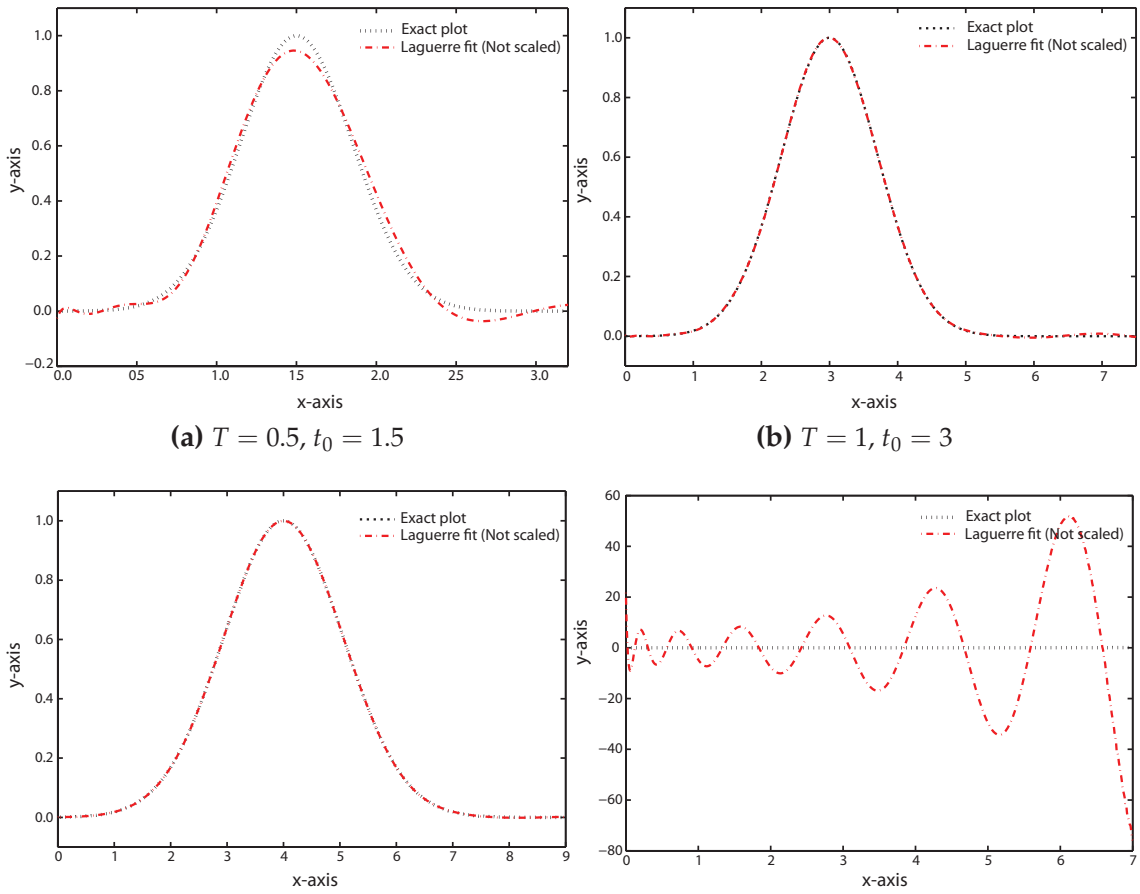

(a) $T = 0.5$, $t_0 = 1.5$ **(b)** $T = 1$, $t_0 = 3$

(c) $T = 1.5$, $t_0 = 4$ **(d)** $T = 5$, $t_0 = 15$

Figure 6.1: Comparison of Laguerre fitting, without scaling, with the exact plot of the corresponding Gaussian function.

where T is the factor determining the width of the input pulse while t_0 determines the time at which the pulse attains its peak value. Thus, the intensity and time units were set relative to major characteristics of the input pulse; its peak intensity, I_0 and its temporal width controlling parameter, T, which is related to full-width half maximum value by $2\sqrt{2\ln(2)}T$. The scale I/I_0 was used for radiance in the following simulations. The time units were normalized by a scaling factor T_s, spatial units by Z_s and scattering and absorption coefficients by $1/Z_s$.

In the present study the scaling factor T_s was set such that $T_s = T/1.5$. This

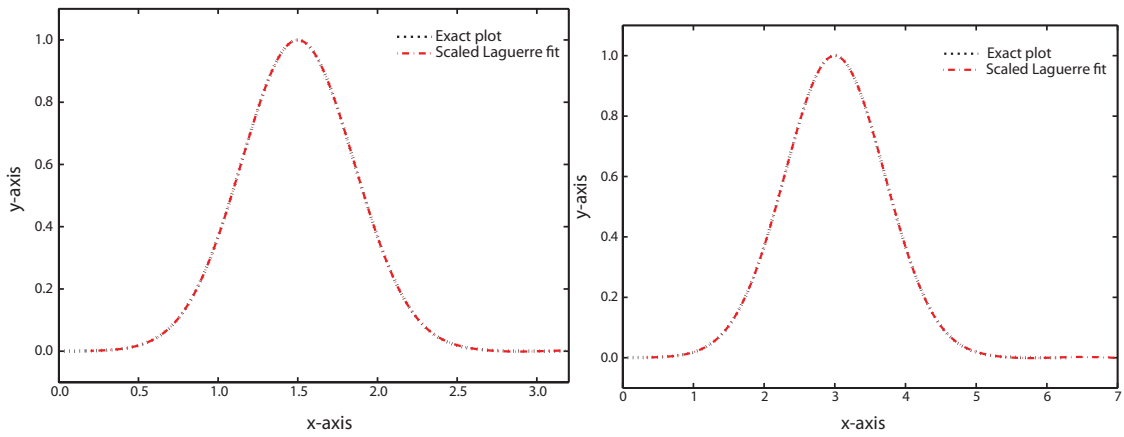

(a) $T = 0.5$, $t_0 = 1.5$ **(b)** $T = 1$, $t_0 = 3$

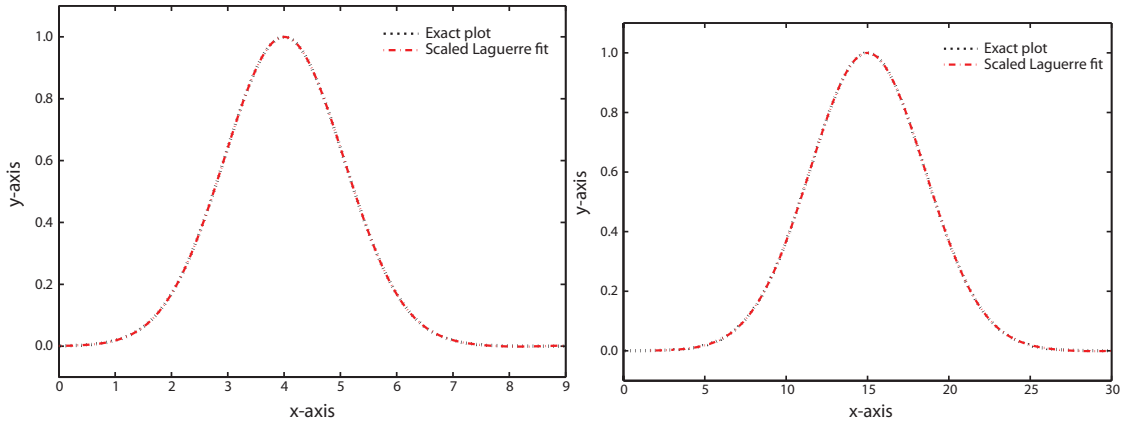

(c) $T = 1.5$, $t_0 = 4$ **(d)** $T = 5$, $t_0 = 15$

Figure 6.2: Comparison of Laguerre fitting, after scaling with the factor T_s, with the exact plot of the corresponding Gaussian function.

normalization factor was chosen due to the fact that the Laguerre approximation of the Gaussian pulse is very accurate for pulses with $T = 1.5$ or greater. This effect is shown in Fig. 6.1 and Fig. 6.2. Figure 6.1 presents a comparison of direct Laguerre approximation (i.e. without scaling with T_s) with the exact plot of the Gaussian pulse, for four different pulse widths. This shows that the Laguerre approximations for pulses with $T = 1$ and $T = 1.5$ are very accurate. However, for the $T = 1$ case, a very small bump appears for $6.5 < x < 7.5$ (see Fig. 6.1b). Such inaccuracies can be eliminated by choosing a larger number of Laguerre coefficients. However, if computational efficiency is also of concern, better scaling can be used to reduce the required number of Laguerre coefficients. Therefore, in the simulations the $T = 1.5$ and $t_0 = 4$ approximation was used. A pulse with different T and t_0 values should be scaled and shifted accordingly to obtain $T = 1.5$ and $t_0 = 4$ before the Laguerre fit is carried out. The results obtained by the simulations were scaled and shifted back (reversing this process). This idea is illustrated in Fig. 6.2. Four different Gaussian pulses with different T and t_0 values were scaled and shifted (up or down) to obtain the Gaussian pulse with $T = 1.5$ and $t_0 = 4$ and a Laguerre fit was carried out. Then the scaling and shifting was reversed and the resulting fit was plotted with the exact plot of the corresponding pulse. It is clearly shown in Fig. 6.2 that this scaled Laguerre fit produces very accurate approximations.

It is interesting to note that with this scaling, it is possible to obtain very accurate results even for the very narrow pulses used in many biomedical applications. For pulses with other shapes, it is recommended that a least square error fit is used to obtain a Gaussian approximation, subsequently setting T_s to the width of that Gaussian pulse divided by 1.5. With the Laguerre fit it is not possible to approximate any pulse shape to an arbitrary accuracy because of numerical considerations. Therefore, in practice, there is a finite domain in which this ap-

proximation is valid. However, as can be seen in Fig. 6.2 this domain expands as T is increased. However, since in the proposed algorithm the Laguerre polynomials were propagated with the pulse, the approximation was always accurate in the domain of interest (i.e. the domain in which the Laguerre fit is accurate extends a few time units beyond the required observation point). A discussion of the observation window in which the Laguerre approximation is accurate can be found in Chapter 4.

In the simulations $Z_s = v \times \overline{T}$ was used. Here, $\overline{T}$ can be chosen to suit the particular application. However, these scaling factors should be chosen carefully so that the matrices that are used remain well-conditioned. For the simulations presented in this section, without loss of generality, $T/\overline{T} = 1.5$ was chosen so that $Z_s = v \times \frac{T}{1.5}$. In this section a line over the letters is used to denote quantities with normalized units.

6.3.2 Computational complexity

For the simulations, an observation volume of $-1 < \overline{x} < +1$, $-1 < \overline{y} < +1$ and $0 < \overline{z} < 2$ was considered. However, refractive index-matched boundaries were assumed in all three dimensions. Therefore, in order to minimize effects from internal reflections at the boundaries the simulation volume was taken to be larger than the observation volume in all three dimensions ($-5 < \overline{x} < +5$, $-5 < \overline{y} < +5$ and $0 < \overline{z} < 5$). The total number of voxels used in the finite volume computations was 108000. The number of voxels considered in the observation volume was 1728. The number of discrete ordinates taken for the simulations was 80. The discrete ordinates for S_8 approximation given in Table 16.1 of reference [15] were used. The two main drawbacks of the discrete ordinates method are false scattering and the ray effect [4, 15]. False scattering is due to spatial discretiza-

tion errors. When a single collimated beam is traced through an enclosure by the discrete ordinates method, the beam will gradually widen as it moves farther away from its point of origin; this unphysical effect, even in the absence of real scattering, is called false scattering [15]. False scattering can be reduced by using finer meshes [15]. The ray effect is due to errors in angular discretization and can be reduced by increasing the sizes of the meshes [15]. Therefore, if a finer spatial mesh is used to reduce the false scattering, a finer angular quadrature scheme should be used to reduce the ray effect [15]. Thus, if the Laguerre DOM method proposed in this chapter is used with a finer mesh, it should be accompanied by an increased number of discrete ordinates in order to minimize numerical errors.

The Gaussian pulse shape can be represented accurately using about 40 Laguerre polynomials. Increasing the number of polynomials up to 63 enables further refinement in the results. The incident Gaussian pulse in Fig. 6.4 can be approximated by 20 Laguerre polynomials with a normalized root mean squared deviation (NRMSD) of 8.07% in the observation window. A discussion of the observation window in which the Laguerre approximation is accurate can be found in Chapter 4 and in reference [21]. The NRMSD can be reduced to 1.5% by using 40 polynomials. A further reduction up to 0.39% can be achieved by using 63 polynomials. However, increasing this number further does not improve the approximation because machine accuracy limitations hinder further numerical improvements.

The simulation presented in this section was carried out on a computer with 2 Intel CPUs at 2.5 GHz. For the three-dimensional simulation of the proposed method (Laguerre DOM) shown in Fig. 6.7 to Fig. 6.10, with 63 Laguerre polynomials, it took 9 minutes and 1 second. For simulating the same problem using Transient DOM, the same machine took 34 minutes and 6 seconds. In reference

[2] the authors state that their method may take several minutes to dozens of hours for simulations, depending on the specified problem and the grid size. The efficiency of the proposed Laguerre DOM might be even better for more complex problems than that considered here.

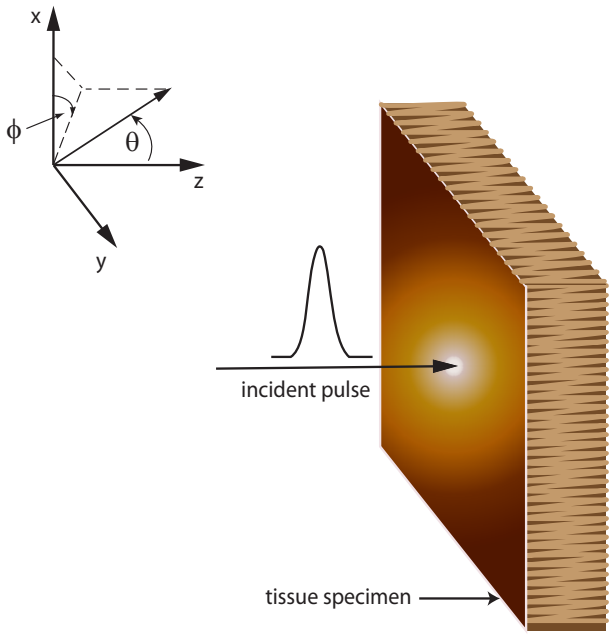

Figure 6.3: Short laser pulse incident on the biological tissue layer.

Figure 6.3 shows a short laser pulse of Gaussian shape incident on a biological tissue layer at $(\overline{x} = 0, \overline{y} = 0, \overline{z} = 0)$. This is the model used for the simulations presented in this section. For all the simulations, $\widetilde{T} = 1.5$ and $\widetilde{t_0} = 4$ for the input pulse given by Eq. (4.41) as shown in Fig. 6.4. The normalized velocity $\widetilde{v} = 1$ and the normalized thickness of the tissue layer at which the results were obtained was $\widetilde{z} = 2$. The isotropic phase function ($P(\mathbf{\Omega}'; \mathbf{\Omega}) = 1$) was used in the simulations. However, the proposed method is able to handle any other phase function.

For Figures 6.5 to 6.12, $\widetilde{\sigma_t} = 1$, $\widetilde{\sigma_s} = 0.98$ and the direction of incidence is $u = 1$. Figures 6.5 and 6.6 show the variation of irradiance with time and along x-axis at

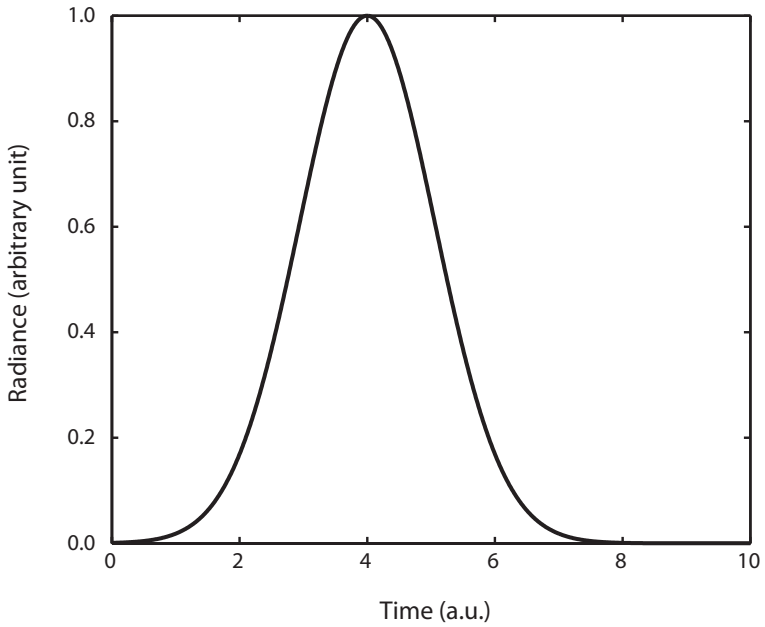

Figure 6.4: Incident Gaussian pulse (with $I_0 = 1$ in Eq. (4.41)).

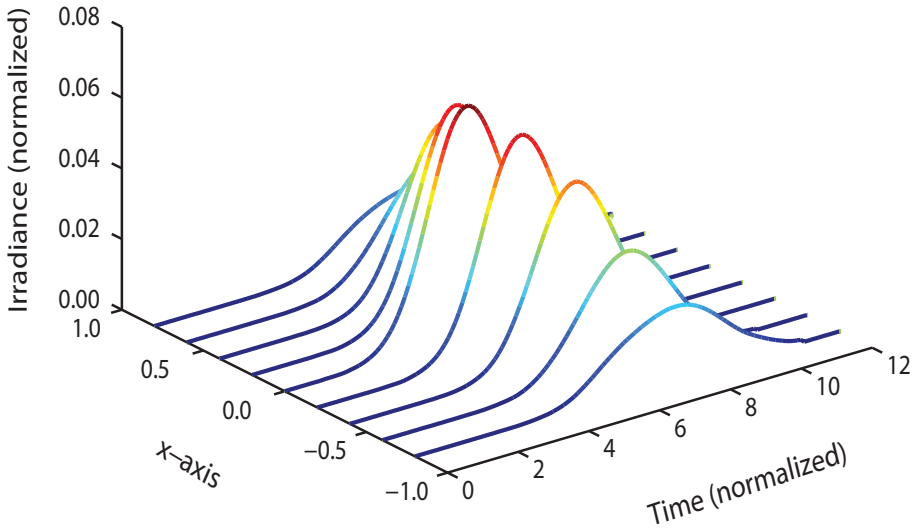

Figure 6.5: Variation of irradiance with time and x coordinate for the two-dimensional PTE, using Laguerre DOM.

$\overline{z} = 2$, for the two-dimensional PTE using the two methods. Figure 6.5 indicates that the time shift of the peak value of the irradiance profile increases as $\overline{x}$ moves

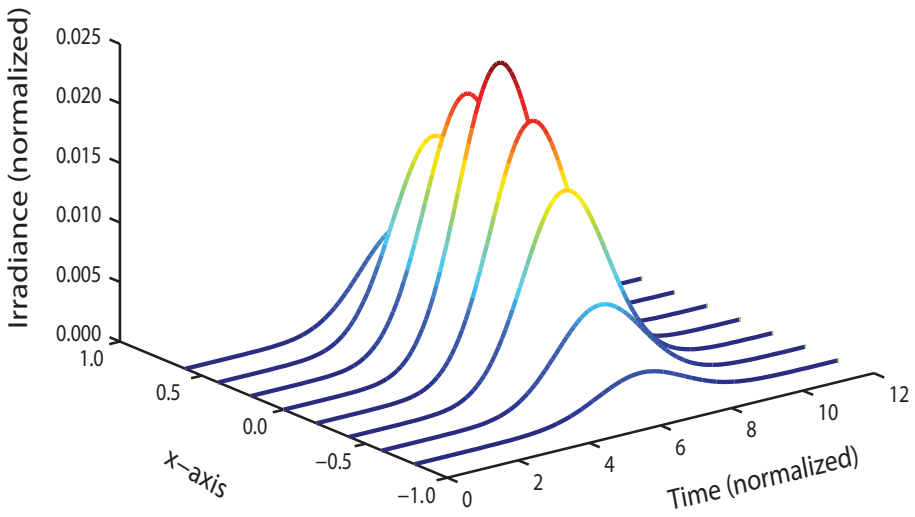

Figure 6.6: Variation of irradiance with time and x coordinate for the two-dimensional PTE, using Transient DOM.

away from $\overline{x} = 0$. The reason for this is that light takes the shortest time to reach $(\overline{x} = 0, \overline{z} = 2)$ point and the time increases as the point moves away from $\overline{x} = 0$ central axis. However, in the simulation obtained using Transient DOM shown in Fig. 6.6 this physical phenomenon is not clearly visible.

Figures 6.7 to 6.10 show the variation of intensity with time, along x and y axes, at $\overline{z} = 2$, for the three-dimensional PTE using Laguerre DOM. In these figures the value of the normalized irradiance (ranging from 0 to 16×10^{-4}) is represented by the color scale. Figures 6.7 to 6.10 were obtained using the same data set. Figure 6.7 shows a slice plane at $\overline{y} = 0$. Thus, in Fig. 6.7 the variation of irradiance with time along the x-axis on $(\overline{y} = 0, \overline{z} = 2)$ plane is shown. As expected, the light reaches $(\overline{x} = 0, \overline{y} = 0)$ point first as rays traveling at an angle to the central axis $(\overline{x} = 0, \overline{y} = 0)$ take longer to reach $\overline{z} = 2$ plane (because the diagonal distance is more than the central axis distance and the speed is constant). For the same reason, the irradiance profile decays first at $(\overline{x} = 0, \overline{y} = 0)$ and later at other points. The more a point moves away from the central axis, the longer it takes the irradiance profile to decay.

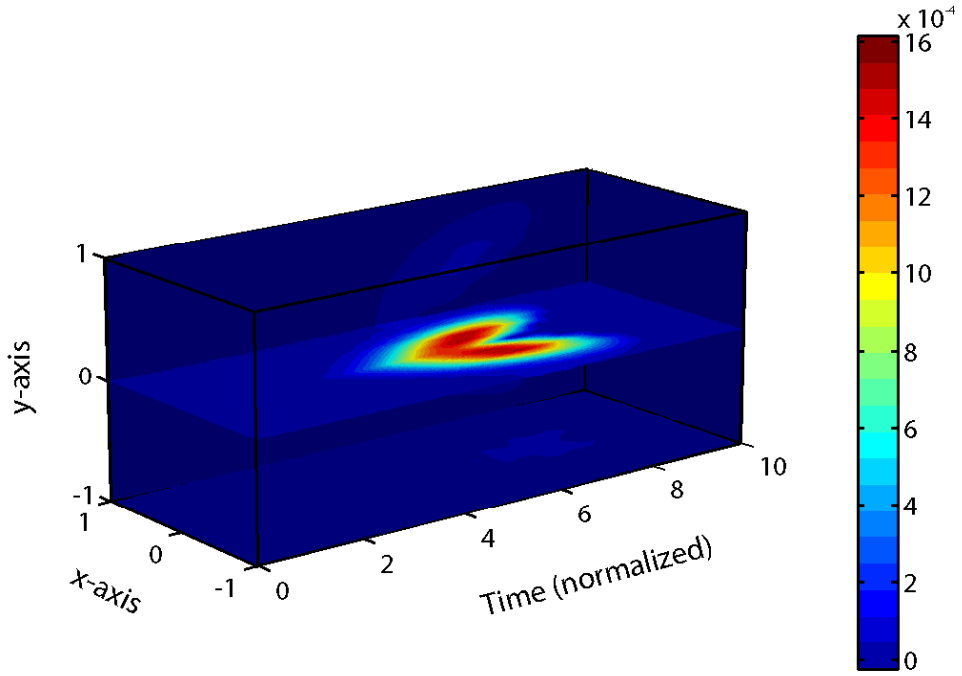

Figure 6.7: Variation of irradiance with time, x coordinate and y coordinate at $\bar{z} = 2$ for 3D PTE, using Laguerre DOM (Slice plane at $\bar{y} = 0, \bar{z} = 2$).

Figure 6.8 shows the variation of irradiance along x and y axes on $\bar{z} = 2$ plane at $\bar{t} = 6$. With isotropic scattering and normal incidence a circular spatial distribution on the xy plane was obtained. From Fig. 6.7 it can be seen that at $\bar{t} = 6$ points around $(\bar{x} = 0, \bar{y} = 0)$ are receiving the second half of the Gaussian pulse (i.e. the maximum irradiance has been reached earlier) and points further away from the central axis are receiving light corresponding to the maximum or the first half of the incident pulse. This phenomenon is reflected in Fig. 6.8. However, in the simulation result shown in Fig. 6.7 and Fig. 6.8, an uncharacteristically low number of photons can be seen along the central axis and the majority of diffuse photons appear off axis resulting in a well-defined shape. The reason

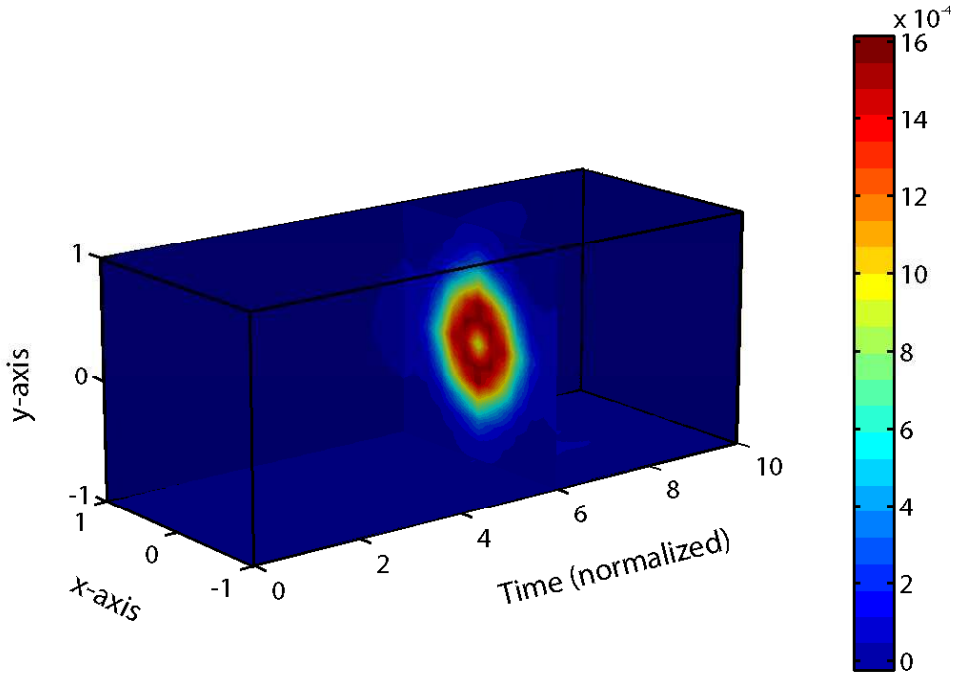

Figure 6.8: Variation of irradiance with time, x coordinate and y coordinate at $\overline{z} = 2$ for 3D PTE, using Laguerre DOM (Slice plane at $\overline{z} = 2$, $\overline{t} = 6$).

for this phenomenon is not yet clear, and we intend to investigate this issue using Monte-Carlo techniques in the future. Figures 6.9 and 6.10 show that the irradiance profile at $\overline{z} = 2$ is symmetrical along x and y axes due to isotropic scattering and normal incidence.

Figures 6.11 and 6.12 show the variation of intensity with time, along x and y axes, at $\overline{z} = 2$, for the three-dimensional PTE using Transient DOM as proposed in reference [2]. The temporal profile in Fig. 6.11 obtained using this method is different to that in Fig. 6.7. Since a Gaussian-shaped input was used, the irradiance profile should start decaying at $(\overline{x} = 0, \overline{y} = 0, \overline{z} = 2)$ before at other points. The further away the observation point moves from the central axis, the longer it

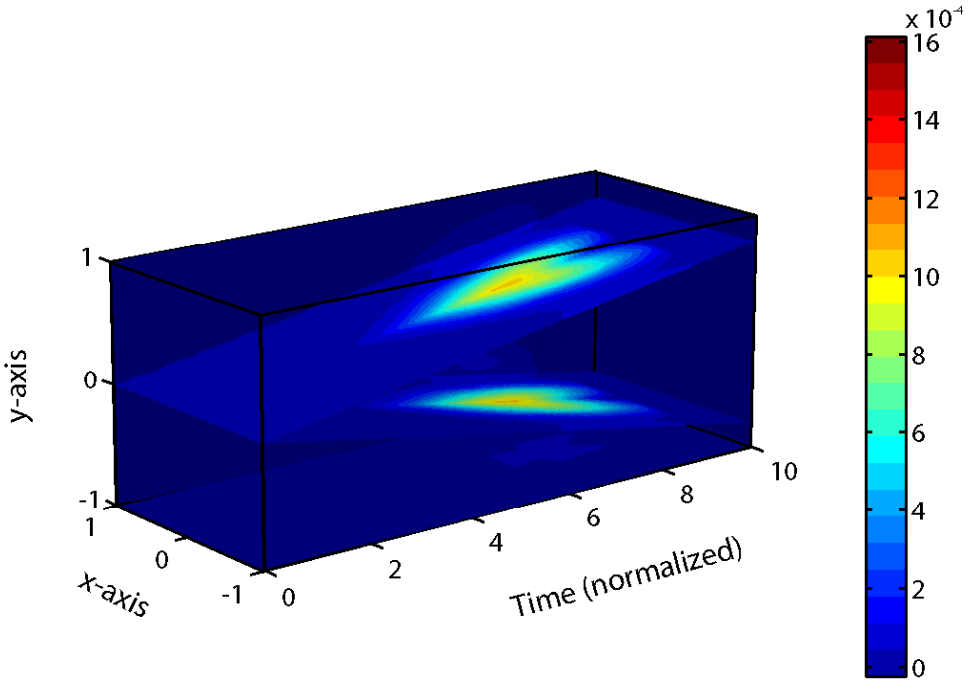

Figure 6.9: Variation of irradiance with time, x coordinate and y coordinate at $\bar{z} = 2$ for 3D PTE, using Laguerre DOM.

should take for the decay to start. This difference in Fig. 6.7 and Fig. 6.11 may be due to the strong numerical diffusion and false propagation in Transient DOM of Guo and Kumar [2]. In reference [2] the authors state that an obvious disadvantage of transient analysis using their method is that numerical diffusion and false propagation are inevitable. In order to minimize numerical diffusion, the spatial grid and the time step are required to be as fine as possible. The size of time step affects the transient behavior. Figures 3 and 4 in reference [2] show influences of time step and spatial grid on the temporal behavior, with a comparison to Monte Carlo simulations. Figure 3 clearly shows that the Transient DOM cannot capture the abrupt rise of transmittance in the early time period. In Laguerre DOM, however, there is no discretization in timescale. The entire time domain of the input pulse is represented as a truncated series of Laguerre polynomials and then the

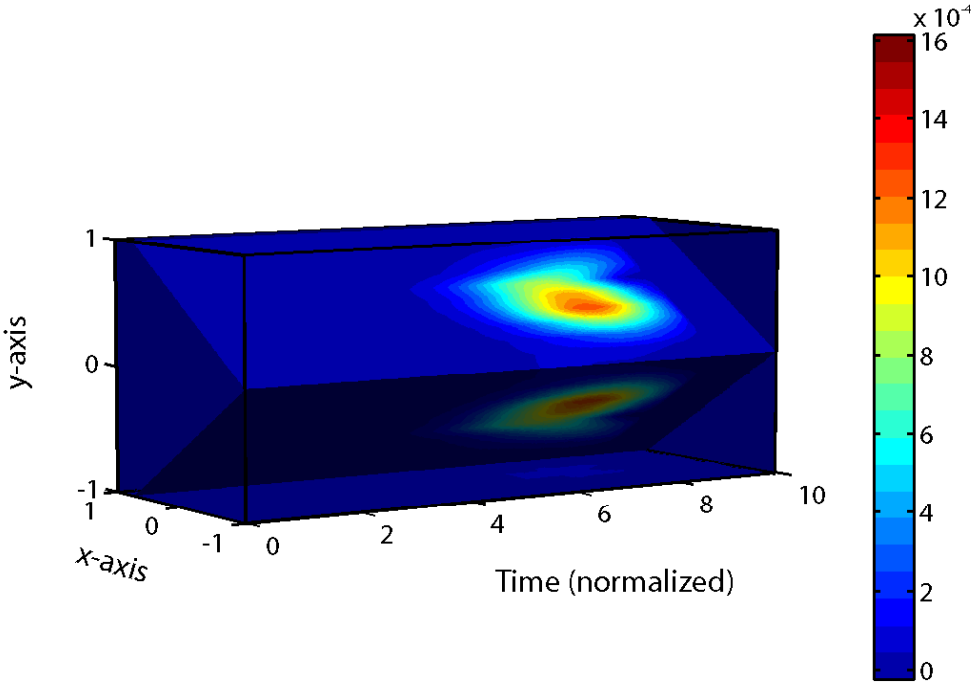

Figure 6.10: Variation of irradiance with time, x coordinate and y coordinate at $\bar{z} = 2$ for 3D PTE, using Laguerre DOM.

PTE is solved for each Laguerre coefficient separately. Also, by using the substitution in Eq. (6.2) the PTE is mapped to a moving reference frame with the pulse.

In reference [2], the authors have used Duhamel's superposition theorem, which can only be applied to linear systems, to incorporate the time-dependent boundary conditions. This theorem relates the solution of the problem subject to the time-dependent boundary condition to the solution subject to time-independent unit step input. The Laguerre DOM represents the time-dependency of the boundary condition using a Laguerre expansion. Then, a set of time-independent equations corresponding to each Laguerre coefficient is solved separately using DOM. Thus, one possible explanation for the difference in temporal and spatial irradiance profiles might be the strong numerical diffusion and false propagation in

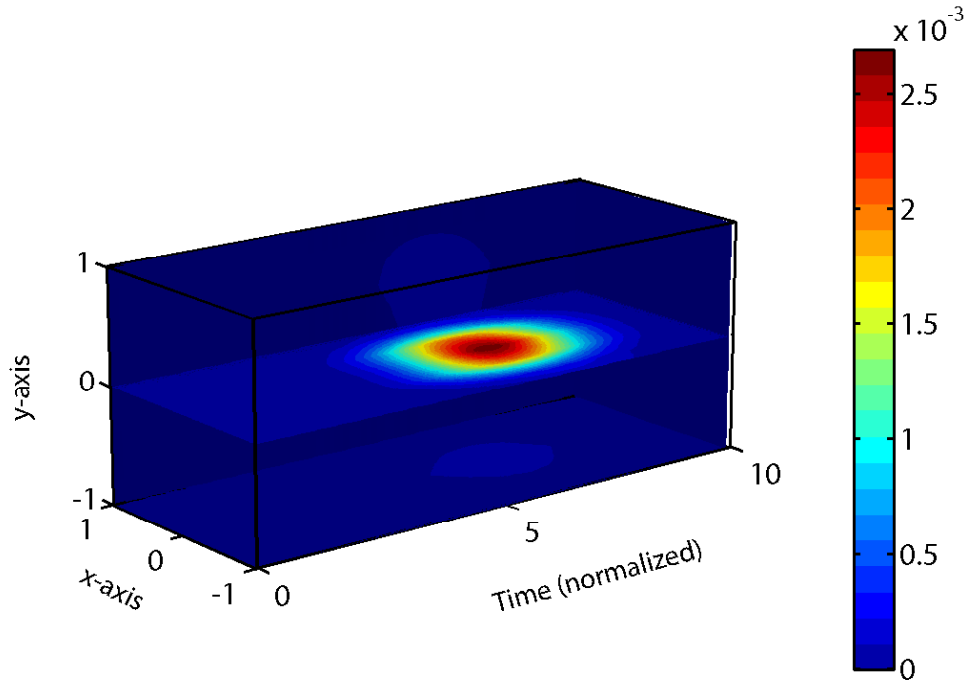

Figure 6.11: Variation of irradiance with time, x coordinate and y coordinate at $\overline{z} = 2$ for 3D PTE, using Transient DOM (Slice plane at $\overline{y} = 0, \overline{z} = 2$).

Transient DOM of Guo and Kumar [2].

6.4 Conclusions

This chapter has introduced a novel technique for modeling multi-dimensional transient photon transport for applications in bio-sensing and in short pulse propagation through turbid media. The proposed method uses a transformation to eliminate the transient term in the transient PTE. It then expands the radiance using a Laguerre basis to automatically account for causality while providing an efficient basis suitable for calculations. This reduces the original transient PTE to a steady state version. Hence, the discrete ordinates method, using a finite volume approach can be used to solve for the radiance.

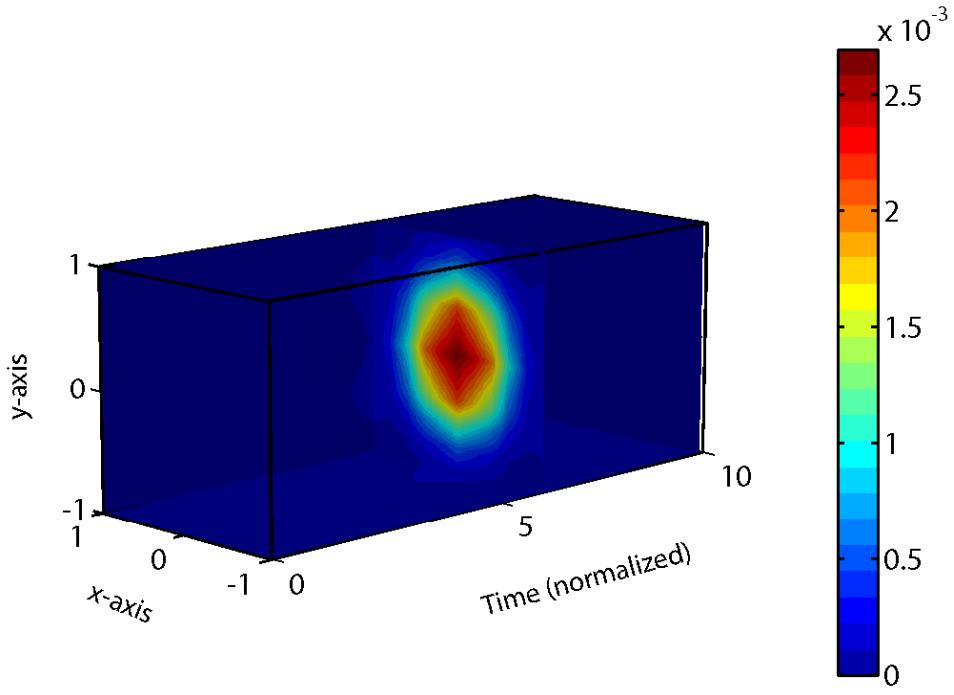

Figure 6.12: Variation of irradiance with time, x coordinate and y coordinate at $\bar{z} = 2$ for 3D PTE, using Transient DOM (Slice plane at $\bar{z} = 2, \bar{t} = 6$).

Since the time dependence is expanded using a Laguerre basis, all the sampling points in the time domain are obtained in a single execution, as opposed to the time marching techniques used in existing solution methods. This makes the proposed algorithm much faster when the intensity profile is required at a particular point or a plane over a time interval. In addition, the use of the Laguerre expansion to represent time dependency enables modeling the system with any arbitrary input pulse shape, using only a few Laguerre polynomials. Specifically, the Gaussian pulse shape used in many practical applications can be accurately represented using a few Laguerre polynomials, as opposed to the discrete sampling used in most existing models. Also, this expansion implicitly imposes the causality of the system.

6.5 References

[1] K. F. Evans, "The spherical harmonics discrete ordinate method for three-dimensional atmospheric radiative transfer," *Journal of Atmospheric Science*, vol. 55, pp. 429–446, 1998.

[2] Z. Guo and S. Kumar, "Three-dimensional discrete ordinates method in transient radiative transfer," *Journal of Thermophysics and Heat Transfer*, vol. 16, no. 3, pp. 289–296, 2002.

[3] G. L. Stephens, "Radiative transfer through arbitrarily shaped optical media. Part I: A general method of solution," *Journal of Atmospheric Science*, vol. 45, no. 12, pp. 1818–1836, 1988.

[4] Z. M. Tan and P. F. Hsu, "Transient radiative transfer in three-dimensional homogeneous and non-homogeneous participating media," *Journal of Quantitative Spectroscopy & Radiative Transfer*, vol. 73, pp. 181–194, 2002.

[5] C. C. Handapangoda, M. Premaratne, D. M. Paganin, and P. R. D. S. Hendahewa, "Technique for handling wave propagation specific effects in biological tissue: Mapping of the photon transport equation to Maxwell's equations," *Optics Express*, vol. 16, no. 22, pp. 17 792–17 807, 2008.

[6] K. W. Johnson, J. J. Mastrototaro, D. C. Howey, R. L. Brunelle, P. L. Burden-Brady, N. A. Bryan, C. C. Andrew, H. M. Rowe, D. J. Allen, B. W. Noffke, W. C. McMahan, R. J. Morff, D. Lipson, and R. S. Nevin, "In vivo evaluation of an electroenzymatic glucose sensor implanted in subcutaneous tissue," *Biosensors and Bioelectronics*, vol. 7, pp. 709–714, 1992.

[7] D. Moatti-Sirat, F. Capron, V. Poitout, G. Reach, D. S. Bindra, Y. Zhang, G. S. Wilson, and D. R. Thevenot, "Towards continuous glucose monitoring: In vivo evaluation of a miniaturized glucose sensor implanted for several days in rat subcutaneous tissue," *Diabetologia*, vol. 35, pp. 224–230, 1992.

[8] V. Poitout, D. Moatti-Sirat, G. Reach, Y. Zhang, G. S. Wilson, F. Lemonnier, and J. C. Klein, "A glucose monitoring system for on line estimation in man of blood glucose concentration using a miniaturized glucose sensor implanted in the subcutaneous tissue and a wearable control unit," *Diabetologia*, vol. 36, pp. 658–663, 1993.

[9] C. C. Handapangoda, M. Premaratne, and D. M. Paganin, "Simulation of a device concept for noninvasive sensing of blood glucose levels," in *Information and Automation for Sustainability (ICIAFS), 2007. Third International Conference*, Melbourne, Australia, December 2007, pp. 31–34.

[10] ——, "Simulation of embedded photonic crystal structures for blood glucose measurement using Raman spectroscopy," in *2008 International Conference on Nanoscience and Nanotechnology*, Melbourne, Australia, February 2008.

[11] Z. Guo and K. Kim, "Ultrafast-laser-radiation transfer in heterogeneous tissues with the discrete ordinates method," *Applied Optics*, vol. 42, no. 16, pp. 2897–2905, 2003.

[12] J. C. Chai, P. F. Hsu, and Y. C. Lam, "Three-dimensional transient radiative transfer modeling using the finite-volume method," *Journal of Quantitative Spectroscopy & Radiative Transfer*, vol. 86, pp. 299–313, 2004.

[13] A. Sawetprawichkul, P. F. Hsu, and K. Mitra, "Parallel computing of three-dimensional Monte Carlo simulation of transient radiative transfer in participating media," in *Proceedings of the 8th AIAA/ASME Joint Thermophysics and Heat Transfer Conference*. St. Louis, Missouri: American Institute of Aeronautics and Astronautics, 2002, pp. 1–10.

[14] J. V. P. de Oliveira, A. V. Cardona, M. T. Vilhena, and R. C. Barros, "A semi-analytical numerical method for time-dependent radiative transfer problems in slab geometry with coherent isotropic scattering," *Journal of Quantitative Spectroscopy & Radiative Transfer*, vol. 73, pp. 55–62, 2002.

[15] M. F. Modest, *Radiative Heat Transfer*, 2nd ed. Boston: Academic Press, 2003, ch. The method of discrete ordinates, pp. 513–522.

[16] C. C. Handapangoda and M. Premaratne, "Implicitly causality enforced solution of multidimensional transient photon transport equation," *Optics Express*, vol. 17, no. 26, pp. 23 423–23 442, 2009.

[17] S. Chandrasekhar, *Radiative Transfer*. New York: Dover Publications, 1960.

[18] K. D. Lathrop, "Spatial differencing of the transport equation: Positive vs accuracy," *Journal of Computational Physics*, vol. 4, no. 4, pp. 475–498, 1968.

[19] W. A. Fiveland, "Three-dimensional radiative heat-transfer solutions by the discrete ordinates method," *Journal of Thermophysics and Heat Transfer*, vol. 2, no. 4, pp. 309–316, 1988.

[20] S. C. Chapra and R. P. Canale, *Numerical Methods for Engineers*, 4th ed. New York: McGraw-Hill, 2002.

[21] C. C. Handapangoda, M. Premaratne, L. Yeo, and J. Friend, "Laguerre Runge–Kutta–Fehlberg method for simulating laser pulse propagation in biological tissue," *IEEE Journal of Selected Topics in Quantum Electronics*, vol. 14, no. 1, pp. 105–112, 2008.

CHAPTER 7

A Numerical Technique for Mapping the Photon Transport Equation to Maxwell's Equations

This chapter presents a technique for mapping the photon transport equation to Maxwell's equations. The phase information required in Maxwell's equations is retrieved from an intensity profile obtained by solving the photon transport equation. The transport-of-intensity equation is solved using the full multigrid algorithm for the purpose of phase retrieval.

7.1 Introduction

OPTICAL techniques in biomedical applications such as optical tomography and light-aided sensing of substances have been the subject of intense interest recently [1]. These techniques of sensing substances in tissue or blood require foreign structures to be implanted (or embedded) in tissue in order to condition the optical signals. Therefore, having a detailed understanding of how light interacts with tissue is required. Owing to its ability to accurately represent light propagation through tissue, wave propagation through biological tissue is modeled using the photon transport equation (PTE) [2, 3]. However, the

interaction of electromagnetic energy through implanted structures can be best studied using Maxwell's equations. Therefore, in order to model wave propagation through tissue with implanted foreign structures a mapping of the PTE to Maxwell's equations is required.

This chapter proposes a technique to map the photon transport equation to Maxwell's equations using phase-retrieval techniques. To the author's best knowledge no work has been reported to date which addresses the problem of coupling these two sets of equations. The maximum safe exposure of laser light for the skin is $0.1\,\mathrm{J/cm^2}$ per pulse or $1.0\,\mathrm{W/cm^2}$ for continuous exposure [4]. However, structures such as photonic crystals can be implanted to obtain enhanced signals by properly engineering the photon density of states. The technique proposed in this chapter can be used to model such foreign structures implanted in tissue. The work presented in this chapter has been published in Optics Express [5].

This chapter is organized in five sections. Section 7.2 presents the derivation of the transport of intensity equation for phase construction. Section 7.3 discusses how the phase information is constructed from the irradiance profile. Section 7.4 concludes the chapter by summarizing the key features and advantages of the proposed technique.

7.2 Derivation of the transport of intensity equation for phase construction

The transport of intensity equation (TIE) relates phase and intensity and hence can be used to construct the unknown phase from known intensity values. In this section, the derivation of the TIE is presented.

The following identities are used in this derivation:

$$\nabla \times [\nabla \times \mathbf{f}] = \nabla[\nabla \cdot \mathbf{f}] - \nabla^2 \mathbf{f}. \tag{7.1}$$

$$\nabla \times [g\mathbf{f}] = g[\nabla \times \mathbf{f}] + [\nabla g] \times \mathbf{f}. \tag{7.2}$$

$$\nabla^2[ab] = a\nabla^2 b + b\nabla^2 a + 2\nabla a \cdot \nabla b. \tag{7.3}$$

The derivation starts with Maxwell's equations given below.

$$\nabla \times \mathbf{E}(x,y,z,t) + \frac{\partial}{\partial t}\mathbf{B}(x,y,z,t) = \mathbf{0}, \tag{7.4}$$

$$\nabla \times \mathbf{H}(x,y,z,t) - \frac{\partial}{\partial t}\mathbf{D}(x,y,z,t) = \mathbf{J}(x,y,z,t), \tag{7.5}$$

$$\nabla \cdot \mathbf{D}(x,y,z,t) = \rho(x,y,z,t), \tag{7.6}$$

$$\nabla \cdot \mathbf{B}(x,y,z,t) = 0, \tag{7.7}$$

where $\nabla = \left(\frac{\partial}{\partial x}\mathbf{i} + \frac{\partial}{\partial y}\mathbf{j} + \frac{\partial}{\partial z}\mathbf{k}\right)$, $\mathbf{D}$ is the electric flux density, $\mathbf{B}$ is the magnetic flux density, $\mathbf{E}$ is the electric field, $\mathbf{H}$ is the magnetic field, ρ is the charge density, $\mathbf{J}$ is the current density, (x,y,z) are Cartesian coordinates and t is time. For linear, isotropic materials $\mathbf{D} = \varepsilon\mathbf{E}$ and $\mathbf{B} = \mu\mathbf{H}$ where ε is the electrical permitivity and μ is the magnetic permeability of the medium. For static materials ε and μ are independent of time and for non-magnetic materials μ is a constant, which is approximately equal to the magnetic permeability of free space (μ_0) for most materials. Therefore, for a static, non-magnetic material without any current or charge densities (i.e. $\mathbf{J} = \mathbf{0}$ and $\rho = 0$), Maxwell's equations reduce to:

$$\nabla \times \mathbf{E}(x,y,z,t) + \mu_0 \frac{\partial}{\partial t}\mathbf{H}(x,y,z,t) = \mathbf{0}, \tag{7.8}$$

$$\nabla \times \mathbf{H}(x,y,z,t) - \varepsilon(x,y,z)\frac{\partial}{\partial t}\mathbf{E}(x,y,z,t) = \mathbf{0}, \tag{7.9}$$

$$\varepsilon(x,y,z)\nabla \cdot \mathbf{E}(x,y,z,t) = 0, \tag{7.10}$$

$$\mu_0 \nabla \cdot \mathbf{H}(x,y,z,t) = 0. \tag{7.11}$$

Taking curl on both sides of Eq. (7.8) results in

$$\nabla \times [\nabla \times \mathbf{E}(x,y,z,t) + \mu_0 \frac{\partial}{\partial t}\mathbf{H}(x,y,z,t)] = \nabla \times \mathbf{0},$$
$$\nabla \times [\nabla \times \mathbf{E}(x,y,z,t)] + \mu_0 \nabla \times [\frac{\partial}{\partial t}\mathbf{H}(x,y,z,t)] = \mathbf{0}. \tag{7.12}$$

Use of the vector identity given by Eq. (7.1) in Eq. (7.12) results in

$$\nabla[\nabla \cdot \mathbf{E}(x,y,z,t)] - \nabla^2 \mathbf{E}(x,y,z,t) + \mu_0 \frac{\partial}{\partial t}\nabla \times \mathbf{H}(x,y,z,t) = \mathbf{0}. \tag{7.13}$$

Use of Eq. (7.10) in Eq. (7.13) results in

$$\mu_0 \frac{\partial}{\partial t}\nabla \times \mathbf{H}(x,y,z,t) - \nabla^2 \mathbf{E}(x,y,z,t) = \mathbf{0}. \tag{7.14}$$

Taking curl on both sides of Eq. (7.9) results in

$$\nabla \times [\nabla \times \mathbf{H}(x,y,z,t) - \varepsilon(x,y,z)\frac{\partial}{\partial t}\mathbf{E}(x,y,z,t)] = \nabla \times \mathbf{0}$$
$$\text{i.e. } \nabla \times [\nabla \times \mathbf{H}(x,y,z,t)] - \frac{\partial}{\partial t}\nabla \times [\varepsilon(x,y,z)\mathbf{E}(x,y,z,t)] = \mathbf{0}. \tag{7.15}$$

Use of the vector identity given by Eq. (7.1) in Eq. (7.15) results in

$$\nabla[\nabla \cdot \mathbf{H}(x,y,z,t)] - \nabla^2 \mathbf{H}(x,y,z,t) - \frac{\partial}{\partial t}\nabla \times [\varepsilon(x,y,z)\mathbf{E}(x,y,z,t)] = \mathbf{0}. \tag{7.16}$$

Use of Eq. (7.11) in Eq. (7.16) results in

$$\nabla^2 \mathbf{H}(x,y,z,t) + \frac{\partial}{\partial t}\nabla \times [\varepsilon(x,y,z)\mathbf{E}(x,y,z,t)] = \mathbf{0}. \tag{7.17}$$

Use of the vector identity given by Eq. (7.2) in Eq. (7.17) results in

$$\nabla^2 \mathbf{H}(x,y,z,t) + \frac{\partial}{\partial t}\left[\varepsilon(x,y,z)\nabla \times \mathbf{E}(x,y,z,t) + [\nabla \varepsilon(x,y,z)] \times \mathbf{E}(x,y,z,t)\right] = \mathbf{0}.$$

$$\text{i.e. } \nabla^2\mathbf{H}(x,y,z,t) + \varepsilon(x,y,z)\frac{\partial}{\partial t}\nabla\times\mathbf{E}(x,y,z,t) + [\nabla\varepsilon(x,y,z)]\times\frac{\partial}{\partial t}\mathbf{E}(x,y,z,t) = \mathbf{0}. \tag{7.18}$$

Taking time derivative on both sides of Eq. (7.8) results in

$$\frac{\partial}{\partial t}\nabla\times\mathbf{E}(x,y,z,t) + \mu_0\frac{\partial^2}{\partial t^2}\mathbf{H}(x,y,z,t) = \mathbf{0}. \tag{7.19}$$

Taking time derivative on both sides of Eq. (7.9) results in

$$\frac{\partial}{\partial t}\nabla\times\mathbf{H}(x,y,z,t) - \varepsilon(x,y,z)\frac{\partial^2}{\partial t^2}\mathbf{E}(x,y,z,t) = \mathbf{0}. \tag{7.20}$$

Use of Eq. (7.9) and Eq. (7.19) in Eq. (7.18) results in

$$\nabla^2\mathbf{H}(x,y,z,t) - \mu_0\varepsilon(x,y,z)\frac{\partial^2}{\partial t^2}\mathbf{H}(x,y,z,t) + [\nabla\varepsilon(x,y,z)]\times\frac{1}{\varepsilon(x,y,z)}\nabla\times\mathbf{H}(x,y,z,t) = \mathbf{0}.$$

$$\text{i.e. } \left[\varepsilon(x,y,z)\mu_0\frac{\partial^2}{\partial t^2} - \nabla^2\right]\mathbf{H}(x,y,z,t) = \frac{1}{\varepsilon(x,y,z)}[\nabla\varepsilon(x,y,z)]\times\nabla\times\mathbf{H}(x,y,z,t). \tag{7.21}$$

Use of Eq. (7.20) in Eq. (7.14) results in

$$\varepsilon(x,y,z)\mu_0\frac{\partial^2}{\partial t^2}\mathbf{E}(x,y,z,t) - \nabla^2\mathbf{E}(x,y,z,t) = \mathbf{0}.$$

$$\text{i.e. } \left[\varepsilon(x,y,z)\mu_0\frac{\partial^2}{\partial t^2} - \nabla^2\right]\mathbf{E}(x,y,z,t) = \mathbf{0}. \tag{7.22}$$

If the scatterers slowly vary over length scales comparable to the wavelength of the incident radiation, the right hand side of Eq. (7.21) can be neglected [6]. Hence, for a static (i.e. the electrical permittivity and the magnetic permeability are independent of time), non-magnetic (i.e. with constant permeability) medium without any current or charge densities inside, and with scatterers which slowly vary over length scales comparable to the wavelength of the incident radiation,

the Maxwell's equations can be reduced to

$$\left[\varepsilon(x,y,z)\mu_0\frac{\partial^2}{\partial t^2}-\nabla^2\right]\mathbf{E}(x,y,z,t)=\mathbf{0}, \tag{7.23}$$

and

$$\left[\varepsilon(x,y,z)\mu_0\frac{\partial^2}{\partial t^2}-\nabla^2\right]\mathbf{H}(x,y,z,t)=\mathbf{0}. \tag{7.24}$$

From Eq. (7.23) and Eq. (7.24), since there is no mixing between any of the components of the electric and the magnetic field vectors, a scalar theory [6] can be used. Thus,

$$\left[\varepsilon(x,y,z)\mu_0\frac{\partial^2}{\partial t^2}-\nabla^2\right]\Psi(x,y,z,t) \;=\; 0. \tag{7.25}$$

In Eq. (7.25) $\Psi(x,y,z,t)$ describes the electromagnetic field and it is a complex quantity. Using the Fourier integral $\Psi(x,y,z,t)$ can be expressed as [6]

$$\Psi(x,y,z,t) \;=\; \frac{1}{\sqrt{2\pi}}\int_0^\infty \psi_\omega\,(x,y,z)\,e^{-j\omega t}\,d\omega, \tag{7.26}$$

where ω is the angular frequency. Use of Eq. (7.26) in Eq. (7.25) results in

$$\left[\nabla^2+\varepsilon_\omega(x,y,z)\mu_0c^2k_0^2\right]\psi_\omega\,(x,y,z) \;=\; 0, \tag{7.27}$$

where $\nabla^2=\left(\frac{\partial^2}{\partial x^2}+\frac{\partial^2}{\partial y^2}+\frac{\partial^2}{\partial z^2}\right)$, c is the speed of light in free space and $k_0=\omega/c$ is the wave number in free space. Then, identifying $\varepsilon_\omega(x,y,z)\mu_0c^2$ as the square of the position-dependent refractive index, $n_\omega(x,y,z)$, of the medium, Eq. (7.27) can be re-written as

$$\left[\nabla^2+{k_0}^2n_\omega^2(x,y,z)\right]\psi_\omega\,(x,y,z) \;=\; 0, \tag{7.28}$$

which is called the homogeneous Helmholtz equation [6].

In order to incorporate scattering, $\psi_\omega(x,y,z)$ in Eq. (7.28) is expressed as a perturbed plane wave [6]:

$$\psi_\omega(x,y,z) = \widetilde{\psi}_\omega(x,y,z)\, e^{jkz}, \tag{7.29}$$

where e^{jkz} represents the unscattered plane wave and $\widetilde{\psi}_n(x,y,z)$ represents the complex envelope [7]. That is, the paraxial condition is considered here where the rays are not exactly parallel to each other; or in other words, a field with perturbed wave fronts. Use of Eq. (7.29) in Eq. (7.28) results in

$$\nabla^2\left(\widetilde{\psi}_\omega(x,y,z)\, e^{jkz}\right) + k_0^2 n_\omega^2(x,y,z)\,\widetilde{\psi}_\omega(x,y,z)\, e^{jkz} = 0. \tag{7.30}$$

Use of the identity given by Eq. (7.3) in Eq. (7.30) and simplifying results in [6]

$$\left[\nabla_{xy}^2 + \frac{\partial^2}{\partial z^2} + 2jk_0\frac{\partial}{\partial z} + k_0^2\left(n_\omega^2(x,y,z) - 1\right)\right]\widetilde{\psi}_\omega(x,y,z) = 0, \tag{7.31}$$

where $\nabla_{xy}^2 = \left(\frac{\partial^2}{\partial x^2} + \frac{\partial^2}{\partial y^2}\right)$. With the paraxial approximation the envelope, $\widetilde{\psi}_\omega(x,y,z)$, is considered to be "beam-like" so that its second derivative in the z direction is much smaller in magnitude than its second derivative in the x and y directions. Therefore, the $\frac{\partial^2}{\partial z^2}\widetilde{\psi}_\omega(x,y,z)$ term in Eq. (7.31) can be dropped. Then Eq. (7.31) reduces to

$$\left[\nabla_{xy}^2 + 2jk_0\frac{\partial}{\partial z} + k_0^2\left(n_\omega^2(x,y,z) - 1\right)\right]\widetilde{\psi}_\omega(x,y,z) = 0. \tag{7.32}$$

Let

$$\widetilde{\psi}_\omega(x,y,z) = \sqrt{I}e^{j\phi}. \tag{7.33}$$

Here, I represents the irradiance (units: W.m^{-2}.Hz^{-1}) and ϕ represents the phase.

Using Eq. (7.33) in Eq. (7.32) and separating the imaginary part results in the following relationship [6, 8]:

$$\nabla_{xy} \cdot \left(I\left(x,y,z\right) \nabla_{xy} \phi\left(x,y,z\right) \right) = -k \frac{\partial I\left(x,y,z\right)}{\partial z}. \tag{7.34}$$

Equation (7.34) is called the transport-of-intensity equation (TIE). It shows how the intensity and the phase are related, and this forms the basis of the phase construction. The next section discusses how to retrieve the phase information from the intensity profile by solving Eq. (7.34).

7.3 Construction of phase information from the irradiance profile

To construct the phase the TIE in Eq. (7.34) is re-written as

$$I\left(x,y,z\right) \nabla_{xy}^2 \phi\left(x,y,z\right) + \frac{\partial I\left(x,y,z\right)}{\partial x} \frac{\partial \phi\left(x,y,z\right)}{\partial x} + \frac{\partial I\left(x,y,z\right)}{\partial y} \frac{\partial \phi\left(x,y,z\right)}{\partial y} = -k \frac{\partial I\left(x,y,z\right)}{\partial z}. \tag{7.35}$$

Equation (7.35) can be solved for $\phi\left(x,y,z\right)$ numerically using a suitable technique such as the full multigrid algorithm [9, 10], a Green-function method [8] or a fast-Fourier-transform-based method [11, 12].

Of these techniques for solving the TIE, the full multigrid algorithm [9, 10, 13], which solves the TIE exactly is adopted in the present work. Equation (7.35) is a linear, elliptic partial differential equation of the second order and has a unique solution if $I\left(x,y,z\right) > 0$ over a simply-connected planar region [14].

The full multigrid algorithm used in this work is briefly described below, as explained in reference [13]. Further details of this algorithm can be obtained from

reference [13]. Equation (7.35) can be expressed as

$$\Gamma u = f, \tag{7.36}$$

where $\Gamma = \left(I\left(x,y,z\right) \nabla_{xy}^2 + \frac{\partial I(x,y,z)}{\partial x}\frac{\partial}{\partial x} + \frac{\partial I(x,y,z)}{\partial y}\frac{\partial}{\partial y} \right)$, $u = \phi\left(x,y,z\right)$ and $f = -k\frac{\partial I(x,y,z)}{\partial z}$. In multigrid methods, the original equation is discretized on a uniform grid. Equation (7.35) can be discretized as follows:

$$\begin{aligned} &\left(\frac{I_{i+1,j} - I_{i-1,j}}{2\Delta}\right)\left(\frac{\phi_{i+1,j} - \phi_{i-1,j}}{2\Delta}\right) + \left(\frac{I_{i,j+1} - I_{i,j-1}}{2\Delta}\right)\left(\frac{\phi_{i,j+1} - \phi_{i,j-1}}{2\Delta}\right) \\ &+ I_{i,j}\left(\frac{\phi_{i-1,j} + \phi_{i,j-1} + \phi_{i+1,j} + \phi_{i,j+1} - 4\phi_{i,j}}{\Delta^2}\right) = f_{i,j}, \end{aligned} \tag{7.37}$$

where $i = 1, \ldots, M$, $j = 1, \ldots, M$ for $M \times M$ grid points. Also, $I_{i,j} = I\left(x_i, y_j, z\right)$, $\phi_{i,j} = \phi\left(x_i, y_j, z\right)$, $\Delta = x_{i+1} - x_i = y_{j+1} - y_j$ and $f_{i,j} = -k\frac{\partial I\left(x_i,y_j,z\right)}{\partial z}$. By solving the PTE on two closely separated planes $z = z$ and $z = z + \delta z$, two intensity profiles are obtained. Thus, the following approximations can be used in Eq. (7.37).

$$I\left(x,y,z\right) \approx \frac{I\left(x,y,z+\delta z\right) + I\left(x,y,z\right)}{2}, \tag{7.38}$$

and

$$\frac{\partial I\left(x,y,z\right)}{\partial z} \approx \frac{I\left(x,y,z+\delta z\right) - I\left(x,y,z\right)}{\delta z}. \tag{7.39}$$

In Eq. (7.38) and Eq. (7.39) I represents the irradiance. However, the PTE solves for the radiance, I_{PTE}. I and I_{PTE} are related by

$$I = \int_{2\pi} I_{PTE} \cos\theta \, d\Omega, \tag{7.40}$$

where θ is the zenith angle in a spherical coordinate system and $d\Omega$ is an infinitesimal solid angle [15, 16]. This conversion of the intensity is required because in the PTE the ray model of optics is used, but in Maxwell's equations the wave model is used; and these two models deal with different definitions of intensity,

radiance and irradiance, respectively.

Since the intensity and its partial derivatives with respect to x, y and z can be approximately calculated from the two intensity profiles, as shown in Eq. (7.38) and Eq. (7.39), the only unknown in Eq. (7.37) is $\phi_{i,j}$. Hence, the full multigrid algorithm can be used to solve Eq. (7.37) for $\phi_{i,j}$ and thus the phase can be retrieved on each grid point.

Equation (7.36) can be discretized on a uniform grid with mesh size h as

$$\Gamma_h u_h = f_h. \tag{7.41}$$

If $\tilde{u}_h$ denotes an approximate solution to Eq. (7.41), then the error in $\tilde{u}_h$ is

$$v_h = u_h - \tilde{u}_h, \tag{7.42}$$

and the residual or the defect is

$$d_h = \Gamma \tilde{u}_h - f_h. \tag{7.43}$$

Since Γ_h is a linear operator, the error satisfies

$$\Gamma_h v_h = -d_h. \tag{7.44}$$

In order to find the next approximate solution, Γ_h should be approximated in order to find v_h. Classical iteration methods, such as Jacobi or Gauss-Seidel can be used to do this. The next approximation is generated by

$$\tilde{u}_h^{new} = \tilde{u}_h + v_h. \tag{7.45}$$

Next, an appropriate approximation Γ_H of Γ_h is formed on a coarser grid with mesh size H. Then the residual equation, Eq. (7.44), is approximated by

$$\Gamma_H v_H = -d_H. \tag{7.46}$$

Since Γ_H has smaller dimensions, Eq. (7.46) is easier to solve than Eq. (7.44). In the full multigrid algorithm, the first approximation is obtained by interpolating from a coarse-grid solution and at the coarsest level the algorithm starts with the exact solution [13]. Using the full multigrid algorithm as detailed above Eq. (7.36) can be solved for u. Thus, the phase at each grid point, $\phi_{i,j}$ is retrieved.

Regarding the validity and accuracy of deterministic phase retrieval using the transport-of-intensity equation, Eq. (7.34), the following three remarks can be made.

1. The TIE has been widely employed for quantitative phase retrieval using monochromatic and polychromatic electromagnetic fields in both the visible-light and X-ray region, given a series of defocused intensity images. The TIE has also been successfully solved for the phase using matter waves such as electrons and neutrons. A review of this work can be found in reference [17].
2. Since the TIE is the continuity equation associated with the paraxial equation [8], an exact solution to which is furnished by the Fresnel diffraction integral [6], its regime of validity is restricted to paraxial beam-like fields. Interestingly, it may be used with both coherent and partially-coherent fields, a point which has been studied from both a theoretical [18] and an experimental [19] perspective.
3. Errors in the phase retrieved using a TIE analysis are primarily due to two sources: the finite-difference approximation to the right-hand-side of the

TIE (Eq. (7.34)) that is given in Eq. (7.39), together with the presence of noise in the detected images. While the latter factor is irrelevant in the context of the analysis presented in this chapter, errors in the retrieved phase due to the former effect need to be considered. For an analysis of both factors, see reference [20]. The upshot of this analysis is that the error in the TIE-retrieved phase, due to a non-infinitesimal spacing δz (cf. Eq. (7.39)), leads to a blurring of the retrieved phase which becomes negligibly small if δz tends to zero from above. Reference [20] develops an expression for the optimal δz in the presence of a given level of noise, this optimal defocus distance being proportional to the cube root of the standard deviation of the noise.

Typical reconstruction accuracies from experiments involving TIE-based phase retrieval are in the order of 1-5% [6, 19].

7.4 Conclusions

This chapter introduced a novel strategy by which Maxwell's equations and the photon transport equation can be seamlessly integrated to analyze electromagnetic radiation in tissue-like media. In this technique, radiance profiles on two planes that are separated by an infinitesimal distance, obtained by solving the PTE, are first converted to two irradiance profiles. The phase information at the tissue-implant interface is then retrieved using this information using a phase retrieval technique. This retrieved phase information and the irradiance profile on one of the planes are then combined to determine the electric and magnetic fields at the interface. Light propagation through the implant can then be modeled using Maxwell's equations. By using this technique it is possible to analyze diffraction effects within the framework of photon transport theory.

The proposed technique can be used to assist the development of biomedical instruments that can be used for non-invasive diagnosis of diseases. Moreover, it enables the calculation of the light energy distribution within tissue structures with surgically-implanted foreign structures.

7.5 References

[1] S. Kumar, K. Mitra, and Y. Yamada, "Hyperbolic damped-wave models for transient light-pulse propagation in scattering media," *Applied Optics*, vol. 35, pp. 3372–3378, 1996.

[2] M. Premaratne, E. Premaratne, and A. J. Lowery, "The photon transport equation for turbid biological media with spatially varying isotropic refractive index," *Optics Express*, vol. 13, pp. 389–399, 2005.

[3] C. C. Handapangoda, M. Premaratne, L. Yeo, and J. Friend, "Laguerre Runge-Kutta-Fehlberg method for simulating laser pulse propagation in biological tissue," *IEEE Journal of Selected Topics in Quantum Electronics*, vol. 14, pp. 105–112, 2008.

[4] W. D. Burnett, "Evaluation of laser hazards to the eye and the skin," *American Industrial Hygiene Association Journal*, vol. 30, pp. 582–587, 1969.

[5] C. C. Handapangoda, M. Premaratne, D. M. Paganin, and P. R. D. S. Hendahewa, "Technique for handling wave propagation specific effects in biological tissue: Mapping of the photon transport equation to Maxwell's equations," *Optics Express*, vol. 16, no. 22, pp. 17 792–17 807, 2008.

[6] D. M. Paganin, *Coherent X-Ray Optics*. New York: Oxford University Press, 2006.

[7] M. Born and E. Wolf, *Principles of Optics*, 7th ed. Cambridge: Cambridge University Press, 1999.

[8] M. R. Teague, "Deterministic phase retrieval: A Green's function solution," *Journal of the Optical Society of America*, vol. 73, pp. 1434–1441, 1983.

[9] T. E. Gureyev, C. Raven, A. Snigireva, I. Snigireva, and S. W. Wilkins, "Hard x-ray quantitative non-interferometric phase-contrast microscopy," *Journal of Physics D: Applied Physics*, vol. 32, pp. 563–567, 1999.

[10] L. J. Allen and M. P. Oxley, "Phase retrieval from series of images obtained by defocus variation," *Optical Communications*, vol. 199, pp. 65–75, 2001.

[11] T. E. Gureyev and K. Nugent, "Phase retrieval with the transport-of-intensity equation. II. Orthogonal series solution for nonuniform illumination," *Journal of Optical Society of America A*, vol. 13, pp. 1670–1682, 1996.

[12] ——, "Rapid quantitative phase imaging using the transport of intensity equation," *Optical Communications*, vol. 133, pp. 339–346, 1997.

[13] W. H. Press, S. A. Teukolsky, W. T. Vetterling, and B. P. Flannery, *Numerical Recipes In C: The Art Of Scientific Computing*, 2nd ed. Cambridge: Cambridge University Press, 1992.

[14] T. E. Gureyev, A. Roberts, and K. A. Nugent, "Partially coherent fields, the transport of intensity equation, and phase uniqueness," *Journal of Optical Society of America A*, vol. 12, pp. 1942–1946, 1995.

[15] K. S. G. E. Thomas, *Radiative Transfer in the Atmosphere and Ocean*. Cambridge: Cambridge University Press, 1999.

[16] R. Ramamoorthi and P. Hanrahan, "On the relationship between radiance and irradiance: determining the illumination from images of a convex lambertian object," *Journal of Optical Society of America A*, vol. 18, pp. 2448–2459, 2001.

[17] D. Paganin and K. A. Nugent, "Non-interferometric phase determination," *Advances in Imaging and Electron Physics*, vol. 118, pp. 85–127, 2001.

[18] ——, "Non-interferometric phase imaging with partially coherent light," *Physical Review Letters.*, vol. 80, pp. 2586–2589, 1998.

[19] A. Barty, K. A. Nugent, D. Paganin, and A. Roberts, "Quantitative optical phase microscopy," *Optics Letters*, vol. 23, pp. 817–819, 1998.

[20] D. Paganin, A. Barty, P. J. McMahon, and K. A. Nugent, "Quantitative phase-amplitude microscopy III: The effects of noise," *Journal of Microscopy*, vol. 214, pp. 51–61, 2004.

CHAPTER 8

Modeling Pulse Propagation through a Metal Screen with a Slit Implanted in Tissue

---

This chapter contains theoretical analysis and numerical simulation of pulse propagation through a slit in a metal screen implanted in tissue. This simulation uses the coupling technique proposed in the previous chapter.

8.1 Introduction

THIS chapter presents an analysis of laser pulse propagation through a slit in a metal screen implanted in tissue. The mapping technique proposed in Chapter 7 to simulate light propagation through structures implanted in tissue can be used for several useful applications. One application of this method is simulating light propagation through photonic crystal structures implanted in tissue. Photonic crystal structures can be used to enhance the efficiency of Raman spectroscopy for detecting concentrations of various molecules in blood or tissue fluid. Another application of the technique proposed in the previous chapter is simulating light propagation through gold nanoshells or nanoneedles embedded

in tissue. These embedded nano-structures are used to treat cancer [1, 2].

In order to demonstrate the applicability and accuracy of the proposed method, a much simpler structure, a metal screen with a slit, is used in this chapter. Even though this example might not have a useful application in terms of medical diagnosis, it helps to present the proposed technique without involving additional complexity that might mask the important aspects of this technique. A detailed analysis of the application of this proposed technique to a more useful and more complicated structure (i.e. a photonic crystal structure) is provided in Appendix B. However, simulation of light propagation through a photonic crystal structure involves extensive work and requires a significant amount of time. Simulation of light propagation through tissue having implanted photonic crystal structures, with gold clusters embedded in them, is recommended as further research in Chapter 9. The analysis presented in this chapter will lead to analyses of more useful and complex implants.

Light propagation in scattering and absorbing media such as biological tissue is modeled by the photon transport equation (PTE) [3, 4] which is written in terms of the magnitude of the intensity but not the phase. Light propagation through a slit in a metal screen is described by Maxwell's equations [5–7], which take into consideration both the magnitude and the phase of the electric and magnetic fields, together with the vectorial character of these fields.

The mapping technique developed in Chapter 7 is used for the simulations here. The work presented in this chapter has been published in Optics Express [8].

This chapter is organized as follows. Section 8.2 carries the theoretical analy-

sis of modeling wave propagation through a metal screen with a slit implanted in tissue. Section 8.3 provides the simulation results for the composite slab of tissue layer and the metal screen with a slit, a discussion of those results and possible extensions of the proposed technique. Section 8.4 concludes the chapter by summarizing the key features and advantages of the proposed technique.

8.2 Theoretical analysis

In this section, the mapping technique proposed in Chapter 7 is applied for analyzing wave propagation through tissue with an implanted metal screen with a slit.

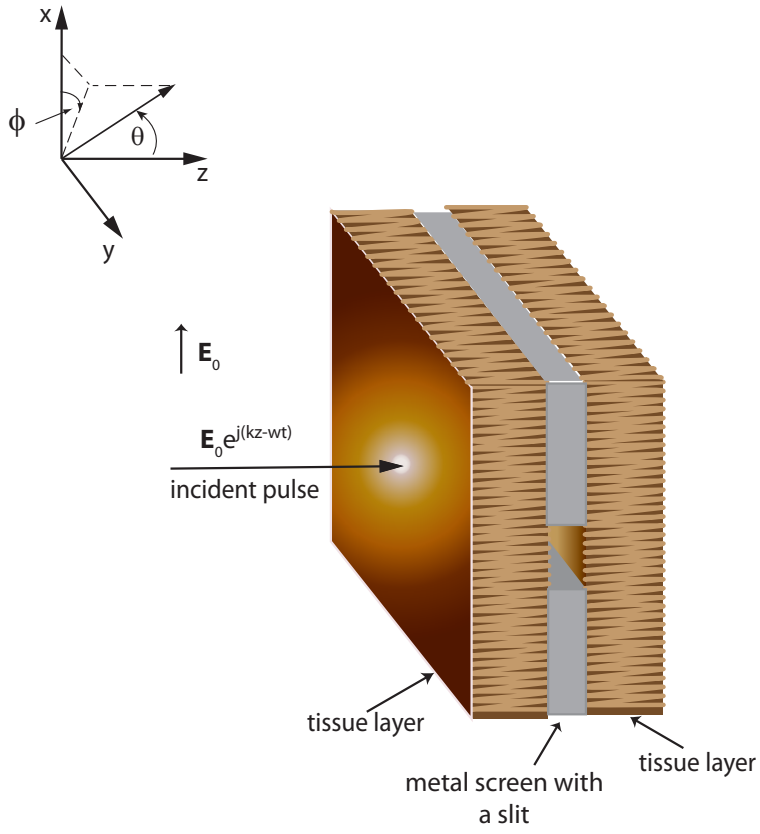

Figure 8.1: Metal screen implanted in biological tissue.

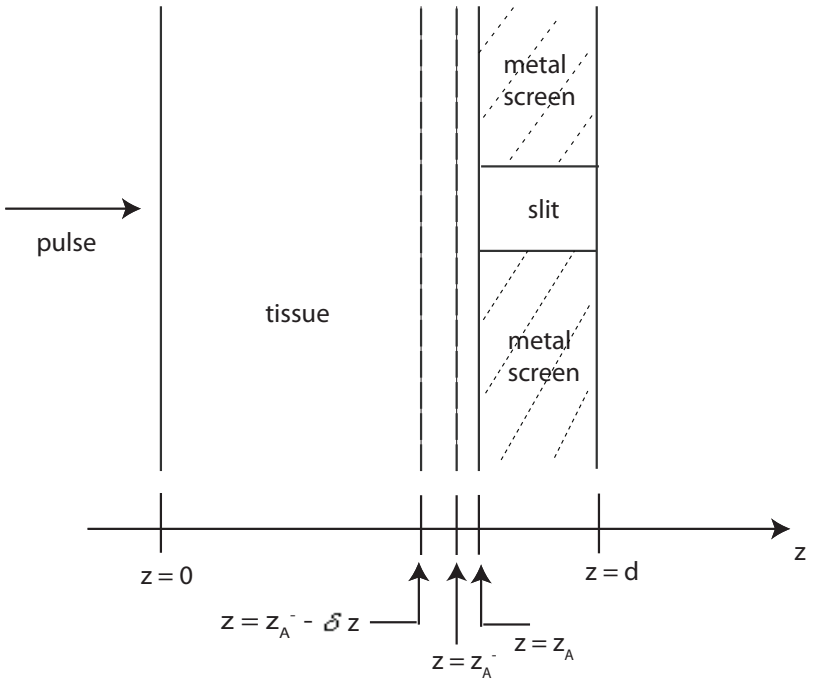

Figure 8.2: End elevation of the tissue-metal screen model.

Figure 8.1 shows a composite object composed of a layer of biological tissue and a layer of a metal screen with a slit, and Fig. 8.2 shows the end elevation of Fig. 8.1. A short laser pulse is incident on the tissue layer as shown. In general, due to the index mismatch at the interface, radiation is reflected. Even though the proposed method can easily handle such reflections at interfaces, due to the increased mathematical complexity in formulation which masks the main points of the proposed algorithm, the analysis is limited to an index-matched surrounding at the left boundary of the tissue layer. A brief discussion of handling index-mismatches is provided in Chapter 4. However, the reflections at the tissue-metal screen interface and metal screen-tissue interface will be taken into consideration with a detailed formulation.

This example focuses on obtaining the magnitude and the phase of the field from the intensity profile at $z = z_A$ and then converting these to the correspond-

ing electric and magnetic fields, so that the field due to the slit in the metal screen can be modeled. Then, at the exit of the metal screen, the electric and magnetic fields can be converted back to the intensity profile so that the tissue layer beyond this plane can be modeled by solving the PTE.

For modeling light propagation through biological tissue, (i.e. up to the tissue-metal screen interface), the PTE, given by Eq. (6.1), is used. Without loss of generality, it is considered that there is no source contained inside the medium which results in $F(z, u, \phi, t) = 0$ in Eq. (6.1).

The solution method proposed in Chapter 6 can be used to solve the PTE from $z = 0$ to $z = z_{A^-}$. Thus, the radiance profile at the plane just before the tissue-metal screen interface (i.e. at $z = z_{A^-}$) is obtained. However, in order to model the propagation of the laser pulse beyond this plane, Maxwell's equations should be used. Maxwell's equations require the phase of the field in addition to the magnitude. Thus, the phase information of the field at $z = z_{A^-}$ should be retrieved in order to model the light propagation through the slit in the metal screen.

In order to apply the phase retrieval technique presented in the previous chapter, first the radiance profile, I_{PTE} obtained by solving Eq. (6.1) should be converted to an irradiance profile I, using the relationship given in Eq. (7.40). Thus, the irradiance at $z = z_{A^-}$, I_{A^-}, and at $z = z_{A^- - \delta z}$, $I_{A^- - \delta z}$, can be obtained by solving the PTE for radiance and integrating over the hemisphere. Then, the approximations given in Eq. (7.38) and Eq. (7.39) are used in order to solve the TIE. That is,

$$I \approx \frac{I_{A^-} + I_{A^- - \delta z}}{2}, \tag{8.1}$$

and

$$\frac{\partial I}{\partial z} \approx \frac{I_{A^-} - I_{A^- - \delta z}}{\delta z}. \tag{8.2}$$

The full multigrid algorithm [9, 10] is then used to solve the TIE, given by Eq. (7.34), for the phase, $\phi(x, y, z)$. Thus, the phase at the tissue-metal screen interface is retrieved using the intensity values at two infinitesimally separated planes.

Once the phase is retrieved, if the incident electric field is known, the field at the tissue-metal screen interface can be obtained. If the incident polarization vector is $\mathbf{E_0}$, as shown in Fig. 8.1, the electric field at $z = z_A^+$ can thus be written as

$$\mathbf{E}_A = \sqrt{I_{A^-}} e^{j\phi_A} e^{j(kz - \omega t)} \mathbf{E}_0. \tag{8.3}$$

Then, the corresponding magnetic field at $z = z_A^+$ can be obtained from

$$\mathbf{H}_A = j\frac{1}{\omega} \nabla \times \mathbf{E}_A. \tag{8.4}$$

Thus, the incident electric and magnetic fields at the interface have been obtained. In order to calculate the field distribution just after the metal screen with the slit, the technique introduced by Neerhoff and Mur [5] is adopted in the present work. However, a time-dependent incident profile is considered, as opposed to the time-independent profile used by Neerhoff and Mur. Since the time variation is very slow, the technique introduced by Neerhoff *et al.*[5] can be applied for the case discussed here, as outlined below.

TM polarization is considered here and the magnetic field is assumed to be approximately time harmonic and constant in y direction as shown in Fig. 8.3. Thus

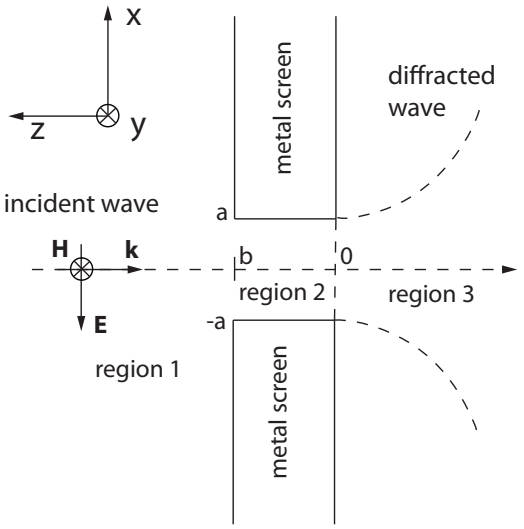

Figure 8.3: Propagation of an incident wave through a slit in a thick metal screen.

$$\mathbf{H}_y(x,y,z,t) = U(x,z,t)\, e^{-j\omega t}\mathbf{e}_y, \tag{8.5}$$

where $\mathbf{e}_y$ is the unit vector in y direction. Since the time variation of $U(x,z,t)$ is very slow, it approximately satisfies the Helmholtz equation. Hence,

$$\left(\nabla^2 + k_j^2\right) U_j(x,z,t) = 0, \tag{8.6}$$

where $j = 1,2,3$ and k_j is the wave number in region j. The field in region 1 can be decomposed into three components:

$$U_1(x,z,t) = U^i(x,z,t) + U^r(x,z,t) + U^d(x,z,t), \tag{8.7}$$

where U^i represents the incident field, U^r represents the field that would be reflected if there were no slit in the screen and U^d represents the diffracted field in region 1 due to the presence of the slit [6]. Each term on the right hand side of Eq. (8.7) approximately satisfies the Helmholtz equation. Also, it can be shown

that [5, 6],

$$U^i(x,z,t) = e^{-jk_1 z}, \tag{8.8}$$

and

$$U^r(x,z,t) = U^i(x,2b-z,t). \tag{8.9}$$

With the above set of equations and standard boundary conditions for a perfectly conducting screen, there exists a unique solution for the diffraction problem [6]. Thus, the field in region 3, close to the metal screen can be obtained using the two-dimensional Green's theorem as discussed in [5] and [6].

Once the electric field values $\left(\mathbf{E}_{d_2}\right)$ just after the metal screen is obtained, these can be combined to obtain the intensity (i.e. the irradiance) using the relationship

$$I = \frac{1}{2} v \epsilon |\mathbf{E}|^2, \tag{8.10}$$

where v and ϵ are the propagation speed and the permittivity in the medium, respectively. Once the irradiance profile on the plane $z = d_2$ is obtained, it should be converted back to a radiance profile so that the PTE can be used to model the light propagation beyond this plane. Figure 8.4 shows a strategy that can be used for mapping the irradiance profile to the radiance profile, as required for solving the PTE. In Fig. 8.4 , the axes (x, y, z) represent the global coordinate system used in solving the PTE; also shown is the ray-centred spherical coordinate system used to describe the irradiance-to-radiance mapping forward hemisphere.

Based on the work of Ramamoorthi *et al.* [11], this strategy uses a hemisphere positioned centrally at the ray propagation direction and uses the relationship

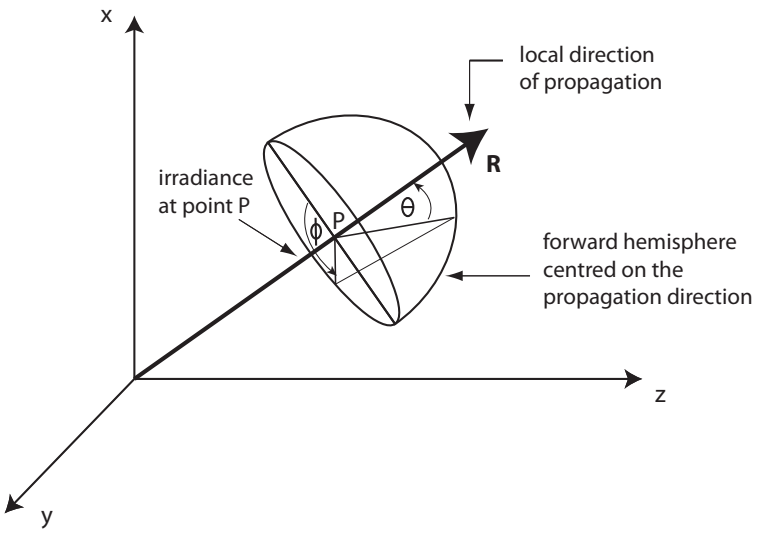

Figure 8.4: An illustration of the strategy used for mapping radiance to irradiance.

between radiance and irradiance given by Eq. (7.40), and spherical harmonic representation to achieve this task. These authors have shown that the irradiance can be represented as a simple convolution of the incident illumination [11]. Therefore, the radiance can be obtained by a deconvolution operation. Ramamoorthi *et al.* [11] have derived a simple closed-form formula for the irradiance in terms of spherical harmonic coefficients of the incident illumination [11].

Once the irradiance profile on the plane $z = d_2$ is converted back to a radiance profile at each point, in the forward hemisphere at the interface, the technique introduced in Chapter 6 can be used to model the light propagation through the remaining layers of tissue.

8.3 Numerical results and discussion

The simulation of the proposed technique was carried out using Matlab^{TM}. In the simulations, all the units were normalized as detailed in Chapter 4. The input

pulse was taken to be a Gaussian pulse (see Fig. 8.5) given by Eq. (4.41).

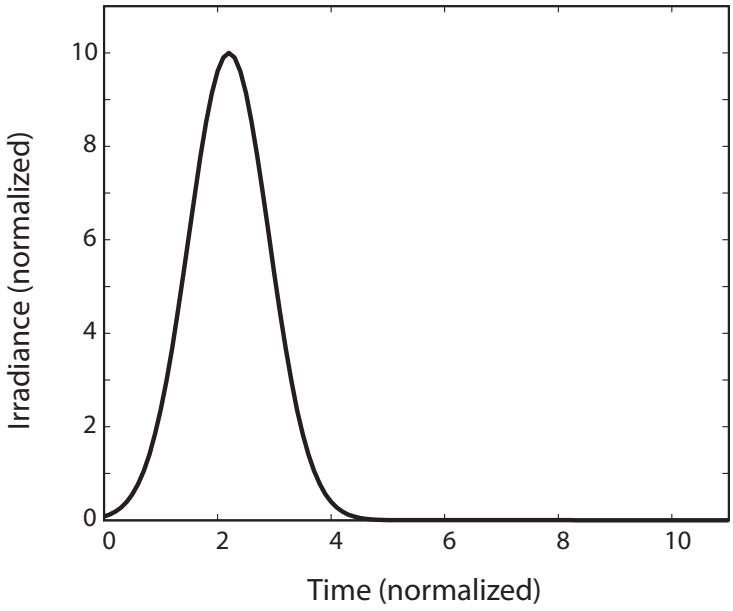

Figure 8.5: The incident radiance profile on the tissue layer (with arbitrary units).

Figure 8.5 shows the irradiance profile, in a particular direction, incident on the centre of the tissue layer from the left hand side on Fig. 8.1. The proposed technique does not depend on the type of input source. Therefore, in order to minimize the additional mathematical complexity which might mask the main idea of the proposed technique, the input source is assumed to have the same radiance profile in all directions in the forward hemisphere, as depicted in Fig. 8.5. However, the proposed technique can be applied to other kinds of input sources; for example, one may use the technique proposed by Ramamoorthi *et al.* [11], to construct an input radiance profile with a non-uniform profile.

Figure 8.6 shows the irradiance profile at $z = 2$, on a plane just before the tissue-metal screen interface, obtained by solving the PTE using the technique proposed in Chapter 6. Here, a tissue layer with a normalized scattering coeffi-

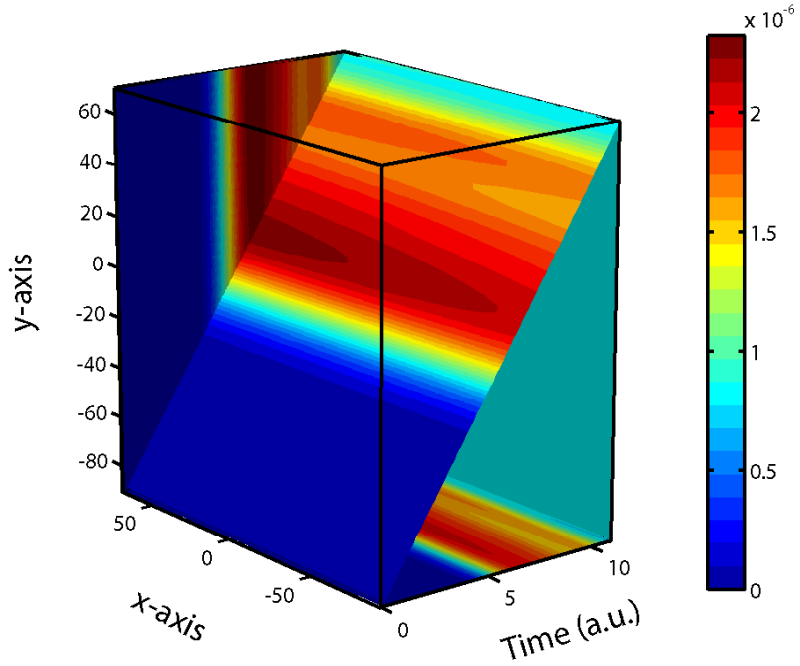

Figure 8.6: The irradiance profile on a plane just before the tissue-metal screen interface (with arbitrary units).

cient of 0.3, normalized absorption coefficient of 0.5 and the Henyey-Greenstein phase function [12] with an asymmetry factor of 0.7 was used. The normalized velocity was taken to be 1 while the refractive index of the tissue layer was assumed to be 1.37. Figure 8.6 shows how the irradiance profile on the (x, y) grid at $z = 2$ varies with time.

Using the same technique, the irradiance profile at $z = 1.95$ was obtained, and these two profiles were used to retrieve the phase of the field at $z = 2$. For phase retrieval, first, the code given in reference [13] for the full multigrid algorithm was translated to Matlab scripting, and then modified to solve the TIE, which involved slight modifications to some subroutines. Then, the irradiance values and the phase values were combined according to Eq. (8.3) to construct the electric field at $z = 2$, which is shown in Fig. 8.7.

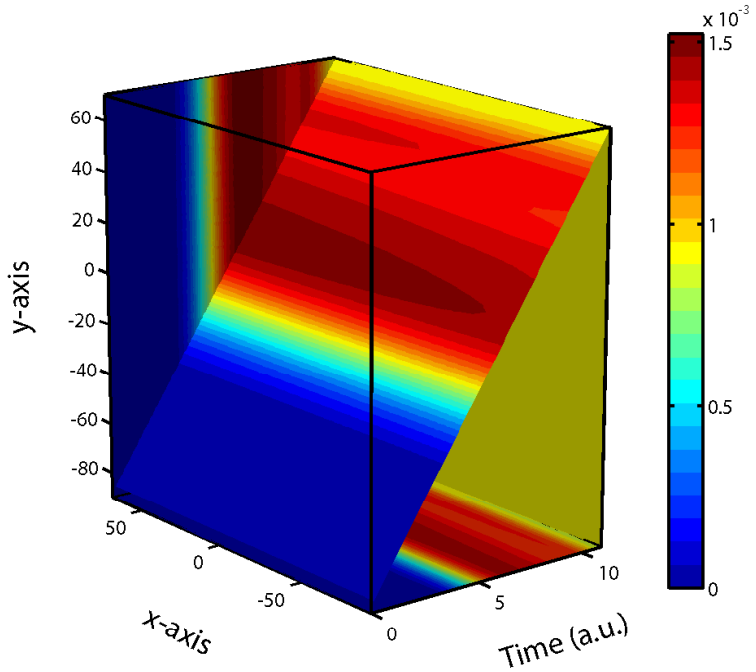

Figure 8.7: The electric field distribution on a plane just before the tissue-metal screen interface (with arbitrary units).

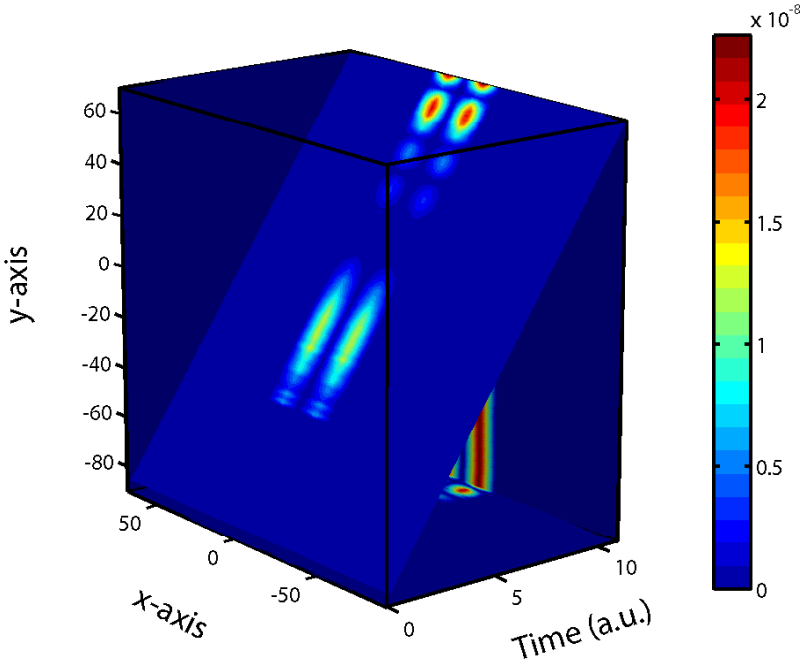

Figure 8.10: The electric field component in the x-direction on a plane just after the tissue-metal screen interface (with arbitrary units).

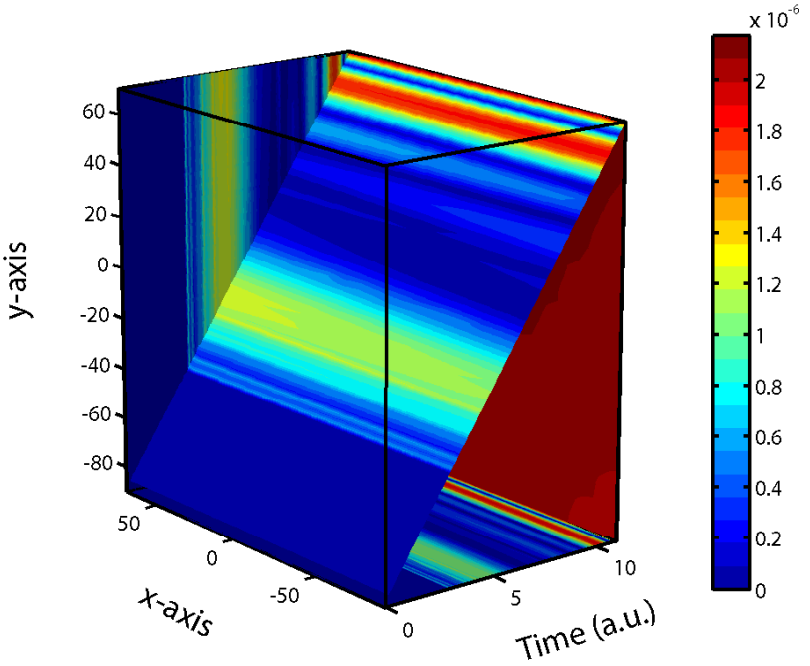

Figure 8.8: The magnetic field distribution on a plane just before the tissue-metal screen interface (with arbitrary units).

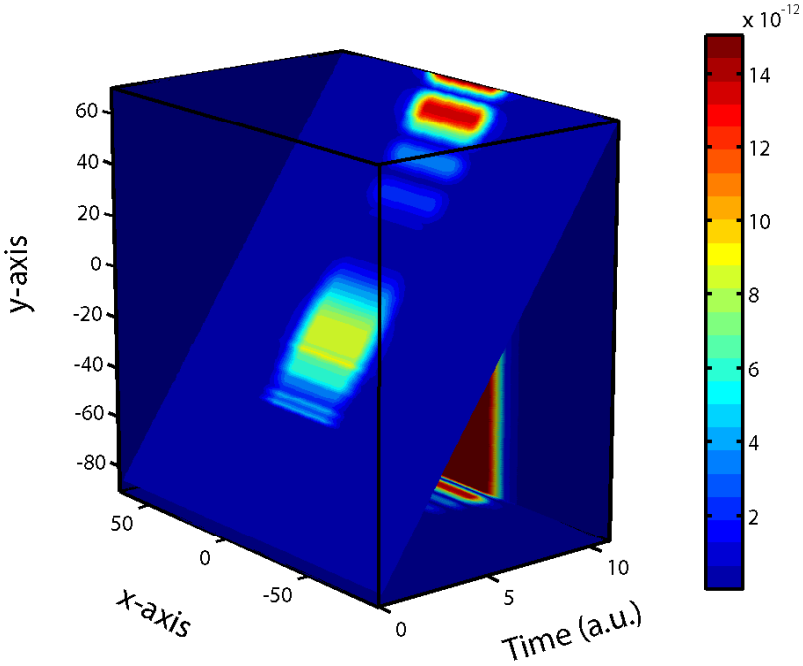

Figure 8.11: The electric field component in the z-direction on a plane just after the tissue-metal screen interface (with arbitrary units).

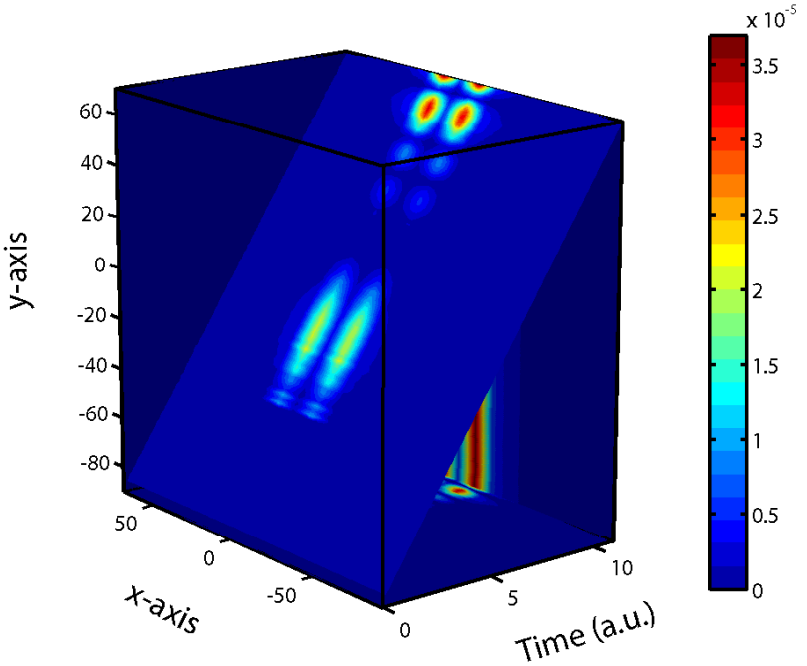

Figure 8.9: The magnetic field distribution on a plane just after the tissue-metal screen interface (with arbitrary units).

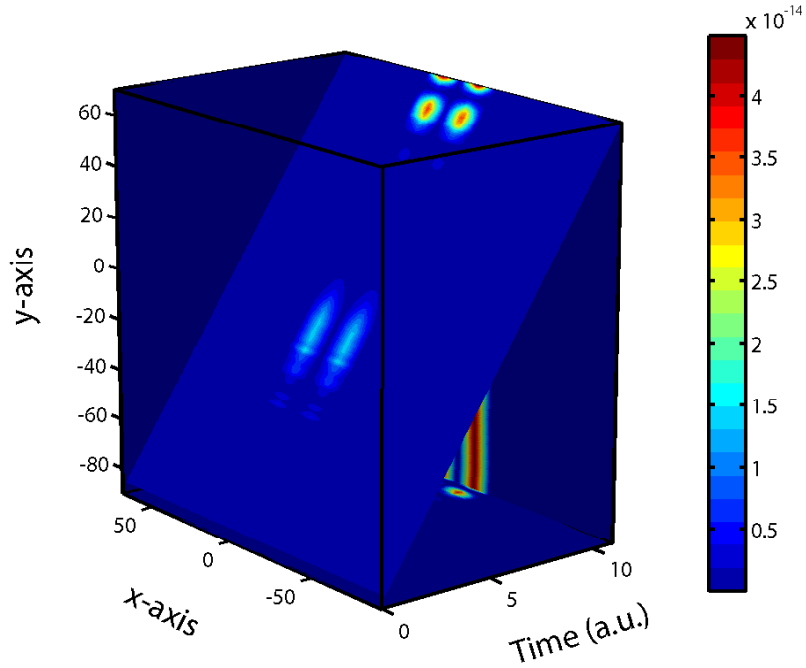

Figure 8.12: The irradiance profile on a plane just after the tissue-metal screen interface (with arbitrary units).

Equation (8.4) was used to calculate the magnetic field distribution on a plane just before the metal screen, using the electric field distribution. This result is shown in Fig. 8.8. Then, the field distribution on a plane just after the screen was obtained using the technique introduced by Neerhoff and Mur [5], as discussed in the previous section. The magnetic and electric fields thus obtained are shown in Figures 8.9, 8.10 and 8.11. The irradiance profile constructed according to Eq. (8.10) is shown in Fig. 8.12.

8.4 Conclusions

This chapter has presented the theoretical analysis of wave propagation through tissue with an implanted metal screen with a slit, which uses the technique of mapping the photon transport equation to Maxwell's equations proposed in the previous chapter. This work includes a technique for analyzing diffraction effects within the framework of photon transport theory. The proposed technique was implemented and some simulation results were presented.

In modeling wave propagation through biological tissue with the metal screen implanted, the PTE models wave propagation through the tissue layer. At the interface, the phase is retrieved from the irradiance profile and thus the electromagnetic field is determined. The wave propagation through the slit of the metal screen is modeled using Maxwell's equations. Then, the electromagnetic field is converted back to an irradiance profile at the exit of the metal screen.

8.5 References

[1] J. L. Li and M. Gu, "Gold-nanoparticle-enhanced cancer photothermal therapy," *IEEE Journal of Selected Topics in Quantum Electronics*, 2009, accepted for inclusion in a future issue of this journal.

[2] S. W. Han, C. Nakamura, Y. Imai, N. Nakamura, and J. Miyake, "Monitoring of hormonal drug effect in a single breast cancer cell using an estrogen responsive GFP reporter vector delivered by a nanoneedle," *Biosensors and Bioelectronics*, vol. 24, pp. 1219–1222, 2009.

[3] M. Premaratne, E. Premaratne, and A. J. Lowery, "The photon transport equation for turbid biological media with spatially varying isotropic refractive index," *Optics Express*, vol. 13, pp. 389–399, 2005.

[4] C. C. Handapangoda, M. Premaratne, L. Yeo, and J. Friend, "Laguerre Runge-Kutta-Fehlberg method for simulating laser pulse propagation in biological tissue," *IEEE Journal of Selected Topics in Quantum Electronics*, vol. 14, pp. 105–112, 2008.

[5] F. L. Neerhoff and G. Mur, "Diffraction of a plane electromagnetic wave by a slit in a thick screen placed between two different media," *Applied Scientific Research*, vol. 28, pp. 73–88, 1973.

[6] S. V. Kukhlevsky, M. Mechler, L. Csapo, K. Janssens, and O. Samek, "Enhanced transmission versus localization of a light pulse by a subwavelength metal slit," *Physical Review B*, vol. 70, p. 195428, 2004.

[7] J. D. Joannopoulos, R. D. Meade, and J. N. Winn, *Photonic Crystals : Molding the Flow of Light*. New Jersey: Princeton University Press, 1995.

[8] C. C. Handapangoda, M. Premaratne, D. M. Paganin, and P. R. D. S. Hendahewa, "Technique for handling wave propagation specific effects in biological tissue: Mapping of the photon transport equation to Maxwell's equations," *Optics Express*, vol. 16, no. 22, pp. 17 792–17 807, 2008.

[9] T. E. Gureyev, C. Raven, A. Snigireva, I. Snigireva, and S. W. Wilkins, "Hard x-ray quantitative non-interferometric phase-contrast microscopy," *Journal of Physics D: Applied Physics*, vol. 32, pp. 563–567, 1999.

[10] L. J. Allen and M. P. Oxley, "Phase retrieval from series of images obtained by defocus variation," *Optical Communications*, vol. 199, pp. 65–75, 2001.

[11] R. Ramamoorthi and P. Hanrahan, "On the relationship between radiance and irradiance: Determining the illumination from images of a convex Lambertian object," *Journal of Optical Society of America A*, vol. 18, pp. 2448–2459, 2001.

[12] K. S. G. E. Thomas, *Radiative Transfer in the Atmosphere and Ocean*. Cambridge: Cambridge University Press, 1999.

[13] W. H. Press, S. A. Teukolsky, W. T. Vetterling, and B. P. Flannery, *Numerical Recipes in C: The Art of Scientific Computing*, 2nd ed. Cambridge: Cambridge University Press, 1992.

CHAPTER 9

Conclusions and Recommendations for Further Research

This chapter concludes the dissertation with an account of the contributions made. It also provides some recommendations for future work which are based on the current research.

9.1 Summary of contributions

THE research reported in this dissertation provides four major contributions to the field of numerical simulation of pulse propagation through biological tissue for sensing applications. First, a technique for simulating laser pulse propagation through tissue is proposed, addressing some drawbacks of existing techniques. This was done by solving the one-dimensional photon transport equation (PTE). An implicitly causality-enforced solution method for multi-dimensional photon transport was then developed. Another contribution is the development of an approximate numerical technique for modeling optical pulse propagation through weakly scattering biological tissue with a varying refractive index and varying scattering and absorption coefficients. A technique for simulating laser pulse propagation through tissue with implanted foreign structures

is then proposed, by mapping the photon transport equation to Maxwell's equations. More details of each of these contributions are provided in this section.

9.1.1 A numerical technique for simulating one-dimensional transient photon transport in biological tissue

The Laguerre Runge-Kutta-Fehlberg method proposed in Chapter 4 of this dissertation is used for solving the time dependent PTE. This numerical technique makes it possible to efficiently simulate laser pulse propagation through biological tissue.

This method has several advantages over other existing techniques that are used to solve the one-dimensional transient PTE. In this proposed solution technique the zenith and azimuthal angle dependencies are removed using the discrete ordinates method, and the final reduced set of equations is solved using the Runge-Kutta-Fehlberg (RKF) method. Therefore, intensity profiles at several grid points (or planes) over the whole time spectrum can be obtained in a single execution of the algorithm, as opposed to having several executions either for each spatial point (or plane) or for each instance of time. This makes the proposed technique more efficient and faster than most existing techniques.

Many biomedical applications use ultra-short laser pulses of a Gaussian profile. However, existing methods for solving the time-dependent PTE approximate the actual Gaussian profile by some other shape, mostly a square pulse. The method proposed in this dissertation uses a Laguerre expansion to represent the time dependency. This makes it possible to represent the actual input pulse very accurately. In addition, any arbitrary shape can be represented accurately using only a few Laguerre polynomials, which makes this technique useful if any other pulse shape is to be used for a particular application. Another advantage of this

proposed method is that the causality of the system is implicitly imposed since Laguerre polynomials are causal.

The proposed technique can be easily extended to higher dimensions (i.e. to solve the two-dimensional and three-dimensional PTE) and to inhomogeneous media in which the scattering and absorption coefficients as well as the refractive index change from point to point. Detailed descriptions of these cases were presented in Chapters 5 and 6.

This work has been reported in the IEEE Journal of Selected Topics in Quantum Electronics.

9.1.2 A numerical technique for characterizing light propagation through inhomogeneous tissue

An approximate numerical technique for simulating optical pulse propagation through weakly scattering biological tissue was developed in Chapter 5. This was carried out by solving the transient PTE in biological tissue that includes varying refractive index and varying scattering and absorption coefficients. The proposed technique involves first tracing the ray paths defined by the refractive index profile of the medium. This ray tracing is carried out by solving the Eikonal equation using a Runge-Kutta integration algorithm. The one-dimensional transient PTE is solved only along these ray paths, minimizing the overall computational burden of the resulting algorithm. The main advantage of this proposed algorithm is that it enables the discretization of the pulse propagation space adaptively by taking optical depth into account. Therefore, computational efficiency can be increased without compromising the accuracy of the algorithm. In addition, the causality of the system is implicitly imposed. Another advantage is that the whole time spectrum is spanned in a single execution of the algorithm.

This work has been reported in the Journal of Biomedicine and Biotechnology.

9.1.3 A numerical technique for simulating multi-dimensional transient photon transport in biological tissue

A novel method for solving the multi-dimensional transient photon transport equation for laser pulse propagation in biological tissue was proposed in Chapter 6. In this technique a Laguerre expansion is used to represent the time-dependency of the incident short pulse. Owing to the intrinsic causal nature of Laguerre functions, this technique automatically preserves the causality constrains of the transient signal. This expansion of the radiance using a Laguerre basis transforms the transient photon transport equation to the steady state version. The resulting equations are then solved using the discrete ordinates method, using a finite volume approach. This method offers the advantage of representing the intensity with a high accuracy using only a few Laguerre polynomials. In addition, the whole time spectrum is spanned in a single execution of the algorithm making it a very efficient technique. With this proposed method any arbitrary input pulse shape can be handled.

This work has been reported in Optics Express.

9.1.4 A numerical technique for mapping the photon transport equation to Maxwell's equations

A numerical technique for mapping the photon transport equation, which governs light propagation through tissue, to Maxwell's equations, which govern light propagation through implanted structures, was proposed in Chapter 7. This technique can be used to simulate light propagation through biological tissue with

implanted foreign structures. This problem has not been addressed in the research literature to date, despite the very promising applications in optical diagnostic procedures.

The proposed technique involves obtaining the electric and magnetic fields to be used in Maxwell's equations from the irradiance profile produced by the photon transport equation. The phase information required for this purpose can be obtained using a phase retrieval technique such as the full multigrid algorithm.

This work has been reported in Optics Express.

The major contribution of this research as a whole is the development of a numerical technique to simulate light pulse propagation through biological tissue with implants. Despite the very useful potential applications, this problem has not been addressed in the research literature to date.

9.2 Recommendations for further research

This section provides a number of suggestions for further research to extend or modify the work presented in this dissertation.

9.2.1 Comparing simulation results obtained using the proposed techniques to those obtained experimentally

The Laguerre-Runge-Kutta Fehlberg method proposed in Chapter 4 of this dissertation was validated for three special cases for which the results are intuitive. In addition, simulation results obtained using this method were compared to those obtained using an existing method. Simulation results obtained using the Laguerre DOM proposed in Chapter 6 were also compared to those obtained using

an existing method. A discussion of the validity and the accuracy of the technique proposed to map the PTE to Maxwell's equations was provided in Chapter 7. In addition, it is recommended that the numerical techniques proposed in this dissertation be compared or validated against experimental results, as a topic of further research.

9.2.2 Using surface enhanced Raman scattering to enhance Raman scattering in tissue

Raman scattering results in inelastic scattering of light by molecules in the medium. That is, the energy of the incident photon is either decreased (Stokes Raman scattering) or increased (Anti-Stokes Raman scattering). Stokes Raman scattering occurs when a molecule falls to a stable excited state by absorbing energy from a photon, resulting in a decreased frequency of light. On the other hand, anti-Stokes Raman scattering occurs when an excited molecule interacts with a photon and falls to a less energetic state, releasing some of the energy it possessed before this interaction, resulting in an increase in the frequency of light [1].

The observed frequency shifts are independent of the excitation frequency and provide specific information about the chemical structure of the sample [2]. Hence, the excitation frequency can be chosen to suit a particular sample [2]. Raman spectroscopy has excellent fingerprinting capabilities when compared with other optical techniques [3]. Therefore, Raman spectroscopy can be used to uniquely detect substances in blood or tissue fluid, such as glucose. However, the small Raman scattering cross-section results in very low signal levels, making the use of this technique in biomedical applications inefficient [1, 3]. Since Raman scattering is a non-linear process, a high intensity is required to initiate this process. However, for safety reasons, the incident intensity used in optical detection techniques should be relatively low as reported in Chapter 3. Photonic crystal structures im-

planted in tissue can be used to overcome this problem. The photon density of states of a photonic crystal structure redistributes near the band gap frequencies as explained in detail in Appendix B. This enhancement of the photon density of states can be exploited to initiate and enhance Raman scattering with relatively low power incident pulses.

It has been found recently that colloidal gold can be used to amplify the efficiency of Raman scattering of adsorbed molecules by 14 to 15 orders of magnitude. This process is called surface-enhanced Raman scattering (SERS). The ultra-high sensitivity of SERS allows spectroscopic detection of single molecules, with very low concentrations, under ambient conditions [3, 4]. Colloidal gold has been used safely in rheumatoid arthritis treatments for 50 years [4]. The very high increase of the Raman signal resulting from SERS is primarily due to the electromagnetic field enhancements associated with surface-plasmon resonance [5].

Since microfluidic devices can dispense small volumes of samples, the capability of detecting low quantities of biomolecules has become more critical [5]. SERS can be used for this purpose which results in high sensitivity [5]. The SERS technique, based on metallic nanostructures, has been applied to several fields such as the detection of environmental pollutants and investigation of adsorption and reaction processes at electrochemical interfaces [6]. Using lasers, coherent anti-Stokes Raman scattering (CARS) can generate a stronger signal than ordinary Raman scattering, but the sensitivity of CARS is not as high as that of SERS and also the former has not reached the single-molecule level [5]. However, by combining SERS and CARS, it is possible to obtain significant signal gain [5].

Having gold clusters inside photonic crystals implanted in tissue results in

surface-enhanced Raman scattering (SERS). This phenomenon can be exploited to enhance otherwise weak optical signals that are used in optical diagnostic procedures. Modeling of photonic crystals implanted in tissue with gold clusters inside them can be carried out by extending the work presented in Chapter 7 and Appendix C. Appendix C proposes a method to determine the reflectance and transmittance at the tissue-photonic crystal interface. However, modeling of light propagation through the photonic crystals involves numerically solving Maxwell's equations in a periodic dielectric structure. This involves extensive work which requires significant effort and time. Having gold clusters inside the photonic crystal structure increases the complexity of the problem. However, the numerical techniques proposed in this dissertation can be extended to model light propagation through photonic crystals with gold clusters implanted in tissue. This modeling would have very useful biomedical applications.

9.2.3 Modeling thermal ablation and considering temperature changes in laser irradiated tissue

In laser surgery high power CO_2 lasers are used to remove excessive tissue [7]. In thermal laser ablation, the water contained in the tissue absorbs the energy of the incident laser beam and vaporizes, leaving behind only the tissue debris [7]. Development of a model for thermal ablation of tissue is difficult because there is an abrupt change in thermal behaviour at the water-steam phase transition temperature and the heat flow and mass removal occur simultaneously [8]. In addition, there are difficulties associated with incorporating scattering into such a model [8]. However, some attempts to model thermal ablation of tissue can be found in the research literature [8, 9]. It is recommended that the techniques developed in this dissertation be extended or modified to improve the modeling of thermal ablation of tissue.

Visible and near-infrared lasers cause thermal destruction of tissue. The extent of this destruction is governed by heat deposition in tissue, heat transfer and temperature-dependent rate reactions [10]. The extent and degree of tissue damage depends on the magnitude, time duration and placement of the deposited heat in tissue [10]. The heat deposition in tissue is due only to photons that are absorbed [10]. Absorbed laser light results primarily in a rise in the tissue temperature according to its specific heat. Heat is then diffused from the deposition region by thermal conduction and other processes [11]. This phenomenon can be modeled using the bioheat equation, which is a diffusion equation with cooling and heating terms due to blood perfusion and boundary effects [11].

For applications in which ultrashort pulses are used, the medium is usually treated as a cold medium. This is because when an ultrashort laser pulse is used as the incident source, the emission from the media is negligible. Thus, the work presented in this dissertation did not take temperature distribution into account. However, it is recommended that the techniques developed in this dissertation be extended to include temperature distributions which can be used in other applications where the medium cannot be treated as a cold medium.

9.2.4 Considering coherence and polarization effects of light propagated through tissue

Sankaran *et al.* [12] have demonstrated significant differences in the propagation of polarized light through biological tissue. They have measured the depolarization of linearly and circularly polarized light versus propagation distance. Their results indicate that linearly polarized light survives through longer propagation distances than circularly polarized light in biological tissue [12]. Wang *et al.* [13] showed that the temporal distribution of the light transmittance through scattering media is independent of the incident polarization state.

Filtering of weakly scattered photons from multiply scattered photons can enhance the resolution and contrast in optical images of tissue [12]. As the discrimination criterion, by which to reject multiply scattered photons, the degree of polarization may be used [12]. Polarization discrimination will be effective for imaging through less than about a centimeter of soft tissue [14].

Unscattered photons retain coherence and phase while multiple scattering destroys these properties [14]. The performance of coherent methods requires the existence of a transmitted coherent component [14]. In coherent gating light transmitted through a medium is combined spatially and temporally with a reference beam [14]. Coherence properties of light are used in optical coherence tomography (OCT), which is an optical imaging technique and has great potential in diagnosis where conventional biopsy is dangerous or ineffective [15]. OCT uses the partial coherence properties of a light source to image structures in a turbid medium such as tissue [16]. This technique uses a two-beam interferometer with two arms, the sample arm and the reference arm. The sample is positioned in the sample arm. The optical path length in the reference arm acts as a gate on the detection, selecting only the light backscattered from the sample that has traveled the same optical path length. Interference fringes are formed when the optical path length of light backscattered from the sample matches that from the reference [16].

The photon transport equation does not include coherence information and coherence was not taken into account in the work presented in this dissertation. Polarization effects have also not been considered. However, it is recommended that the present work be extended to incorporate these effects for applications such as optical imaging of tissue using polarization or coherent gating.

9.2.5 Considering refractive index mismatches at interfaces

In photon transport theory, the effects of reflection and refraction on the boundary are significant. The mismatch of the refractive indices at interfaces leads to increasing photon flight time due to the internal reflections [17]. If there is a refractive index mismatch at the tissue-external medium interface, light will be internally reflected back into the tissue at the interface [18]. Therefore, calculations of internal fluence rates for photodynamic therapy dosimetry or estimates of tissue optical properties based on reflectance require an understanding of, and a treatment for, the index mismatch [18]. Specular reflection arising due to refractive index mismatch at the interface yields photons which have not "sampled" the tissue interior. Hence, these photons do not yield information about the internal tissue absorption and scattering properties [19]. Therefore, estimates of tissue properties based on reflectance require appropriate treatment of this issue.

Various approaches have been developed to include mismatched boundary conditions [17]. When the diffusion approximation is used, the boundary conditions at the interface are derived using Fresnel's equations by balancing the fluence rate and photon current crossing the interface [18]. Guo *et al.* [20] used Snell's law and the Fresnel coefficients to calculate reflectivity at the tissue-air interface. They considered the effect of Fresnel boundary in modeling such interfaces. Their results showed that the simulated transmitted signals were broadened and amplified under specularly reflecting boundary conditions as compared to those under diffusely reflecting boundary conditions. Guo *et al.* [20] used the discrete ordinate method to simulate laser propagation in tissue. By using Snell's law and Fresnel coefficients, the specular reflectivity at each discrete angle direction can be calculated.

Churmakove *et al.* [17] simulated photon migration in a randomly inhomo-

geneous, highly scattering and absorbing medium with a plane boundary, using the Monte Carlo method. In their study, they considered the spatial photon sensitivity profile, spatially resolved diffuse reflectance and angular and spatial photon detector weight distributions in terms of Fresnel's reflection and refraction on the boundary. They predicted the effect of refractive index match, using the Monte Carlo method and diffusion approximation [17]. Haskell *et al.* [21] examined three boundary conditions commonly applied to the surface of a semi-infinite turbid medium, using the method of images. They found that, when an aluminium foil was placed on the surface of a tissue phantom, phase and modulation data were closer to the results for an infinite-medium geometry. Haskell *et al.* [21] concluded that non-invasive measurements of optically thick tissue require a rigorous treatment of the tissue boundary, and they suggested a unified partial-current-extrapolated boundary approach. They used the diffusion approximation in their work. The extrapolated boundary condition and the partial-current boundary condition can be used to account for Fresnel reflections that arise from the refractive-index mismatch at the tissue-air interface [21].

Lagendijk *et al.* [22] considered the effect of internal reflection of propagation waves in strongly scattering media using a diffusion approach. They found that the influence of internal reflection can be very strong when backscattering and transmission through relatively thin slabs are considered. They further stated that, when transmission through relatively thick slabs is considered, this effect can be accounted for by renormalizing the diffusion coefficient with a length-scale dependent reduction factor. Lagendijk *et al.* [22] used Green functions to calculate the degree to which coherent backscattering and diffusive transport, in reflection and transmission, are affected by internal reflection. They showed that for experiments requiring backscattering geometries internal reflection modifies the outcome significantly.

Ripoll *et al.* [23] derived integral equations for diffuse photon density waves at a refractive index mismatched interface, based on a surface-integral formalism. They used the diffusion approximation and considered a diffuse-diffuse interface with index mismatch. They presented numerical results by solving these integral equations without any further approximations. Ripoll *et al.* [23] showed that multiple-scattering contribution due to surface roughness can be neglected even when an index mismatch is present. Zhu *et al.* [24] showed that the effect of internal reflection due to refractive index mismatch can be quantitatively accounted for using a single parameter. They achieved this by incorporating a reflection coefficient into the boundary condition of the diffuse light. Farrell *et al.* [18] presented an experimental investigation of the effect of the refractive index mismatch at the tissue interface on the internal light fluence rate. Presently, more complete studies are being carried out to demonstrate the influence of refractive index matching on image reconstruction of inhomogeneities in a medium [17].

In this dissertation it was assumed that the refractive index matched interfaces at the input. However, this work can be easily extended to incorporate refractive index-mismatches at interfaces. A brief account of how this could be done was outlined in Chapter 4. It involves calculating the specular reflectivity from Fresnel's equations. For applications based on reflectance profiles it would be better to incorporate index mismatches.

9.2.6 Modeling light propagation through muscles

There are several types of human tissue, such as muscle fibres and white matter of the brain, that have properties that depend not only on location but also on direction [25, 26]. Experiments have been conducted to show that this anisotropy of

tissue affects light propagation [25, 26]. There are some indications that photon transport theory may break down in the case of muscle, which can be considered as highly structured tissue. This is because the alignment of fibres in muscle may cause measurable wave interference effects and scattering cannot be considered random [27]. Muscles are made up of several different structures such as fibre cells, blood vessels, nerves and lymphatic vessels. Prediction of exact absorption and scattering coefficients for muscle tissue is impossible due to the irregular forms and different sizes of these structures [28]. The scattering process in muscular tissue is anisotropic [28]. Light absorption in muscles is mainly due to myoglobin and the haemoglobin present in the red blood cells in the blood vessels [28].

Heino *et al.* [25] considered in detail an anisotropic scattering and light propagation model based on the photon transport equation. They provided a discussion of a possible model for anisotropic scattering applicable in the photon transport framework and also derived the corresponding anisotropic diffusion approximation. Heiskala *et al.* [26] proposed a Monte Carlo model that solves the photon migration problem in an arbitrary voxel-based geometry and an arbitrary form of tissue anisotropy. They derived the anisotropic diffusion equation from the anisotropic photon transport equation implemented by their Monte Carlo model. Kienle *et al.* [29] carried out a study using a two-layered diffusion model to determine non-invasively the haemodynamics of muscles in the extremities. This study was based on their previous work of solving the diffusion equation for a two-layered geometry having an infinitely thick second layer in the steady state. In reference [29] the authors concentrated mainly on determining the absorption coefficient of the muscle layer.

It is recommended that the novel numerical techniques proposed in this dis-

sertation be modified or extended to simulate light propagation through muscle tissues.

9.3 References

[1] S. K. Freeman, *Applications of Laser Raman Spectroscopy*. John Wiley & Sons, Inc., 1974.

[2] R. J. McNichols and G. L. Cote, "Optical glucose sensing in biological fluids: An overview," *Journal of Biomedical Optics*, vol. 5, no. 1, pp. 5–16, 2000.

[3] I. Nabiev, I. Chourpa, and M. Manfait, "Applications of Raman and Surface-Enhanced Raman Scattering spectroscopy in medicine," *Journal of Raman Spectroscopy*, vol. 25, pp. 13–23, 1994.

[4] X. Qian, X. H. Peng, D. O. Ansari, Q. Y. Goen, G. Z. Chen, D. M. Shin, L. Yang, A. N. Young, M. D. Wang, and S. Nie, "In vivo tumor targeting and spectroscopic detection with surface-enhanced Raman nanoparticle tags," *Nature Biotechnology*, vol. 26, no. 1, pp. 83–90, 2007.

[5] T. W. Koo, S. Chan, and A. A. Berlin, "Single-molecule detection of biomolecules by surface-enhanced coherent anti-Stokes Raman scattering," *Optics Letters*, vol. 30, no. 9, pp. 1024–1026, 2005.

[6] T. Vo-Dinh, F. Yan, and M. B. Wabuyele, "Surface-enhanced Raman scattering for medical diagnostics and biological imaging," *Journal of Raman Spectroscopy*, vol. 36, pp. 640–647, 2005.

[7] G. Laufer, "Primary and secondary damage to biological tissue induced by laser radiation," *Applied Optics*, vol. 22, no. 5, pp. 676–681, 1983.

[8] F. Partovi, J. A. Izatt, R. M. Cothren, C. Kittrell, J. E. Thomas, S. Strikwerda, J. R. Kramer, and M. S. Feld, "A model for thermal ablation of biological tissue using laser radiation," *Lasers in Surgery and Medicine*, vol. 7, pp. 141–154, 1987.

[9] J. Langerholc, "Moving phase transitions in laser-irradiated biological tissue," *Applied Optics*, vol. 18, pp. 2286–2293, 1979.

[10] A. J. Welch, "The thermal response of laser irradiated tissue," *IEEE Journal of Quantum Electronics*, vol. QE-20, no. 12, pp. 1471–1481, 1984.

[11] R. A. London, M. E. Glinsky, G. B. Zimmerman, D. S. Bailye, D. C. Eder, and S. L. Jacques, "Laser-tissue interaction modeling with LATIS," *Applied Optics*, vol. 36, no. 34, pp. 9068–9074, 1997.

[12] V. Sankaran, M. J. Everett, D. J. Maitland, and J. T. Walsh, "Comparison of polarized-light propagation in biological tissue and phantoms," *Optics Letters*, vol. 24, no. 15, pp. 1044–1046, 1999.

[13] X. Wang, L. V. Wang, C. W. Sun, and C. C. Yang, "Polarized light propagation through scattering media: Time-resolved Monte Carlo simulations and experiments," *Journal of Biomedical Optics*, vol. 8, no. 4, pp. 608–617, 2003.

[14] J. C. Hebden, S. R. Arridge, and D. T. Delpy, "Optical imaging in medicine: I. Experimental techniques," *Physics in Medicine & Biology*, vol. 42, pp. 825–840, 1997.

[15] M. E. Brezinski and J. G. Fujimoto, "Optical coherence tomography: high-resolution imaging in nontransparent tissue," *IEEE Journal of Selected Topics in Quantum Electronics*, vol. 5, no. 4, pp. 1185–1192, 1999.

[16] J. F. de Boer, T. E. Milner, M. J. c. van Gemert, and J. S. Nelson, "Two-dimensional birefringence imaging in biological tissue by polarization-sensitive optical coherence tomography," *Optics Letters*, vol. 22, no. 12, pp. 934–936, 1997.

[17] D. Y. Churmakov, I. V. Meglinski, and D. A. Greenhalgh, "Influence of refractive index matching on the photon diffuse reflectance," *Physics in Medicine & Biology*, vol. 47, pp. 4271–4285, 2002.

[18] T. J. Farrell and M. S. Patterson, "Experimental verification of the effect of refractive index mismatch on the light fluence in a turbid medium," *Journal of Biomedical Optics*, vol. 6, no. 4, pp. 468–473, 2001.

[19] B. C. Wilson and S. L. Jacques, "Optical reflectance and transmittance of tissues: Principles and applications," *IEEE Journal of Quantum Electronics*, vol. 26, no. 12, pp. 2186–2199, 1990.

[20] Z. Guo and K. Kim, "Ultrafast-laser-radiation transfer in heterogeneous tissues with the discrete-ordinates method," *Applied Optics*, vol. 42, no. 16, pp. 2897–2905, 2003.

[21] R. C. Haskell, L. O. Svaasand, T. T. Tsay, T. C. Feng, and M. S. M. B. J. Tromberg, "Boundary conditions for the diffusion equation in radiative transfer," *Journal of the Optical Society of America A*, vol. 11, no. 10, pp. 2727–2741, 1994.

[22] A. Lagendijk, R. Vreeker, and P. D. Vries, "Influence of internal reflection on diffusive transport in strongly scattering media," *Physics Letters A*, vol. 136, pp. 81–88, 1989.

[23] J. Ripoll and M. N. Vesperinas, "Index mismatch for diffuse photon density waves at both flat and rough diffuse–diffuse interfaces," *Journal of the Optical Society of America A*, vol. 16, no. 8, pp. 1947–1957, 1999.

[24] J. X. Zhu, D. J. Pine, and D. A. Weitz, "Internal reflection of diffusive light in random media," *Physical Review A*, vol. 44, no. 6, pp. 3948–3959, 1991.

[25] J. Heino, S. Arridge, J. Sikora, and E. Somersalo, "Anisotropic effects in highly scattering media," *Physical Review E*, vol. 68, p. 031908, 2003.

[26] J. Heiskala, T. N. I. Nissil*ä*, S. J*ä*rvenp*ää*, and E. Somersalo, "Modeling anisotropic light propagation in a realistic model of the human head," *Applied Optics*, vol. 44, no. 11, pp. 2049–2057, 2005.

[27] A. J. Welch and M. J. V. Gemert, *Optical-Thermal Response of Laser-Irradiated Tissue*. New York: Plenum Press, 1995.

[28] J. R. Zijp and J. J. T. Bosch, "Optical properties of bovine muscle tissue in vitro; A comparison of methods," *Physics in Medicine & Biology*, vol. 43, pp. 3065–3081, 1998.

[29] A. Kienle and T. Glanzmann, "In vivo determination of the optical properties of muscle with time-resolved reflectance using a layered model," *Physics in Medicine & Biology*, vol. 44, pp. 2689–2702, 1999.

APPENDIX A

The electromagnetic theory and the photon transport theory

This appendix provides a summary of how electromagnetic theory compares with postulates of the photon transport theory based on Fante's work.

In an isotropic, nondispersive medium with a permittivity $\epsilon + \epsilon_1(\mathbf{r})$ and a permeability μ, if the electric and magnetic fields are monochromatic, the electric field, $\mathbf{E}$ can be expressed as

$$\mathbf{E}(\mathbf{r}, t) = \frac{1}{\sqrt{2}}\mathbf{E}(\mathbf{r})e^{-j\omega t} + \frac{1}{\sqrt{2}}\mathbf{E}^*(\mathbf{r})e^{j\omega t}, \tag{A.1}$$

where $\mathbf{r}$ represents the position and t is time. μ and ϵ represent a background. If ϵ_1 is real the ensemble-averaged electromagnetic energy density within the medium can be written as [1, 2]

$$\langle U(\mathbf{r})\rangle = \frac{\mu}{2}\left\langle|\mathbf{H}(\mathbf{r})|^2\right\rangle + \frac{\epsilon}{2}\left\langle|\mathbf{E}(\mathbf{r})|^2\right\rangle + \frac{1}{2}\left\langle\mathbf{E}^*\cdot\mathbf{P}\right\rangle, \tag{A.2}$$

where $\mathbf{H}$ is the magnetic field strength and $\mathbf{P}(\mathbf{r}) = \epsilon_1(\mathbf{r})\mathbf{E}(\mathbf{r})$. $\mathbf{E}(\mathbf{r})$, $\mathbf{H}(\mathbf{r})$ and $\mathbf{P}(\mathbf{r})$

can be written in terms of their Fourier decomposition into plane waves as

$$\mathbf{E}(\mathbf{r}) = \int_0^\infty \int k^2 \mathbf{e}(\mathbf{k}) e^{j\mathbf{k}.\mathbf{r}} d\Omega dk \tag{A.3}$$

$$\mathbf{H}(\mathbf{r}) = \int_0^\infty \int k^2 \mathbf{h}(\mathbf{k}) e^{j\mathbf{k}.\mathbf{r}} d\Omega dk \tag{A.4}$$

$$\mathbf{P}(\mathbf{r}) = \int_0^\infty \int k^2 \mathbf{p}(\mathbf{k}) e^{j\mathbf{k}.\mathbf{r}} d\Omega dk \tag{A.5}$$

Substituting Eq. (A.3) to Eq. (A.5) in Eq. (A.2) results in

$$\langle U(\mathbf{r}) \rangle = \int Q(\mathbf{r}, \mathbf{s}) d\Omega, \tag{A.6}$$

where

$$Q(\mathbf{r}, \mathbf{s}) = \frac{1}{2} \int_0^\infty k^2 e^{jk\mathbf{s}.\mathbf{r}} \left\langle \mu \mathbf{h}(\mathbf{k}) \cdot \mathbf{H}^*(\mathbf{r}) + [\epsilon \mathbf{e}(\mathbf{k}) + \mathbf{p}(\mathbf{k})] \cdot \mathbf{E}^*(\mathbf{r}) \right\rangle dk, \tag{A.7}$$

and $\mathbf{s}$ is a unit vector in the direction of $\mathbf{k}$ such that $\mathbf{k} = k\mathbf{s}$. Similarly, it can be shown that the Poynting vector, $\mathbf{S}$ can be written as [2]

$$\langle \mathbf{S}(\mathbf{r}) \rangle = \int \mathbf{R}(\mathbf{r}, \mathbf{s}) d\Omega, \tag{A.8}$$

where

$$\mathbf{R}(\mathbf{r}, \mathbf{s}) = \frac{1}{2} \int_0^\infty k^2 e^{jk\mathbf{s}.\mathbf{r}} \left\langle \mathbf{E}^*(\mathbf{r}) \times \mathbf{h}(\mathbf{k}) - \mathbf{H}^*(\mathbf{r}) \times \mathbf{e}(\mathbf{k}) \right\rangle dk. \tag{A.9}$$

It is evident from Eq. (A.6) and Eq. (A.8) that $Q(\mathbf{r}, \mathbf{s})$ and $\mathbf{R}(\mathbf{r}, \mathbf{s})$ can be identified as the angular components in the direction $\mathbf{s}$ of the average energy density and Poynting vector, respectively [2]. Thus, the energy dW which is transported across a surface element dA onto the solid angle $d\Omega$ centered about $\mathbf{s}$ in a time interval dt can be expressed as

$$dW = (\mathbf{R} \cdot \mathbf{n}) dA d\Omega dt, \tag{A.10}$$

where $\mathbf{n}$ is the unit normal to the surface element dA.

In the photon transport theory it is postulated that the energy dW which is transported across a surface element dA onto the solid angle $d\Omega$ centered about $\mathbf{s}$ in a time interval dt is given by

$$dW = I(\mathbf{r}, \mathbf{s})(\mathbf{s} \cdot \mathbf{n}) dA d\Omega dt, \tag{A.11}$$

where $\mathbf{n}$ is the unit normal to dA and I is the radiance. The radiance, I, is postulated to be related to the average energy density through [2]

$$\langle U(\mathbf{r}) \rangle = \frac{1}{v} \int I(\mathbf{r}, \mathbf{s}) d\Omega, \tag{A.12}$$

where v is the propagation speed in the medium. By comparing Eq. (A.12) and Eq. (A.6) it can be seen that these two expressions are consistent when

$$I(\mathbf{r}, \mathbf{s}) = vQ(\mathbf{r}, \mathbf{s}). \tag{A.13}$$

A more detailed analysis of whether and when the postulates of the photon transport theory are satisfied when I is expressed by Eq. (A.13) is presented in reference [2]. This reference also contains a more rigorous derivation of the photon transport equation.

References

[1] J. Startton, *Electromagnetic Theory*. New York, USA: McGraw-Hill, 1941.

[2] R. L. Fante, "Relationship between radiative-transport theory and Maxwell's equations in dielectric media," *Journal of the Optical Society of America*, vol. 71, no. 4, pp. 460–468, 1981.

APPENDIX B

Photonic crystals

This appendix provides a concise description of photonic crystals.

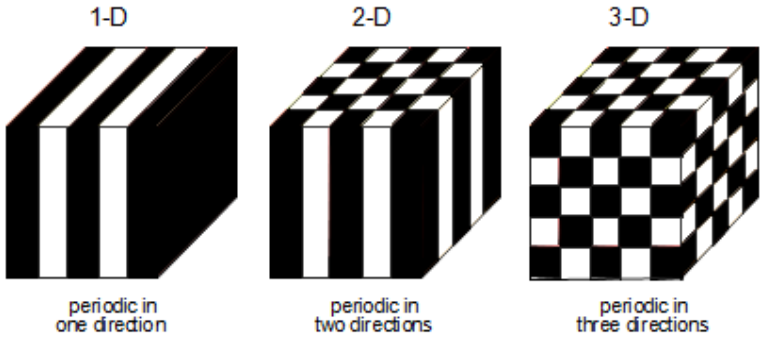

Figure B.1: Schematic illustration of one-dimensional, two-dimensional and three-dimensional photonic crystals [1].

Photonic crystals are low-loss periodic dielectric structures, whose refractive index periodically changes in space, along one direction (one-dimensional), along two directions (two-dimensional) or along all three axes (three-dimensional) [2, 3] as shown in Fig. B.1. The refractive index modulation is in a scale that can be compared to the wavelength propagated in the device [4]. These photonic crystals result in band gaps for photons, which are analogous to band gaps for electrons in semiconductors. Light with frequencies in the photonic band gap is forbidden to

propagate inside the photonic crystal. Thus, if a light wave whose frequency lies in the photonic band gap is sent onto a face of a photonic crystal, the amplitude of this wave decays exponentially and thus extended propagation is prevented [2]. In photonic crystals, different topologies of the structure provide optical band gaps for different polarizations of light [4].

Defects introduced into the photonic crystal structure can be useful in many applications. Defects allow localizing of modes which belong to the band gap. Point defects can be used as microcavities and linear defects can be used as wave guides. Another application of photonic crystals is dielectric mirrors [2]. Influences of defects in photonic crystals can be computed using Wannier functions [5].

Photonic crystals can be used to control the spontaneous emission of light and to localize the photons [6]. Spontaneous emission arises from the intricate interplay between a radiating system and its surrounding environment, and thus, the spontaneous emission in a photonic crystal can be enhanced, attenuated or suppressed by changing the density of electromagnetic states at the transition frequency [7]. It is possible to engineer the photonic density of states in a photonic crystal and this in turn enables enhancement of nonlinear Raman process without increasing the excitation intensity [8]. This is possible because the dip in the photon density of states in the band gap coexists with enhanced density of states just outside it [9]. That is, the photon density of states is increased near the band edges [6]. Figures B.2 and B.3 from [9] show this phenomenon graphically. Solid lines in these figures correspond to continuous media with various refraction indices and dashed lines show redistribution of density of states in photonic band-gap structures.

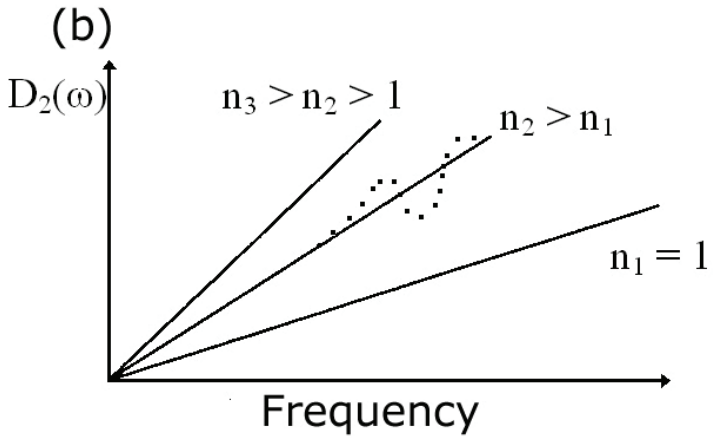

Figure B.2: Density of photon states in two-dimensional space [9].

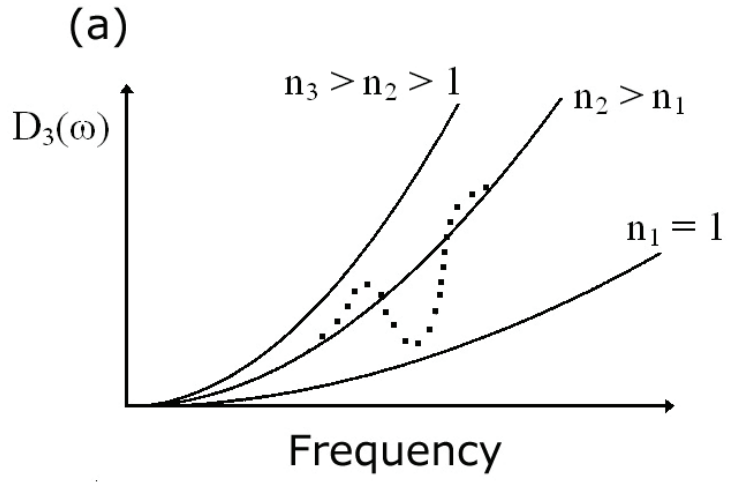

Figure B.3: Density of photon states in three-dimensional space [9].

One of the most efficient Raman spectroscopic techniques is based on the strongly surface-enhanced Raman scattering (SERS) effect [8]. The enhancement of the Raman signal and the Raman scattering rate are facilitated by the strong local enhancement of the electromagnetic field [8]. Hence, the possibility to engineer the photon density of states of a photonic crystal structure in a desired fashion can be exploited to strongly modify the Raman scattering of light from active elements embedded in these structures [8]. Enoch *et al.* [6] have demonstrated that it is possible to obtain an angular confinement of emission together

with an enhancement of the emitted power when emitting dipoles are embedded in a photonic crystal. Fan *et al.* [7] have shown that a thin slab of two-dimensional photonic crystal significantly alters the radiation pattern of spontaneous emission. Also, by eliminating all guided modes at the transition frequencies, spontaneous emission can be coupled entirely to free space modes, which results in a greatly enhanced extraction efficiency [7].

Light propagation through photonic crystals can be modeled using Maxwell's equations. The two curl equations of Maxwell's equations can be combined to obtain the master equation [2]

$$\nabla \times \left(\frac{1}{\varepsilon(\mathbf{r})} \nabla \times \mathbf{H}(\mathbf{r}) \right) = \left(\frac{\omega}{c} \right)^2 \mathbf{H}(\mathbf{r}) \tag{B.1}$$

which should then be solved for the modes, $\mathbf{H}(\mathbf{r})$, for a given frequency. Here, the magnetic permeability, μ, is assumed to be unity, which is true for most of the dielectric materials. There are two ways of describing the behaviour of light in photonic crystals: the band structure and Bloch modes [10]. The band structure describes the allowed frequency bands in infinite photonic crystals, while the corresponding Bloch modes describe electromagnetic field profiles in the crystals [10]. The finite difference time domain (FDTD) method is used to compute numerically the behaviour of light in finite crystals and this method does not make any assumption about crystal periodicity [10].

Figure B.4 from reference [11] shows the band structure of a one-dimensional photonic crystal composed of silicon and air. Figures B.5 and B.6 show a square lattice of a two-dimensional photonic crystals, composed of dielectric cylinders in air, and its band structure. There are two different sets of photonic band structures: the real band structure, which shows the dispersion relation of photons with respect to the propagating Bloch modes, and the complex band structure,

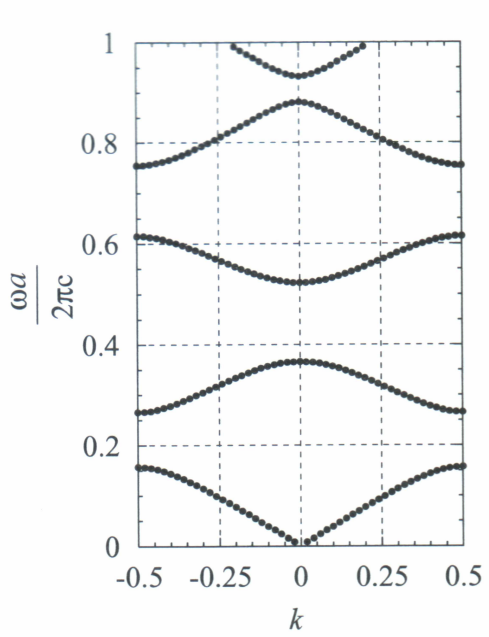

Figure B.4: Band structure of a one-dimensional photonic crystal composed of silicon and air [11].

which shows the decay constants of the evanescent modes in addition to the wave vectors of propagating modes [12].

Photonic crystals near photonic bandgap frequency behave as if they have a certain effective refractive index which is not limited by the refractive index of composing materials, but is determined by the photonic band structure [13]. Thus, the effective refractive index of a photonic crystal can be smaller than unity or negative without absorption, and Snell's law can still be used to describe the light propagation [13]. The dispersion relation shows the relationship of the frequency with the wave number. The group velocity of a radiational eigenmode is given by the gradient of the dispersion curve [1]. That is,

$$\mathbf{v}_g = \frac{\partial \omega}{\partial \mathbf{k}}, \tag{B.2}$$

where $\mathbf{v}_g$ is the group velocity, ω is the angular frequency and $\mathbf{k}$ is the wave

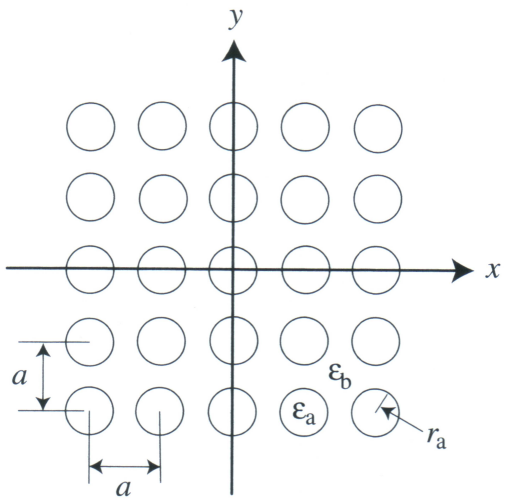

Figure B.5: A two-dimensional square lattice composed of circular cylinders [1].

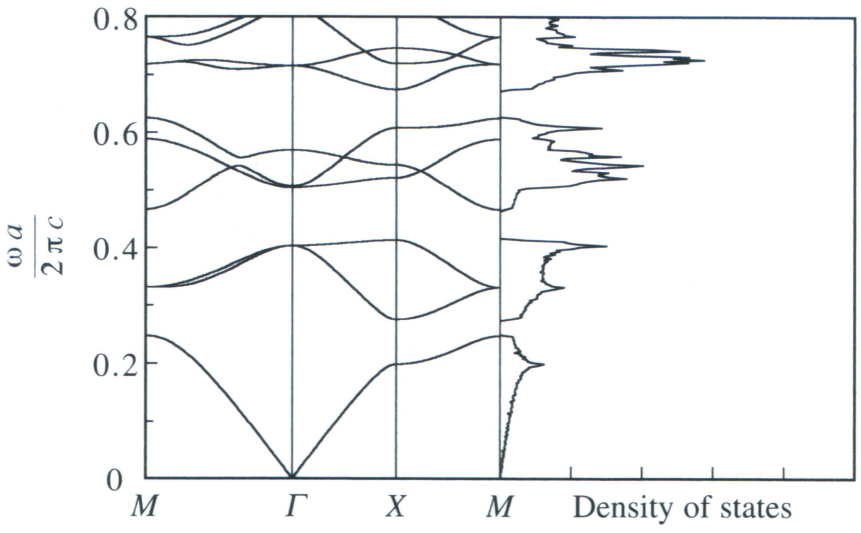

Figure B.6: Photonic band structure of a two-dimensional square lattice composed of circular cylinders, of dielectric constant 9, in air, and with a ratio of the lattice constant to the radius of the cylinders 1:0.38 [1]

number. Thus, the photonic crystal structure can be modeled using an effective refractive index, η_{eff}, which can be obtained using [1]

$$\nabla_{\mathbf{k}}\omega = \frac{c}{\eta_{eff}}\hat{\mathbf{k}}, \tag{B.3}$$

where $\nabla_{\mathbf{k}} = \frac{\partial}{\partial k_x}\mathbf{u}_x + \frac{\partial}{\partial k_y}\mathbf{u}_y + \frac{\partial}{\partial k_z}\mathbf{u}_z$, $\hat{\mathbf{k}}$ is the unit vector parallel to $\mathbf{k}$ and $\mathbf{u}_x$, $\mathbf{u}_y$ and $\mathbf{u}_z$ are unit vectors along x, y and z axes, respectively. Once the effective refractive index is calculated, the transmission coefficient of the photonic crystal can be approximated by that of a uniform medium [1]. Transmission and reflection at photonic crystal interfaces can also be computed by other methods [10]; for example using transfer [14] or scattering matrices [15]. Istrate *et al.* [10] showed that the band structure and Bloch modes can be used not only to give a generalized description of light in infinite photonic crystals, but also to find the amplitude and phase of light reflected and transmitted from interfaces in systems made using finite and semi-infinite photonic crystals. They obtained the equivalent of the Fresnel coefficients for photonic crystals [10]. An interesting property of photonic crystals is the focusing of light caused by negative effective refractive index in the vicinity of the photonic band gap [13]. Thus, photonic crystals can be used as flat lenses and to rectify the problem of divergence caused by scattering in different directions [3, 13, 16].

Basic methods of modeling photonic crystals can be categorized as frequency domain methods (such as the plane wave method) and time domain methods (such as the finite difference time domain method) [4]. The most commonly used methods are the plane wave method (PWM) and the finite difference time domain (FDTD) method [4].

References

[1] K. Sakoda, *Optical Properties of Photonic Crystals*. Germany: Springer, 2005.

[2] J. D. Joannopoulos, R. D. Meade, and J. N. Winn, *Photonic Crystals: Molding the Flow of Light*. Princeton University Press, 1995.

[3] A. Martinez, H. Miguez, A. Griol, and J. Marti, "Experimental and theoretical analysis of the self-focusing of light by a photonic crystal lens," *Physical Review B*, vol. 69, p. 165119, 2004.

[4] D. Szymanski and S. Patela, "Modeling of photonic crystals," International Students and Young Scientists Workshop: Photonics and Microsystems. IEEE, 2005, pp. 79–82.

[5] K. Busch, S. F. Mingaleev, A. G. Martin, M. Schillinger, and D. Hermann, "The Wannier function approach to photonic crystal circuits," *Journal of Physics: Condensed Matter*, vol. 15, pp. R1233–R1256, 2003.

[6] S. Enoch, B. Gralak, and G. Tayeb, "Enhanced emission with angular confinement from photonic crystals," *Applied Physics Letters*, vol. 81, no. 9, pp. 1588–1590, 2002.

[7] S. Fan, P. R. Villeneuve, and J. D. Joannopoulos, "High extraction efficiency of spontaneous emission from slabs of photonic crystals," *Physical Review Letters*, vol. 78, no. 17, pp. 3294–3297, 1997.

[8] L. Florescu and X. Zhang, "Semiclassical model of stimulated Raman scattering in photonic crystals," *Physical Review E*, vol. 72, p. 016611, 2005.

[9] S. V. Gaponenko, "Effects of photon density of states on Raman scattering in mesoscopic structures," *Physical Review B*, vol. 65, p. 140303(R), 2002.

[10] E. Istrate, A. A. Green, and E. H. Sargent, "Behavior of light at photonic crystal interfaces," *Physical Review B*, vol. 71, p. 195122, 2005.

[11] K. Inoue and K. Ohtaka, *Photonic Crystals: Physics, Fabrication and Applications*. Germany: Springer, 2004.

[12] C. S. Feng, L. M. Mei, L. Z. Cai, X. L. Yang, S. S. Wei, and P. Li, "A plane-wave-based approach for complex photonic band structure and its applications to semi-infinite and finite system," *Journal of Physics D: Applied Physics*, vol. 39, pp. 4316–4323, 2006.

[13] M. Notomi, "Negative refraction in photonic crystal," *Optical and Quantum Electronics*, vol. 34, pp. 133–143, 2002.

[14] P. M. Bell, J. B. Pendry, L. M. Moreno, and A. J. Ward, "A program for calculating photonic band structures and transmission coefficients of complex structures," *Computer Physics Communications*, vol. 85, no. 2, pp. 306–322, 1995.

[15] N. Stefanou, V. Karathanos, and A. Modinos, "Scattering of electromagnetic waves by periodic structures," *Journal of Physics: Condensed Matter*, vol. 4, no. 36, pp. 7389–7400, 1992.

[16] K. Guven, K. Aydin, K. B. Alici, C. M. Soukoulis, and E. Ozbay, "Spectral negative refraction and focusing analysis of a two-dimensional left-handed photonic crystal lens," *Physical Review B*, vol. 70, p. 205125, 2004.

APPENDIX C

Modeling pulse propagation through tissue with an implanted photonic crystal structure

---

This appendix contains the theoretical analysis of pulse propagation through tissue with an implanted photonic crystal structure. Photonic crystal structures implanted in biological tissues can be used to non-invasively detect various substances inside the body using low power laser light. A novel algorithm for modeling laser pulse propagation through a biological tissue specimen with an implanted photonic crystal is proposed in this appendix. Light propagation through biological tissue is modeled using the photon transport equation (PTE), whereas light propagation through the photonic crystal structure is modeled using Maxwell's equations. The mapping technique proposed in Chapter 7 is used to couple these two sets of equations.

Optical techniques in biomedical applications such as optical tomography and non-invasive sensing of substances have been receiving tremendous interest recently [1]. These imaging and sensing techniques use laser light sources and spectroscopic techniques for detecting abnormalities. Among the spectroscopic techniques for detection of substances inside the body using laser light, Raman spectroscopy is very promising due to the uniqueness of the Raman spectrum of a molecule. Raman scattering is a nonlinear process and hence requires a high

photon density of states to excite it. However, the maximum safe exposure of laser light for the skin is $0.1\,J/cm^2$ per pulse or $1.0\,W/cm^2$ for continuous exposure [2]. In order to excite Raman scattering while keeping the power of the laser source within the safe exposure limits, photonic crystal structures implanted in tissue can be used.

The redistribution of the photon density of states in photonic crystals can be exploited to excite and enhance Raman scattering for frequencies adjacent to those in the photonic band-gap without increasing the excitation intensity [3, 4]. This is possible because the probability of Raman scattering is proportional to the photon density of states [3]. The presence of surface-enhanced Raman scattering (SERS) active metal clusters, such as silver and gold, inside the photonic crystal structure results in drastic redistribution of the electromagnetic field in space and the photon density of states also redistributes [3]. Thus, by using photonic crystal structures with SERS active metal clusters, the weak Raman signal can be enhanced by up to a million times [5, 6].

In this appendix, a technique to model light propagation through photonic crystal structures implanted in biological tissue is developed. Light propagation in biological tissue is modeled by the photon transport equation [7, 8] which is written in terms of the magnitude of the intensity but not the phase. Light propagation in photonic crystal structures is described by Maxwell's equations [9] which take into consideration both the magnitude as well as the phase of the electric and magnetic fields. Therefore, the mapping technique developed in Chapter 7 is used to couple these two sets of equations at the tissue - photonic crystal interface by retrieving the phase information from the intensity profile.

Figure C.1 shows a composite object composed of a layer of biological tissue

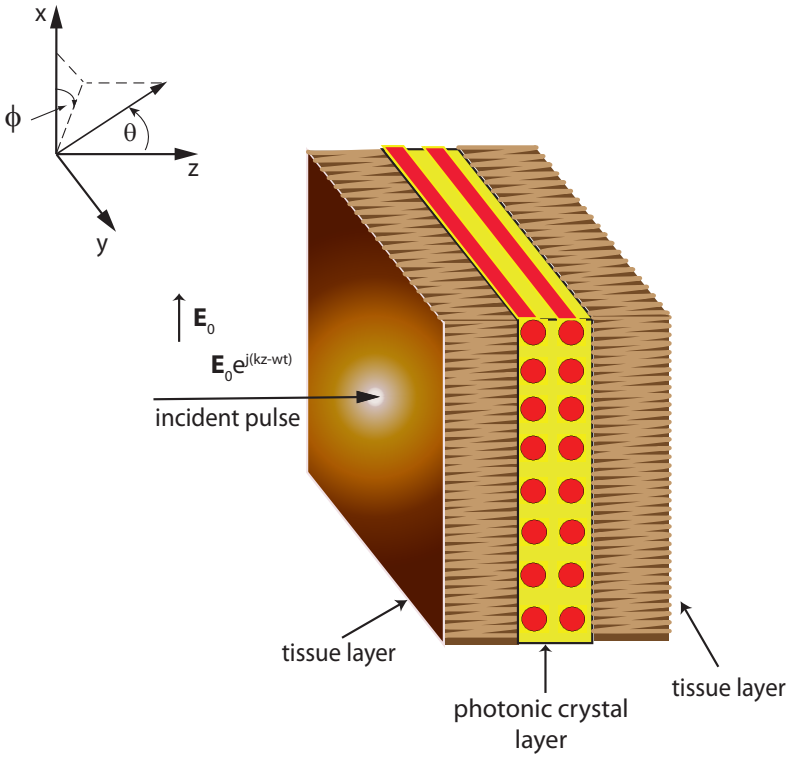

Figure C.1: Photonic crystal implanted in biological tissue

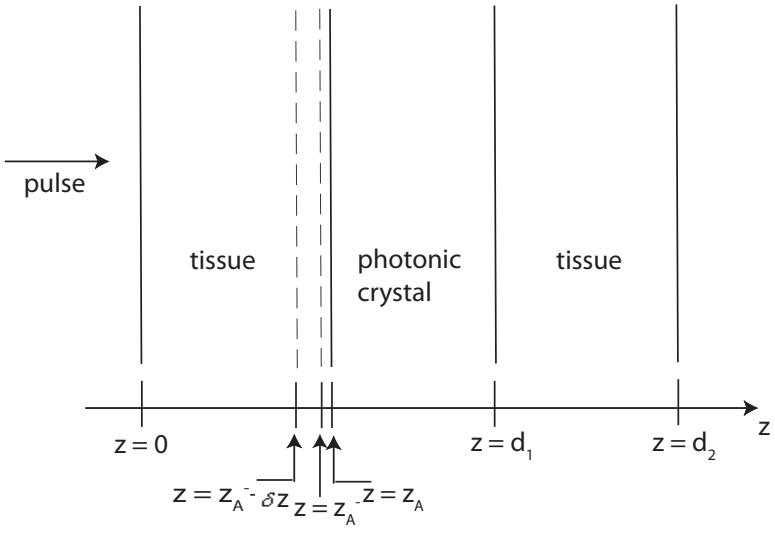

Figure C.2: End elevation of the tissue-photonic crystal model

and a layer of a photonic crystal structure, and Fig. C.2 shows the end elevation of Fig. C.1. A short laser pulse is incident on the tissue layer as shown. In general,

due to the index mismatch at the interface, radiation is reflected. Even though the proposed method can easily handle such reflections at interfaces, due to the increased mathematical complexity in formulation which masks the main points of proposed algorithm, the analysis is limited to an index-matched surrounding at the left boundary of the tissue layer as well as at the right boundary of the photonic crystal layer. However, the reflections at the tissue-photonic crystal interface and photonic crystal-tissue interface will be taken into consideration with a detailed formulation.

Modeling pulse propagation up to the tissue-photonic crystal interface is the same as that for the metal screen example discussed in Chapter 8. The phase at this interface can be obtained by solving the TIE using the full multigrid algorithm, and the electric and magnetic fields can be obtained using Eq. (8.3) and Eq. (8.4).

Once the incident electric and magnetic fields at the interface have been obtained, in order to calculate the field distribution inside the photonic crystal structure, the reflectance and transmittance at the tissue-photonic crystal interface should be known.

The photonic crystal structure can be modeled using an effective refractive index, η_{eff}, which can be obtained using [11]

$$\nabla_{\mathbf{k}}\omega = \frac{c}{\eta_{eff}}\hat{\mathbf{k}}, \tag{C.1}$$

where $\nabla_{\mathbf{k}} = \frac{\partial}{\partial k_x}\mathbf{u}_x + \frac{\partial}{\partial k_y}\mathbf{u}_y + \frac{\partial}{\partial k_z}\mathbf{u}_z$, ω is the angular frequency, $\mathbf{k}$ is the wave vector, $\hat{\mathbf{k}}$ is the unit vector parallel to $\mathbf{k}$ and $\mathbf{u}_x$, $\mathbf{u}_y$ and $\mathbf{u}_z$ are unit vectors along x, y and z axes, respectively. The relationship between the angular frequency,

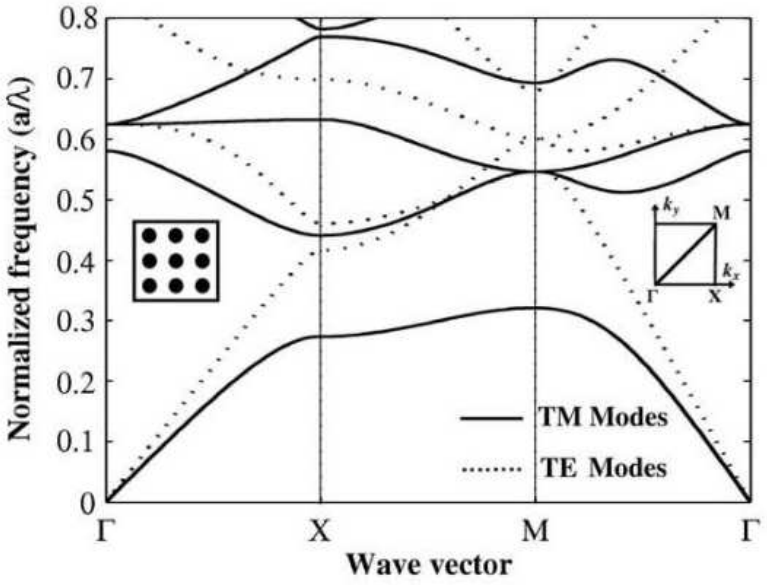

Figure C.3: Band diagram of a square lattice composed of cylindrical dielectric rods, with a relative permittivity of 9 and a radius of 0.2 times the period of the lattice, in air [10].

ω, and the wave number, $\mathbf{k}$, is given by the dispersion relation of the photonic crystal [11]. This relationship can be calculated and plotted in a band diagram. Figure C.3 shows the band diagram of a square lattice composed of cylindrical dielectric rods, with a relative permittivity of 9 and a radius of 0.2 times the period of the lattice, in air, from reference [10]. It is evident from Eq. (C.1) that the effective refractive index of the photonic crystal structure, corresponding to a particular wave number, can be found using the gradient of its band diagram.

Once the effective refractive index is calculated, the transmission coefficient can be approximated by that of a uniform medium [11]. Let the amplitude of the incident electric vector be E and $E_{\parallel}$ and $E_{\perp}$ be the components parallel and perpendicular to the plane of incidence, respectively. Then, from Fresnel formulae

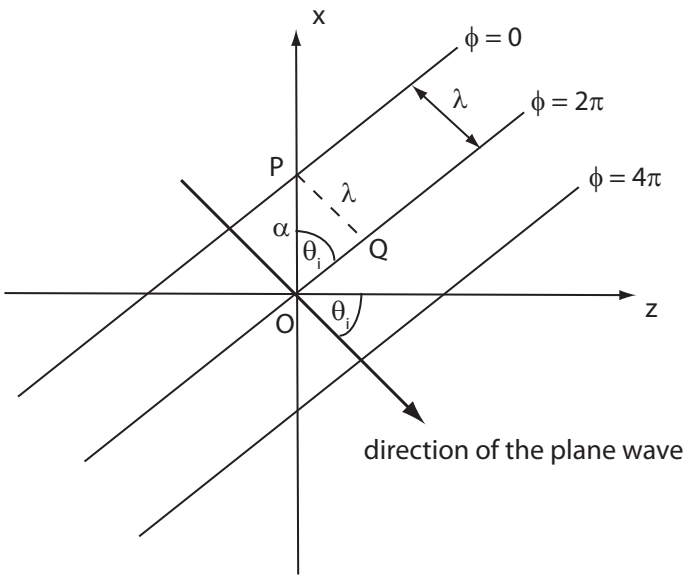

Figure C.4: A plane wave in two-dimensional geometry.

and using Snell's law, the transmitted electric vector can be obtained by [12]

$$T_{\parallel} = \frac{2\eta_T \eta_{eff} \cos\theta_i}{\eta_{eff}^2 \cos\theta_i + \eta_T \sqrt{\eta_{eff}^2 - \eta_T^2 \sin^2\theta_i}} E_{\parallel}, \tag{C.2}$$

and

$$T_{\perp} = \frac{2\eta_T \cos\theta_i}{\eta_T \cos\theta_i + \sqrt{\eta_{eff}^2 - \eta_T^2 \sin^2\theta_i}} E_{\perp}, \tag{C.3}$$

where η_{eff} is the effective refractive index of the photonic crystal, η_T is the refractive index of the tissue and θ_i is the angle of incidence of the wave. Hence, in order to find the transmission coefficients using the above equations, the angle of incidence, θ_i, of the wave should be found first. Figure C.4 shows a plane wave of λ wavelength making an angle θ_i with the z-axis. In this figure, $PQ = \lambda$ and $\angle POQ = \theta_i$. If PO is taken to be α,

$$\alpha = \frac{\lambda}{\sin\theta_i}, \tag{C.4}$$

and

$$\begin{aligned} \frac{\partial \phi}{\partial x} &= \frac{2\pi}{\alpha}, \\ &= \frac{2\pi}{\lambda} \sin\theta_i. \end{aligned} \tag{C.5}$$

Therefore, for a two-dimensional geometry,

$$\begin{aligned} \theta_i(x) &= \sin^{-1}\left(\frac{\lambda}{2\pi}\frac{\partial \phi}{\partial x}\right), \\ &\approx \frac{\lambda}{2\pi}\frac{\partial \phi}{\partial x} \quad \text{for small} \theta_i. \end{aligned} \tag{C.6}$$

Similarly, for a three-dimensional geometry,

$$\begin{aligned} |\theta_i(x,y)| &= \sin^{-1}\left(\frac{\lambda}{2\pi}|\nabla_{xy}\phi|\right), \\ &\approx \frac{\lambda}{2\pi}|\nabla_{xy}\phi| \quad \text{for small} \theta_i. \end{aligned} \tag{C.7}$$

Hence, for a plane wave incident on the tissue-photonic crystal interface,

$$|\nabla_{xy}\phi_A| = \frac{2\pi}{\lambda}\sin\theta_i. \tag{C.8}$$

Thus, the angle of incidence can be obtained by

$$|\theta_i| = \sin^{-1}\left[\frac{\lambda}{2\pi}|\nabla_{xy}\phi_A|\right]. \tag{C.9}$$

The phase profile at $z = z_A$, obtained using the phase retrieval technique discussed in Chapter 7 can be used to find the quantity $|\nabla_{xy}\phi_A|$ of Eq. (C.9).

The field at each point on the tissue-photonic crystal interface can be resolved into parallel and perpendicular components and Eq. (C.2) and Eq. (C.3) can be used to find the transmitted field components. Then, the two transmitted com-

ponents can be combined to find the resultant transmitted field at each point at this interface.

The next step is to calculate the field distribution inside the photonic crystal. Light propagation through photonic crystal structures is governed by Maxwell's equations [9]. The finite difference time domain technique can be used to solve Maxwell's equations and hence the field distribution at the exit of the photonic crystal layer can be obtained. Commercially available software for modeling photonic crystals may be used for this purpose.

Then, at the photonic crystal-tissue interface the field will be again resolved to a TE and TM wave in order to find the proportion that is transmitted into the tissue layer. At this interface, the reflection coefficients are for the TE wave

$$\Gamma'_{TE} = \frac{\eta_{eff}\cos\theta_i - \sqrt{\eta_T^2 - \eta_{eff}^2\sin^2\theta_i}}{\eta_{eff}\cos\theta_i + \sqrt{\eta_T^2 - \eta_{eff}^2\sin^2\theta_i}}, \tag{C.10}$$

and for the TM wave,

$$\Gamma'_{TM} = \frac{\eta_T^2\cos\theta_i - \eta_{eff}\sqrt{\eta_T^2 - \eta_{eff}^2\sin^2\theta_i}}{\eta_T^2\cos\theta_i + \eta_{eff}\sqrt{\eta_T^2 - \eta_{eff}^2\sin^2\theta_i}}. \tag{C.11}$$

Once the field transmitted into the tissue layer is obtained, the TE and TM components can be combined to obtain the resultant field. Then, the electric field, $\left(\mathbf{E}_{d_2}\right)$, can be used to obtain the intensity (i.e. the irradiance) using the relationship

$$I = \frac{1}{2}v\epsilon|\mathbf{E}|^2, \tag{C.12}$$

where v and ϵ are the propagation speed and the permittivity in the medium, respectively. Once the irradiance profile at the plane $z = d_2$ is obtained, it should

be converted back to a radiance profile so that the PTE can be used to model the light propagation beyond this plane as for the example with an implanted metal screen. This can be carried out using the technique discussed in Chapter 8. The method proposed in Chapter 6 can then be used to model the light propagation through the remaining layers of tissue.

References

[1] S. Kumar, K. Mitra, and Y. Yamada, "Hyperbolic damped-wave models for transient light-pulse propagation in scattering media," *Applied Optics*, vol. 35, pp. 3372–3378, 1996.

[2] W. D. Burnett, "Evaluation of laser hazards to the eye and the skin," *American Industrial Hygiene Association Journal*, vol. 30, no. 6, pp. 582–587, 1969.

[3] S. V. Gaponenko, "Effects of photon density of states on Raman scattering in mesoscopic structures," *Physical Review B*, vol. 65, p. 140303, 2002.

[4] L. Florescu and X. Zhang, "Semiclassical model of stimulated Raman scattering in photonic crystals," *Physical Review E*, vol. 72, p. 016611, 2005.

[5] F. J. Garcia-Vidal and J. B. Pendry, "Collective theory for surface enhanced Raman scattering," *Physical Review Letters*, vol. 77, pp. 1163–1166, 1996.

[6] M. Moskovits, "Surface-enhanced spectroscopy," *Reviews of Modern Physics*, vol. 57, pp. 783–826, 1985.

[7] M. Premaratne, E. Premaratne, and A. J. Lowery, "The photon transport equation for turbid biological media with spatially varying isotropic refractive index," *Optics Express*, vol. 13, pp. 389–399, 2005.

[8] C. C. Handapangoda, M. Premaratne, L. Yeo, and J. Friend, "Laguerre Runge-Kutta-Fehlberg method for simulating laser pulse propagation in biological tissue," *IEEE Journal of Selected Topics in Quantum Electronics*, vol. 14, pp. 105–112, 2008.

[9] J. D. Joannopoulos, R. D. Meade, and J. N. Winn, *Photonic Crystals : Molding the Flow of Light*. New Jersey: Princeton University Press, 1995.

[10] J. M. Lourtioz, H. Benisty, V. Berger, and J. M. Gerard, *Photonic Crystals: Towards Nanoscale Photonic Devices*, 2nd ed. Verlag Berlin Heidelberg: Springer, 2008.

[11] K. Sakoda, *Optical Properties of Photonic Crystals*, 2nd ed. Germany: Springer, 2005.

[12] M. Born and E. Wolf, *Principles of Optics*, 7th ed. Cambridge: Cambridge University Press, 1999.